





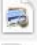













2003 Hall Hammer Hansen Harren Hattori Ho Hogt Horsely Hsiung Hu Huefner Hunter Hupfer Hlady Hibbs Caldwell Herron Dryden

ew Arrange By Action Share Edit Tags

ame	^	Date Modified	Size	Kind
 Hall 1979 ESCA Monolayers ma king.pdf		Aug 11, 2006, 6:50 PM	1.7 MB	PDF D
 Hammer 2000 Biolum Classrm.pdf		Feb 10, 2006, 7:58 PM	460 KB	PDF D
 Hansen 1988 Lysozyme Adsorption XPS ely horsley herron hlady.pdf		Aug 23, 2014, 8:41 AM	3.5 MB	PDF D
 Harren 1975 Cells Surfaces Polym...reprints hill lyman hibbs smith.pdf		Nov 10, 2018, 7:55 PM	485 KB	PDF D
 Hattori 1978 HEMA Surface Tension king.pdf		Sep 16, 2010, 7:01 PM	291 KB	PDF D
 Hattori 1985 Fibroblasts hibbs gregonis king.pdf		Aug 11, 2006, 7:25 PM	1.6 MB	PDF D
 Ho 1991 2D Electrophoresis nyquist caldwell hlady.pdf		Aug 12, 2006, 9:05 PM	3.5 MB	PDF D
 Hogt 1985 Wetting Zeta Potentials gregonis kim dankert feijen.pdf		Aug 13, 2006, 9:16 PM	3.2 MB	PDF D
 Horsley 1987 Lysozyme TIRF Brash bk herron hlady.pdf		Aug 13, 2006, 9:29 PM	2.2 MB	PDF D
 Horsley 1991 Adsorption Lysozyme Quench Herron Hlady.pdf		Oct 11, 2006, 8:32 PM	2 MB	PDF D
 Hsiung 1997 ICPMS Interferences Costa Ash.pdf		Oct 11, 2006, 8:42 PM	2.8 MB	PDF D
 Hu 85 Pyro Kapton Polyimide.pdf		Oct 12, 2006, 9:45 PM	936 KB	PDF D
 Hu 87 ESR Pyro Polyimide DeVries.pdf		Oct 11, 2006, 8:51 PM	1.8 MB	PDF D
 Hu 88 Structure Pyro PolyImide dryden.pdf		Oct 12, 2006, 7:28 PM	1.5 MB	PDF D
 Hu 88 XPS STM Pyro Polyimide Feng.pdf		Oct 11, 2006, 8:58 PM	845 KB	PDF D
 Huefner Waitzman Kern Andrade 2003 IEEE Cost Reducing.pdf		Apr 2, 2003, 12:34 PM	387 KB	PDF D
 Hunter 82 Heart MW PU TASAIO Coleman Kessler.pdf		Oct 11, 2006, 9:03 PM	1.6 MB	PDF D
 Hupfer 81 XPS Paths PdiAcetylenes schupp ringsdorf.pdf		Oct 12, 2006, 8:59 PM	596 KB	PDF D

Hall - 79 ESCA
Mono

PHOTOELECTRON MEAN FREE PATHS IN BARIUM STEARATE LAYERS

S. M. HALL, J. D. ANDRADE,* S. M. MA and R. N. KING

*Department of Materials Science and Engineering and Surface Analysis Laboratory,
University of Utah, Salt Lake City, Utah 84112 (U.S.A.)*

(First received 5 February 1979; in final form 16 March 1979)

ABSTRACT

Barium stearate monolayers were deposited on polished clean germanium and copper substrates using the Blodgett technique. Film thicknesses were determined by ellipsometry by assuming the films were optically isotropic with a refractive index of 1.5 and an absorption coefficient of zero. X-ray photoelectron spectroscopy intensity ratios, obtained at 223 K to minimize vaporization, were used to determine electron inelastic mean free paths (IMFP) in the barium stearate layers. The substrate photoelectron lines cover a binding energy range of 1200 eV. IMFP values range from approximately $27 \pm 5 \text{ \AA}$ at about 230 eV to $65 \pm 12 \text{ \AA}$ at about 1480 eV kinetic energy. The approximately linear shape of this function, together with the throughput function of the instrument, suggests that over the binding energy range of 0-600 eV, the photoelectron mean free paths and throughput effects in the Hewlett-Packard instrument approximately cancel.

INTRODUCTION

The interpretation of X-ray photoelectron spectroscopy data often requires information on electron mean free paths as a function of electron kinetic energy in a variety of materials. Such data are important in determining the escape depth or the sampling depth from which the X-ray photoelectron spectroscopy signal arises in order to evaluate the surface sensitivity or insensitivity of a particular experiment properly and to perform quantitative analyses [1]. Mean free path data as a function of photoelectron kinetic energy are required in order to quantitate properly regions of the photoelectron spectrum differing widely in binding energy. A number of authors have argued that photoelectron mean free paths in various classes of solids should be considerably different [2]. Others argue that photoelectron mean free paths in solids ought to be approximately the same and should follow the same kinetic energy function [3].

* To whom correspondence and reprint requests should be addressed.

A number of studies have appeared in which X-ray photoelectron mean free paths in organic solids have been measured [3-6]. The most common method utilizes the organic overlayer technique in which a homogeneous organic thin film of known thickness is deposited on an appropriate substrate, generally a metal. X-ray photoelectron spectra are then determined for the main photoelectron lines of the substrates as well as for those of the film. The film and substrate peak intensities are a function of film thickness. It is usually assumed that substrate line intensities decay exponentially with increasing thickness of the organic overlayer and that the organic overlayer line intensity increases until a signal corresponding to an infinite film thickness is obtained. The equations and expressions have been presented in the literature [3] and need not be repeated here. Another approach is to utilize essentially infinitely thick solids of different types and, knowing the photoelectric cross-sections, to measure absolute intensities directly and utilize this information for determining photoelectron mean free paths [4].

The range of values at present available in the literature extends from the work of Clark and Thomas [3] as a lower limit to the works of Cadman et al. [4] and Evans et al. [5] as more or less an upper bound. The range in values is quite considerable; the issue is still controversial and unsettled [7, 8].

Our own studies were initiated largely for internal use in the Surface Analysis Laboratory. In view of the present controversy, it may be useful to present them to the scientific community. The study is based on organic overlayers deposited on well characterized metal substrates with photoelectron lines of widely varying kinetic energies, for the purpose of obtaining photoelectron mean free paths as a function of kinetic energy on a commercial spectrometer.

MATERIALS

Germanium and copper were chosen as substrates for several reasons: (1) availability; (2) characterized optical properties; (3) the photoelectron lines from germanium and copper cover a wide range of kinetic energy and yet overlap sufficiently to provide a test for the possible effect of the properties of the substrate on electron mean free path data. Polished germanium single crystals were obtained from Harrick Scientific Corporation, Ossining, New York. High-purity (99.999%) copper was obtained locally. The copper samples were polished with 0.5- μ m alumina paste, washed in distilled water, ultrasonically cleaned in methanol, and dried in a laminar flow filtered air bench [9]. Film thicknesses were obtained from ellipsometry data, using a Rudolph Research model RR2000 automatic laser ellipsometer with a 6328-Å wavelength and a 70° angle of incidence in air. A refractive index, n , for barium stearate monolayers of 1.50 was assumed; the absorption

coefficient, k , was assumed to be zero [10]. Given these assumptions the organic film thickness is a simple calculation from straightforward ellipsometry equations [11]. Barium stearate monolayers were prepared in a conventional Langmuir trough by standard methods [12] and transferred to the clean metal substrates by withdrawing the previously immersed metal substrate through the film and up into the air phase [9]. The solution was 3×10^{-5} M barium chloride and 5×10^{-4} M KHCO_3 with a pH of 7.0–7.2. Barium stearate was deposited onto the trough surface from a hexane solution. The compression pressure of the monolayer was maintained at $16\text{--}17 \text{ dyn cm}^{-1}$. The layers were transferred to the solid at a rate of 0.5 cm min^{-1} . Deposition ratios were monitored by comparing the geometric area of the substrate to the change in the area of the monomolecular film maintained at constant pressure.

A potential problem with such layers used for high vacuum photoelectron spectroscopy may be the vacuum stability of the films at $10^{-7}\text{--}10^{-9}$ torr. A number of previous studies suggested the films might not be vacuum stable. For example, Gaines and Roberts [13] showed that for barium stearate up to 10% of the film disappears upon pumping at a 10^{-6} -torr vacuum for 30 min at room temperature. For stearic acid the vapor pressures can be considerably higher, leading to a greater loss under the same conditions.

The vacuum stability of the films was evaluated at 223 K at 1×10^{-9} torr. At this temperature hydrocarbon and other impurities in the vacuum could be expected to condense on the sample and increase the apparent thickness of any layer. To test the cleanliness of the vacuum a copper sample was inserted, cooled to 223 K and repeated carbon and copper scans taken as a function of time. No mechanical pumping or oil diffusion pumping was used. No significant change in carbon or copper intensity occurred in 2 h of vacuum exposure. The same experiment was repeated for barium stearate monolayers and multilayers deposited on copper substrates. Samples were handled and loaded in a dry nitrogen atmosphere. There was no detectable contamination nor loss of organic film at 223 K for up to 1 h of vacuum exposure, the maximum time utilized for these studies. We thus conclude that the films are stable at 223 K for the purposes of this study; we further conclude that no significant hydrocarbon contamination occurred during the photoelectron spectroscopy analyses.

X-ray photoelectron spectroscopy was done with a Hewlett-Packard 5950B ESCA spectrometer using monochromatic $\text{Al K}\alpha_{1,2}$ radiation. The sample X-ray source analyzer geometry is such that the take-off angle with respect to the sample normal is 51.5° [14]. Photoelectron spectra were obtained utilizing ten scans over a 20-eV binding energy range. The carbon peak was scanned on each and every sample. Because the metal substrates were not sputter-cleaned in vacuum, each initial metal sample did contain a layer of organic contamination as determined from the carbon scans. This, of course, influenced the ellipsometry readings, so that the substrate optical

TABLE 1
ORBITALS SCANNED AND ENERGIES SAMPLED FROM EACH OF THE SUBSTRATES

Substrate	Orbital	Binding energy (eV)	Kinetic energy (eV)
Cu	3d	3	1480
	3p _{3/2, 1/2}	75	1408
	3s	122	1361
	Auger		
	L ₃ M ₄₅ M ₄₅	"570" ^a	913
	Auger		
	L ₃ M ₂₃ M ₄₅	"650" ^a	833
	2p _{3/2}	932	551
	2p _{1/2}	952	531
Ge	3d _{3/2, 5/2}	30	1453
	3p _{1/2, 3/2}	122	1361
	3s _{1/2}	182	1301
	Auger		
	L ₃ M ₄₅ M ₄₅	"342" ^a	1141
	2p _{3/2}	1217	266

^a Position of Auger peak in photoelectron spectrum.

parameters represent an average of the pure metal, metal oxide and organic contamination layer. Table 1 lists the binding energies, atomic orbitals, scan conditions, and kinetic energies for the two different substrate materials.

The basic experiment was as follows: a clean substrate was examined in the ellipsometer to determine substrate optical constants. The same substrate was then utilized in the electron spectrometer and the intensities of the appropriate lines determined and recorded. The substrate was then removed and the organic film deposited on it; the sample was analyzed by ellipsometry to obtain the film thickness, inserted into the electron spectrometer, and cooled to 223 K [9]. The photoelectron intensities were then obtained. The same probe position was used for each experiment. The sample was again studied by ellipsometry to confirm the film thickness and optical properties. The experimental conditions for the examination of coated and uncoated samples were essentially identical.

The electron mean free paths were determined by simple peak intensity ratios of the coated and uncoated samples, thus instrument throughput function and photoelectron cross-section corrections were not necessary.

RESULTS AND DISCUSSION

Ellipsometry readings were taken at four different sites on the sample in

TABLE 2

COMPILATION OF THE EXPERIMENTAL POINTS OBTAINED ALONG WITH THE AVERAGE INELASTIC MEAN FREE PATH, λ , FOR EACH PEAK AND THE STANDARD DEVIATION s FOR THIS AVERAGE

BE	KE	Sample	λ	$\bar{\lambda}$	s
3	1480	Cu1	57.2	65.2	12.2
		Cu2	82.6		
		Cu3	64.3		
		Cu4	56.5		
30	1453	Ge1	67.8	65.6	11.8
		Ge2	53.3		
		Ge3	80.9		
		Ge4	60.5		
75	1408	Cu1	56.9	64.4	13.0
		Cu2	83.8		
		Cu3	60.3		
		Cu4	56.7		
122	1361	Cu1	43.3	58.5	13.5
		Cu2	55.4		
		Cu3	77.3		
		Cu4	48.1		
		Ge1	61.3		
		Ge2	49.9		
		Ge3	79.9		
		Ge4	52.4		
182	1301	Ge1	62.4	63.6	1.0
		Ge2	64.3		
		Ge4	63.8		
342	1141	Ge1	56.3	49.8	8.8
		Ge2	41.1		
		Ge3	58.4		
		Ge4	43.3		
570	913	Cu1	38.2	40.8	4.3
		Cu2	46.7		
		Cu3	41.1		
		Cu4	37.2		
650	833	Cu2	47.5	42.6	5.0
		Cu3	37.5		
		Cu4	42.8		
932	551	Cu1	31.3	32.1	5.7
		Cu2	40.4		
		Cu3	28.8		
		Cu4	27.8		

TABLE 2 (Continued)

BE	KE	Sample	λ	$\bar{\lambda}$	s
952	531	Cu1	31.3	33.4	8.9
		Cu2	46.3		
		Cu3	25.9		
		Cu4	29.9		
1217	266	Ge1	28.8	26.6	4.7
		Ge2	22.1		
		Ge3	32.1		
		Ge4	23.2		

the region which would be examined by X-ray photoelectron spectroscopy. The four different regions sampled about 50% of the total surface area examined by XPS. At each different reading site, four different polarizer settings were chosen and azimuth (α) and ellipticity (ϵ) recorded for each of these settings [11]. The details of the ellipsometry calculations are available [9, 11]. α and ϵ were converted to Δ and ψ by classical equations [11] and then utilized to calculate the refractive index, n , and the absorption coefficient, k , for the substrate [9]. The coated samples were measured in the same way; thickness was calculated from the α and ϵ data by using the deduced n , k values for the substrate and assuming n for the film was 1.5 and k for the film was zero. The values obtained were in general agreement with published data for the thickness of barium stearate films [9, 12]. The thickness calculated was corrected for the take-off angle geometry of 51.5° to obtain an effective film thickness for the particular experiment. The intensity values for the particular photoelectron line for each substrate and substrate-film combination were then appropriately ratioed and the mean free path, λ , was calculated from the equation: $\lambda = d' \ln I/I_0$, where d' is the effective film thickness; $d' = d/\cos 51.5^\circ = 1.606d$, where d is the actual film thickness; I_0 is the intensity of the particular line on the uncoated substrate; and I is the intensity on the stearate-coated substrate.

Table 2 is a compilation of the experimental points obtained and the λ values calculated for each peak. These values are plotted in Fig. 1 as a function of both binding energy and kinetic energy; the kinetic energy is estimated to be $1487 - \phi - \text{BE}$, where BE is the charge-corrected binding energy, and ϕ is assumed to be 4.0 eV, the photoelectric work function of gold. The center line in Fig. 1 is the average data. The upper and lower lines represent the + and - single standard deviation values of the fitted curve. Although the data have been plotted as and fitted to a second-order polynomial [9], it is clear that it can be fitted just as well by a straight line (Fig. 2). These studies suggest that over the kinetic energy range of the Hewlett-Packard instrument photoelectron mean free paths in barium

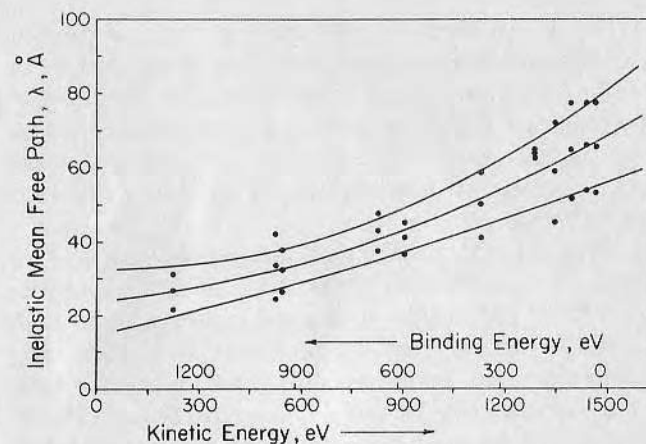


Fig. 1. Binding energy and kinetic energy vs. mean free path. Center line is the best-fit polynomial [9] for the kinetic energy range from 250 to 1480 eV of the average values (Table 2); upper and lower curves are the best-fit polynomials for the $+$ and $-$ single standard deviations (Table 2).

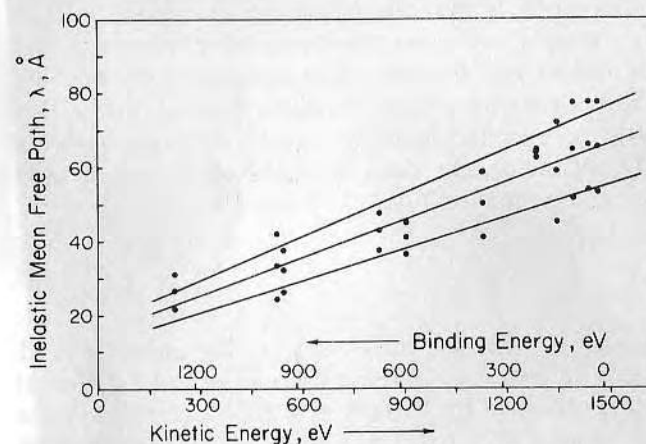


Fig. 2. Same as Fig. 1 but plotted assuming a linear function for the kinetic energy range from 250 to 1480 eV.

stearate monolayers range from approximately $27 \pm 5 \text{ \AA}$ at 230 eV to $65 \pm 12 \text{ \AA}$ at about 1480 eV kinetic energy. The data do not suggest any special exponential dependence on kinetic energy.

Although the film molecules may be tilted with respect to the surface normal, the tilt would not be expected to be very great. In view of the 51.5° take-off angle in this experiment, it is unlikely that channeling could have played any major role in these experiments.

Since one might be tempted to use such data to attempt to depth-profile organic surfaces non-destructively by ratioing photoelectron lines of

different binding energies, it is appropriate to examine the instrument throughput function for the Hewlett-Packard spectrometer. Some estimates have been made by the Hewlett-Packard design staff during the early design of the instrument. The throughput function increases in a roughly linear manner with binding energy in the range of 0–600 eV and curves upward significantly for higher binding energy (lower kinetic energy) electrons [9]. Because of the nature of the throughput function and the mean free path—kinetic energy relationship (Fig. 1), the product of the inelastic mean free path, λ , and the throughput is approximately constant over the binding energy range of 0 to about 600 eV [9]; thus, in this range, the effects of λ and throughput approximately cancel. Neglecting mean free path and throughput in this binding energy range introduces an error no greater than about 10% [9]. This is not true, however, for binding energies above 600 eV as the throughput-IMFP product is a strong function of binding energy in this region [9]. Better measurements will, of course, provide better throughput and mean free path values. Until then, for semi-quantitative ESCA purposes with the Hewlett-Packard instrument, one can assume the two effects approximately cancel over the range of 0–600 eV binding energy.

A serious deficiency in this study is that the organic contamination layer may affect the ellipsometry results and thus the deduced thickness of the organic layer. Although the values we obtained were reasonable considering the deposition ratios and the known properties of barium stearate layers, this is a possible error and should be checked in more refined studies. Substrate effects did not significantly influence the experimental results as indicated by the overlap of the copper and germanium data in Tables 1 and 2.

CONCLUSION

The fact that these data agree with the data obtained by Cadman et al. [4] and Evans et al. [5] using an entirely different technique and a different instrument, and with the data obtained by Anderson and Swalen [6] using a similar technique, suggests that the errors may not be too great. Our intention is to use these numbers as estimates until better numbers become available. The question of mean free paths in organic materials is still largely open, as evidenced by the substantial controversies in the literature [7, 8].

ACKNOWLEDGEMENTS

This work was supported in part in NIH grants HL 16921 and HL 18519. The support of the University of Utah Faculty Research Committee is appreciated. The assistance of Dr. Mike Kelly, Surface Science Laboratories and Hewlett-Packard Co. in providing information on the instrument throughput function is greatly appreciated.

REFERENCES

- 1 C. J. Powell, *Am. Lab.*, April (1978) 17.
- 2 R. Holm and S. Storp, in A. R. West (Ed.), *Molecular Spectroscopy*, Heyden, London 1977, p. 482.
- 3 D. T. Clark and H. R. Thomas, *J. Polym. Sci., Polym. Chem. Ed.*, 15 (1977) 2843.
- 4 P. Cadman, G. Gossedge and J. D. Scott, *J. Electron Spectrosc. Relat. Phenom.*, 13 (1978) 1.
- 5 S. Evans, R. G. Pritchard and J. M. Thomas, *J. Phys. C*, 10 (1977) 2483.
- 6 H. R. Anderson, Jr. and J. D. Swalen, *J. Adhesion*, 9 (1978) 197.
- 7 P. Cadman, S. Evans, G. Gossedge and J. M. Thomas, *J. Polym. Sci., Polym. Lett.*, 16 (1978) 461.
- 8 D. T. Clark, H. R. Thomas and D. Shuttleworth, *J. Polym. Sci., Polym. Lett.*, 16 (1978) 465.
- 9 S. Hall, B.S. Thesis, Department of Materials Science and Engineering, University of Utah, August 1977; single copies available upon request.
- 10 R. Steiger, *Helv. Chim. Acta*, 54 (1971) 2645.
- 11 H. R. Muller, *Adv. Electrochem. Electrochem. Eng.*, 9 (1973) 167.
- 12 G. L. Gaines, Jr., *Insoluble Monolayers at Liquid-Gas Interfaces*, Interscience N.Y., 1966, 386 pp.
- 13 G. L. Gaines, Jr. and A. W. Roberts, *Nature*, 197 (1963) 787.
- 14 M. A. Kelly and C. E. Tyler, *Hewlett-Packard J.* July (1973) 2.

[43] Bioluminescence as a Classroom Tool for Scientist Volunteers

By MARA HAMMER and JOSEPH D. ANDRADE

"One of the best tools any teacher can have is a person who knows and understands science and technology."¹ A practicing scientist.

Background

A major shift in science education is now being implemented. There is a growing interest in hands-on, discovery-based science education. There is also interest in treating science as a coherent, integrated field of inquiry that can deal with complex multidisciplinary subjects and problems.²

Bioluminescence is an ideal subject with which to experience the scientific process and critical science concepts and themes, particularly in upper elementary and junior high school.³ We have developed bioluminescent dinoflagellate cultures that enable teachers and students to experience bioluminescence, as well as closed ecosystems, circadian rhythms, and a variety of principles related to protozoa, optics, and chemistry. Much of the experience is conducted in the dark. Science in the dark has been an effective way to reduce science anxiety and fears and to encourage teachers to develop fresh, positive, and instructive attitudes toward hands-on science in their classrooms.

The intrigue of bioluminescence reaches far beyond the science classroom. For example, the beautiful blue light can be an inspiration to students interested in creative writing. Experiences with the dinoflagellate, *Pyrocystis lunula* (little fire moons), can begin with a poem:

Little fire moons dance in the sea
Making the waves glow mysteriously
Little fire moons come play with me.
And we will dance together in the sea

¹ Sharing Science With Children: A Survival Guide for Scientists and Engineers, North Carolina Museum of Life and Science, P.O. Box 15190, Durham, North Carolina 27704.

² F. J. Rutherford and A. Ahlgren, "Science for All Americans (The Project 2061 Report)." Oxford Univ. Press, 1990.

³ M. G. Jones, Bioluminescence: Activities that will receive glowing reviews. *The Science Teacher*, Jan. 19 (1993).

Tiny artists can be captivated by their mystery and beauty. Aldo Leopold, the noted conservationist, relates an account of when he first became a conservationist. He saw a gray wolf die and noticed the "fierce green fire" in her eyes. It was a moment he never forgot.⁴ Perhaps seeing the "cold blue fire" of nature's living lights can inspire others in the same way.

There is a growing awareness of the need for scientists and other professionals as role models in school classrooms. Students need to learn science skills in elementary school that can be built upon in the upper grade levels. Unfortunately, many elementary school teachers do not have any science background and are, therefore, uncomfortable teaching science. In many cases they do not have the resources to conduct meaningful science experiments. Bioluminescence is a wonderful tool to help students and teachers start thinking and acting like scientists. Practicing scientists are needed as regular, serious volunteers in the classroom. By volunteering your time at a local elementary, middle, or high school, being a guest speaker at an after school science club, being a friendly resource for local teachers, or allowing field trips through your laboratory, you can sow the seeds of science and make a lasting impact on impressionable young minds and on their teachers.

The Need for Scientists in Science Education

The structure of education in the United States is based on the concept that what students learn in elementary school is built upon in middle and high school. "Failure to educate and excite students in science in the early years is a primary reason for the inadequacy of the learning of science in later years."^{5,6} Unfortunately, many students do not receive a background in science. What they do receive is often book learning, rote answers and memorization.⁷ They are not taught to think like scientists. They are not taught to find a problem and to test a hypothesis. Scientists in the classroom provide a vital link in encouraging today's students to become tomorrow's responsible, informed citizens and scientists. In most cases, when the student reaches college, it is much harder to capture their interest, and it is a daunting task to teach them basics they should have learned in middle and high school.

The way science is commonly taught leads many students to believe it

⁴ A. Leopold, "A Sand County Almanac." Ballantine Books, New York, 1959.

⁵ National Research Council, "Fulfilling the Promise: Biology Education in the Nation's Schools," p. 6. National Academy Press, 1990.

⁶ Academic Preparation in Science: "Teaching for the Transition from High School to College," 2nd ed. The College Entrance Examination Board, New York, 1990.

⁷ Foundations: The Challenge and Promise of K-8 Science Education Reform, National Science Foundation, NSF 97-76, p. 68.

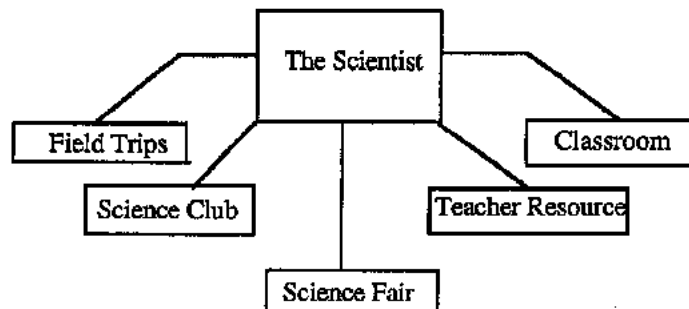


FIG. 1. Ways in which practicing scientists can participate in school-based science education.

is a "hard subject." A possible reason for this attitude is the difficulty of relating abstract concepts to concrete, real-life situations. The National Research Council has recommended that "the major objective of elementary school science courses should be to foster positive attitudes about and respect for the natural world, rather than to acquire detail. Children in grades 3–6 might be especially sensitive, because it is in those grades that "likes" and "dislikes" become established. . . . Exciting experiences in the early grades can lead to science-related career decisions."⁵ This is why it is vital that scientists become involved in precollege education.

Involvement

There are many ways to become involved in K–12th grade science education and many resources are available to help you have a productive, enjoyable visit and to establish a relationship with the students and teacher. Some of these resources include "Chemists in the Classroom," a brochure produced by the American Chemical Society,⁸ and "Sharing Science with Children: A Survival Guide for Scientists and Engineers"¹ (Fig. 1).

Becoming involved is the first and sometimes the most difficult step. A good way to begin is to participate in one of the national "Weeks." National Science and Technology Week has been designated by the National Science Foundation as the last week in April, National Chemistry Week is usually in early November, and National Engineering Week is the third week in February. Other professional societies also support community outreach programs through schools, museums, and other institutions. Contact your

⁸ "Chemists in the Classroom" Prehigh School Science Office, American Chemical Society, 1155 Sixteenth St., NW, Washington, DC 20036, phone: (202)452-2113.

national professional organization to find out what programs and resources are available. If you are a parent, talk to your child's teacher or school principal about volunteering in the classroom.

Planning your visit: Find out at what level the teacher and the students feel comfortable. Ask for suggestions. Consult with the teacher about the level and depth of your presentation. Find out if the topic, demonstrations, and experiments are appropriate for the age and attention span of your audience. Teachers are not experts in teaching science, but they are experts in teaching children. Remember, you are there to be a role model, to present a lesson and experience on a specific topic, and to offer career information. One of the most interesting topics is *you* and what *you* do.⁸

Presenting the topic: Involve the students in the activities. Doing is a lot more interesting than lecturing. Involve the teacher as well as the students. Do not let the teacher leave. Make it clear to the teacher that your participation is a partnership with him/her. One of your goals is to educate and empower the teacher, as well as the students. Ask questions that encourage students to make predictions, offer explanations, state an opinion, or offer conclusions. Be aware of your vocabulary. Define words that students may not know and relate those terms to common everyday experiences. Use analogies and metaphors. It may be helpful to give the teacher a vocabulary list before your visit. You must connect and relate your topics to the students and to the world around them. It is important that the students leave with the connection between experimental science and practical applications. Remember to emphasize the importance of safety. Demonstrate to students the proper way to handle and dispose of chemicals. If the students are required to wear safety gear, set the example. Before you leave, help set up an experiment that the class can continue. Give the students an assignment that they can complete on their own. Invite them to write, call, or e-mail if they have any questions.^{1,8}

Finally, follow up with the teacher and the class. This is essential to reinforce the concepts that you presented. Ways to follow up can include a return visit to build on what you taught previously or offering suggestions to the teacher on activities that she/he can do with the class to reinforce what was taught. These could include an extension of the science concept, a related science topic, the history of that aspect of science, an experiment that can be done as a class, or ways to connect the science topic with art, literature, or other subjects in the curriculum.

Other ways to become involved are to participate as a judge at a science fair, act as a consultant/advisor to students on their science fair projects, organize or be a guest speaker at an after school science club, provide summer research opportunities for high school students and teachers in

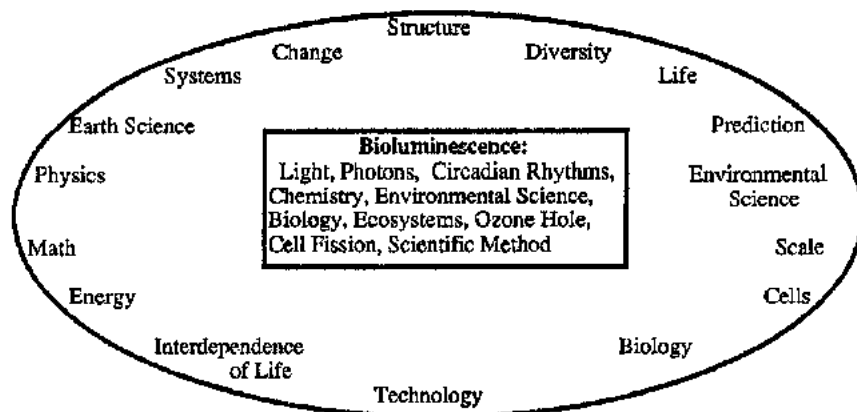


FIG. 2. Some of the Project 2061-Benchmarks for Science Literacy concepts and themes that can be experienced using bioluminescence.

your laboratory or institution, and organize field trips through your research facilities or to a local spot of scientific interest.⁹

What You Can Do with Bioluminescent Dinoflagellates

Benchmarks for Science Literacy–Project 2061¹⁰ is a set of guidelines established by the American Association for the Advancement of Science. The benchmarks are guidelines for what all students should know and be able to do in science at given grade levels (Fig. 2).

Bioluminescent dinoflagellates can be an effective way to teach and reinforce these basic science concepts. Bioluminescent dinoflagellates are an ideal teaching tool because they are unique. Few students or teachers have ever experienced them, so they do not have any preconceived notions about what to expect. It is a subject they have never failed. Much of the teaching and discovery is done in the dark where people are inherently less intimidated.

Bioluminescent dinoflagellates are available from many sources.¹¹ The

⁹ A. K. Campbell Field Trip, 2–3 September, 1994, Marine Biological Association, Plymouth, in "Bioluminescence and Chemiluminescence: Fundamentals and Applied Aspects" (A. K. Campbell, L. J. Kricka, and P. E. Stanley, eds.), p. 232. Wiley, New York, 1994.

¹⁰ American Association for the Advancement of Science, "Benchmarks for Science Literacy (Project 2061)." Oxford Univ. Press, New York, 1993.

¹¹ Source for bioluminescent dinoflagellates: Provasoli-Guillard National Center for the Culture of Marine Phytoplankton (CCMP), Bigelow Laboratory for Ocean Science, P.O. Box 475, McKown Point, West Boothbay Harbor, Maine 04575-0475. <http://ccmp.bigelow.org>, phone: (207)633-2173, fax: (207)633-6584 Carolina Biological, e-mail <http://living@carolina.com>, phone: 1-800-334-5551, fax: 1-800-222-7112.

University of Utah's Center for Science Education and Outreach¹² provides *Pyrocystis lunula* sealed in small polyethylene bags, essentially a "miniecosystem." *Pyrocystis fusiformis* is available through Carolina Biological. We also use dried "sea fireflies" (*Vargula hilgendorfi*) in some of our demonstrations (available from Sigma).

By involving students and teachers in the exploration of topics and phenomena they have never seen before, they experience the scientific process in action and learn basic science skills and processes. Dinoflagellates motivate the asking of questions; the students become detectives solving the mysteries of the world around them. Students learn to understand that hypotheses are to be tested and retested. A simple question such as "why is the light blue" can become a whole research project involving light, photons, optics, evolution, adaptation, and the optical properties of water.

It is very interesting to involve the students and the teacher in the nature of luminescence itself—what is light, where does it come from, how does it originate?—and to observe, compare, and contrast such phenomena as thermal luminescence, fluorescence, phosphorescence, chemiluminescence, and bioluminescence. Chemiluminescent demonstrations are readily available and are exciting for the students.^{13,14} An explanation of the difference between warm and cold light can lead into a discussion of energy efficiency. For example, in a conventional light bulb, 90% of the total energy disappears as heat. The bioluminescent enzyme reaction produces light with almost no heat, which makes it nearly 100% efficient.^{15,16} Various fluorescent minerals and a small UV black light provide a great deal of material for observations, hypotheses, experiments, and discussions. The fluorescent whitener used in most laundry detergents and present in significant quantity on the students' own clothes is a very popular topic. Chemiluminescent light sticks, available in most hardware stores, as well as in science-related gift shops, have been used and experienced by many of the children and teachers, but with little scientific thought or consideration. Once the concept of chemically generated light, so called cool light, is firmly established, then the connection can be made that bioluminescence is basically chemical luminescence produced by living organisms.

¹² Center for Science Education and Outreach, University of Utah, Bioengineering, 50 S Central Campus DR. RM 2480, Salt Lake City, Utah 84112-9202, phone (801)581-4171. e-mail: <http://www.utah.edu/cise/bioluminescence.html>

¹³ H. Brandl, S. Albrecht, and T. Zimmermann, in "Bioluminescence and Chemiluminescence: Molecular Reporting with Photons" (J. W. Hastings, L. J. Kricka, and P. E. Stanley, eds.), p. 196. Wiley, New York, 1997.

¹⁴ F. McCapra, *Methods Enzymol.* **305** [42] 2000 (this volume).

¹⁵ S. Brodin and G. Wettermark, "Bioluminescence Analysis," p. 1. VCH, New York, 1992.

¹⁶ M. Toner, *Int. Wildlife* May/June, p. 33 (1994).

The firefly analogy is always useful and popular. Fireflies have a short season and are unavailable in some parts of the country at any time. A short film clip of fireflies in action is incredibly popular. A particularly good video of bioluminescent organisms, including a good section on fireflies, is David Attenborough's "Talking to Strangers," a program in the *Trials of Life* series.¹⁷ From fireflies one can get into a discussion of marine bioluminescence, including the more spectacular jelly fish and giant squid type species well illustrated in the Attenborough video. We usually use the excuse that it is hard to carry the organisms around, so we prefer to work with microscopic ones, the dinoflagellates. It is useful to begin this discussion with marine bioluminescence as observed by sailors and fishermen throughout history: the blue glow of the sea and of the waves.

Dinoflagellates are unicellular, flagellated organisms. They are found throughout the world in both marine and freshwater environments and are responsible for many of the algae blooms known as red tides. Bioluminescent dinoflagellates are found only in marine habitats. There are no known freshwater bioluminescent dinoflagellates. Most, but not all, of the bioluminescent dinoflagellates are photosynthetic. The best known bioluminescent dinoflagellates are *Gonyaulax polyedra*, *Noctiluca scintillans*, *Pyrodinium bahamense*, and several species of *Pyrocystis*.¹⁸ These dinoflagellates can be cultured in the laboratory or classroom. They require a light/dark cycle with 6–8 hr of darkness in a 24-hr period. They also require moderate temperatures, generally between 11.5 and 21.5°. Bioluminescent dinoflagellates are regulated by a circadian rhythm. They produce light most intensely during their night phase. For classroom presentations the dinoflagellates should receive light at "night" and dark by "day," reversing their normal cycle, to maximize light production during normal classroom hours. In dinoflagellates, bioluminescence is produced in response to mechanical stimulation. Light is also produced when weak acid is added to a sample of dinoflagellates.

Closed Ecosystems

We seal our dinoflagellates in low-density polyethylene bags, using a heat sealer. Each bag becomes its own colony. When we visit classrooms we often get questions about how living things can live in a sealed environment, which leads to a wonderful discussion on closed ecosystems. We talk about

¹⁷ David Attenborough, "Talking to Strangers." *The Trials of Life* series, available from Ambrose Video, 1290 Avenue of the Americas, Suite 2245, New York, NY 10104. The last 15 min of the video are on bioluminescence.

¹⁸ F. J. R. Taylor, "Biology of Dinoflagellates." Blackwell Scientific Publications, Palo Alto, CA, 1987.

what living things need to survive and the different requirements for plants and animals. One of the requirements of *P. lunula* is light. Dinoflagellates are considered "masters of photosynthesis."^{19,20} They have the ability to harvest light in wavelengths that green plants miss and are able to convert light into stored energy very efficiently.²¹ After we discuss the importance of light, we talk about nutrient requirements and how the dinoflagellates use vitamins and minerals from the fortified sea water. The bags we use are semipermeable, allowing the exchange of gases. We also discuss Biosphere²² and the closed systems that will be required for long duration space travel.

Division Rates

Cell division can be studied with the bioluminescent dinoflagellates. Students can set up microscopes focusing on a single cell and can watch daily to see the changes as the cell divides. *P. lunula* divides approximately every 7 days. However, at any point in time a colony of dinoflagellates will have cells in all stages of cell division. A fun activity for students is a cell division scavenger hunt, where the students look for, and draw, as many stages of the dinoflagellates' division process as they can find. For students who have never used a microscope, the dinoflagellates make an interesting subject to learn microscope skills and to teach concepts such as scale. Many elementary classrooms do not have microscopes, so you may need to borrow and bring one or more.

Circadian Rhythms

In humans, a biological clock, or circadian rhythm, is responsible for when we get tired, hungry, and why we feel jet lag. In bioluminescent dinoflagellates, the circadian rhythm regulates when the cell should bioluminesce and photosynthesize.^{23,23a,24} In most cases, the dinoflagellates will only produce light during the "night." The intensity of continuous light

¹⁹ R. Lewis, Photosynthesis the Plankton Way. *Photonics Spectra*, Sept., p. 46 (1996).

²⁰ E. Hoffman, P. M. Wrench, F. P. Sharples, R. G. Hiller, W. Welte, and K. Diederichs, "Structural Basis of Light Harvesting by Carotenoids: Peridinin-Chlorophyll-Protein from *Amphidinium carterea*," *Science* **272**, 1788 (1996).

²¹ A. S. Moffat, Form Follows Function When Plants Harvest Light, *Science* **272**, 1743 (1996).

²² D. A. Sietloff, "Biosphere 2: A World in Our Hands." Biosphere Press, Oracle, Arizona, 1995.

²³ D. Morse, L. Fritz, and J. W. Hastings, "What is the Clock? Transitional Regulation of Circadian Bioluminescence," *Biochem. Physiol.* **94 C** 129 (1989).

^{23a} T. Roenneberg and W. Taylor, *Methods Enzymol.* **305** [?] 2000 (this volume).

²⁴ P. Colepiccolo, T. Roenneberg, D. Morse, W. Taylor, and J. W. Hastings, Circadian Regulation of Bioluminescence in the Dinoflagellate *Pyrocystis lunula*, *J. Phycol.* **29**, 173 (1993).

has a large effect on how the natural clock runs. Different colors of light have different effects on dinoflagellates. For example, bright red light makes the clock "tick" slower, lengthening its day. Continuous blue light shortens the phytoplankton's day.²⁵ You can reset the biological clock in your dinoflagellates so that day is night, manipulating them to glow during class time. To do this, give the dinoflagellates light at night and keep them in the dark during the day. For *P. lunula*, 3 to 4 days are needed for complete resetting of the clock.

Several classroom experiments can focus on circadian rhythms. For example, the physiological changes that occur during the dinoflagellates' night and day phases can be seen by putting one dinoflagellate colony on a regular light-dark cycle where it gets light during the day and darkness at night and a second colony on an alternate cycle where it gets light at night and is in the dark during the day. The class can compare both colonies under the microscope at the same time. Another experiment could be to deprive the dinoflagellates of light completely, give them light continuously, give them varying degrees (1, 2, 5 hr) of light a day or give them different intensities of light and observe the luminescence and physiology of the dinoflagellates over time.

Toxicity/Environment

Bioluminescent dinoflagellates have been used to test sea water for the toxicity of pollutants. Classroom projects involving bioluminescent bacteria can be used as well.^{26,27} To perform this experiment, several different household chemicals can be used. Students can bring the chemicals from home or you can provide them. Chemicals can include laundry soap, bleach, vinegar, milk, baking soda, and oil. Before anything is added to the sample, students should be able to observe and roughly quantitate the dinoflagellates' bioluminescence. A small amount of each chemical is then added to the sample of bioluminescent dinoflagellates. It is important to deal with control experiments and basic chemical parameters such as pH. There are, of course, many measures of toxicity. One might be an acute toxicity, in which the presence of the chemicals directly impacts the chemical/biological nature of the dinoflagellates, directly impairing their ability to produce light. Another form of toxicity might be more "chronic" in nature, perhaps

²⁵ W. J. Cromie, Bioluminescence: Evolution's Novelty. *Harvard Gazette*, Feb. 16, p. 13 (1990).

²⁶ V. A. Kratasyuk, A. M. Kuznov, and J. I. Gitelson, Bacterial Bioluminescence in Ecological Education, in "Bioluminescence and Chemiluminescence: Molecular Reporting with Photons" (J. W. Hastings, L. J. Kricka, and P. E. Stanley, eds.) p. 177. Wiley, New York, 1997.

²⁷ D. Lapota, D. E. Rosenberger, and D. Duckworth, A Bioluminescent Dinoflagellate Assay for Determining Toxicity of Coastal Waters, "Bioluminescence and Chemiluminescence: Fundamentals and Applied Aspects" (A. K. Campbell, L. J. Kricka, and P. E. Stanley, eds.), p. 156. Wiley, New York, 1994.

impairing the organism's health and well-being over a period of several days. Still another may have to do with the ability of the organism to continue to divide and expand the population. The degree of "toxicity" could be measured by how long the dinoflagellates continue to glow.

The conclusions from such experiments can be related to the effects of pollution on the environment. Photosynthetic dinoflagellates and other marine phytoplankton utilize carbon dioxide from the atmosphere. On a global scale, annual phytoplankton photosynthesis is roughly equivalent to that of plants and trees on land. Organic matter, including phytoplankton, settles slowly to the deep ocean in the form of dead particulate matter. This organic carbon is colonized by bacteria and other microorganisms and slowly degrades to carbon dioxide as it descends to the ocean floor. This whole process creates a carbon sink that serves to concentrate carbon dioxide in the deep sea. If phytoplankton cease to exist, the deep sea reservoir of carbon dioxide would eventually equilibrate with the atmosphere, tripling the atmospheric carbon dioxide and altering the earth's climate through the greenhouse effect.²⁸ This discussion can lead to the topics of photosynthesis, the ozone hole,²⁹ the greenhouse effect, and the food web. Photosynthetic dinoflagellates are primary producers.³⁰ Much of the life in the ocean is dependent on phytoplankton, without which there would be very little life in the world's oceans.^{28,31}

By integrating these different concepts students can see that although science is normally separated into small parts in order to be investigated and studied, all the parts are interrelated and interdependent. Bioluminescent dinoflagellates are a valuable tool for teaching integrated science themes and concepts.

Our Experiences^{32,33}

When we introduce students to bioluminescence using dinoflagellates, we make sure the room is completely dark. A room with no windows is

²⁸ S. W. Chisholm, What Limits Phytoplankton Growth? *Oceanus* 35, 36 (1992).

²⁹ R. C. Smith, B. B. Prezelin, K. S. Baker, R. R. Bidigare, N. P. Boucher, T. Coley, D. Karentz, S. MacIntyre, H. A. Matlick, D. Menzies, M. Ondrusek, Z. Wan, and K. J. Waters, "Ozone Depletion: Ultraviolet Radiation and Phytoplankton Biology in Antarctic Waters," *Science* 225, 925 (1992).

³⁰ K. Steidger, Phytoplankton Ecology: A Conceptual Review Based on Eastern Gulf of Mexico Research. *CRC Crit. Rev. Microbiol.*, Sept., p. 49 (1973).

³¹ R. Baum, Phytoplankton Seen as an Atmospheric CO₂ Control. *C & EN*, May 28, p. 7 (1990).

³² J. D. Andrade, J. Tobler, M. Lisonbee, and D. Min, in "Bioluminescence and Chemiluminescence: Status Report" (A. A. Szalay, L. J. Kricka, and P. E. Stanley, eds.), p. 69. Wiley, New York, 1993.

³³ J. D. Andrade, M. Lisonbee, and D. Min, in "Bioluminescence and Chemiluminescence: Fundamentals and Applied Aspects" (A. K. Campbell, L. J. Kricka, and P. E. Stanley, eds.), p. 371. Wiley, New York, 1994.

ideal but black paper or aluminum foil over windows and in cracks works well. We allow the students to become dark adapted. While their eyes are adjusting, we talk about how the eyes dark adapt. In some cases, we excite a light stick and pass it around. We explain chemical reactions and how the chemicals in the light stick make cold light. We also use wintergreen lifesavers to introduce the students to triboluminescence.³⁴ When the students' eyes have adapted and the room is completely black, we gently and unexpectedly toss out the dinoflagellates in sealed bags. Ideally every student catches their own bag. This is when the fun really starts. The questions start to pour out. What is it? Why is the light blue? When we tell them that the contents of the bags are alive, the students want to know what is in the bags, how do they get air? Why do they only make light when they are shaken? Will shaking kill them? We encourage them to formulate hypotheses and to discard hypotheses. After many of the questions are addressed we turn on the lights. The students are usually a bit disappointed when the bags appear to contain only murky water. We usually use a microscope so the students can see the dinoflagellates. This introduction is only the first step. Now the students can do experiments using *their* dinoflagellates. They take the bags home and are encouraged to continue their observations and experiments.

What Others Are Doing

Dr. Mariam Polne-Fuller, at the University of California, Santa Barbara, uses bioluminescent dinoflagellates to enhance lessons for K-12 grades. She has found bioluminescent dinoflagellates to be a wonderful tool for sharing the excitement of research and the fun of learning and teaching. Some of these lessons are

- K-3 Light, Invisible Partners, the Scientific Method, and Let Us See the Lights in the Dark Sea
- 3-6 The Living Cell, Plankton, and the Surprises in Science
- 7-12 Water Column Migrators, Intracellular Motion, and Do Plants See Light.³⁵

Dr. Polne-Fuller runs the Young Marine Scientists³⁶ program as part of the Marine Science Institute at the University of California, Santa Barbara.

³⁴ W. L. Dills, Jr., "The Great Wintergreen Candy Experiment," *Science Scope*, Nov./Dec., p. 24 (1992).

³⁵ M. Polne-Fuller, Personal Correspondence, e-mail: polne@lifesci.ucsb.edu.

³⁶ Young Marine Scientists -<http://research.ucsb.edu/msi/msitexts/YMSP/ymsp.htm>

This program provides research opportunities for undergraduates and K-12 teachers and their students. The participants are involved in hands-on activities using practical materials. Through this program, teachers and students are offered direct exposure to working scientists.

Real Scientist is a commercially available kit that utilizes bioluminescent bacteria and CD-ROM technology to provide hands-on science experiences.³⁷

Green fluorescent protein (GFP)³⁸ from the bioluminescent jellyfish *Aequorea victoria* has been used in cell and developmental biology as a fluorescent marker for gene expression.^{39,40} These techniques are being developed for high school laboratory use. Kratasyuk *et al.*,²⁶ at the Russian Academy of Science have used bioluminescence as a tool in ecological education by using bioluminescent bacteria to test toxic substances and media. There is a new coloring book on bioluminescence by Edith Widder (published by the Harbor Branch Oceanographic Institute, 1998), which is an ideal way to reach very young children. There are also several excellent web pages featuring bioluminescence⁴¹ and articles on bioluminescence for science education.⁴²

Summary

There is a great need for practicing scientists to volunteer their time and expertise in the K-12th grade science classroom. We have found that bioluminescence is a fun and exciting way to teach basic science concepts and is an excellent tool for the volunteering scientist. We have had very positive reactions from both teachers and students. The excitement of the

³⁷ P. E. Andreotti, T. Berthold, P. E. Stanley, and F. Berthold, in "Bioluminescence and Chemiluminescence: Molecular Reporting with Photons" (J. W. Hastings, L. J. Kricka, and P. E. Stanley, eds.), p. 181. Wiley, New York, 1997. Microlab Systems Corporation, Boca Raton, FL 33428.

³⁸ Green Fluorescent Protein, http://util.ucsf.edu/sedat/marsh/gfp_gateway.html <http://www.wam.umd.edu/~cha/research.htm>

³⁹ M. W. Cutler, D. F. Davis, and W. W. Ward, in "Bioluminescence and Chemiluminescence: Fundamentals and Applied Aspects" (A. K. Campbell, L. J. Kricka, and P. E. Stanley, eds.), p. 383. Wiley, New York, 1994.

⁴⁰ D. A. Yernool, P. V. Reddy, D. F. Davis, and W. W. Ward, in "Bioluminescence and Chemiluminescence: Molecular Reporting with Photons" (J. W. Hastings, L. J. Kricka, and P. E. Stanley, eds.), p. 192. Wiley, New York, 1997.

⁴¹ The Bioluminescence Web Page <http://lifesci.ucsb.edu/~biolum/http://cdlib.phys.msu.su/GenPhys/Optica/HM/Lec26/biolumin.htm>

⁴² <http://biotech.biology.arizona.edu/primer/readings/bioluminescence.html>

students when they first see bioluminescence is contagious. Bioluminescent dinoflagellates are one of the easiest ways to introduce students to this fascinating topic. Many activities and experiments can be done using the bioluminescent dinoflagellates and many students and teachers could benefit from your knowledge and expertise. See you in the classroom!⁴³

⁴³ Please share your bioluminescent classroom experiences with Mara, e-mail: pid@msu.com, or Joe, e-mail: joe.andrade@m.cc.utah.edu.

THE ADSORPTION OF LYSOZYMES: A MODEL SYSTEM

J. Hansen^{a)}, K. Ely, D. Horsley^{a)}, J. Herron, V. Hlady^{b)}, and J. D. Andrade*

Department of Bioengineering, University of Utah, Salt Lake City, Utah, 84112, USA

^{b)} R. Boskovic Institute, Zagreb, Yugoslavia

Abstract - Hen egg white lysozyme was adsorbed onto clean borosilicate glass and n-pentyl silane-treated glass surfaces. Both modified (reductively methylated) and native lysozyme were studied. Variable angle X-ray photoelectron spectroscopy (VA-XPS) suggested differences in the nature of the adsorbed layer depending on substrate properties, as well as on degree of methylation of the protein. Adsorbed film thickness (as measured in the dehydrated state by XPS) ranged from 14 Å on hydrophilic glass to 25 Å on the hydrophobic surface. Degree of surface coverage ranged from 45% on the hydrophobic to 69% on the hydrophilic surface. The results suggest that lysozyme unfolds to a greater extent and covers more surface on the hydrophilic glass, possibly due to strong electrostatic interactions at the pH 7.4 conditions used in the study. An analysis of the surface structure of native hen lysozyme by molecular graphics has also been performed, suggesting that adsorption on hydrophobic surfaces should occur via the hydrophobic patch opposite the enzyme active site cleft.

A comparison with human lysozyme has also been made using total internal reflection fluorescence (TIRF) spectroscopy to measure protein adsorption on model surfaces. The two proteins have significantly different interfacial properties.

INTRODUCTION

A better understanding of protein adsorption is needed in many areas of medicine and biology. The general factors involved in protein adsorption are qualitatively recognized. The key problem is to begin developing models and mechanisms to understand and predict protein adsorption, hopefully quantitatively (1).

Protein structure is complex, with a multiplicity of intermolecular interactions, surface functional groups, and conformational dynamics (2). Relatively simple, well-understood proteins (such as lysozymes) can now be viewed and modeled using interactive computer graphics, permitting all possible orientations of the protein with respect to the surface to be sampled and "viewed," thereby permitting the formulation of specific interaction hypotheses (1,2). Modern molecular modelling, using the atomic coordinates for proteins with known three-dimensional structures (over two hundred proteins), allow the investigator to more fully appreciate and understand the richness and distribution of protein surface structures and domains.

Detailed studies and models of lysozyme adsorption are an appropriate first step to a general understanding of proteins at interfaces. Hen and human lysozymes form an ideal model system with which to initiate the effort because their 3-D structures are well-known, because they are readily available, because they are resistant to denaturation, thereby simplifying the analysis, and because they are important to tears and contact lenses. An understanding of human lysozyme interactions with contact lens materials is essential to the

^{a)} Submitted in partial fulfillment of the M.S. degree in Bioengineering, University of Utah

31. D. Horsely, J. Herron, V. Hlady, and J. D. Andrade, In T. Horbett and J. Brash, eds., *Proteins at Interfaces*, ACS Symp. Series 343, 290-305 (1987)
32. V. Hlady, D. R. Reinecke, and J. D. Andrade, *J. Colloid Interface Sci.* **111**, 555 (1986)
33. S. H. Banyard, C. C. F. Blake, and I. D. A. Swan, in *Lysozyme*, E. F. Osserman, R. E. Canfield, and S. Beychok, eds., Academic Press, 71 (1974)
34. P. J. Artymiuk and C. C. F. Blake, *J. Mol. Biol.* **152**, 737 (1981)
35. C. C. F. Blake, D. F. Loenig, G. A. Mair, A. C. T. North, D. C. Phillips, and V. R. Sarma, *Nature* **206**, 757 (1965)
36. C. C. F. Blake, L. N. Johnson, G. A. Mair, A. C. T. North, D. C. Phillips and V. R. Sarma, *Proc. Roy. Soc. B167*, 318 (1967)
37. C. C. F. Blake, G. A. Mair, A. C. T. North, D. C. Phillips, and V. R. Sarma, *Proc. Roy. Soc. B167*, 365 (1967)
38. R. J. Feldmann and D. H. Bing, *Teaching Aids for Macromolecular Structure*, Taylor-Merchant Corp., New York
39. D. Eisenberg and A. D. McLachlan, *Nature* **319**, 199 (1986)
40. I. Elliott, C. Doyle, and J. D. Andrade, *J. Electron Spectrosc.* **28**, 303 (1983)
41. T. Yamashita and H. B. Bull, *J. Colloid Interface Sci.* **24**, 310 (1967)
42. R. Scheller, M. Janchen, and H. Prumke, *Biopolymers* **14**, 1553 (1975)
43. M. E. Koshland, F. M. Englberger, M. J. Erwin, S. M. Gaddone, *J. Biol. Chem.* **238**, 1343 (1963)
44. F. C. Greenwood, in *Principle of Competitive Protein Binding Assay* (1971), W.D. Odell and W. H. Daughady, eds., Lippincott, Philadelphia, 288 (1971)
45. A. Van der Scheer, J. Feijen, J. K. Elhorst, P. G. L. C. Krugers-Dagneaux, and C. A. Smolders, *J. Colloid Interface Sci.* **66**, 136 (1978)
46. R. E. Crandall, J. Janatova, and J. D. Andrade, *Prep. Biochem.* **11**, 111 (1981)
47. G. Halperin, M. Breitenbach, Tauber-Finkelstein, and S. Shaltiel, *J. Chromatogr.* **215**, 211 (1981)
48. H. R. Perkins, *Royal Soc. of Lond. Proc.* **167**, 443 (1967)
49. M. R. J. Salton, *Med. Hyg.* **22**, 985 (1964)
50. M. R. Bruzzesi, E. Chiancone, and E. Antonini, *Biochemistry* **4**, 1796 (1965)
51. R. C. Deonier and J. W. Williams, *Biochemistry* **9**, 4260 (1970)
52. B. L. Karger, A. Figueroa, X. M. Lu, N. Grinberg, and P. Byrd, *Biol. Chem-Hoppe-Seyler*, **368**, 753 (1987)
53. S. Endo, Y. Saito, and W. Wada, *Anal. Biochem.* **131** 108-120 (1983)
54. J. L. Fasnaugh and F. E. Regnier, *J. Chromatog.* **359**, 131-146 (1986)
55. R. K. Sandwick and K. J. Schray, *J. Colloid Interface Sci.* **115**, 130-138 (1987)
56. W. Norde and W. G. M. Pikaar-Heuvel, *Biol. Chem. Hoppe-Seyler* **368** 766 and personal communication (1987)
57. J. Feder and I. Giaever, *J. Colloid Interface Sci.* **78**, 144-154 (1980)
58. J. D. Andrade, J. Herron, V. Hlady, and D. Horsley, *Croat. Chem. Acta* **60** (1987) in press
59. A-P Wei, M.S. thesis, University of Utah, in preparation

/ last page

minimization and elimination of contact lens deposits. Most of the basic work on lysozyme adsorption has utilized the hen protein, whereas the major protein constituent of such deposits is human tear lysozyme—a major protein component of the tears.

Lysozyme was the first enzyme and the second protein to have its detailed molecular structure determined by X-ray crystallography. Lysozyme from hen egg white is a compact, relatively small molecule of dimensions $45 \times 30 \times 30 \text{ \AA}$ with a molecular weight of approximately 14,000 daltons. Its roughly prolate spheroidal shape is divided in two by a deep cleft—the molecule's most striking feature and the source of its enzymatic activity. There are four intrachain disulfide bonds in the single polypeptide chain of 129 amino acids which contribute to the great stability of the molecule. The disulfide bonds and high degree of ordered secondary and tertiary structure make it quite resistant to denaturation (3).

Hen lysozyme is one of the most extensively studied and well-understood proteins (3,4). It has a net positive charge due to its high lysine content. Its surface is relatively hydrophobic. Two-thirds of its 45 hydrophobic amino acid residues are at least partially on the protein surface and exposed to solvent. The combination of both a strong hydrophobic and electrostatic (positive) character results in interesting adsorption properties (5,6).

Lysozyme is second only to lactoferrin as the major protein component of the tears in the human (7,8). It is also found in human milk and other secretions. The primary structure of all human lysozymes studied to date are identical (4). Lysozyme is a bacteriolytic protein, catalyzing the decomposition of cell wall polysaccharides of *micrococcus lysodeikticus*. In addition to binding to a variety of mono- and polysaccharides (3), lysozyme binds to acidic proteins (including albumin), lipoproteins, and to itself. A dimer form becomes pronounced at $\sim \text{pH } 7$ for solution concentrations greater than 2 to 10 mg/ml. Lysozyme in normal tears is expected to be in the monomer form.

The interfacial properties of hen lysozyme are extensively reviewed in Reference 5—much of the available work has utilized the air/solution and oil/aqueous solution interfaces (9). Only recently have adsorption studies on polymers and contact lens materials begun to appear (10-16). Holly and Refojo did much of the earlier work (10). Ratner and Horbett have shown (11) that high water content lenses, particularly the methacrylic acid copolymers, can adsorb (and possibly absorb) large amounts of lysozyme. The commercial lenses studied have very different lysozyme-binding properties. Gachon et al. (12) showed that lysozyme is the major constituent adsorbed from a human tear analog solution. Castillo et al. (13) have shown that lysozyme is selectively adsorbed on high water content gels, and mucin is the major component adsorbed on pure polyhydroxyethyl methacrylate (PHEMA) gels. Proust and Baszkin have also studied mucin adsorption (14,15). Castillo et al. studies of in vivo spoiled lense show that lysozyme is the main constituent in the deposits (13).

There may be a problem with the effect of the label on the adsorption properties. Chen et al. have shown (16) that hen lysozyme radio-labeled by reductive methylation (which dimethylates the lysine amino groups), adsorbs differently from unlabeled material. It is likely that iodination may also affect the adsorption process (17,18).

Clearly lysozyme is adsorbing at least in part by an electrostatic mechanism on methacrylic acid-containing lenses. It is known that ion-exchange chromatography of lysozyme is very pH sensitive—changes of 0.1 pH unit can lead to significant differences in retention (Reference 3, p. 677). Tear film

pH can vary from 7.1-7.8 (7), possibly having an effect on lysozyme adsorption.

Hen and human lysozymes are significantly different (6,31). It is reasonable to expect that the two proteins will exhibit different adsorption characteristics. The human material is less resistant to denaturation and crystallizes differently than the hen—also the two proteins do not exhibit strong cross reactivity with antisera, suggesting substantial differences in the surface nature of the two proteins.

EXPERIMENTAL (5,6)

Materials. Amorphous silica microscope slides were obtained from ESCO products. The silanes 3-amino-propyltriethoxysilane (APS) and dimethyldichlorosilane (DDS) were both purchased from Petrarch Systems Inc. Hen egg-white lysozyme (3X crystalline) and human milk lysozyme (highly purified, salt-free powder) were products of Calbiochem. The fluorescence standard, 5-hydroxytryptophan methyl ester hydrochloride (TrpOH) was also a product of Calbiochem. PBS buffer ($\text{pH } 7.4$, $[\text{KH}_2\text{PO}_4]=0.013\text{M}$, $[\text{Na}_2\text{HPO}_4]=0.054\text{M}$, $[\text{NaCl}]=0.1\text{M}$) made from analytical grade reagents and low conductivity water was used to prepare all protein and fluorescence standard solutions. These solutions were prepared fresh, prior to each experiment.

Preparation of Surfaces. Adsorption studies were performed using charged and hydrophobic surfaces. Amorphous silica microscope slides were used as the substrate for all surfaces. Slides were cleaned in hot (80 degrees C) chromic acid for 20-30 minutes, cooled to room temperature, and then rinsed well in ultra-pure water (Milli-Q reagent water system). Slides were then desiccated for 12 hours at 100 degrees C. Cleanliness was confirmed by the measurement of Wilhelmy plate contact angle (no hysteresis with a clean surface).

The amorphous silica microscope slides exhibit an intrinsic negative charge at $\text{pH } 7.4$ (the surface silanol groups have been determined as having a pK_a of 5-7 by several workers (19-21)) and were used without further modification for adsorption of lysozyme onto negatively-charged surfaces. The average ζ potential of equivalent silica slides was determined by Van Wagenen et al. (22) to be -65 mV .

Positively-charged surfaces were prepared by reacting the cleaned microscope slides with 3-amino-propyltriethoxysilane (APS). At $\text{pH } 7.4$, the end amino group ($\text{pK}_a=10-11$) of the immobilized APS molecule bears a positive charge. Clean slides were dip cast in a solution of 5% APS (v/v) in ethanol- H_2O (95:5), and allowed to react for 30 minutes. Slides were then rinsed several times in H_2O , followed with ethanol.

Non-covalently bound APS was removed by vacuum desiccation at 60 degrees C for 12 hours. The measured contact angles of the APS coated slides exhibited mean values of 70 degrees advancing angle and 20 degrees receding angle with less than 10% variability among several APS coated surfaces. The average ζ potential of similarly prepared APS coated slides was determined by Van Wagenen et al. (22) to be -32 mV .

Hydrophobic surfaces were prepared by dip casting cleaned microscope slides with dimethyldichlorosilane (DDS). A similar protocol was used for DDS as for APS, except that the reaction mixture for DDS was 10% DDS (v/v) in dry toluene, and slides were rinsed with ethanol before rinsing with H_2O in order to remove the toluene. The measured contact angles of the DDS coated slides exhibited mean values of 110 degrees advancing angle and 90 degrees receding angle with less than 10% variability among several DDS coated surfaces.

Earlier studies (5) employed n-pentyl silanized glass slides.

Hen Lysozyme Solutions. High labeled lysozyme was prepared by reductive methylation (16,23) with slight modifications. Hen egg white lysozyme in the amount of 200 mg in 100 ml of phosphate buffered saline (PBS), 1.14 g Na_2HPO_4 + 0.22 g KH_2PO_4 + 8.5 g NaCl to 1 liter, pH 7.4, was reacted with 0.295 ml formaldehyde (1:100 37% formaldehyde: H_2O). Prior to the addition of formaldehyde, 0.1255 g sodium cyanoborohydride (NaCNBH_3) diluted in 1 ml PBS buffer was added to the protein solution. The mixture was allowed to react for 24 hours at 4°C with mild stirring. A Sephadex G-25 column pre-equilibrated with PBS buffer was then used to remove reactants from the protein sample.

Medium labeled and low labeled lysozyme solutions were produced by diluting the high labeled solution with PBS, 1:10 and 1:100, respectively. Native or unlabeled lysozyme was then added to these two solutions until the same protein concentration was reached as the high labeled material.

The labeling process was identical to that performed by Chen et al. (16) except for the fact that the formaldehyde was not tritiated.

A solution of native lysozyme (hereafter referred to as unlabeled lysozyme) was prepared by diluting native crystallized lysozyme with PBS buffer to a concentration equal to the high labeled lysozyme solution.

The concentration of all lysozyme/PBS solutions was determined to be 1.44 mg/ml in PBS by absorbance measurements at 280 nm using a Beckman model 35 UV-visible spectrophotometer with PBS as a reference. The molar extinction coefficient was determined to be $3.1 \times 10^4 \text{ M}^{-1}$. The molecular weight used for the calculations was 1.39×10^4 g/mole.

High labeled and unlabeled lysozyme solutions were characterized by UV absorption and emission fluorescence.

Adsorption Experiments. Protein adsorption experiments were performed at 20°C using the prepared glass surfaces and the unlabeled, high, medium, and low labeled hen lysozyme solutions. All glass cover slips were hydrated in PBS buffer for 15 minutes prior to the experiment. The adsorption was performed in 1 dram glass vials. Each vial contained a glass bead (3 mm in diameter) to support a glass cover slip and 0.33 ml of PBS buffer (see Reference 5 for details). Protein solution was injected below the air-water interface into the PBS solution with a 3 cc disposable syringe. A clean syringe was used for each vial.

Triplicate experiments were performed. The matrix of conditions consisted of three time intervals (1, 10, 100 minutes), two types of glass (cleaned-hydrophilic and silanized hydrophobic), and four types of lysozyme (unlabeled, high labeled, medium labeled, and low labeled).

The adsorption phase was followed by a 1 1/2 minute rinse with PBS buffer. The vial served as a "flow-through" cell and at no time during the rinse did the cover slip pass through an air-water interface. The flow rate was approximately 50 ml/minute. The flow was begun by the slow injection of PBS buffer through the system by a 30 cc disposable syringe. After the injection of 30 cc of PBS buffer, a valve was changed to allow the flow to continue by atmospheric pressure. The 1 1/2 minute rinse with PBS buffer was followed by a rapid rinse of the glass cover slip in double-distilled water. This rapid rinse was performed to ensure removal of buffer salts from the sample which could possibly interfere with the XPS analysis.

The cover slip was then placed in appropriately labeled disposable Petri dishes (Falcon #1029, 100 x 15 mm) with one edge of the cover slip resting on the bottom and one edge of the cover slip resting on the side of the Petri dish. The side of the cover slip which did not contact the 3 mm glass bead was noted, and this side only was analyzed by XPS. The cover slips were allowed to air dry under the hood of a Farr clean bench.

XPS. These adsorption samples were analyzed by XPS. Only samples adsorbed using high labeled and unlabeled hen lysozyme solutions at the 100 minute time interval were analyzed by the variable angle XPS method, described in the next section. XPS is a surface-sensitive, semiquantitative, nondegrading technique used to chemically analyze polymer surfaces. Recently it has been explored as a possible method to analyze protein adsorption (24-26). It is possible to ascertain relative amounts of protein adsorbed on surfaces through XPS analysis.

Radiolabeling provides information on the actual surface concentration of the adsorbed protein, which cannot be determined directly with XPS. However, the radiolabeling procedure allows counting of only those molecules with a label. It is not possible to study the adsorption of unlabeled lysozyme. XPS has the advantage of accounting for all protein molecules on the surface, whether they are labeled or unlabeled. The XPS technique was chosen in order to compare directly the adsorption of labeled lysozyme with that of unlabeled lysozyme. Labeling procedures similar to those of Chen et al. (16) were followed to allow correlation of the results of both studies.

XPS was also performed at variable angles to further analyze the adsorption of labeled and unlabeled lysozyme, providing an estimate of the thickness of the adsorbed protein film and the fraction of surface covered by adsorbed protein. Such information can be useful in examining possible modes of lysozyme adsorption. For example, estimates of the amount of thickness can be compared to the size of the protein to determine probable amount of denaturation or possible number of multiple layers of native protein.

The photoelectron escape depth, which is a function of kinetic energy, determines the volume sampled. The escape depth, or mean free path, for most polymers is 30 to 65 Å (26). The XPS technique is therefore extremely surface sensitive, and thus particularly well-suited to the study of protein adsorption.

Application of the XPS technique to the study of protein adsorption requires an understanding of the effect of an overlayer (i.e., adsorbed protein) on the signal of the substrate (i.e., the glass cover slip). This effect is discussed in detail in Reference 26, where the appropriate equations are derived and presented.

It is necessary that the element used to represent the overlayer (i.e., a layer of adsorbed protein) is not present in the substrate and the element used to represent the substrate (i.e., a glass cover slip) is not present in the overlayer. To study the adsorption of lysozyme on glass surfaces, we chose nitrogen to represent the protein and silicon to represent the glass substrate. The nitrogen to silicon ratio clearly enhances any difference in protein adsorption between different samples. As the nitrogen signal is increased, the silicon signal is correspondingly decreased, owing to attenuation of the substrate signal by the protein overlayer. This ratioing process also simplifies several aspects of the XPS data quantitation. Although absolute concentration cannot be ascertained by XPS, relative amounts of protein adsorbed can be compared from sample to sample (26).

Estimates of the mean free paths were derived using the Ashley theory and parameters discussed in detail in Reference 26.

A Hewlett-Packard 5950B monochromatic AlK α X-ray photoelectron spectrometer was used. The energy of the X-rays was 1487 eV. A variable angle probe (Surface Science Labs, Palo Alto, CA) was used, and the photoelectron exit angles examined varied from 18.5 to 78.5° (with respect to the plane of the sample). The data are processed by the expression (26):

$$\frac{I_p}{I_s} = \frac{I_p^0 f (1 - \exp(-d/\lambda_1 \sin \theta))}{I_s^0 ((1-f) + f \exp(-d/\lambda_2 \sin \theta))} \quad (1)$$

where

- I_s = observed intensity of the substrate signal (silicon-2s)
- I_s^0 = the intensity of the signal from the clean substrate
- f = the fraction of the substrate surface covered by the protein
- d = thickness of the protein layer
- λ_1, λ_2 = inelastic mean free path for the appropriate photoelectrons
- θ = photoelectron take-off angle
- I_p = observed intensity of the protein signal (nitrogen-1s)
- I_p^0 = the intensity of the signal from a pure, thick sample of protein

TIRIF. The TIRIF apparatus used in the later experiments has been described in detail elsewhere (31). The incident light totally internally reflects at the quartz-aqueous interface and produces a standing wave normal to the reflecting interface inside the quartz (the optically more dense medium) due to the superposition of the incident and reflected waves. The electric field of the standing wave has a non-zero amplitude (E^0) at the interface which decays exponentially with distance (z) normal to the interface into the aqueous phase (the optically less dense medium), thereby creating a surface evanescent wave that selectively excites molecules within a few thousand angstroms from the surface.

TIRIF adsorption isotherms were determined at room temperature. Fluorescence emission was generated by exciting at 280 nm and collecting at 335 nm (several workers have shown that tyrosine emission at 335 nm of both human and hen lysozymes is insignificant when exciting at 280 nm (28-30)). Slits of 16-nm half-bandwidth were used in both excitation and emission monochromators. For *in situ* protein adsorption experiments, the TIRIF cell was first primed with buffer and the background fluorescence was taken. The buffer solution was then replaced with external standard (TrpOH) solutions of increasing concentration and the fluorescence intensity recorded (31). After the fluorescence of the TrpOH standard of the highest concentration was recorded, the cell was again flushed with buffer to return the signal to the background level. At this point, 5 ml of the least concentrated protein solution was injected into the cell at a flow rate of 20 ml/min after which the flow was stopped and the protein was allowed to adsorb for 50 minutes (30 minutes after no further increase in surface fluorescence was seen). A shutter was used to prevent overexposure to UV light during the adsorption time. At the end of 50 minutes, the shutter was opened and fluorescence signal was recorded (N_{tot}). The cell was then flushed with buffer (20 ml/min) to remove nonadsorbed proteins and the resulting signal recorded (N_a). The procedure was then repeated for the protein solution of the next higher concentration and so on. In this manner, a step-adsorption experiment was performed as opposed to a single-shot adsorption experiment where the clean surface is exposed only once to each protein solution.

The quantitation scheme developed by Hlady et al. (32) was then used to quantitate the amount of protein adsorbed at each protein concentration from the recorded fluorescence intensities.

The earlier computer graphics display(s) of the α -carbon backbone of hen lysozyme was implemented with an Evans and Sutherland Picture System II interfaced to a DEC 1170 computer. Side chains of selected amino acids were co-displayed for identification of surface residues.

The recent molecular graphics studies of hen and human lysozymes (6,31) were performed, using a Silicon Graphics IRIS-2400 graphics workstation. Computer programs for displaying and manipulating protein models were developed by the computer graphics laboratory at the University of California at San Francisco. The principal program, called MIDAS, acts as a display vehicle for several different data structures, including atomic coordinates in Protein Data Bank format, van der Waals surfaces, solvent-accessible surfaces, and electrostatic potential surfaces.

Atomic coordinates for both hen egg-white and human lysozymes were based on crystallographic structures determined by Blake et al. (33-37) and deposited in the Protein Data Bank (Brookhaven National Laboratory). The distribution of hydrophobic, polar, and charged atoms on the surface of the two proteins was analyzed by calculating Corey-Pauling-Kaitun (CPK) surfaces and coloring atoms according to two coloring schemes (31). Both the Feldmann scheme (38) and the scheme based on the Eisenberg Atomic Solvation Parameter (ASP) (39) were based on how each residue would be charged at pH 7.4.

RESULTS

Computer Modeling for Variable Angle XPS. In order to obtain an appreciation for the nature of equation 1, we chose reasonable values for the photoelectron take-off angle, θ ; the mean free paths for the nitrogen (1s) and silicon (2s) in the adsorbed hen lysozyme film, λ_1 and λ_2 , respectively; thickness of adsorbed protein, d ; and fraction of surface covered by adsorbed protein, f . I_p/I_s was computed by substituting $\theta = 15, 30, 45, 60, 75$, and 90° , $f = 1/4, 1/2, 3/4$, and 1 , $d = 10, 25, 40$, and 55 \AA , and $\lambda_1, \lambda_2 = 20, 40$, and 60 \AA . We assumed $\lambda_1 = \lambda_2$, for this portion of the analysis. The mean free paths were chosen based on studies by Ashley, Clarke, Hall, and others (26). The photoelectron take-off angles were chosen to be evenly dispersed within the range of acceptable values (i.e. 0° - 90°). Values below 15° were considered not to be within the working range of the instrument.

The set of theoretical graphs is presented in Figure 1. The $\log_{10} I_p/I_s$ was used because of the wide range in the I_p/I_s values.

The next step was to determine I_p^0 and I_s^0 experimentally. I_p^0 represents the intensity of the signal of nitrogen (1s) from a pure, thick sample of powdered, crystalline hen lysozyme. It was derived both theoretically and by actual XPS analysis (5).

I_s^0 represents the intensity of the signal from a pure, thick sample of the glass substrate. This factor was determined by XPS analysis and was slightly different for hydrophilic (cleaned) glass and hydrophobic (silanized) glass (28.8 ± 0.2 and 27.3 ± 0.6 , respectively). These values were not determined theoretically (i.e., from empirical formulas for glass) because the exact stoichiometry of the silanized glass was not independently known.

Appropriate experimental I_p/I_s values were determined by first dividing the peak areas for nitrogen (1s) and silicon (2s) by their appropriate cross sectional values and then dividing these two values. These cross section

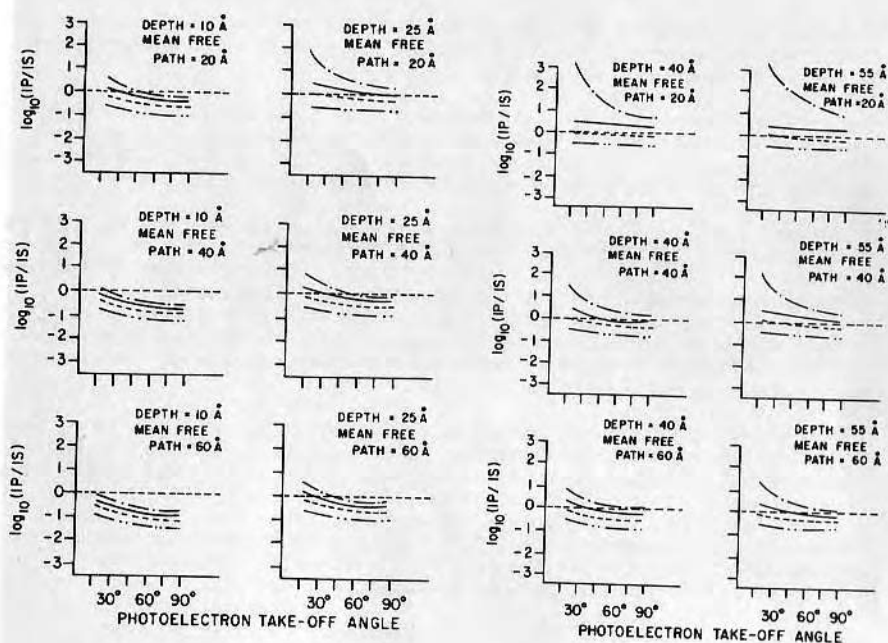


Figure 1: Illustration of Equation 1 by substitution of the values shown for the thickness of adsorbed protein and mean free path. In each graph, the four lines represent the fractional surface coverage, $f=1/4$ (—), $1/2$ (---), $3/4$ (- - -), and 1 (- · - ·) from top to bottom, respectively. Although Equation 1 has two distinct mean free path values (i.e., one for substrate through the overlayer and one for the overlayer), these values are taken as identical for these graphs. Visual comparison of these graphs with experimental data graphed identically allowed elimination of inappropriate values for mean free path (i.e. λ_1 and λ_2) and thickness of the adsorbed protein film. Further visual analysis was then possible by changing λ_1 and λ_2 and comparing these theoretical graphs with the experimental data until it was possible to find a λ_1 and λ_2 which best fit all four sample conditions. The final analysis employed the chosen λ_1 and λ_2 (i.e. 25 Å and 36 Å, respectively), further computer substitutions for thickness of adsorbed protein film and fraction of surface covered by adsorbed protein, and visual comparison of these new theoretical graphs with experimental graphs coupled with numerical comparisons of I_p/I_s experimental and theoretical values. The result was four theoretical curves (see Figure 3) which exhibited the least possible difference with their experimental counterparts for all four sample conditions

values (1.96 and 0.93, respectively) incorporated the instrument throughput function for the Hewlett-Packard 5950B photoelectron spectrometer (40).

The data are summarized in Table 1.

Experimental I_p/I_s values were then compared graphically and numerically with those calculated from assumed values of f and d . (Figure 1) (5).

$\lambda_1=25\text{Å}$ and $\lambda_2=36\text{Å}$ were the best simultaneous solutions for all sets of data. Assuming these mean free path values, the thickness of protein adsorbed, d , and the fraction of surface covered by adsorbed protein, f , were then analyzed by using various possible combinations of d and f to fit the experimental I_p/I_s values. The most precise combination of d and f for each sample condition could usually be found by assuming the mean of the possible theoretical thicknesses to be d and then substituting various values of f (which were also close to the mean of the possible theoretical f 's) until the best matched profile using the criterion of the least sum of squares was obtained. Details are given in Reference 5.

Adsorption Results - "Normal" Angle. Unlabeled (native) hen lysozyme and low, medium, and high labeled hen lysozyme (1.07 mg/ml PBS) were adsorbed onto cleaned (hydrophilic) glass surfaces and n-pentyl silanized (hydrophobic) glass surfaces. Experimental XPS adsorption data for eight sample conditions at the normal angle (38.5°) were obtained and are available (5). There was not much difference between unlabeled lysozyme, medium labeled lysozyme, and low labeled lysozyme at 100 minutes adsorption time (i.e., the values are clustered together between N_{1s}/Si_{2s} ratios of 0.43 and 0.51). However, there is a significant difference in the range of these values when compared to the N_{1s}/Si_{2s} ratios of high labeled lysozyme (i.e., 0.25 - 0.32). There is generally greater protein adsorption on hydrophobic (NPS) glass when compared to hydrophilic glass.

Figure 2 presents the experimental XPS adsorption data for four sample conditions (high labeled and unlabeled on each of the two surfaces) at the normal angle (38.5°), including all data for one standard deviation from the mean (5). The range of values for each sample condition is shown at 1, 10, and 100 minutes. The N_{1s}/Si_{2s} ratios at 100 minutes indicate a clear difference in adsorption behavior between unlabeled lysozyme and high labeled lysozyme on hydrophobic glass and hydrophilic glass. On hydrophobic surfaces alone, a significant difference was observed between unlabeled and medium labeled lysozyme (data not shown—see Ref. 5). These results suggest that when a hydrophobic glass surface is involved, less reductive methylation of lysozyme is required to significantly alter its adsorption behavior. The N_{1s}/Si_{2s} values for adsorption of low labeled and medium labeled lysozyme at 100 minutes differ very little from the N_{1s}/Si_{2s} ratios presented in Figure 2 for unlabeled lysozyme (5).

Adsorption Results-Variable Angle. We further studied the high labeled and unlabeled samples by variable angle XPS. Experimental variable angle XPS adsorption data for these four sample conditions are presented in Figure 3. The I_p/I_s mean values (from equation 1) are plotted as a function of the four photoelectron take-off angles for each of the four sample conditions. The I_p/I_s values present qualitatively the amount of protein present on the surface. Experimental variable angle adsorption data, including data for one standard deviation from the mean of triplicate samples, are presented in Figure 3 for each of the four sample conditions. The data at higher angles (i.e., 78.5° and 58.5°) have a greater reproducibility than the lower angles (i.e., 18.5°). This is to be expected owing to the structure of the XPS instrument and position of the variable angle probe. Precision was compromised by the relatively low signal intensity at 18.5° .

Table 1: Summary of Labeled Hen Lysozyme Study* (5)

Thickness Å (3)		Percent Coverage (3)		Surface Concentration $\mu\text{g}/\text{cm}^2$				
				XPS (4)		H^3 (Ref. 16)		
	Native	H^3	Native	H^3	Native	H^3	Native	H^3
Hydrophilic Glass (1)	16	14	69	54	.15	.10	?	.13
Hydrophobic Glass (2)	25	23	53	45	.18	.15	?	.21

(1) θ adv. = 10 ± 1 ; θ rec = 7 ± 2

(2) θ adv. = 89 ± 1 ; θ rec = 61 ± 3
n-pentyl silane treated

(3) λ best fit to all data +
 λ N 1s in lysozyme = 25\AA
 λ Si2p in glass/lysozyme = 36\AA

(4) from: $d = 100$ Γ ($\mu\text{g}/\text{cm}^2$) (1.4 gr/cc) γ
 γ = % coverage
protein density = 1.4 gr/cc

* 100 min adsorption time from pH 7.4, PBS, ~ 1mg/ml lysozyme, 20°C.
degree of labeling = ~ 1.4 methyl groups per lysozyme molecule

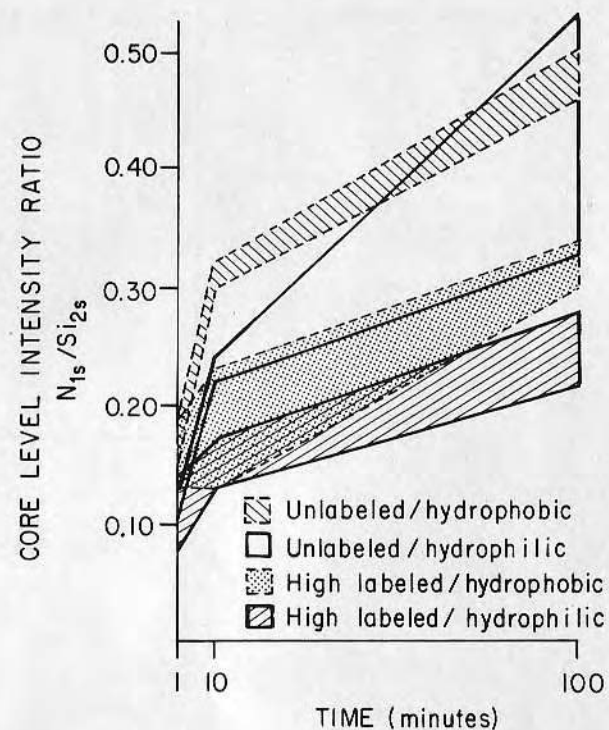


Figure 2: Experimental XPS adsorption data, including data for one standard deviation from the mean, for four sample conditions at the normal angle (38.5°). The range of values for the N_{1s}/Si_{2s} core level intensity ratios for triplicate samples is depicted for unlabeled and high labeled hen lysozyme adsorbed onto hydrophobic and hydrophilic glass for 1, 10, and 100 minutes. Protein concentration was 1.07 mg lysozyme/ml PBS buffer, pH 7.4, at 20°C . The N_{1s}/Si_{2s} ratios at 100 minutes indicate a clear difference in adsorption behavior between unlabeled lysozyme and high labeled lysozyme on hydrophobic glass and hydrophilic glass

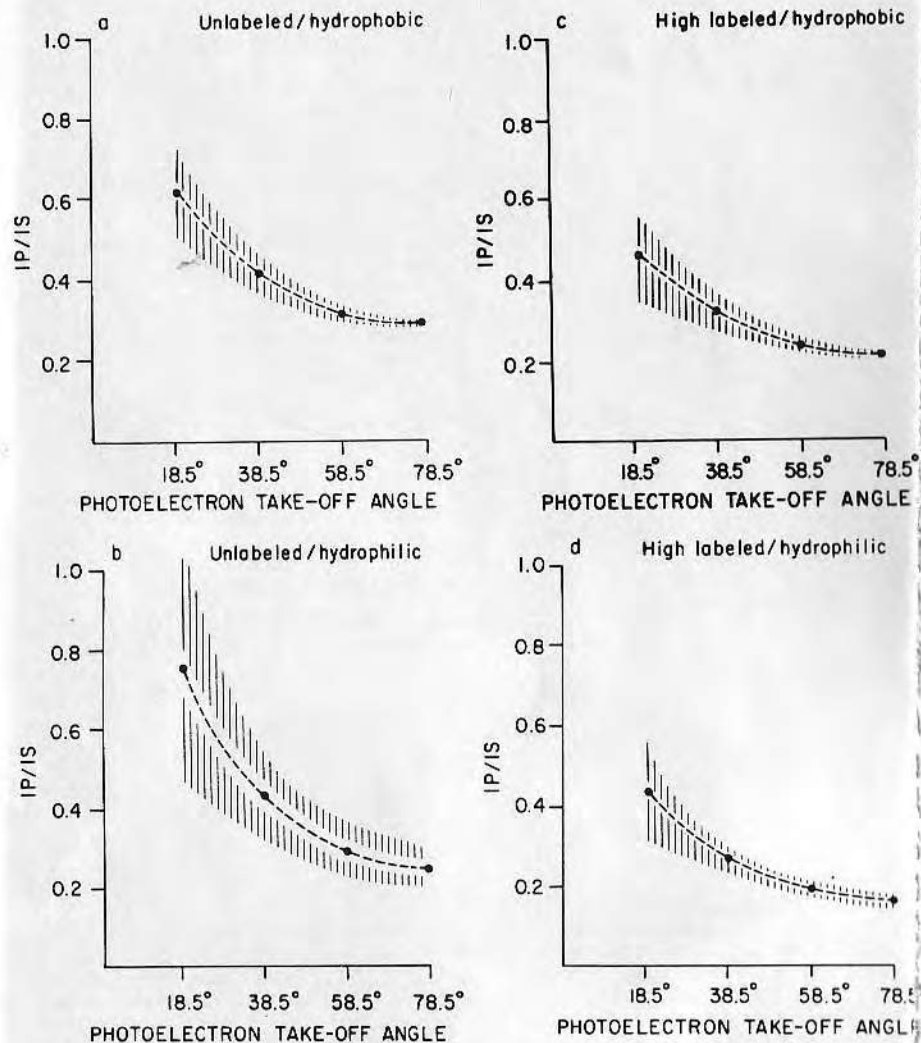


Figure 3: Plot of experimental data for (a) unlabeled hen lysozyme adsorbed onto hydrophobic glass, (b) unlabeled lysozyme adsorbed onto hydrophilic glass, (c) high labeled lysozyme adsorbed onto hydrophobic glass, and (d) high labeled lysozyme adsorbed onto hydrophilic glass. A dashed curve connects the mean I_p/I_s values (●) for three replicates at the four angles shown. The vertically lined area surrounding these four data points represents one standard deviation on either side of the mean. Protein concentration was 1.07 mg lysozyme/ml in PBS buffer at pH 7.4, 20°C. Adsorption time was 100 minutes. These four dashed curves were compared with theoretical curves developed by substituting various values for d , f , λ_1 and λ_2 in Equation 1 as described in Figure 1. Values for the mean free path for adsorbed lysozyme, the mean free path for glass through the adsorbed lysozyme (λ_1 and λ_2 , respectively), thickness of the protein overlayer (d) and the fraction of the substrate surface covered by the protein (f) were thereby determined for the four sample conditions

The 12 samples analyzed by variable angle were the same samples analyzed with the normal XPS probe and discussed earlier. Although the N_{1s}/Si_{2s} ratio had already been calculated for the normal angle (i.e., 38.5°), these values were recalculated using the variable angle probe. No significant difference was found.

By using N_{1s}/Si_{2s} ratios to calculate the I_p/I_s values at all five angles for four sample conditions, it was possible to correlate experimental data with theoretical data, as described earlier. The probable thickness of adsorbed lysozyme, fraction of surface covered by adsorbed lysozyme, mean free path in lysozyme, and mean free path in glass for each of the four sample conditions were calculated. The individual I_p/I_s experimental and I_p/I_s theoretical values were very close and in no case was the difference greater than 6.5% (5). The average percent difference of an individual I_p/I_s experimental value with its theoretical counterpart for all four sample conditions was 2.7%.

The thickness of the adsorbed hen lysozyme film on hydrophobic glass was 23Å and 24Å for high labeled lysozyme and unlabeled lysozyme, respectively, and 14Å and 16Å on hydrophilic glass for high labeled lysozyme and unlabeled lysozyme, respectively. The fraction of surface covered by adsorbed lysozyme is also different for the four sample conditions. On hydrophilic glass, the unlabeled lysozyme film showed a higher coverage (approximately 15% more) than high labeled lysozyme. On hydrophobic glass, the unlabeled lysozyme film showed a greater percent coverage (approximately 8% more) than high labeled lysozyme. When adsorption of unlabeled lysozyme is compared on hydrophilic and hydrophobic glass, a greater thickness of adsorbed protein is noted on the hydrophobic surface (i.e., an increase of 9Å) but the percent coverage is less (i.e., 16% less). Comparison of adsorption of high labeled lysozyme on the hydrophilic and hydrophobic surfaces yields a similar result: a greater depth of adsorbed high labeled lysozyme (i.e., an increase of 9Å) is found on the hydrophobic glass, but again the percent surface covered by protein is less (i.e., 9% less). The data suggest two separate mechanisms for adsorption of lysozyme on hydrophilic and hydrophobic surfaces.

The following equation from Ratner et al. (25) was used to compute the amount of lysozyme adsorbed in $\mu\text{g}/\text{cm}^2$:

$$d = 100 (\mu\text{g}/\text{cm}^2) / 1.4f \quad (2)$$

where

d = thickness of protein layer
 f = the fraction of substrate surface covered by the protein

The density of the protein is assumed to be $1.4\text{g}/\text{cm}^3$ (5,36). On hydrophilic glass, high labeled lysozyme adsorbed in the amount of $1.10 \mu\text{g}/\text{cm}^2$ and unlabeled lysozyme adsorbed in the amount of $0.15 \mu\text{g}/\text{cm}^2$. On hydrophobic glass high labeled lysozyme adsorbed in the amount of $0.15 \mu\text{g}/\text{cm}^2$ and unlabeled lysozyme adsorbed in the amount of $0.18 \mu\text{g}/\text{cm}^2$.

A more accurate picture of the theoretical comparison possible with the experimental data is shown in Figure 4. Computer analysis was utilized to compare experimental I_p/I_s values within one standard deviation with possible theoretical models whose I_p/I_s values would fall within this range for all five angles (5). Once the computer noted a match at all five angles, the thickness of adsorbed lysozyme and fraction of surface covered for adsorbed lysozyme were printed. These combinations of thickness of adsorbed protein and fraction of surface covered by adsorbed protein were plotted in Figure 4.

Figure 4: Results of computer analyses which compared the experimental data one standard deviation from the mean with the possible theoretical combinations of thickness of protein layer (d) and fraction of the substrate surface covered by the protein (f) of Equation 1. When considering one standard deviation from the mean, multiple thickness/percent coverage solutions are possible within this range of I_p/I_s values. The different allowable combinations of d and f were calculated and plotted. Three samples each of the four sample conditions were studied at five different angles to make a total of sixty observations. "1", "2", "3", and "4" represent the best-matched profile for combination of thickness of adsorbed lysozyme and fraction of surface covered for the mean I_p/I_s values for the conditions indicated, as determined by the criterion of the least sum of the squares. The wide variation of combinations of thickness/percent coverage surrounding 1, 2, 3, and 4 represent the standard deviation on either side of these mean I_p/I_s values, as shown in Figure 3. Clear differences in the adsorption behavior of unlabeled and labeled lysozyme on hydrophobic and hydrophilic glass exists despite the many allowable combinations of d and f for I_p/I_s values within one standard deviation.

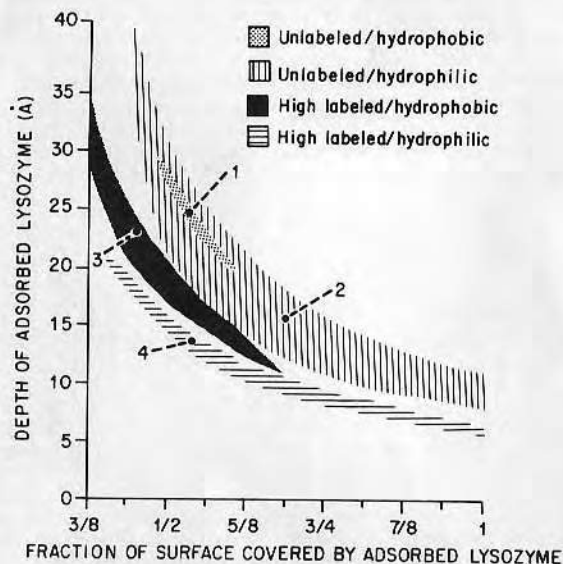


Figure 4 shows that clear differences in the adsorption behavior of unlabeled and high labeled lysozyme on hydrophobic and hydrophilic glass exist despite the many allowable combinations of d and f for I_p/I_s values within one standard deviation.

A one-tailed t-test was performed between the sample conditions to determine the significance of the differences noted. I_p/I_s values were used at 38.5° (the normal angle).

As shown in Figure 4, there is no significant difference in the adsorption of unlabeled lysozyme onto hydrophobic or hydrophilic glass. The adsorption of high labeled lysozyme onto hydrophobic and hydrophilic, as compared by a one-tailed t-test, differed by only 5%. High labeled lysozyme and unlabeled lysozyme, when compared for adsorption to hydrophilic glass, displayed a 5% significant difference. The greatest difference in degree of adsorption was noted between high labeled and unlabeled lysozyme adsorbed onto hydrophobic glass. This difference was found to be significant to the 5% level.

The TIRF-determined step-adsorption isotherms for both hen and human lysozymes on hydrophobic (DDS), negatively-charged (silica), and positively-charged (APS) surfaces have been presented (31). Since the TIRF quantitation scheme used assumes that the quantum yield of the protein does not change upon adsorption (an assumption we are currently trying to test), the actual amount adsorbed may differ from that presented in Reference 31 if this assumption proves to be invalid for these proteins (see discussion below).

The order of both lysozymes' affinity toward the three model surfaces was found to be DDS > silica > APS. The human lysozyme exhibited well defined plateaus on all three surfaces at relatively low protein concentrations (>10 mg/ml), while for the hen lysozyme a definite plateau could only be seen on the DDS surface. Moreover, the amount of human lysozyme adsorbed per surface area appeared to be roughly three times that of the hen lysozyme on equivalent surfaces at low protein concentrations (<5 mg/ml). Again, these results may not be accurate due to the limitations of the TIRF quantitation scheme.

The molecular graphics images of the two lysozymes from a few different viewpoints have been presented (31), using both the Feldman (38) and Eisenberg-based (39) coloring codes. Both lysozymes exhibited a number of similarities. To a first approximation, positively-charged residues were fairly evenly spaced over the entire protein, although the electrostatic surface potentials (ESP) computed for the two proteins showed a slight asymmetric distribution of surface positive charge, with the larger lobe showing more positive character than the smaller lobe (6). Both proteins were seen to have long positive side chains extending into the solvent.

There were approximately one-third as many negatively-charged groups as there were positively-charged groups on the surface of both proteins. These negatively-charged residues barely reach the surface and are not nearly as accessible as the positively-charged residues. ESP calculations have shown that the active site cleft shows the greatest concentration of negative surface charge on both proteins (6).

Nonpolar residues formed a hydrophobic patch in the middle of the back side (opposite the active site cleft) of both proteins. The hydrophobic patch on the human lysozyme appeared to be slightly larger than that on the hen lysozyme.

Perhaps the most dramatic difference in the surface properties of the two lysozymes was seen by the ESP calculations which showed that the human

lysozyme had a significantly greater overall electrostatic surface potential than the hen lysozyme had (6).

DISCUSSION

Labeled Hen Lysozyme XPS Studies (5) Labeling of hen lysozyme by reductive methylation results in the addition of one or two methyl groups on the ϵ -amino group of lysine. High labeling results in the addition of approximately 1.4 methyl groups per protein molecule. The added methyl group will produce some change in the overall hydrophobicity of the molecule and some change in ionic interactions.

While this method of protein modification maintains the gross charge of the molecule, the individual positive charges may be displaced (41). The addition of a methyl group and possible displacement of the individual positive charges may result in some ionic-hydrophobic interaction synergism. Warshel discussed such phenomena briefly in his study of the role of hydrophobic environments in ionic interactions in lysozymes active sites (42).

Although formation of dimers and higher aggregates is possible, especially between pH 5 and 9, hen lysozyme normally exists as a monomer at concentrations of 2.0 mg/ml or lower. Labeling may provide a different result i.e., labeled lysozyme may have a greater tendency toward dimerization. We did not test for all possible aggregation states in our study, but the possibility that lysozyme does not remain monomeric was considered in the evaluation of our results.

The average thickness of adsorbed unlabeled and labeled hen lysozyme on hydrophobic glass, 24Å, was significantly greater than the average thickness on hydrophilic glass, 15Å. The two different thicknesses suggest two separate mechanisms for adsorption of hen lysozyme on these hydrophilic and hydrophobic surfaces. One possible explanation for the decrease of thickness of adsorbed protein is an increase in unfolding or denaturation of adsorbed lysozyme on hydrophilic glass. Although lysozyme has a +8 charge at pH 7.4 (41), it also has several hydrophobic patches on its surface. There are 22 apolar residues on the surface of lysozyme fully or partially exposed to solvent. These residues form a band around the center of the molecule and a significant number of hydrophobic residues which project extensively into solvent are concentrated in an area opposite the cleft (5,6,31). When lysozyme adsorbs onto a hydrophobic surface, it may adsorb at this site opposite the cleft. This position would allow the protein to retain much of its ordered secondary structure. Comparing lysozyme dimensions (30 X 30 X 45 Å) to the average thickness (24 Å) of adsorbed protein on hydrophobic glass further enhances the theory that little unfolding has occurred.

When lysozyme adsorbs onto a hydrophilic surface, it may unfold or denature. This adsorption may be influenced by ionic interaction of the negatively-charged glass with the positively-charged lysozyme. An unfolding of the molecule would permit the positively-charged residues to more uniformly spread out and interact with the surface. These residues also project quite far from the surface of the molecule and ionic interaction could cause conformational changes. If lysozyme unfolds then it would cover the glass surface to a greater extent, inhibiting further adsorption. This inhibition of adsorption could account for the decrease in total adsorption on the glass as compared with the hydrophobic surface. The average greater fraction of surface covered by adsorbed lysozyme on a hydrophilic surface (62%) as opposed to the hydrophobic surface (49%) was shown by the XPS results.

Considering lysozyme dimensions (30 X 30 X 45 Å) and its two lobe structure (Figure 6a,6b), unfolding of the molecule could easily result in an average thickness on hydrophilic glass of 15 Å.

On hydrophilic glass, unlabeled hen lysozyme adsorbs to a slightly greater thickness and with greater coverage than does high labeled hen lysozyme. The labeled protein adsorbs 33% less on hydrophobic surfaces and 42% less on hydrophilic surfaces than does the unlabeled protein. The increase of hydrophobicity and displacement of the lobe of the positive charges of the labeled lysozyme could both increase adsorption on the hydrophobic surface and decrease adsorption on the hydrophilic surface, resulting in the difference in adsorption on the two surfaces.

The concentration of hydrophobic residues opposite the cleft may affect adsorption on a hydrophobic surface; when the distribution of hydrophobic patches is changed such as by reductive methylation labeling, the adsorptive interaction may be affected.

Hen and Human TIRIF Studies (6) The primary problem with the TIRIF quantitation scheme is the fact that it ignores changes that might occur in the quantum yield of the protein upon adsorption. Hlady et al. (32) used a radiolabeling technique to estimate the change in quantum yield that might occur upon adsorption of BSA and IgG onto hydrophilic silica and found that the quantum yield decreased by a factor of at least two for both proteins. Consequently, the TIRIF isotherms for BSA and IgG were at least two-fold less than the isotherms determined by radiolabeling the proteins. The origin of the decreased quantum yield of adsorbed protein would most likely be due to a change in the conformation of the protein upon adsorption.

Several reports have pointed out that iodination of proteins may affect their adsorption to solid surfaces and their chromatographic behavior (43-46). Consequently, we have chosen to determine the quantum yield of unlabeled, adsorbed lysozyme via fluorescence lifetimes. We are currently in the process of modifying our fluorescence equipment to obtain such fluorescence lifetimes (59).

The TIRIF adsorption isotherms for the two lysozymes (31) seem to imply that the human protein has a higher affinity for all three surfaces examined than the hen protein does. Until quantum yield determinations are made, nothing quantitative can be said about these differences in isotherms. However, these TIRIF isotherm differences do suggest an interesting point. Namely, if further research shows that there isn't a significant difference between the two lysozymes with respect to the amounts adsorbed, then these TIRIF isotherms clearly indicate that the adsorption process results in a greater change in Φ / Φ_b (Φ = quantum yield of adsorbed protein, Φ_b = quantum yield of protein in solution) for one of the lysozymes than for the other lysozyme.

The many differences between human and hen lysozymes have been discussed (5,6,31). From these results, one would expect that the two proteins would exhibit differences in their adsorption characteristics, due to their surface differences.

The fact that the human protein has one less disulfide bond and a greater susceptibility to thermal denaturation than the hen protein, suggests that the human protein might also be more susceptible to surface denaturation. Iodide quenching studies of adsorbed lysozyme recently performed in our laboratory, have partially confirmed this prediction on the two hydrophilic surfaces (6).

The TIRIF isotherm results, suggesting that both lysozymes exhibited the overall order of affinity DDS > silica > APS was not surprising. Many

studies of lysozyme adsorption have shown that it has a higher affinity to hydrophobic surfaces than to hydrophilic surfaces (5,16,47). Lysozyme adsorption on hydrophobic surfaces may occur at the site of the hydrophobic patch seen on the back side of both proteins. At pH 7.4, both lysozymes are positively-charged and would be expected to adsorb more strongly to the negatively-charged silica surface than to the positively-charged APS surface. This was seen to be the case for both proteins. As noted above, both lysozymes have long positive side chains extending out into the solvent while the surface negative charges are not nearly as accessible. This point further suggests a preferential adsorption onto negative surfaces. With regard to the effect of electrostatic repulsion between lysozyme and the positively-charged APS surface, it is interesting to note that both Perkins (48) and Salton (47) found that lysozyme activity was inhibited by positively-charged groups in the mucopeptide of bacterial cell walls (lysozyme's biological substrate), presumably due to electrostatic repulsion since the activity was increased when the free amino groups in the mucopeptide were neutralized.

The hen lysozyme showed non-saturating adsorption behavior on both charged surfaces. This may suggest that charged surfaces promote the formation of multiple protein layers at the surface in some manner which is not yet clear. Hen lysozyme forms dimers and higher aggregates under conditions of high protein concentration (5-10 mg/ml) and pH > 5 (3,50,51). This kind of self-association might be going on at the surface where the adsorption process inherently concentrates the proteins.

CONCLUSIONS

X-Ray Photoelectron Spectroscopy (XPS) appears to provide unique and useful information on the adsorption of lysozyme (Table 1). The degree of coverage deduced by the XPS variable angle technique is in the same range as that expected on the random collision frequency/occupancy model (57), which concludes that the percent coverage is in the 55-57% range for random sequential filling of a surface. The difference in thickness between adsorption on hydrophobic and hydrophilic glass may be significant as discussed earlier. There is a difference in percent coverage of the native hen lysozyme on hydrophilic and hydrophobic glass. It is clear that the human and hen material behave very differently. It is also clear that there is considerable evidence that at least the human material undergoes some significant denaturation upon adsorption (6). Recent studies by Karger (52), Sandwick and Schray (55), Regnier (54), and Wada (53) all suggest conformational changes upon adsorption of hen lysozyme. We have recently suggested (58) that adsorption of protein at solid/liquid interfaces, particularly the conformational alteration upon adsorption, can be expected to correlate with their solution denaturation characteristics and with their ability to adsorb at air/water interfaces, i.e. surface tension properties. Such studies are presently ongoing in our laboratories and will be reported at a later date (59).

ACKNOWLEDGMENTS

Portions of the earlier phases of this work (5,16) were supported in part by the Syntex Corp. and NIH grant HL 18519. We thank D. Dong, J. Chen, N. Elliot, J. Warenski, and J. Geisler for their advice, help, and assistance. The more recent work (6,31) was supported by the Center for Biopolymers at Interfaces, University of Utah. We thank J-N Lin and P. Dryden for their help and assistance.

REFERENCES

1. J. D. Andrade, ed., *Protein Adsorption*, Plenum Press, New York, 1985
2. G. E. Schulz and R. H. Schirmer, *Principles of Protein Structure*, Springer-Verlag, New York (1979)
3. T. Imoto, L. N. Johnson, A. C. T. North, D. C. Phillips, and J. A. Rupley, in *The Enzymes*, Vol. 7, 3rd ed., P. D. Boyer, ed., Academic Press, pp. 665-868 (1972)
4. E. F. Osseman, R. E. Canfield, and S. Beychok, eds., *Lysozyme*, Acad. Press (1974)
5. J. Hanson, M.S. thesis, University of Utah (1985)
6. D. Horsley, M.S. thesis, University of Utah (1987)
7. N. J. Van Haeringen, *Surv. Ophthalmol.* 26, 84-96 (1981)
8. R. N. Stuchell, R. L. Farris, I. D. Mandel, *Ophthalmol.* 88, 858-862 (1981)
9. M. C. Phillips, *Chem. and Ind.*, pp. 170-176 (March 5, 1977)
10. F. J. Holly and M. F. Refojo, in J. D. Andrade, ed., *Hydrogels for Medical and Related Applications*, ACS Symp. Series #31, 267-282 (1976)
11. B. D. Ratner and T. A. Horbett, *Trans. Soc. Biomat.* 10, 76 (1984)
12. A. M. Gachon, T. Bilbaut, and B. Dastugue, *Exp. Eye Res.* 40, 105-116 (1985)
13. E. J. Castillo, J. L. Koenig, and J. M. Anderson, Parts 1-4, "*Biomaterials* 5, 319-325 (1984); 6, 338-345 (1985); and 7, 9-16, 89-96, 247-251 (1986)
14. A. Baszkin, J. E. Proust, and M. M. Boissonnade, *Biomaterials* 5, 175-179 (1984)
15. J. E. Proust, A. Baszkin, E. Perez, and M. M. Boissonnade, *Colloids & Surfaces* 10, 43-52 (1984)
16. J. Chen, D. E. Dong, J. D. Andrade, *J. Colloid Interface Sci.* 89, 577-580 (1982)
17. A. Vander Scheer, et al., *J. Colloid Interface Sci.* 66, 136 (1978)
18. F. H. Royce, B. D. Ratner, T. A. Horbett, in S. L. Cooper, N. A. Peppas, A. S. Hoffman, B. D. Ratner, ed., *Biomaterials*, Adv. Chem. Series 199, 453-464 (1982)
19. R. A. Van Wagenen, J. D. Andrade, J. B. Hibbs, *J. Electrochem. Soc.* 123, 1438 (1976)
20. M. L. Hair and W. J. Hertl, *J. Phys. Chem.* 74, 91 (1970)
21. K. Marshall, G. L. Ridgewell, C. H. Rochester, J. Simpson, *Chem. Ind. (London)* 19, 775 (1974)
22. R. A. Van Wagenen et al., *J. Colloid Interface Sci.* 84, 155 (1981)
23. N. Jentoft and D. G. Dearborn, *J. Biol. Chem.* 254, 4359 (1979)
24. B. D. Ratner and T. A. Horbett, *J. Colloid Interface Sci.* 83(2), 630 (1981)
25. R. Paynter and B. D. Ratner, Chapter 5 in *Protein Adsorption*, J. D. Andrade, ed., Plenum Press, New York, 189-216 (1985)
26. J. D. Andrade, Chapter 5 in *Surface and Interfacial Aspects of Biomedical Polymers* 1, J. D. Andrade, ed., Plenum Press, New York, 105-196 (1985)
27. V. Hlady, R. A. Van Wagenen, and J. D. Andrade, in *Surface and Interfacial Aspects of Biomedical Polymers*, Vol 2 *Protein Adsorption*, J. D. Andrade, ed., Plenum Press, p. 81 (1985)
28. T. Imoto, L. S. Forster, J. A. Rupley, and F. Tanaka, *Proc. Nat. Acad. Sci.* 69, 1151 (1971)
29. V. I. Teichberg, T. Plasse, S. Sorell, and N. Sharon, *Biochim. Biophys. Acta* 278, 250 (1972)
30. S. S. Lehrer and G. D. Fasman, *Biochem. Biophys. Res. Comm.* 23, 133 (1966)

PHOTODEGRADATION OF POLYMERS

J. E. Guillet
Department of Chemistry
University of Toronto
Toronto, Canada

Photodegradation of polymeric materials is a subject with both practical and theoretical interest. Studies will be described of various types of degradation reactions, both in solution and in the solid phase. It is shown that many of these reactions have strong requirements of molecular mobility which, in turn, depend on the physical and chemical state of the substrate. Energy transfer processes are also important in both the degradation and stabilization of photochemical processes and examples will be given of the efficiency of such processes.

Degradation reactions can be conveniently followed by changes in the molecular weight of the polymer. Since molecular weight can, in some instances, be measured very precisely, one may use degradation reactions as a probe to study other kinds of photochemical processes in solution.

Interactions of Mammalian Cells and Polymer and Glass Surfaces

By

P.J. Harren, D.W. Hill, D.J. Lyman,
J. Hibbs, J.D. Andrade and L.M. Smith
Department of Materials Science and
Engineering, Department of Microbiology
and the Department of Pathology,
University of Utah, Salt Lake City,
Utah, 84132

Introduction

These experiments were originally initiated in attempts to gain some insight into factors which affect interaction of mammalian cells in vitro & substrate surfaces. Employing contemporary culture techniques, cells of diverse biological properties have been examined when placed in contact with Corning cover glass, Lux plastic cover slips and Teflon FEP film. Other variables investigated included media composition and time of contact of the cells with the substrates.

Materials and Methods

Macrophages used in these studies were obtained from 6 to 10 week old Swiss-Webster or BALB/c mice of either sex. Under ether anesthesia, the animals were decapitated and bled out. The abdomen was disinfected with alcohol and the skin removed. Following injection of 4 ml of Dulbecco's Modified Eagle's Medium (DME) into the peritoneal cavity and light massage, the suspensions of cells were harvested. The resulting cells were washed in fresh medium and resuspended to known concentrations based upon hemocytometer counts.

Macrophages from both normal mice and those infected with the BCG strain of Mycobacterium tuberculosis were utilized in these studies. The latter cells, termed activated macrophages, exhibit increased agglutination when in suspension (J. Immunol. 101:296, 1970), a decreased tendency to migrate (Science 153:80, 1966), enhanced phagocytosis of opsonized erythrocytes (J. Immunol. 110:321, 1973) and the capacity to kill non-contact-inhibited tumor cells in vitro (Science 180:868, 1973).

The medium used in these researches was DME with varying concentrations of fetal calf serum as determined by the experimental design.

The three materials, glass, Lux coverslips and FEP, were prepared for use by solvent cleaning followed by distilled water and vacuum drying. Because of the relatively short observation times, no attempts were made to sterilize the materials. The prepared surfaces were partially characterized by determination of both water and octane contact angles.

Observations of the murine macrophages on the above surfaces were made in three ways. Cell morphologies and the relative degrees of spreading were evaluated by both optical and scanning electron microscopy. Cellular adhesion was quantitated employing a rotating disc-shear technique. This procedure will be described in detail elsewhere.

Results and Discussion

In initial experiments serum concentrations ranging from 0 to 50 percent in DME were used. It was soon seen that few microscopic differences could be noted among macrophage populations on the three surfaces which ranged widely in surface energies. The majority of subsequent studies involved use of 0 to 5 percent serum.

Based upon light microscopy observations, it was evident that even though large differences did exist among the surface properties of the materials used, these differences were not wholly reflected in the morphologies of the cells on the different surfaces except in the case of activated macrophages on the FEP. All macrophages were seen, with time, to assume similar degrees of spreading on all surfaces, the main difference being primarily the time it took for the cells to spread to their final state. It was clearly observed that at a 5 percent serum concentration macrophages tended to spread in a longitudinal form more and to greater extents on the FEP surface than on either the Lux or glass cover slips.

Employing the scanning electron microscope, both normal and activated macrophages were studied on all three surfaces. Fifteen minutes after normal cells were allowed to settle on the three surfaces, some spreading was seen on FEP and Lux materials; a lesser degree of spreading was noted on glass. With increased incubation times, normal cells were well spread on both FEP and glass, but to a lesser extent on the Lux cover slips. Macrophages on the FEP showed an increased tendency to form clumps.

Activated macrophages spread extremely rapidly and extensively in all cases. Within 15 minutes these cells were spread to their full extents on all surfaces irrespective of widely different surface energies.

The one distinct morphological difference indicating intense cellular response to a given surface was seen in the case of activated macrophages in contact with the low energy FEP surface. Extensive cellular aggregation was seen after times as short as two hours in media with either no calf serum or with 5 percent and was more evident in Hank's balanced salt solution with or without 5 percent calf serum. The same reaction was evident with activated macrophages allowed to settle on paraffin coated glass cover slips.

Adhesion experiments performed tended to show that normal macrophages adhered less to the low energy FEP surface after 30 minutes settling time than to either of the other two surfaces. Adhesion after this same time to both the Lux cover slips and to glass appeared to be approximately equivalent. After a 4 hour settling time, the adhesion of the macrophages to the FEP surface appeared to be at least as great, if not greater, as to either glass or Lux. Whereas at a 30 minute settling time, the macrophages adhered about equally to either glass or Lux cover slips; after 4 hours adhesion to the Lux surface appeared to be slightly higher. This discrepancy in adhesion patterns may be explained by considering that the competitive adsorption of protein versus cells from the medium onto the three surfaces would be comparatively minimal after 30 minutes. Therefore, when the cell settles onto the surfaces after 30 minutes it could be expected to encounter the surfaces devoid of protein. Thus, it would be expected to adhere less to the lower energy more hydrophobic FEP surface than to the higher energy, more hydrophilic Lux cover slip or glass surfaces. After 4 hours, however, adsorption of protein would have occurred on all three surfaces, if not at the point where the cell initially makes contact, then at least over that area upon which the cell would eventually spread. Thus, the cell would encounter a substrate whose surface properties may be entirely different than those without adsorbed protein.

Since different proteins are adsorbed at varying rates onto different surfaces, and since configurational changes may occur for the same protein on the three different surfaces used, the properties displayed by these proteinated surfaces used may be quite different in each case. As found from the results after 4 hours, the proteinated surface displayed to the macrophage by the FEP surface shows greater adhesive properties than either of the other two surfaces. Physically, it might be envisioned that the hydrophobic side chains on the protein molecules could bond to the FEP surface through a form of hydrophobic bonding, while the hydrophilic side chains would bond to the hydrophilic macrophage surface through dipole-dipole interactions.

Again, for activated macrophages, a lower amount of adhesion between the cell and the FEP surface than between the cell and either the glass or Lux cover slip after 30 minutes was noted. One may again postulate that this was due to the fact that there was no adsorbed protein film on the surface after this time, and the activated macrophages were contacting the surfaces directly. After a four hour settling time, however, the activated macrophages still showed less adhesion to the FEP surface than to either the glass or Lux surfaces. Since the same protein film which was speculated to be present on the surface of FEP for the experiment run with normal macrophages could still be expected to be coating the surface for the activated macrophage experiments, this lesser adhesion of activated macrophages on FEP after 4 hours cannot be explained by considering the surface and its adsorbed film alone. However, it has been noted that macrophages, when activated, tend to show an increased tendency to clump together in suspension (J. Immunol. 101:296, 1970). This, one may speculate, could be due to an increase in the hydrophobicity of the cellular membrane. If the activated macrophage were to assume a more hydrophobic surface than the normal macrophage, then it could be expected to adhere less to the hydrophilic protein layer we earlier theorized to be present on the FEP surface. This could explain why, after a 4 hour settling time, activated macrophages adhere less to FEP than to glass or Lux cover slips. We must note here that the tendency for macrophages to become more hydrophobic when activated is not substantiated by work done by Thrasher and coworkers (J. Immunol. 110:321, 1973) who found, using contact angle data, that activated macrophages were in fact more hydrophilic.

Lux cover slips and glass surfaces were shown to have similar adhesion properties for macrophages. In the analysis of their surface properties, their total interfacial free energies were found to differ by only 4 dynes/cm. FEP, on the other hand, showed a considerably lower interfacial free energy, and also differed greatly in adhesive properties from the other two surfaces used. Thus, whether the cell, when settling onto a substrate, encounters the base inert surface itself or an adsorbed protein film, its adhesive properties appear to be influenced by the interfacial free energy of the base uncoated surface.

It was also noted in the adhesion experiments that the cells which would remain on the surface after the shear force was applied would not always be those same cells that were most well spread. Many of the cells would be in a rounded form. Thus it is postulated that while a cell that is spread is probably fairly well attached to the surface, a cell that is attached to the surface need not necessarily be spread on it.

BRIEF COMMUNICATION

SURFACE TENSION MEASUREMENTS ON METHACRYLATE MONOMER SOLUTIONS, SELECTED SOLVENTS, AND GEL EXTRACTS

S. Hattori, R. N. King and J. D. Andrade
Department of Materials Science and Engineering
University of Utah
Salt Lake City, Utah 84112

(Received In Final Form 3 February 1978)

Summary

The surface tensions of selected methacrylate monomer and solvent solutions were measured, and calibration curves were generated. The curves were then used to deduce the amounts of water soluble extractables in methacrylate hydrogels by measuring the surface tension of the extractant. The detectability limit (parts per 10,000) and the overall sensitivity of the method suggests its possible use as an extraction monitor test for related biomaterials.

Introduction

It has become increasingly important to ascertain the purity of hydrogels as more of them are developed for biomedical purposes. Solvents and unreacted monomers must be thoroughly extracted. The usual procedure is to extract the gels in water for a designated time. It is assumed that in a matter of days most water soluble impurities are reduced to acceptable levels.

A simple semi-quantitative extraction test for biomaterials is Baier's "Teflon Test" (1). In this test a drop of clean water is placed on a smooth fluoropolymer substrate. The contact angle is measured and recorded. The test material is then allowed to touch the water drop. If there are any water soluble extractable impurities they will lower the surface tension of water and the contact angle will decrease accordingly. This should be a fairly widespread phenomenon, since most organic materials are surface active owing to the differences in bonding characteristics from water. The change in contact angle is read against a contact angle - surface tension chart. The method is a quick semi-quantitative check for the presence of water-extractable impurities. One can utilize the principle of this method and obtain a more quantitative result by direct surface tension measurements.

Methods and Procedures

A Fisher tensiometer was used to determine surface tension by the Du Noüy ring method (2,3). Total wetting of the ring is a major assumption in this method, necessitating rigorous cleaning procedures. The Platinum-Iridium ring

(6 cm circumference) was radiofrequency glow discharged (Tegal Corp., Plasmod System) in dry air at 300 μ Hg for 3 minutes just prior to use. The setup requires about 20 ml of liquid for measurements.

Solutions of both solvents and monomers used for hydrogel polymerization were prepared in known concentrations to generate calibration curves of surface tension versus solution concentration. Solvents of interest included ethylene glycol (EG - Mallinkrodt), triethylene glycol (TEG - Union Carbide), and dimethyl formamide (DMF - Burdick and Jackson Labs). Several monomers of the methacrylate family were evaluated by this method. A typical monomer is 2-hydroxyethyl methacrylate (HEMA - Hydromed Sciences). Methoxyethyl methacrylate (MEMA) and methoxyethoxyethyl methacrylate (MEEMA) represent relatively hydrophobic monomers. They were prepared in this laboratory by transesterification of methyl methacrylate with the appropriate alcohol (4). Methacrylic acid (MAA - Eastman Kodak Co.) and dimethyl aminoethyl methacrylate (DMAEMA - Polysciences) are used to introduce fixed charges into the hydrogels (4). As a consequence of having ionized moieties, HEMA copolymers of MAA (negatively charged) and of DMAEMA (positively charged after quaternization with methyl iodide) are highly swollen in water.

The measurements were taken as follows: The containers with the solutions are set on the stage of the tensiometer. The ring hangs down above the container at the end of a balance arm, which is connected to a torsion wire. The ring is then lowered about 3 mm into the solution. To measure surface tension, the ring is pulled slowly through the solution-air interface by increasing the torque on the wire while simultaneously lowering the stage. When the ring finally breaks through the surface, surface tension is read directly on the calibrated dial in dynes/cm.

Three readings were taken for each solution concentration. The standard deviations were small enough that they are absorbed into the points plotted. The surface tension of distilled water was measured with each set of experiments along with the room temperature, and all subsequent solution values are normalized with respect to the reported value for water of 72.0 dynes/cm at 25° C (5).

Results

Solvents and monomer solution surface tensions are shown in Figures 1 and 2. The surface tension of water is used as a reference. Other reported values are listed in Table 1. For the solutions studied, a 1.0 vol. % concentration of monomer in water was chosen as the upper limit in this work. In the case of MEMA, the solubility limit was reached before 1%. As shown in Figures 1 and 2 the lower limit of detectability of this test is about 5 parts per 10,000 for the monomers and solvents used. In between these limits the curves have linear and non-linear portions. The linear portion would enable one to use the curves as fairly accurate calibration standards for samples with unknown amounts of impurities. Both figures show roughly linear portions to exist between 1 and 0.1%.

Comparison between the surface tension of the pure material with the aqueous solution curves shows that the lower the surface tension of the pure material, the lower the solution surface tension - which is to be expected. HEMA, MAA and EG have fairly strong hydrogen bonding capacities like water, while DMAEMA and DMF have more hydrophobic hydrocarbon side chains. Therefore, for DMAEMA and DMF the overall bonding characteristics are different from that of water, and the result is a strong depression of the solution surface tension.

TABLE 1
Some Reported Surface Tensions

MATERIAL	REPORTED (DYNES/CM)	OBSERVED (DYNES/CM)	REFERENCE
Ethylene Glycol	47.7	48.6	5
Dimethyl Formamide	35.2	37.2	6
Methacrylic Acid	26.5	28.9	7

Preliminary extraction data were compared to these calibration curves and are shown in Table 2. HEMA - 10% MAA and HEMA - 10% DMAEMA copolymers were made with EG (40% [v/v]) as the diluent. The gel is later exchanged with water after polymerization. These were investigated since it was suspected that ionization might make these hydrogels more prone to extraction. The monomers and solvents were degassed and introduced into polypropylene molds. Azobis (methyl isobutyrate) prepared in this laboratory (4) was the initiator. Polymerization proceeded at 60° C for 24 hours under argon. All gels contained 1% (v/v monomer) tetraethylene glycol dimethacrylate (TEGDMA - Polysciences) crosslinker. Aliquots of the polymerized samples (about 100 mg) were placed in 20 ml vials with 20 ml distilled water and subsequently transferred to vials of fresh water at the end of 1, 2, and 4 hours. The surface tension of the water from these vials was measured.

TABLE 2

Preliminary Extraction Data (surface tensions [dynes/cm] of extraction water of hydrogels at the end of 1, 2, and 4 hours, listed in that order)

HYDROGEL	UNIONIZED		IONIZED
	DRIED	NOT DRIED	DRIED
PHEMA		71.1 71.9 71.8	
P(MAA-HEMA)	71.7 71.2 71.2	69.8 71.5 71.5	71.5 71.2 71.4
P(DMAEMA-HEMA)	70.3 71.6 71.5	66.9 70.5 70.6	71.2 71.8 71.7

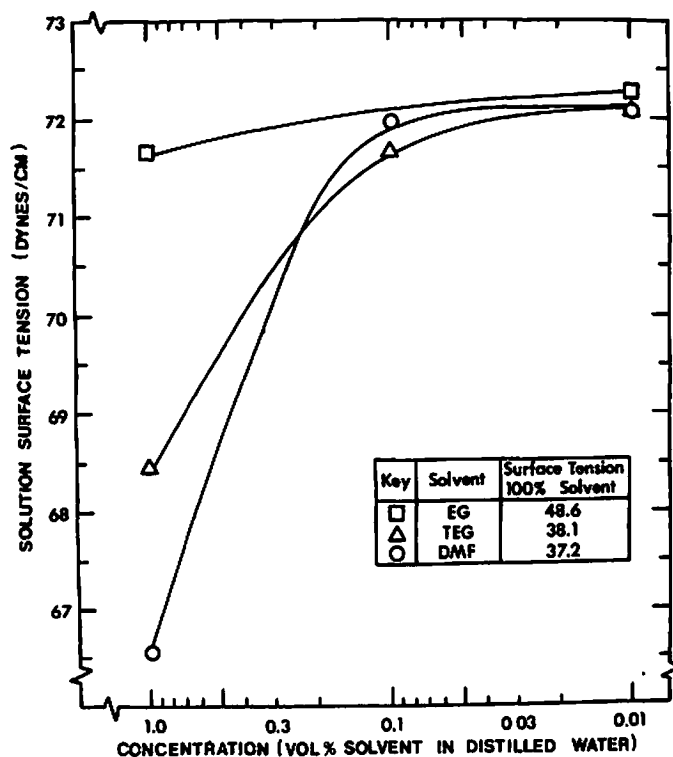


FIG. 1
Surface Tensions of Some Solvent-Water Systems at 25° C.

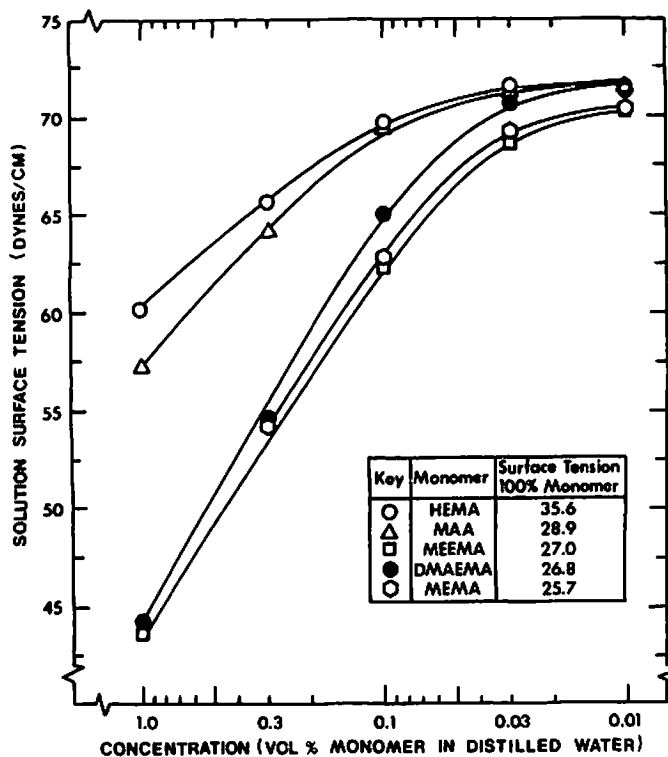


FIG. 2
Surface Tensions of Some Monomer-Water Solutions at 25° C.

Some of the hydrogel samples had to be vacuum dessicated (2 hours at 60° C) so they would not phase separate during the ionization procedure. When they were thus dried, no significant depression could be seen in the surface tension of the extraction water. This implies that vacuum dessication removes most of the solvent and unreacted monomer. It also tells something about polymeric impurities. Had there been any low molecular weight linear polymers, they would probably not be removed by vacuum dessication. Such polymeric impurities are expected to depress surface tension considerably if they are water soluble. Direct immersion of hydrogels in water after release from the mold resulted in significantly lower surface tensions, especially for the one hour values. From the calibration curves, this roughly corresponds to about 1.0% of extractable material. The nature of these impurities, however, cannot be determined since the impurities extract as mixtures. However, all surface tension values eventually approach the surface tension of water at the end of four hours. Experiments with radiolabelled monomers have shown that for many hydrogels, one hour seems sufficient time for extraction (4). The thickness of these hydrogels was about 1 mm. Faster extraction rates can probably be expected with thinner samples.

The data also substantiate the stability of ionized hydrogels. The ionization procedure does not appear to change the network structure enough to make them any more extraction prone than their unionized counterparts.

Discussion

The above method helps one determine the extent of water soluble impurities in a material. To make a complete calibration requires all possible extractables and their combinations with each other in varying concentrations. Unfortunately, this has some practical limitations such as solubility (e.g. MEMA), and a precise knowledge of all types of impurities within the polymer. Much more precise methods of detecting low molecular weight extractants are available for more detailed studies.

The absence of any significant surface tension depression in small volumes of water used for extraction merely indicates that large amounts of water-extractable surface-active materials are not present in the gels. Such gels can then be studied by contact angle and related surface chemistry methods with little risk of artifact due to water extractable impurities.

The technique of water soluble impurity detection can possibly be used in other systems with different solvents, though not for polyacrylamides. The acrylamide monomer is highly polar. One would therefore expect the bonding characteristics, hence the surface tension, to be similar to that of water. This would result in little depression in surface tension of aqueous monomer solutions. Since the monomer is a solid, surface tension values are not available. The polymer solution surface tension values, however, are available (Process Chemicals Department, American Cyanamid Company: Cyanamer^R A-370, P-26, P-250; surface tensions 67.4, 61.1, 75.5 dynes/cm, respectively). Surface tension measured in this laboratory for a 1% (w/w) monomer solution was about 71 dynes/cm. This value, compared to those of the methacrylate monomers, is much closer to that of water.

Conclusion

The technique and measurement of surface tension of the extraction water of hydrogels is discussed. Results from several solvents and monomer solutions indicate the test can detect impurities such as methacrylate monomers and certain solvents as low as 5 parts per 10,000. Comparison with actual extraction data shows monomer and solvent curves can be used as calibration standards. The absence of strong surface tension depression indicates lack of detectable contamination, which will ensure subsequent surface chemical studies, such as contact angle, to be relatively free from water-extractable impurities.

References

1. R. E. BAIER, V. L. GOTT, and A. FERUSE, Trans. Amer. Soc. Artif. Internal Organs 16 50-57 (1970).
2. P. L. DU NOÛY, J. Gen. Physiol. 1 521-524 (1918)..
3. A. W. ADAMSON, Physical Chemistry of Surfaces, 2nd ed., Wiley-Interscience, 1976.
4. D. E. GREGONIS, C. M. CHEN, and J. D. ANDRADE in Hydrogels for Medical and Related Applications, American Chemical Society Symp. Series No. 31, 1976, p. 88, J. D. Andrade, ed.
5. R. C. WEAST, Handbook of Chemistry and Physics, 54th ed., (p. F43-45) Chemical Rubber Co. Press, Cleveland, Ohio (1973).
6. F. BLANKENSHIP and B. CLAMPITT, Proc. of the Oklahoma Acad. of Sci., 106-111 (1950).
7. ROHM AND HAAS CO., Glacial Methacrylic Acid; Glacial Acrylic Acid, CM-411.

Fibroblast Cell Proliferation on Charged Hydroxyethyl Methacrylate Copolymers¹

S. HATTORI, J. D. ANDRADE,* J. B. HIBBS, JR.,† D. E. GREGONIS,
AND R. N. KING

*Department of Materials Science and Engineering, *Department of Bioengineering, and †Department of Internal Medicine, University of Utah, Salt Lake City, Utah 84112*

Received June 22, 1983; accepted September 12, 1983

Two fibroblastic cell lines, 3T3 and 3T12, were grown on hydrophilic hydrogel substrates containing various amounts of positive or negative charge. The materials were copolymers of hydroxyethyl methacrylate (HEMA) and methacrylic acid (MAA), *N,N*-dimethylaminoethyl methacrylate hydrochloride (DMAEMA-HCl), or trimethylaminoethyl methacrylate chloride (TMAEMA-Cl). The samples were prepared as spun cast films on ultraclean glass microscope slides. The cells were grown in 10% fetal bovine serum supplemented Dulbecco's modified medium (DMEM). Both cell lines survived and proliferated on the positively charged DMAEMA-HCl or TMAEMA-Cl copolymers with HEMA. Cells did not survive on the negative MAA-HEMA copolymers nor on the neutral HEMA homopolymers. Proliferation did not correlate with water content of the gel materials. Attachment as well as proliferation did correlate well with zeta potential and mole percentage positive charge as determined by bulk titration data. © 1985 Academic Press, Inc.

INTRODUCTION

Studies of cell adhesion and/or proliferation on synthetic materials incorporating charged moieties have been reported (1-4). To date, however, there has been no systematic characterization of the materials used in such studies, and consequently the interpretation of cell behavior on charged substances remains an open question.

In this paper, the results of cell survival and cell proliferation kinetics are reported as a function of the measured charge on copolymer substrates using standard mouse fibroblast cell lines.

MATERIALS AND METHODS

Polymers. The general polymer system used in this study is shown in Table I. The prep-

aration and characterization details have been previously outlined (5, 6). The polymers were used as thin films obtained by spin casting 1 wt% linear polymer solutions in dimethyl formamide (DMF) onto particulate-free borosilicate glass coverslips (No. 2, 24-mm diam, Sargent-Welch, Anaheim, Calif.). The initial solution contained 1 mole% hexamethylene diisocyanate (HMDIC) as a post-crosslinking agent. The coverslips were cleaned by standard methods in a clean room (6, 7). The polymer surfaces were random and homogeneous, thus minimizing structure effects (8, 9) on the cell growth results.

The positively charged copolymer series (DMAEMA-HCl/HEMA and TMAEMA-Cl/HEMA) adhered strongly to the negatively charged glass substrate. The negatively charged MAA/HEMA series, however, required silanization of the glass support with aminopropyltriethoxy silane (Aldrich Chemical Co., Milwaukee, Wisc.) to ensure good bonding with the MAA/HEMA copolymers (5, 6).

¹ Presented at the symposium "Initial Events on Bioattachment at the Solid-Liquid Interface," held at the American Chemical Society meeting, Las Vegas, Nevada, March 1981, under the auspices of the Colloid Chemistry Division.

TABLE I

Polymers Used in Characterizing Cell Growth on Charged Copolymer Substrates

$\text{General system } \left[\begin{array}{c} \text{CH}_3 \\ \\ \text{CH}_2 - \text{C} \\ \\ \text{C}=\text{O} \\ \\ \text{O} \backslash \text{R} \end{array} \right]_n \text{ : methacrylate esters}$			
R	Name	Abbreviation	Property
$-\text{CH}_2-\text{CH}_2-\text{OH}$	Hydroxyethyl methacrylate	HEMA	Neutral
$-\text{H}$	Methacrylic Acid	MAA	Negatively charged (pH dependent)
$\left[\begin{array}{c} \text{CH}_3 \\ \\ \text{CH}_2 - \text{CH}_2 - \text{N}^+ - \text{H} \\ \\ \text{CH}_3 \end{array} \right] \text{Cl}^-$	Dimethylaminoethyl methacrylate-hydrochloride (ionically quaternized)	DMAEMA-HCl	Positively charged (pH dependent)
$\left[\begin{array}{c} \text{CH}_3 \\ \\ \text{CH}_2 - \text{CH}_2 - \text{N}^+ - \text{CH}_3 \\ \\ \text{CH}_3 \end{array} \right] \text{Cl}^-$	Trimethylaminoethyl methacrylate chloride (covalently quaternized)	TMAEMA-Cl	Positively charged (pH independent)

Prior to casting the polymer solutions were filtered through 1- μm Fluoropore filters (Millipore Corp., Bedford, Mass.). Spin casting was performed in a class 100 laminar flow-hood using a Headway Research Model EC101 spin coater operating at 4000 rpm for 10 sec. Samples were subsequently oven cured under dry nitrogen at 80°C overnight. Three coatings (200 μl total solution volume) were given to assure complete coverage.

The coatings were characterized by X-ray photoelectron spectroscopy. Coating thickness was determined gravimetrically to be greater than 200 Å. Prior to use, the coverslips were stored individually in polystyrene petri dishes (Becton Dickinson Labware, Oxnard, Calif.). Streaming potential measurements (10) were obtained on similarly polymer-coated 1 \times 3-in. microscope slides.

Coverslips were extracted in serum-free Dulbecco's modified media (DMM) 1 day prior to the experiments. This step was designed to extract residual solvent from the

polymer, and at the same time equilibrate the polymer in the media. Each coverslip was placed in 2 ml of DMM and was incubated overnight at 37°C. The following day the extractant media was discarded and the cells were seeded.

An inhibition of cell growth (ICG) test was run on the extracts (Microbiological Development and Control, Inc., Salt Lake City, Utah). The procedure used is a modified version of the Autian method (11) for the evaluation of polymer toxicity to various cell lines. The procedure is based on the premise that cells in the presence of leached toxins would show an inhibited rate of metabolism and hence produce lower than usual amounts of protein. Briefly, the procedure is as follows: modified Eagle's medium (MEM) was used with serum for extraction to conform with the toxicity test protocol. The coverslips were equilibrated overnight at 37°C as usual, and the media (extract) were collected. The extracts were mixed with double strength MEM

and added to an L929 mouse fibroblast cell growth assay tube. After 72 hr of incubation, the total protein content of each tube is measured using the colorimetric methods of Lowry. Percentage inhibition (% ICG) is taken as the percentage change in optical density of the sample tubes over the control tubes, adjusted for zero time, in the absence of extracts. The precision of the ICG procedure is approximately $\pm 10\%$. Values of 10–15% inhibition suggest a low level of inhibition, while values of over 15% are generally considered to be indicative of a toxic material. These values are derived from extensive experiments utilizing direct tissue reaction studies (11). The MEM used in the extraction did not affect cell growth differently compared to DMM as observed in the polymers extracted in both media.

Cells. 3T3 and 3T12 cell lines were obtained from the American Type Culture Collection (ATCC, Rockville, Md.) and maintained in DMM with 10% fetal bovine serum (FBS) at pH 7.4. Cells were trypsinized, counted, and resuspended in DMM + 10% FBS. Trypan blue dye exclusion showed greater than 95% viability. Cells were seeded at low density, 1.3×10^4 cells/dish, for the kinetic studies and 10 times that for the high-density growth studies. The cells were fixed and stained in 2% glutaraldehyde and 10% Giemsa and counted using light microscopy at about 100 \times . Twenty-six measurements were taken at 1-mm intervals across the coverslips and the average number of cells/mm² was calculated.

The kinetic study is defined as follows: the cells were seeded into petri dishes. They were fixed, stained, and counted at intervals of 1, 2, and 3 days for 3T12 cells, and at 2, 4, and 6 days for the slower growing 3T3 cells. The kinetics of cell proliferation are determined from the number of cells counted at these intervals.

In addition 10-min adhesion (attachment) studies were done. The cells were allowed to settle on the coverslips for 10 min and were then fixed and counted. Standard glass and

surface modified polystyrene tissue culture substrates were used as controls. Proliferation at high seeding density (1.3×10^5 cells/dish) was observed at 1 day (3T12) or 2 days (3T3) to see if any difference in proliferation existed between the two cell lines that may not be apparent at low seeding density.

RESULTS

Toxicity

The ICG test showed that the 35% DMAEMA-HCl/HEMA copolymer may be mildly toxic (5). All other materials were nontoxic by the ICG assay.

Cell Attachment and Proliferation

Figures 1 and 2 show the growth curves of 3T3 and 3T12 cells on the various substrates. Symbols of the same type lined up vertically represent the same copolymer type with increasing amounts of added charge. Generally, increasing positive charge supports increasing growth. As seen in Fig. 1, the negatively

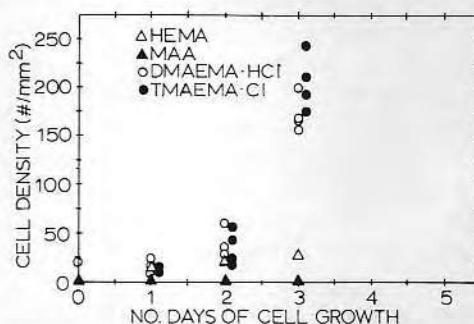


FIG. 1. 3T12 cell proliferation at low seeding density on the substrates indicated. Note particularly the solid circles which are the highly positively charged covalently quaternized copolymer. The cell density increases dramatically between Days 2 and 3 to nearly 250 cells/mm². Referring to Day 3 data, the four solid circles in that column represent increasing positive charge density, showing that the cell density increases with increasing positive charge density. Note that the negatively charged material at comparable charge densities does not support cell growth, as indicated by the solid triangles, even at 3 days. The neutral material, the open triangles, supports some growth but it is minimal even at 3 days. Each point represents three replicates.

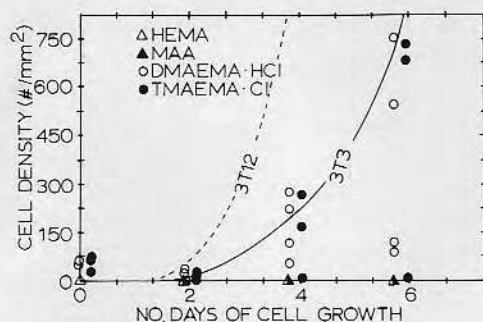


FIG. 2. 3T3 cell growth at low seeding density up to 6 days. The same general results are shown here as in Fig. 1 except that the growth period goes out to 6 days with the consequent higher cell density. In this cell line at 6 days, there is a considerable greater spread in cell density with positive charge character of the copolymer as indicated by the spread in the solid and open circles at Day 6 (compared with Fig. 1).

charged MAA/HEMA copolymers do not support proliferation to any measureable extent. This trend can be seen more clearly in the 2-day growth studies at high seeding density ($10\times$ higher than used for Figs. 1 and 2) in Figs. 3 and 4. Here cell growth is plotted against mole% charge, i.e., moles of charged comonomer, expressed as % of total monomer. Both plots confirm the results shown in Figs. 1 and 2.

There are two aspects that might affect cell proliferation that could be influenced by mole% charge: water content (wet weight of gel/weight of dry polymer) and zeta potential (10). The data for 3T3 cell growth plotted

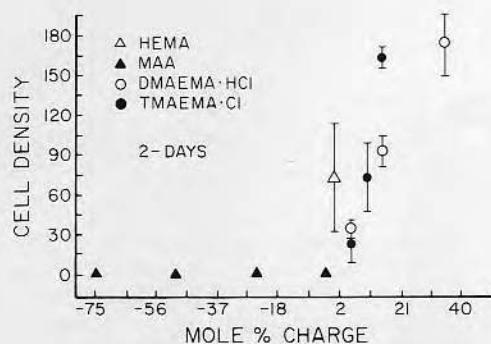


FIG. 3. 3T3 cell growth at 2 days for high seeding density vs mole% charge.

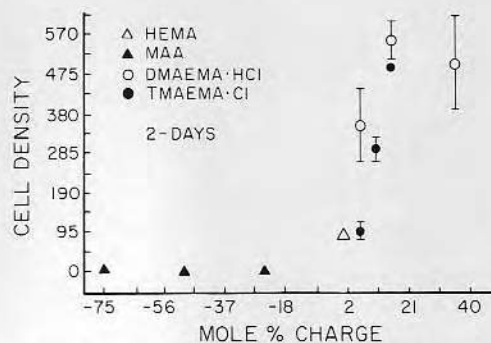


FIG. 4. 3T12 cell growth at 2 days for high seeding density vs mole% charge.

against each of these variables are shown in Figs. 5 and 6. Here cell growth is predominantly dependent on the interfacial charge character, i.e., more growth with positive potential, and to a lesser extent on the degree of swelling.

The trend of cell proliferation on positively charged copolymers presented thus far is initially noticeable in the attachment stage (zero time growth or plating efficiency). Using 3T12 cells as an example, this trend is shown in Fig. 7 (16). In fact, both 3T3 and 3T12 cells attached and proliferated more rapidly on positively charged copolymers. This trend was established 10 min after seeding and persisted throughout the experiments.

In this study the majority of the copolymers contained 1 mole% crosslinker. To see if substrate rigidity (tightening of the network)

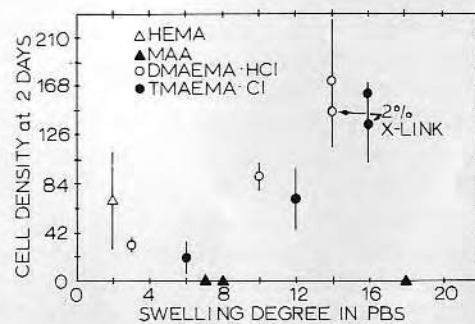


FIG. 5. 3T3 cell growth at two days for high seeding density vs swelling degrees in PBS. Swelling degree = weight of swollen gel/weight of dry gel.

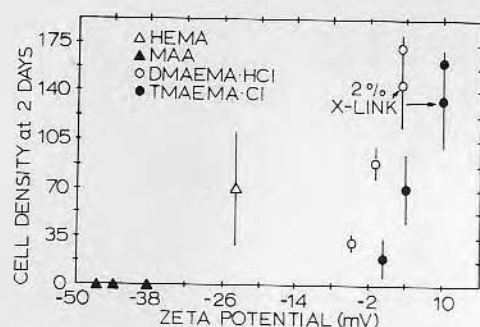


FIG. 6. 3T3 cell growth at 2 days for high seeding density vs substrate zeta-potential.

had any effect, 2% crosslinker concentrations were used for the copolymers containing the highest amounts of charge (hence the highest degree of swelling). The swelling degrees of these polymers (measured on 3% positively and negatively charged HEMA copolymers) were reduced to levels close to those of pHEMA. The cell density results, however, were within the standard deviations of the 1% crosslinker values. If a tighter, more rigid copolymer resulted from the 2% crosslinker, one might expect better growth, especially with the anchorage dependent 3T3 cells. This was not seen.

DISCUSSION

Toxicity

The toxicity test results suggest that, in general, the materials used for this study were not toxic to cells. Therefore, nonproliferation when observed is unlikely to be due to toxic substances leaching from the polymer. The 35% DMAEMA-HCl/HEMA copolymer may be toxic. Although cells generally proliferated on this material, it should be remembered that the charge character of a DMAEMA-HCl/HEMA copolymer is pH dependent thereby influencing both toxicity and cell culture measurements locally. Since the permanently quaternized TMAEMA-Cl/HEMA copolymer is nontoxic, one might speculate that the DMAEMA moiety is the potential toxicant. More rigorous toxicity studies

should be carried out to answer the many questions raised.

Cell Attachment and Proliferation

Since gels are generally regarded as non-supportive for normal cell growth (11-13), it is interesting to note that both 3T3 and 3T12 cells grow on the positively charged gel substrates. According to Figs. 1-4, neither 3T3 nor 3T12 cells appear to prefer DMAEMA-HCl/HEMA copolymers over TMAEMA-Cl/HEMA copolymers or vice versa. In other words, it seems to be the positive charge environment that encourages cell proliferation. In some cases DMAEMA-HCl/HEMA copolymers appeared to support more cell proliferation than TMAEMA-Cl/HEMA copolymers, but not consistently. This inconsistency may be due to the pH dependence of this particular copolymer. The ratio of DMAEMA to DMAEMA-HCl could change with small pH fluctuations. It is conceivable that minute media pH changes could bring about a favorable or hostile growth environment. Even if the bulk media pH were constant, the cells themselves as a result of their metabolism influence the local pH. It is evident that, when working with ionizable species, the importance of maintaining the desired pH cannot be overstressed.

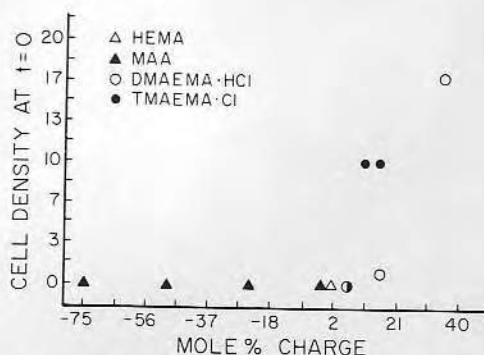


FIG. 7. 3T12 cell attachment (zero time adhesion) at low seeding density vs mole% charge. This is analogous to a plating efficiency assay measured after 10 min of contact time. Cell density in number of cells/mm².

Although both 3T3 and 3T12 cells grow on positively charged gels, the 3T12 cells grow more rapidly (Fig. 1) and within a given time period to a high density (Fig. 4). This behavior is generally expected for the transformed 3T12 cells (12).

In the figures containing cell proliferation against zeta-potential or against water content, it should be noted that pHEMA shows a net negative interfacial charge character, despite the lack of any incorporated charge, perhaps due to adsorbed anions and/or organized water (6). Also, swelling degrees for this particular polymer are quite low, and it may be possible that a rigidity effect offsets the negative interfacial character, resulting in an unexpected marginal growth.

However, as indicated under Results, doubling the amount of crosslinker still does not make cells proliferate on MAA/HEMA copolymers. It appears that constraining the swelling degree to that of a pHEMA is not enough to offset the negative charge of a 3% MAA/HEMA copolymer. If rigidity affected cell proliferation and the apparent amount of negative charges was minimal, by introducing more rigidity into a pHEMA, one might expect to see an increased degree of cell proliferation.

The films cast on glass have different swelling capacities than bulk gels. The exact swelling characteristics of these thin film gels are unfortunately not known. Some of the more highly charged gels have on occasion been noted to be somewhat "slick" on the surface. This could indicate a looser and/or more swollen network at the surface, possibly with dangling ends. In the process of making three coatings, each coating step resolutes the prior one, and also adds more chemical crosslinker (HMDIC). It is reasonable to suggest that the first coat of each film is somewhat immobile. Additional layers, despite the added HMDIC, tend to be less constrained by the rigid glass substrates. Hence the outermost gel coat could conceivably mimic bulk-gel behavior, and results obtained here may apply to bulk gels. On the other hand,

subtle coating thicknesses were shown to affect cell growth. Even though pHEMA is known as a non-cell-adhering material, in thin film form one pHEMA coat supported cell growth. Two or more coatings showed the classical neutral pHEMA gel response, i.e., minimal growth. The results are very similar to those reported by Folkman and Moscona (13). This experiment may suggest the importance of the rigidity of the substrate, i.e., the second and other coats may not have the same rigidity as the initial coat. It may also suggest substrate show through.

The subject of rigidity is important to remember when arriving at a cell proliferation criteria for this system. In this charged hydrogel system, initial attachment reflected subsequent proliferation. However, in a system such as the charged methyl methacrylate copolymers, cells show low or nonexistent attachment to neutral and charged materials, but proliferate after 24 hr, as much as they would on glass.

CONCLUSIONS

This work presents evidence that charge, positive charge in particular, does affect cell adhesion and growth. The involvement of positive charge has been cited by others implying similar adhesion mechanisms (1-4, 14, 15). There is a body of literature, however, which contends negative charge to be most important (16-18). Much of the negative charge work is based on surface-oxidized polystyrene and glass. The charge in these systems has been estimated by dye binding (16, 17). However, these surfaces differ from those of the present work in that they are not hydrophilic in the sense of having an extensive gel interfacial region. Also their surface rigidity is completely different from the materials used in this work. The copolymer gels used in this study exhibit a highly hydrophilic, soft interfacial region (8).

The effect of positive charge at gel-like interfaces has been investigated by others with similar results (2-4, 19, 20) and has

been commercialized for mass cell culture application. Actual measurements of surface charge density are very rare, however (20).

Although the proliferation trends of the cells implied cell/substrate electrostatic interactions, the exact mechanism of adhesion is not known. Different adhesion mechanisms may operate for substrates with different amounts of charge (positive or negative), surface rigidity, and other factors probably mediated by specific protein adsorption properties (21). A more definite interpretation of cell adhesion must await further work with well characterized model materials, including protein adsorption studies, where these factors may be investigated together.

ACKNOWLEDGMENTS

The authors would like to thank Dr. Dennis Coleman and Dr. Lee Smith for their stimulating discussions. Thanks are also extended to Mr. Lyle Brostrom for his help in the preparation of the polymers. The work was supported by NIH Grant HL-16921.

REFERENCES

1. Rembaum, A., Senyei, A. E., and Rajaraman, R., *J. Biomed. Mater. Res. Symp.* **8**, 101 (1977).
2. Van Wezel, A. L., *Nature (London)* **216**, 64 (1967).
3. Rosen, J. J., Gibbons, D. F., and Culp, L. A., in "Hydrogels for Medical and Related Applications" (J. D. Andrade, Ed.), p. 329. ACS Symp. Series, No. 31, Amer. Chemical Soc., Washington, D. C. 1976.
4. Levine, D. W., Wong, I. S., Wang, D. I. C., and Thilly, W. G., *Somatic Cell Gen.* **3**, 149 (1977).
5. Hattori, S., Ph.D. dissertation, University of Utah, June 1980.
6. King, R. N., Ph.D. dissertation, University of Utah, February 1980.
7. Coleman, D. L., Ph.D. dissertation, University of Utah, August 1980.
8. Rovinsky, Y. A., and Slaunaya, I. L., *Exp. Cell Res.* **84**, 199 (1974).
9. Weiss, P. A., *Perspect. Biol. Med.* **14**, 182 (1971).
10. Van Wagenen, R. A., and Andrade, J. D., *J. Colloid Interface Sci.* **76**, 305 (1980).
11. Autian, J., *J. Artif. Organs* **1**, 53 (1977).
12. Paul, J., "Cell and Tissue Culture." Churchill Livingstone, Edinburgh, 1973.
13. Folkman, J., and Moscona, A., *Nature (London)* **273**, 345 (1978).
14. Jacobson, B. S., and Branton, D., *Science* **195**, 302 (1977).
15. Maceira-Coelho, A., Berumen, L., and Avrameas, S., *J. Cell. Physiol.* **83**, 379 (1975).
16. Maroudas, N. G., *J. Theor. Biol.* **40**, 417 (1975).
17. Rappaport, C., in "Chemistry of Biosurfaces" (M. L. Hair, Ed.), Vol. 2, p. 449. Marcel Dekker, New York, 1977.
18. Anstein, D. F., and Hartman, P. M., *Clin. Microbiol.* **2**, 46 (1978).
19. Iwig, M., Lasch, J., and Glaesser, D., *Cell. Differ.* **9**, 1 (1980).
20. Levine, D. W., Wang, D. I. C., and Thilly, W. G., *Biotechnol. Bioeng.* **21**, 821 (1979).
21. Grinnell, F., *Int. Rev. Cytol.* **50**, 65 (1977).

Interaction of plasma proteins with heparinized gel particles studied by high-resolution two-dimensional gel electrophoresis

C.-H. Ho,* V. Hlady,[†] G. Nyquist, J. D. Andrade,[‡] and K. D. Caldwell

Department of Materials Science & Engineering, Center for Biopolymers at Interfaces, and Department of Bioengineering, 2480 MEB, University of Utah, Salt Lake City, Utah 84112

In order to further the understanding of protein-surface interactions in the coagulation system, we have chosen to study plasma protein adsorption onto heparin-immobilized surfaces. Heparin-binding proteins are abundant in plasma: a search of amino acid sequences revealed that many plasma proteins have possible heparin binding sites. Plasma protein adsorption to the heparinized surfaces is monitored by a novel technique in which the solution depletion of proteins is analytically determined using quantitative two-dimensional polyacrylamide gel electrophoresis (2-D PAGE). This method enables simultaneous, quantitative detection of the majority of plasma proteins before, during, and after their adsorption onto high surface area adsorbents. Using computerized densitometry of silver-stained 2-D PAGE gels, the amount of

each protein can be determined from the integrated optical density of each protein "spot." Kinetics of adsorption and adsorption isotherms of four important heparin binding proteins, antithrombin III (ATIII), complement factor C3 (C3), apolipoprotein AI (Apo-AI) and apolipoprotein AIV (Apo-AIV) are reported in this paper. From the adsorption isotherms, the apparent binding constants of each protein-immobilized heparin complex, K_a , were calculated. The surface binding constants were of the same order of magnitude as the respective solution binding constants in the literature. The surface binding constants followed the same order as the respective solution binding constants: K_a (ATIII) > K_a (Apo-AIV) > K_a (C3) > K_a (Apo-AI), indicating that protein binding to the immobilized heparin used is not essentially different from solution binding.

INTRODUCTION

There are over 200 proteins in human plasma.¹⁻³ Most plasma proteins are highly surface active^{4,5} and their interfacial processes can result in coagulation, activation of the complement system or cell adhesion, particularly of platelets and leukocytes. In addition, cell-surface interactions, generally mediated through protein interfaces, are important in endothelial cell adhesion and culture.⁶

*Submitted in partial fulfillment of the requirements for the MSc degree in Materials Science and Engineering.

[†]On leave of absence from "Ruder Boskovic" Institute, P. O. Box 1016, 41000 Zagreb, Croatia, Yugoslavia.

[‡]To whom correspondence should be addressed.

Journal of Biomedical Materials Research, Vol. 25, 423-441 (1991)

© 1991 John Wiley & Sons, Inc.

CCC 0021-9304/91/040423-19\$04.00

Plasma protein adsorption is a complex process and includes the competition between different proteins for the surface binding site(s). This competitive adsorption, often referred to as the Vroman effect,^{4,7,8} is a function of the particular protein-surface affinity and concentration. Analytical techniques for studying protein adsorption from plasma are usually limited by a difficulty in determining the contribution of a particular protein. The usual method is to label one particular protein and then add it to plasma so that its adsorption can be measured. Several different experiments are needed, each performed with a different labeled protein, in order to obtain composite adsorption information. This is a tedious task when many plasma proteins need to be considered. Besides, the use of the label creates a possibility of perturbing the protein or influencing the adsorption process.

Here we report the development of an experimental method by which the competitive adsorption of plasma proteins can be studied without the use of labels. We employ high-resolution quantitative two-dimensional polyacrylamide gel electrophoresis (2-D PAGE) for detection of the amount of plasma protein in the solution, prior to and after adsorption. Thus, 2-D PAGE applied as a solution depletion method enables both simultaneous identification and quantitative detection of most plasma proteins at the same time. The protein in the gels is detected by silver staining; the sensitivity of the method is appropriate for adsorption studies. So far, one dimensional electrophoresis has been used by Mulzer and Brash⁹ and by Horbett et al.¹⁰ to study the composition of adsorbed protein layers after their elution from surfaces. Interactions of plasma proteins with artificial surfaces *in vivo* and *in vitro* was studied qualitatively by Owen et al. in 1985 using 2-D electrophoresis.¹¹

For the purpose of development and verification of the method, we have selected a well-characterized model system for initial studies: a subset of plasma proteins which bind heparin and heparin-derivatized adsorbents. Heparin-binding domains are present in many plasma proteins. For example, fibronectin, an important cell adhesion protein, contains several different binding domains, including heparin-binding regions.¹² Heparin-binding proteins are among the most important proteins in plasma with regard to coagulation and thrombosis, and their specific binding functions and amino acid sequences are relatively well defined. Antithrombin III and thrombin adsorption on sulfonated polystyrene, a synthetic heparin-like material, was studied by Jozefowicz et al.^{13,14} Interaction between thrombin and heparin-PVA hydrogel was studied by Sefton et al.¹⁵

BACKGROUND

Heparin

Heparin is an important anticoagulant, used clinically to minimize thrombus formation on artificial surfaces. Heparin has the ability to combine with a large number of proteins. The complexes can be distinguished as those

which originate from relatively nonspecific heparin-protein interactions and those which are due to more specific heparin-protein interactions, such as the heparin binding sites in antithrombin III (ATIII) or fibronectin (FN).

From the structural point of view, heparin is a sulfated polysaccharide composed of alternating units of hexuronic (D-glucuronic or L-iduronic) acid and D-glucosamine.¹⁶ Heparin preparations are heterogeneous with respect to molecular weight, ranging from 3 to 40 KD. Heparin fragments consisting of at least 18–20 monosaccharide units are needed for the thrombin-antithrombin III interaction. The basic unit structures for heparin binding with protein are pentasaccharide, hexasaccharide, and octasaccharide.¹⁷

Heparin-binding proteins

Antithrombin III (ATIII) is a natural anticoagulant with a major role in controlling the activity of proteases in the blood coagulation system. Its inhibitory properties are accelerated by the presence of heparin, which binds to ATIII and dramatically increases the rate of enzyme-inhibitor complex formation. The association constant of ATIII and heparin is approximately 10^7 M^{-1} , which makes ATIII the highest affinity heparin-binding protein.¹⁸

Other plasma proteins that can bind to heparin include: fibronectin (FN), vitronectin (VN), complement factor C3 (C3), histidine-rich glycoprotein (HRG), plasminogen (PMG), heparin co-factor II (HC II), apolipoproteins (Apo-AI, Apo-AII, Apo-AIV, Apo-B, Apo-CI, Apo-CII, Apo-CIII, Apo-E), and others. The basic data for heparin-binding proteins are listed in Table I¹⁻³ and Table II.¹⁹

Using the amino acid sequence of these proteins (available in the literature, see Table III) we have identified their potential heparin-binding sites. In each

TABLE I
Summary of Properties of Major Heparin-Binding Proteins
(Excluding Apolipoproteins¹⁻³)

Protein Symbol	ATIII	FN	VN	HRG	PMG	HCII	C3
Conc. in human plasma (mg/100 mL)	20–40	25–40	25–30	5–15	6–25	>9	55–120
M.W. (Dalton)	56,000	440,000	65,000	58,500	92,000	65,600	185,000
Isoelectric point (IEP)	4.9–5.2	5.5–6.2	4.8–5.3	—	5.6	5.0–5.2	5.5–6.0
Carbohydrate content (%)	15	5	10	11	1.5	9.9	2
S _{20,w} (S)	4.1	12–14	4.6	3.8	4.2	4.31	9.5
E ₍₂₈₀₎ (1%)	6.5	12.8	—	5.9	17.0	11.7	10.0

TABLE II
Summary of Properties of Apolipoproteins¹⁹

Protein Symbol	Apo-AI	Apo-AII	Apo-AIV	Apo-B	Apo-CI	Apo-CII	Apo-CIII	Apo-E
Conc. in human plasma (mg/100 mL)	100-200	30-40	16-20	90-110	4-6	3-5	12-14	3-6
M.W. (Dalton)	29,016	17,440	46,000	500,000	6,300	8,824	8,764	34,145
Isoelectric point (IEP)	4.5-5.9	4.9	5.5	—	7.5	4.9	4.7-5.0	5.9
Carbohydrate content (%)	0	0	0	0	0	0	3	0

TABLE III
List of Known Heparin-Binding Proteins, Their Plasma Concentrations, Estimated Heparin-Binding Affinity, and Their Possible Heparin-Binding Site Sequences and Related Changes

Protein ^a	Affinity ^b	Possible Heparin-Binding Sequence ^c	Charges (+/-)	Reference
AT III	High(10 ⁷ M ⁻¹)	-Arg-----Arg-Val-Trp-	+++	20
		-Lys-----Pro-Glu-----Lys-----Ser-Leu-Ala-----Lys-----Val-Glu-----Lys-	+ · - + · · · + · - +	
PMG		-Lys-----Phe-Pro-Asn-----Lys-----Asn-Leu-----Lys-----	+ · · + · · + +	
		-Lys-----Lys-----Cys-Pro-Gly-----Arg-	+++ · +	21
		-Arg-----Pro-Asn-----Lys-Pro-Gly-Val-Tyr-Val-Arg-----Val-Ser-----Arg-	+ · + + · · · + · + · +	
HRG		-Lys-----Arg-----Arg-----Arg-	++++	22
VN		-Arg-----Phe-----Arg-----His-----Arg-	+ · + +	23,24
		-Arg-----Ser-Gln-----Arg-----Gly-His-Ser-----Arg-----Gly-----Arg-	+ · + + · · · + · +	
C3		-Lys-----Thr-Pro-----Lys-----Tyr-Phe-----Lys-	+ · + + · +	
		-Lys-----Gly-----Arg-----Leu-Leu-----Lys-----Ala-Gly-----Arg-	+ · + + · + · +	25
		-Lys-----Lys-----Asn-----Lys-Leu-Thr-Gln-Ser-Lys-	+++ + · · +	
		-Arg-----Met-Asp-----Lys-----Val-Gly-----Lys-----Tyr-Pro-----Lys-	+ · - + · + · + · +	
		-Lys-----Asp-----Lys-----Asn-----Arg-	+ - + +	
		-Lys-----Glu-Asp-Gly-----Lys-----Leu-Asn-----Lys-----Leu-Cys-----Arg-	+ - - + · + · + · +	
		-Lys-----Cys-----Arg-----Glu-Ala-Leu-----Lys-----Leu-Glu-Glu-----Lys-	+ · + - + · + · - +	
FN		-Arg-----Val-----Arg-----Val-Thr-Pro-----Lys-----Glu-----Lys-	+ · + · + + - +	
		-Arg-----Ala-----Arg-Ile-Thr-Gly-Tyr-Ile-Ile-Lys-----Tyr-Glu-----Lys-	+ · + · · · · + · - +	28
		-Arg-Glu-Val-Val-Pro-Arg-----Pro-----Arg-	+ - · · + + +	
ApoC-III		-Lys-----His-Ala-Thr-----Lys-----Thr-Ala-----Lys-	+ · · + + · +	25
ApoB		-Arg-----Lys-----Tyr-----Arg-	+++ +	
		-Lys-----Lys-----Tyr-----Arg-	+++ +	
		-Lys-----Lys-----Asn-----Lys-----His-----Arg-	+++ + +	
		-Arg-----Lys-----Arg-----Gly-Leu-----Lys-	+++ + · +	25,29,30,31
		-Arg-----Arg-----Gln-His-Leu-----Arg-	+++ + +	
ApoE		-Arg-----Lys-----Arg-	+++	25,29,32
		-Arg-----Leu-----Arg-----Ala-----Arg-	+ · + + +	
ApoA-IV		-Arg-----Leu-Ala-----Lys-----Asp-Ser-Glu-----Lys-----Leu-----Lys-	+ · + + - - + · +	25
ApoA-I	Low	-Arg-----Gln-----Arg-----Leu-Ala-Ala-----Arg-Leu-Glu-Ala-Leu-Lys-	+ · + · · + · - · · +	25

TABLE III (continued)

Protein ^a Affinity ^b	Possible Heparin-Binding Sequence ^c								Charges (+/-)	Reference
ApoA-II	-Lys-Ser-Tyr-Phe-Glu- Lys-----Ser-----Lys-								+ . . . - + . +	25
ApoC-I	-Lys-----Val-----Lys-----Glu-----Lys-----Leu-----Lys-								+ . + - + . +	25
ApoC-II Low(10^5 M^{-1})	-Lys-----Leu-----Arg---Asp-Leu-Tyr-Ser---Lys-								+ . + - . . . +	25
	SO ₃ ⁻		SO ₃ ⁻		SO ₃ ⁻		SO ₃ ⁻			
	O		O		O		O			
Heparin Model ^d	GLN	IDU	GLN	IDU	GLN	GLU	GLN			

^aAbbreviations: ATIII = Antithrombin III; PMG = Plasminogen; HRG = Histidine-rich glycoprotein; VN = Vitronectin; FN = Fibronectin; C3 refers to the binding of C3b, derived from complement C3; Apo refers to the Apolipoproteins; ApoA proteins are primarily in high density lipoproteins (HDL); ApoB is the major protein in low density lipoprotein (LDL) and is also in very low density lipoproteins (VLDL); ApoC proteins are found in VLDL; ApoE is in VLDL and also in LDL;

^bAffinity: Depends on the particular heparin-binding sequence, binding constant, hydrophilicity, charge (+/-) etc. [18, 26, 27], (i). highest is ATIII at about 10^7 M^{-1} (ii) lowest may be around 10^5 M^{-1}

^cPossible heparin-binding sequence: We have used ATIII and ApoE, whose sequences have been identified, as a model to predict the heparin binding sequences in the other proteins.

^dHeparin model: GLN: D - glucosamine; GLU: D - glucuronic acid; IDU: L - iduronic acid.

protein the predicted heparin-binding site contains three or four basic amino acids, arginine or lysine, which alternate every three or four amino acids. Similar regions have been recently identified as heparin-binding sites in 21 different proteins.³³ Table III lists probable heparin-binding regions in many heparin-binding proteins.

MATERIALS AND METHODS

The adsorbent

The study of protein adsorption by any solution depletion method requires the use of an adsorbent with a high surface area. We chose typical affinity chromatography materials as adsorbents. Three different commercially available heparin-agarose particles, Heparin Sepharose CL-6B (Pharmacia, Piscataway, NJ), Affi-Gel Heparin (BIO-RAD, Richmond, CA) and Progel-TSK Heparin-5PW (Supelco Inc., Bellefonte, PA), were initially evaluated by measuring their binding capacity for each of three purified proteins: ATIII (Sigma, St. Louis, MO) HRG (Calbiochem, San Diego, CA), and FN (Calbiochem, San Diego, CA), respectively. The amount of adsorbed protein was determined by the difference in UV absorbance in the solution. It was found that the Heparin Sepharose CL-6B had the highest binding capacity of the three materials examined (Fig. 1). On the basis of this result Heparin Sepharose CL-6B was chosen for all further experiments. One gram of dry Heparin Sepharose CL-6B is approximately equal to 4 mL of hydrated, packed gel.

The adsorbate

We chose human plasma as our adsorbate-solvent mixture. Blood was drawn from several healthy human donors and collected by using 5 mL Vacutainer Brand evacuated blood collection tube (Becton Dickinson and Company) which contained 0.05 mL of 15% EDTA solution (7.5 mg). Plasma was separated from the blood cells by centrifugation at room temperature for 20 min at 1790g. The plasma was pooled from various donors and stored frozen at -20°C .

The adsorption kinetics experiments

In these experiments, the concentration of plasma solution and the amount of Heparin Sepharose CL-6B were kept constant while the adsorption time was varied (from 10 min to 780 min). Typically, 0.02 g Heparin Sepharose CL-6B particles and 0.5 mL human plasma were mixed in a 1.5-mL vial and diluted with Tris-buffer at pH 7.4 to 1.5 mL. The plasma was diluted to 1/3. After continuous mixing by rotation at room temperature, the mixture was allowed to sediment by gravity (about 3 min) and 10 μL of the supernatant was removed for 2-D PAGE analysis.

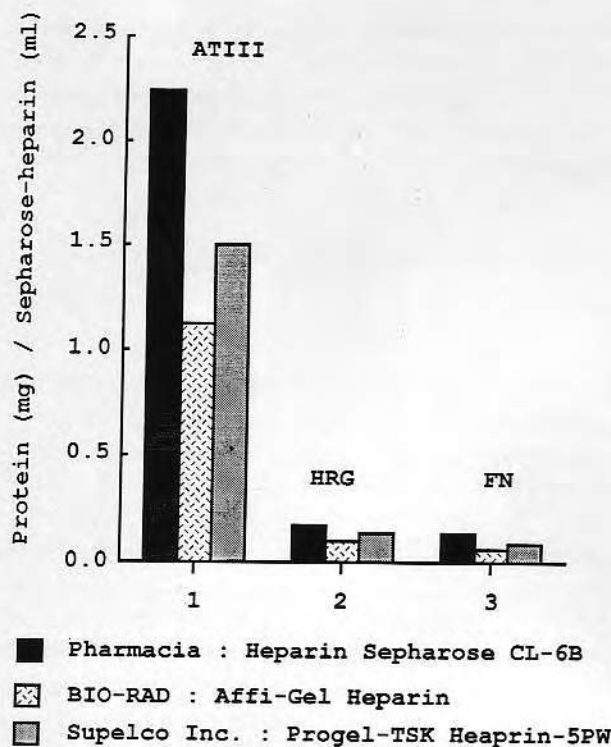


Figure 1. Binding of three proteins: antithrombin III (ATIII), histidine-rich glycoprotein (HRG), and fibronectin (FN) to three different commercially available heparinized gel particles.

The adsorption "isotherm" experiments

In these experiments the concentration of plasma solution and the adsorption time were kept constant while the amount of Heparin Sepharose CL-6B was varied from approximately 0.01 g to 0.09 g (0.04 mL to 0.36 mL packed gel). Adsorbent was diluted with Tris-buffer at pH 7.4 to 1.0 mL and 0.5 mL human plasma was added. After 13 h of continuous mixing by rotation at room temperature, the mixture was allowed to sediment by gravity (about 3 min) and 10 μ L of plasma sample was removed for 2-D PAGE analysis.

The protein separation and detection method

We used high-resolution quantitative two-dimensional polyacrylamide gel electrophoresis (2-D PAGE) for protein separation and detection. In this method unknown proteins from a mixture are first separated according to their isoelectric point (in the first dimension) and then according to their molecular weight (in the second dimension) (Figs. 2 and 3).

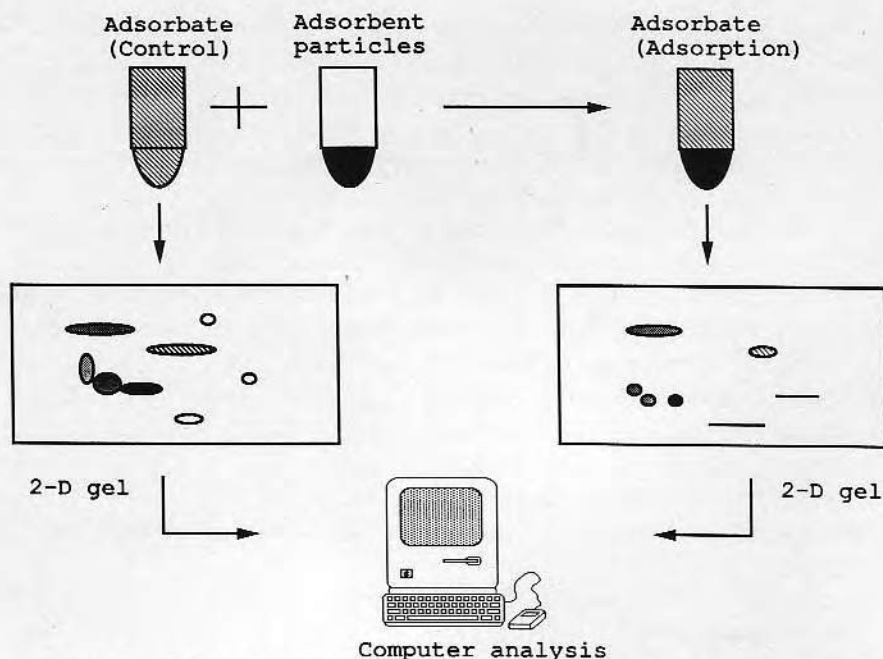


Figure 2. Schematic of the protein adsorption experiment: a sample of protein solution is analyzed using 2-D PAGE before and after the solution is depleted by adsorption on high-surface-area adsorbent.

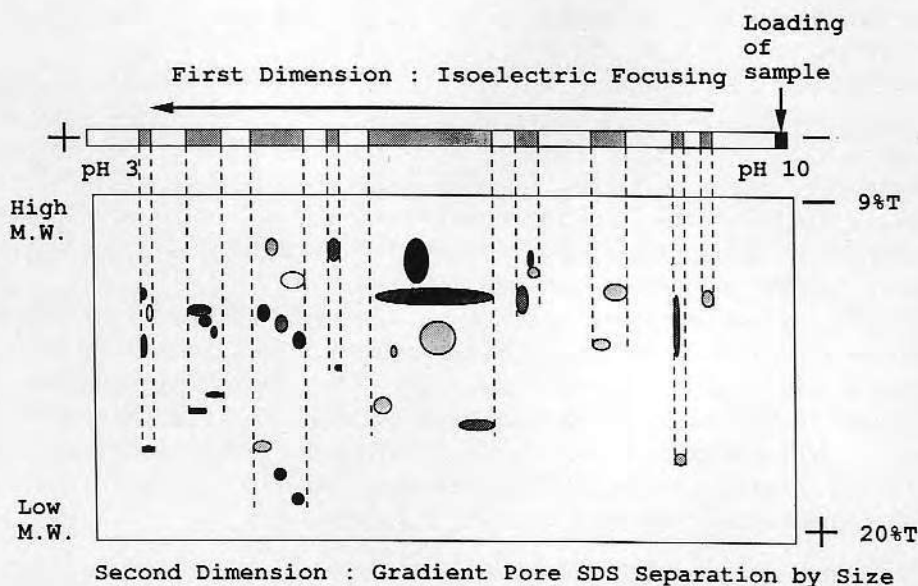


Figure 3. Resolution of proteins by 2-D PAGE. The protein sample is loaded on the basic side (pH 10) of the IEF tube gel (first dimension), and then separated by the respective isoelectric points. Following the separation in the first dimension, the IEF gel is placed on the top of a slab gel (second dimension) in which proteins are separated by their respective molecular sizes.

We have used the ISO-DALT system (Hoefer Scientific Instruments, San Francisco, CA), developed by Anderson and co-workers.^{34,35} The chemicals for 2-D PAGE process were purchased from different sources:

(1) Sodium dodecyl sulfate (SDS), urea, Nonidet P-40 (NP-40), glycine, N, N'-methylene-bis-acrylamide (BIS) and acrylamide (for IEF, first dimension gel), (BDH, imported by Hoefer Scientific Instruments, San Francisco, CA).

(2) 3-[(3-cholamidopropyl) dimethylammonio] 1-propanesulfonate (CHAPS), Tris-HCl, Tris-base, glutaraldehyde (Sigma, St. Louis, MO).

(3) Dithiothreitol (DTT), N, N, N', N'-tetramethylethylenediamine (TEMED), ammonium persulfate, bromophenol blue and acrylamide (for DALT, second dimension gel) (BIO-RAD, Richmond, CA).

(4) Glycerol, ammonium hydroxide (E.M. Science, Cherry Hill, NJ).

(5) Ampholyte (3-10) (Serva, Westbury, NY).

(6) Silver nitrate (Aldrich, Milwaukee, WI).

(7) Formaldehyde solution (Mallinckrodt, Inc., Paris, KY).

(8) Phosphoric acid, hydrochloric acid, and acetic acid (J.T. Baker Inc., Phillipsburg, NJ).

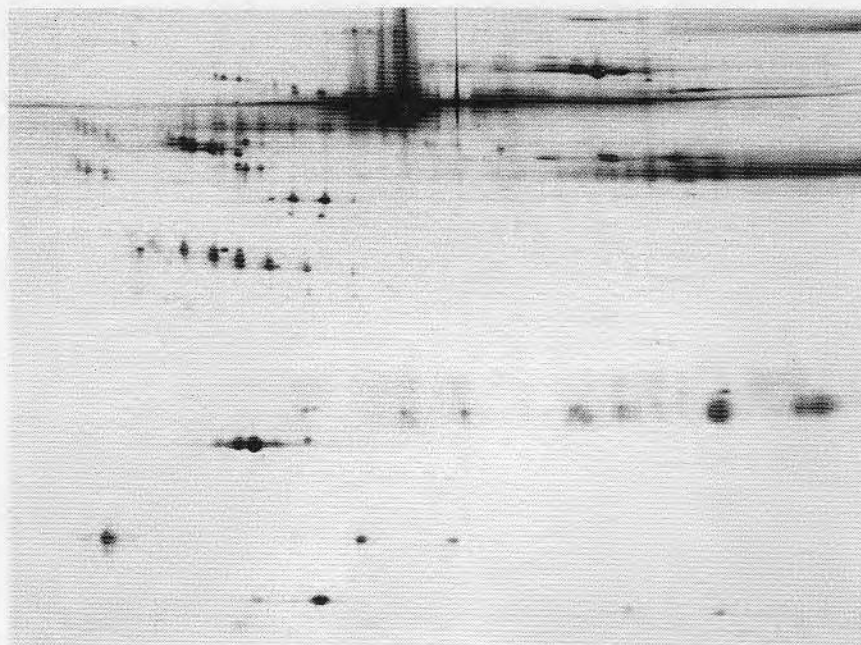
First, the isoelectric focusing (IEF) gel was prepared as ISO-mix solution containing 4% cross-linker with acrylamide and BIS, urea, CHAPS, NP-40, and carrier ampholytes 3-10. After polymerization, the gels were prefocused for 1 h at 200 V before the samples were loaded. Plasma samples to be analyzed were diluted with solubilization buffer (1:1) containing 2% SDS, CHAPS, DTT, glycerol, and Tris-HCl at pH 7.4 and loaded with a Hamilton micro-syringe on top of the IEF tube gel. The tube gels were run at 20,000–22,000 Volt-hours (from 20 h at 1,000 V to 22 h at 1,000 V).

Second, the slab gels used for the second dimension were formed by feeding heavy and light acrylamide solutions to the DALT gradient maker, thereby creating a density gradient in the gel. After polymerization of the slab gels, the protein-containing IEF gels, together with the equilibrium solution (10% glycerol, DTT, 2% SDS, Tris-base, bromophenol blue and HCl), were applied on top of the slab gels and fixed in place with the agarose. Electrophoresis was carried out at 50–60 mA per gel for 9–12 h.

Finally, high-sensitivity silver staining was employed for protein detection after the separation.³⁶ The freshly run slab gels were fixed in a solution of 50% ethanol and 10% acetic acid overnight. After rinsing, the gels were placed in a 2% glutaraldehyde solution buffered to pH 9.5, for at least 1 h. The gels were then stained in diluted solution of 0.7% silver nitrate, rinsed, developed, and "stopped" according to the ISO-DALT manual.³⁵ The 2-D PAGE gel of normal human plasma (1/30 dilution) is shown in Figure 4.

The quantification of proteins in gels

In order to find the most optimal densitometric system for the quantitative detection of proteins in the two-dimensional gels, we have evaluated several commercial products and finally decided to custom-build a computerized



(a)

Figure 4. 2-D PAGE gel for normal human plasma sample (1/30 dilution), mixed with sample solubilizer 1:1, 25 μ L loaded onto gel. Soybean trypsin inhibitor (STI), used in adsorption experiment as external standard, is also indicated. (a) Photograph picture of the part of actual gel, (b) outline of the same region of the same gel with identified proteins: (1) albumin; (2) transferrin; (3) fibrinogen α chain; (4) fibrinogen β chain; (5) Ig γ chain; (6) fibrinogen γ chain; (7) Ig λ chains; (8) Ig κ chains; (9) haptoglobin α_2 chain; (11) prealbumin; (10) hemoglobin β chain; (12) soybean trypsin inhibitor (STI); (13) Apo-AI; (14) Apo-AIV; (15) haptoglobin β chain; (16) Gc globulin; (17) antithrombin III; (18) α_1 antitrypsin; (19) Ig A; (20) hemopexin; (21) α_1 -antichymotrypsin; (22) α_1 -B glycoprotein; (23) α_2 HS glycoprotein.

densitometric system. The basis of the system is a thermoelectrically cooled charge-coupled device (CCD) camera (14-bits, Photometrics LTD, Tucson, AR) interfaced with a Macintosh II computer via appropriate electronics and a DMA board NB-DMA-8, (National Instruments, Austin, TX). Typically, the two-dimensional gels were placed on a cold-light source (Aristo, Roslyn, NY) and a transmission image of the gel was recorded. The resulting intensities were corrected for uneven output of the light source and compressed to 8 bits/pixel.

Images of the gels were stored in the computer for further processing. Image 1.26 (W. Rasband, NIH) software was used to analyze the data. The images were calibrated using optical density standards (precalibrated photographic step tablet by Kodak). The photographic step tablet was recorded by the CCD camera and a corrected transmission of each step was measured to obtain a calibration curve. The calibration was then applied to each of the two-dimensional gel images. The measurement of the optical density of each

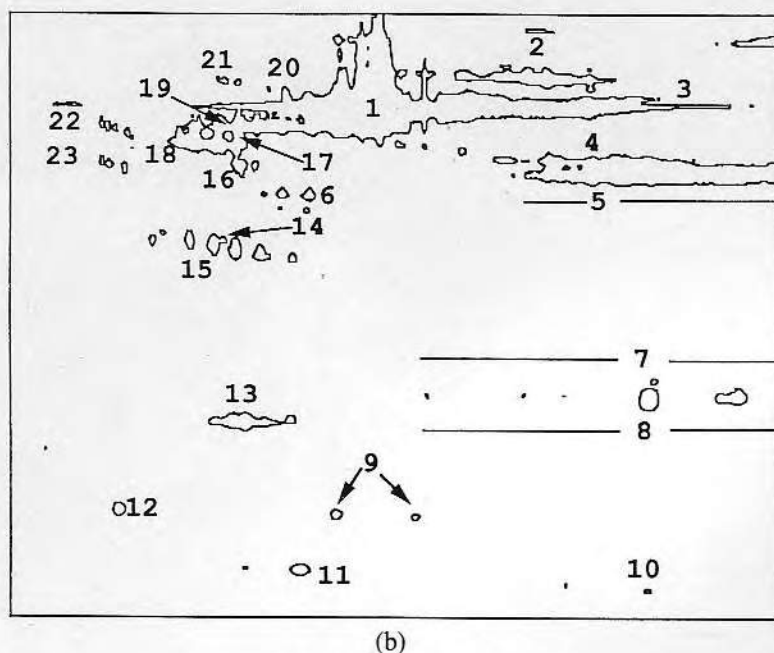


Figure 4. (continued)

protein spot was made by drawing the outline of each spot or of a region. The software automatically subtracts local background and calculates the integrated optical density for a given area.

Because we used pooled plasma in our study, the absolute initial concentration of each protein was not precisely known. Instead, we used the fractional depletion, F , of each protein to describe the binding of a specific protein to the surface. F was calculated as a ratio of the integrated optical volume densities of a given protein after and before solution depletion by adsorption, respectively:

$$F = \frac{(\text{integrated optical density}) \text{ after depletion by adsorption}}{(\text{integrated optical density}) \text{ before depletion by adsorption}}$$

The fractional depletion can be easily transformed into the corresponding fractional adsorption, $1 - F$. The results presented in this paper are plotted as $1 - F$ vs. time (min) or vs. adsorbent weight (g).

To fully correct for experimental differences between different gels within one batch, a known standard protein was incorporated into each sample. This protein can be added separately onto the IEF gel before sample is loaded on the IEF tube gel (so-called extrinsic standard), or it can be chosen from among those existing plasma proteins which do not become depleted by adsorption in the sample (so-called intrinsic standard). In either case, normalization of integrated optical density of proteins of unknown concentration with respect to the integrated optical density of such standard will account for variations in staining and loading procedures during each experiment.

We used soybean trypsin inhibitor (STI) as our extrinsic standard, because it showed only a single spot on the two-dimensional gel, and its location did not overlap with other plasma protein patterns.

Of the heparin-binding proteins, only ATIII, C3, Apo-AI and Apo-AIV were easily detected on the two-dimensional gels. The reasons that other heparin-binding proteins could not be detected was due mainly to inappropriate gel cross-linking density and staining conditions for those particular proteins. For example, FN is a high-molecular-weight protein (220KD after DTT treatment) which penetrates into the gels very slowly due to our gel cross-linking density range (9%T to 20%T). Apo-AII, Apo-CI, Apo-CII, and Apo-CIII are low-molecular-weight proteins (lower than 10KD) and pass through the gel to its lowest part under present gel cross-linking density range. To detect those proteins, gels with a different cross-link density should be used, i.e., < 9%T for FN and > 20%T for Apo-AII, Apo-CI, Apo-CII, and Apo-CIII. VN, HRG, and HCII were not detected in the diluted plasma sample, but could be easily detected using purified protein samples. Their poor detectability from plasma is not fully understood yet. It is probably related to their efficiency of silver staining and/or their loss to the walls of vials or electrophoresis plates. This problem will be addressed in future studies. In this paper we chose to focus on the adsorption of four heparin-binding plasma proteins: ATIII, C3, Apo-AI, and Apo-AIV.

RESULTS AND DISCUSSION

The adsorption kinetics and "isotherm" experiments were performed in triplicate. The error bars represent the standard deviation of three different experiments. Figure 5 shows the results of the adsorption kinetics experiments for C3, ATIII, Apo-AIV, and Apo-AI. The rapid increase in fractional adsorption of ATIII and Apo-AI indicates a high affinity to Heparin Sepharose CL-6B: ATIII was almost completely removed from solution; the fractional adsorption for Apo-AI at 30 min was up to $0.55 \pm 14\%$. The fractional adsorption of C3 was up to $0.15 \pm 9\%$ and Apo-AIV was up to $0.20 \pm 11\%$ after approximately 200 min. Assuming that equilibrium has been reached after 13 h, ATIII showed the highest binding affinity with Heparin Sepharose CL-6B (Fig. 5). The pore size of Heparin Sepharose CL-6B is about 100 Å and the porosity is about 65%. The estimated time for ATIII to diffuse into Heparin Sepharose CL-6B is of the order of 1 to 2 min. Therefore, the initial diffusion process was complete before our first sampling time (10 min after initiation of adsorption).

The results of the adsorption "isotherm" experiments are given in Figure 6, where the fractional adsorption of the four proteins is given as a function of the amount of the adsorbent in the system. The maximal fractional adsorption value of ATIII was the largest (ca. 1.0), C3 was second (ca. $0.60 \pm 15\%$), Apo-AI (ca. $0.40 \pm 12\%$) and Apo-AIV were the smallest (ca. $0.40 \pm 14\%$).

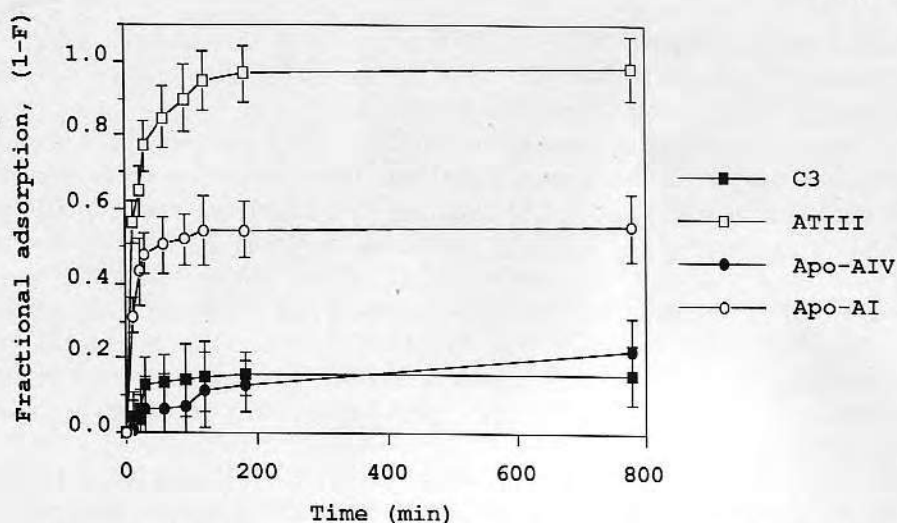


Figure 5. Results of the adsorption kinetics experiments: fractional adsorption, $1 - F$, of ATIII, C3, Apo-AI, and Apo-AIV shown as a function of the adsorption time.

In order to compare the heparin binding by these four proteins in solution and at the heparin gel/solution interface, we have estimated the apparent protein-immobilized heparin binding constants, $K_{a(\text{surface})}$, from the initial portions of the adsorption isotherms (dashed lines in Fig. 7), using the following binding reaction scheme: $P + A_s = PA_s$ and equations

$$K_{a(\text{surface})} = [PA_s]/[P] \cdot [A_s] \quad (1)$$

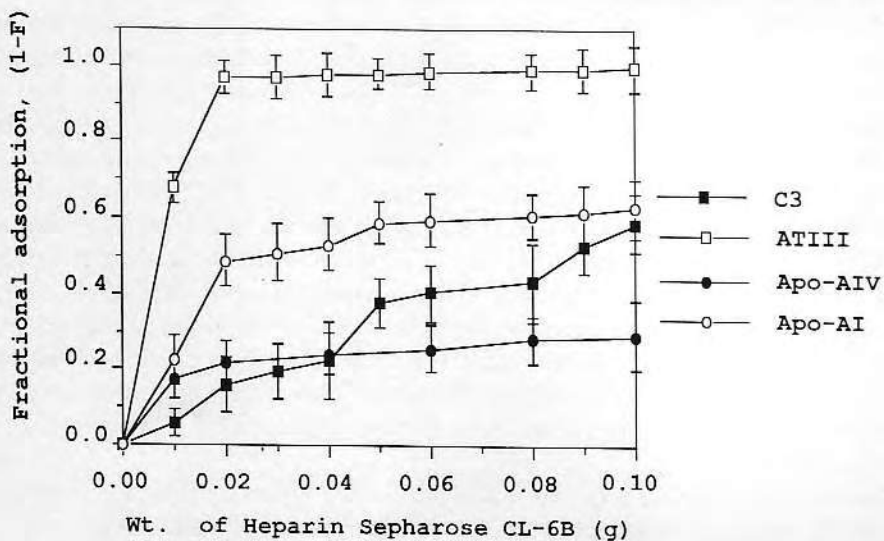


Figure 6. Results of the adsorption "isotherm" experiments: fractional adsorption, $1 - F$, of ATIII, C3, Apo-AI, and Apo-AIV shown as a function of the amount of Heparin Sepharose CL-6B in the system.

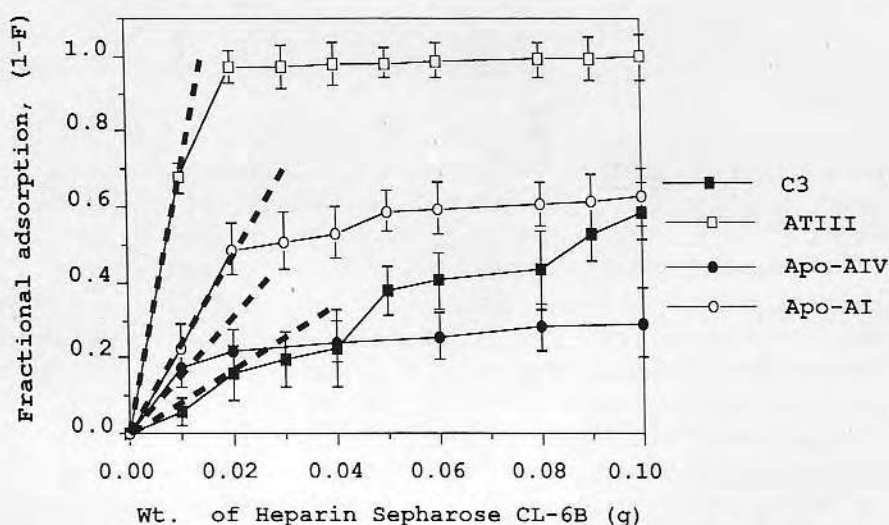


Figure 7. Results of the adsorption "isotherm" experiments: fractional adsorption, $1 - F$, of ATIII, C3, Apo-AI, and Apo-AIV. The initial slopes of the adsorption isotherms used in calculation of $K_{a(\text{surface})}$ are shown by dashed lines.

$$\nu = \frac{[PA_s]}{[P] + [PA_s]} = \frac{K_{a(\text{surface})}[A_s]}{1 + K_{a(\text{surface})}[A_s]} \quad (2)$$

where $[]$ denotes concentrations of protein, P , surface-immobilized heparin, A_s , and surface protein-heparin complex PA_s and ν is the bound fraction of protein, which is equal to $(1 - F)$. The weight fraction of heparin in the Heparin Sepharose CL-6B was 0.4% (as communicated by Pharmacia). Total molar concentration of heparin in the experimental system, $A_s(\text{tot})$, was calculated using a heparin molecular weight of 11.2 KD. Equation (2) can be rewritten as:

$$K_{a(\text{surface})} = \nu / (1 - \nu) ([A_s(\text{tot})] - \nu[P_{\text{tot}}]) \quad (3)$$

where subscripts tot denote total concentrations of A and P , respectively. The apparent binding constants are listed in Table IV.

We note the K_a values are in the same order of magnitude as the respective, estimated solution binding constants given in Table III. We also note that the apparent binding constants of the protein-heparin complexes follow the same

TABLE IV
List of Apparent Binding Constants
of ATIII, C3, Apo-AI, and Apo-AIV for Heparin-Sepharose CL-6B

Protein	$P_{(\text{tot})}$	$K_{a(\text{surface})}$
ATIII	$2.3 \times 10^{-6} \text{ M}$	$1.3 \times 10^7 \text{ M}^{-1}$
Apo-AIV	$1.4 \times 10^{-6} \text{ M}$	$0.8 \times 10^5 \text{ M}^{-1}$
C3	$2.2 \times 10^{-6} \text{ M}$	$0.4 \times 10^5 \text{ M}^{-1}$
Apo-AI	$1.2 \times 10^{-5} \text{ M}$	$0.2 \times 10^5 \text{ M}^{-1}$

order as in solution: $K_a(\text{ATIII}) > K_a(\text{Apo-AIV}) > K_a(\text{C3}) > K_a(\text{Apo-AI})$, indicating that protein binding to the immobilized heparin is not essentially different from binding in solution.

Equation (2) implies reversible binding of protein to Heparin Sepharose CL-6B. In the present study the desorption of bound proteins was not studied. Therefore, the application of Equation (2) is not entirely supported by our experiments. Heparin is frequently used as a chromatographic ligand in the separation and purification of proteins from complex mixtures. Its binding to proteins is largely electrostatic in nature and, hence, reversible.³³ In addition, proteins bind very weakly to unsubstituted Sepharose as determined in preliminary experiments (not shown here).³⁷ Hence, the assumption of reversible binding to Heparin Sepharose CL-6B is probably justified.

The sensitivity of 2-D PAGE as applied to plasma protein adsorption depends on several factors: concentration of given protein in plasma, its staining efficiency, and linearity of integrated optical density with protein concentration. Ideally, small changes (a few percent) of protein concentration can be easily determined as a change in the optical density. However, the accuracy of the method is still far from satisfactory. It appears that the loading of the sample on the first dimension gel, transfer of the IEF gel to the second dimension slab gel, and variation in silver staining and developing conditions are the "weakest" points in the method. Full analysis of how these and other factors influence overall sensitivity and accuracy of this novel tool for protein adsorption is under investigation.³⁷

CONCLUSIONS

(1) Almost 50 plasma protein patterns have been identified on two-dimensional gels, and a subset of heparin-binding plasma proteins has been mapped and identified.

(2) Quantitative two-dimensional polyacrylamide gel electrophoresis has been successfully used as a method to study the competitive adsorption of plasma proteins.

(3) An external standard of known concentration, soybean trypsin inhibitor, was used to normalize the measurement of optical density for gel-to-gel variations.

(4) We have custom-built a densitometric apparatus based on a CCD camera and image analysis software and used it to analyze the two-dimensional gels.

(5) Adsorption results using four heparin-binding proteins (ATIII, C3, Apo-AIV, and Apo-AI) showed that the method is applicable for the study of protein adsorption from complex mixtures like plasma. Both adsorption kinetics as well as binding data were obtained.

(6) The apparent binding constants of the surface protein-heparin complex were found to be of the same order as the respective binding constants in the solution: $1.3 \times 10^7 \text{ M}^{-1}$ (ATIII), $0.8 \times 10^5 \text{ M}^{-1}$ (Apo-AIV), $0.4 \times 10^5 \text{ M}^{-1}$ (C3), and $0.2 \times 10^5 \text{ M}^{-1}$ (Apo-AI).

(7) The advantage of the present method is that it requires no label, and the adsorption of many proteins can be studied simultaneously. The disadvantages are that it is time-consuming, staining is difficult to control, it requires large surface area materials, and its sensitivity and accuracy at the present stage are not as good as with the traditional labeling methods.

We gratefully acknowledge the assistance of Ms. C. Stenelov (Karolinska Hospital, Stockholm, Sweden) in establishing our two-dimensional electrophoresis lab and Dr. J. Edwards (National Institute of Standards and Technology, Gaithersburg, MD) for extremely helpful advice and training. We also thank Drs Norman and Leigh Anderson (Large Scale Biology Corp., Rockville, MD) and Dr. Dennis Reeder (National Institute of Standards and Technology, Gaithersburg, MD) for helpful advice. We thank Dr. D.F. Mosher (University of Wisconsin, Madison, WI) and Dr. D.M. Tollefson (Washington University, St. Louis, MO) who provided purified heparin binding proteins. We also thank Dr. T. Oolman (University of Utah) for advice on mass transfer and Dr. W. Rasband (NIH) for the image analysis software. This work has been supported by the Center for Biopolymers at Interfaces, University of Utah, a University-Industry-State research consortium.

References

1. F.W. Putnam, "Progress in plasma proteins," in *The Plasma Proteins*, Vol. 4, 2nd ed., Plenum Press, New York, 1985, pp.1-45.
2. F.W. Putnam, "Alpha, beta, gamma, omega—the structure of the plasma proteins," in *The Plasma Proteins*, Vol. 4, 2nd ed., Plenum Press, New York, 1985, pp. 46-167.
3. H.G. Schwick and H. Haupt, "Human plasma proteins of unknown function," in *The Plasma Proteins*, Vol. 4, 2nd ed., Plenum Press, New York, 1985, pp. 168-221.
4. J.D. Andrade, "Principles of protein adsorption," in *Protein Adsorption*, Plenum Press, New York, 1985, pp. 1-89.
5. E.F. Leonard, et al. "Blood in contact with natural and artificial surfaces," *Ann. N.Y. Acad. Sci.*, **516**, (1987).
6. L.M. Graham, J.C. Stanley, and W.E. Burkel, "Endothelial seeding of synthetic vascular grafts," in *Endothelial Cells*, U. Ryan (ed.), CRC Press, Boca Raton, 1987, pp. 217-228.
7. T. Horbett, "Mass action effects on competitive adsorption of fibrinogen from hemoglobin solutions and from plasma," *Thromb. Hemost.*, **51**, 79 (1984).
8. L. Vroman, "The importance of surfaces in contact phase reaction," *Sem. Thromb. Hemost.*, **13**, 79-85 (1987).
9. S.R. Mulzer and J.L. Brash, "Identification of plasma proteins adsorbed to hemodialyzers during clinical use," *The third world biomaterials congress*, 1988, p. 473.
10. T.A. Horbett, P.K. Weathersby, and A.S. Hoffman, "The preferential adsorption of hemoglobin to polyethylene," *J. Bioeng.*, **1**, 61-78 (1977).
11. D.R. Owen, C.M. Chen, J.A. Oschner, and R.M. Zone, "Interactions of plasma proteins with selective artificial surfaces," *Trans. ASAIO*, **31**, 240-243 (1985).
12. K. Skorstengard, "Purification and complete primary structure of bovine plasma fibronectin," *Eur. J. Biochem.*, **154**, 15-29 (1986).
13. V. Migonney, C. Fougnot, and M. Jozefowicz, "Heparin-like tubings," *Biomaterials*, **9**, 413 (1988).
14. C. Fougnot, M. Jozefowicz, and R.D. Rosenberg, "Affinity of purified thrombin or ATIII for two insoluble anticoagulant polystyrene derivatives: I. In vitro adsorption studies," *Biomaterials*, **4**, 294-298 (1983).

15. B. A. H. Smith and M. V. Sefton, "Permeability of a Heparin-Polyvinyl alcohol hydrogel to thrombin and ATIII," *J. Biomed. Mater.-Res.*, **22**, 673-685 (1988).
16. I. Bjork and U. Lindahl, "Mechanism of the anticoagulant action of heparin," *Mol. Cell. Biochem.*, **48**, 161-182 (1982).
17. J. C. J. Stiekema, "Heparin and its biocompatibility," *Clin. Nephrol.*, **26**, S3-S8 (1986).
18. U. Lindahl, L. Thunberg, G. Backstrom, J. Riesenfeld, K. Nordling, and I. Bjork, "Extension and structural variability of ATIII binding sequence in heparin," *J. Biol. Chem.*, **259**, 12368-12376 (1984).
19. A. M. Scanu, "Plasma apolipoproteins: gene structure, function and variants," in *The Plasma Proteins*, Vol. 5, 2nd ed., Plenum Press, New York, 1987, pp. 142-191.
20. L. Roka and Th. Eckhardt, "ATIII: properties and function," *Prothrombin and Other Vitamin K Proteins*, Vol. 2, CRC Press, Boca Raton, 1986, pp. 1-15.
21. V. V. Novokhatny, "Domains in human plasminogen," *J. Mol. Biol.*, **179**, 215 (1984).
22. T. Koide, D. Foster, and S. Odani, "The heparin-binding site(s) of HRG," *FEBS Lett.*, **194**, 242-244 (1986).
23. S. Suzuki, A. Oldberg, E. G. Hayman, M. D. Pierschbacher, and E. Ruoslahti, "Complete amino acid sequence of human vitronectin deduced from cDNA. Similarity of cell attachment sites in vitronectin and fibronectin," *EMBO J.*, **4**, 2519-2524 (1985).
24. S. Suzuki, M. D. Pierschbacher, E. G. Hayman, K. Nguen, Y. Ohgren, and E. Ruoslahti, "Domain structure of vitronectin," *J. Biol. Chem.*, **259**, 15307-15314 (1984).
25. W. C. Barker, "Appendix: sequences of plasma proteins," *The Plasma Proteins*, Vol. 5, 2nd ed., Plenum Press, New York, 1987, pp. 365-402.
26. M. J. Griffith, "The heparin-enhanced ATIII/thrombin reaction is saturable with respect to both thrombin and ATIII," *J. Biol. Chem.*, **257**, 13899-13902 (1982).
27. C. Fougnot, M. Jozefowicz, and R. D. Rosenberg, "Affinity of purified thrombin or ATIII for two insoluble anticoagulant polystyrene," *Biomaterials*, **4**, 294-298 (1983).
28. T. E. Petersen, K. Skorstengaard, and K. Vibe-Pedersen, "Primary structure of fibronectin," in *Fibronectin*, D. F. Mosher (ed.), Academic Press, New York, 1989, pp. 1-24.
29. T. L. Innerarity, "Functional domains of ApoE & ApoB," *Acta Med Scand. Suppl.*, **715**, 51 (1987).
30. T. J. Knott, "Protein sequence and identification of structure domain of ApoB," *Nature*, **323**, 734 (1986).
31. N. Hirose, "Isolation and characterization of heparin-binding site of human ApoB," *Biochemistry*, **26**, 5505 (1987).
32. A. D. Cardin, "Binding of heparin to human ApoE," *Biochem. Biophys. Res. Comm.*, **134**, 783 (1985).
33. A. D. Cardin and H. J. Tr. Weintraub, "Molecular modeling of protein-glycosaminoglycan interactions," *Atherosclerosis*, **9**, 21-32 (1989).
34. N. L. Anderson, R. P. Tracy, and N. G. Anderson, "High-resolution 2-D electrophoretic mapping of plasma proteins," in *The Plasma Proteins*, Vol. 4, 2nd ed., Plenum Press, New York, 1985, pp. 221-271.
35. L. Anderson, "Operation of the ISO-DALT system," Large Scale Biology Corp. (1988).
36. R. C. Switzer, C. R. Merrill, and S. Shifrin, "A highly sensitive silver stain for detecting protein and peptides in polyacrylamide gels," *Anal. Biochem.*, **98**, 231-237 (1979).

INTERACTION OF PLASMA PROTEIN

441

37. C-H. Ho, "Competitive adsorption of plasma proteins studied by high resolution two dimensional polyacrylamide gel electrophoresis," M. Sc., University of Utah (1990).

Received November 10, 1989

Accepted July 24, 1990

Wettability and ζ Potentials of a Series of Methacrylate Polymers and Copolymers

A. H. HOGT,* D. E. GREGONIS,† J. D. ANDRADE,† S. W. KIM,‡
J. DANKERT,§ AND J. FEIJEN*

*Department of Chemical Technology, Section of Biomaterials, Twente University of Technology, P.O. Box 217, 7500 AE Enschede, The Netherlands; †Department of Materials Science and Engineering, Department of Bioengineering and Surface Analysis Laboratory, University of Utah, Salt Lake City, Utah 84112; ‡Department of Pharmaceutics, University of Utah, Salt Lake City, Utah 84112; and §Department of Hospital Infections, University Hospital, Oostersingel 59, Groningen, The Netherlands

Received September 12, 1984; accepted November 27, 1984

Polymers and copolymers of different methacrylates were synthesized and coated on glass slides. The surfaces of the polymer films were characterized by their water contact angles and ζ potentials using the Wilhelmy plate technique and streaming potential measurements, respectively. From contact-angle measurements information was also obtained about mobility of surface polymer chains. Receding contact angles of methyl methacrylate (MMA) copolymers containing hydrophilic or charged units were decreased as compared to the MMA homopolymer. When charged hydroxyethyl methacrylate (HEMA) copolymers were compared with the HEMA homopolymer, the advancing contact angles increased, probably due to reorientation of surface polymer chains. The receding contact angles of poly(alkyl methacrylates) first increased and then decreased with increasing side-chain lengths. These changes were related to the mobility of the different polymers. Incorporation of positively or negatively charged groups in MMA or HEMA polymers accordingly changed the ζ potential of the polymers.

© 1985 Academic Press, Inc.

INTRODUCTION

The tissue or blood compatibility of materials implanted or inserted in the human body is strongly dependent on the surface properties of the materials (1, 2). The characterization of the biomaterial surfaces is considered of ultimate importance for the development of improved biomedical devices (3, 4).

To study the effects of different substrate surface properties on biological interactions, a series of materials with well-characterized surface properties was prepared. Methacrylate polymers and its copolymers were chosen as model systems with varying surface hydrophobicity, surface charge, or polymer chain mobility. The synthesis and surface characterization of these polymers are described. The wettability and surface mobility of the polymers were determined by the Wilhelmy

plate technique (5). The ζ potentials of a series of charged copolymer surfaces were determined by streaming potential measurements (6). Results obtained for the methyl methacrylate, hydroxyethyl methacrylate, and alkyl methacrylate (co)polymers are discussed in terms of interfacial energies and surface mobility.

MATERIALS AND METHODS

Polymer Synthesis and Characterization

The synthesis of methacrylate polymers and copolymers is well known (7-14). The methacrylate polymers and copolymers used in this study were poly(methyl methacrylate) (MMA), poly(hydroxyethyl methacrylate) (HEMA), and MMA/HEMA copolymers (mole ratios (%): 75/25, 50/50, and 25/75), copolymers of MMA with methacrylic acid

(97 MMA/3 MAA and 85 MMA/15 MAA), and with trimethylaminoethyl methacrylate-HCl salt (97 MMA/3 TMAEMA-Cl and 85 MMA/15 TMAEMA-Cl), copolymers of HEMA with MAA (97/3 and 85/15) and with TMAEMA-Cl (97/3 and 85/15), poly(*n*-butyl methacrylate) (BMA), poly(*n*-hexyl methacrylate) (HMA), and poly(*n*-dodecyl methacrylate) (DDMA). The polymers were synthesized by radical polymerization using 2,2'-azobis(methyl isobutyrate) as initiator as described earlier (8-10). MMA was purchased from Aldrich Chemical Company, Milwaukee, Wisconsin; HEMA was a gift from Hydro-Med Sciences, Inc., New Brunswick, New Jersey; TMAEMA was purchased from Alcolac, Inc., Baltimore, Maryland; the other methacrylate esters were purchased from Polyscience, Inc., Warrington, Pennsylvania.

¹H-NMR spectra (270 MHz) were recorded on a Jeol FF270 NMR spectrometer. Mole ratios in the MMA/HEMA copolymers were calculated from the integrated peak areas of the HEMA-ester CH₂ protons and the polymer backbone CH₂ and CH₃ protons. The mole ratios in the HEMA/TMAEMA-Cl copolymers were calculated from the ratio of the TMAEMA-Cl tri-*N*-methyl protons and the polymer CH₂ and CH₃ protons of the backbone. The samples were analyzed in 5% (w/v) solutions in CDCl₃, DMSO-*d*₆, or D₂O.

The amounts of MAA and TMAEMA-Cl in the copolymers were determined by titration of methacrylic acid groups in MMA/MAA and HEMA/MAA copolymers in a chloroform, dimethyl formamide, ethanol, and water mixture with 0.1 *N* NaOH using a combined glass-calomel electrode. The amount of chloride in the trimethylaminoethyl methacrylate-HCl groups in MMA/TMAEMA-Cl and HEMA/TMAEMA-Cl copolymers was determined by potentiometric titration with 0.01 *N* AgNO₃ in an acetic acid-water mixture using a combined silver electrode. Mole ratios of monomers in the copolymers calculated from NMR and titration data are given in Table I. Titrations were performed in duplicate.

TABLE I

Copolymer Mole Ratios Calculated from ¹H-NMR and Titration Data

Copolymer	Mole ratio	
	NMR ^a	Titration
75 MMA/25 HEMA	78:22	—
50 MMA/50 HEMA	51:49	—
25 MMA/75 HEMA	29:71	—
97 MMA/3 MAA	—	97.0:3.0
85 MMA/15 MAA	—	88.9:11.1
97 MMA/3 TMAEMA-Cl	—	96.2:3.8
85 MMA/15 TMAEMA-Cl	—	86.2:13.8
97 HEMA/3 MAA	—	97.5:2.5
85 HEMA/15 MAA	—	89.4:10.6
97 HEMA/3 TMAEMA-Cl	95:5	96.9:3.1
85 HEMA/15 TMAEMA-Cl	82:18	86.8:13.2

^a Mole ratios calculated from integrated peak areas.

Preparation of Polymer Films

Polymer films were prepared by slow, uniform dipping of chromic acid cleaned glass slides (Bev-l-edge, No. DSO, Proper Manufacturing Co., 3 × 1 in., 0.9-1.0 mm) or microscope coverslips (Corning Type 2940, No. 1½, 24 × 50 mm, 0.16-0.19 mm) in polymer solutions (3-6% (w/v)) which were filtered through Teflon membrane filters (0.5 μm, Type FHLPO 4700, Millipore Corp., Bedford, Mass.).

Silane pretreatments were sometimes required to improve the adhesion of polymers to the glass. A vapor-phase silanization treatment similar to that described by Haller (15) was used. γ-Aminopropyl triethoxysilane (APS, Aldrich) and *n*-pentyl triethoxysilane (amyltriethoxysilane, nPS, Petrarch Chemicals, Inc., Bristol, Penn.) were applied. To solutions of HEMA, HEMA/MAA, and HEMA/TMAEMA-Cl copolymers, 1 mole% hexamethylene diisocyanate (HMDIC, Aldrich) based on the amount of the moles of HEMA present was added as a crosslinker. In this way the films were effectively bound to the aminopropyl silanized glass. The films were cured for 3 h at 60°C in a nitrogen atmosphere. The polymer films used for

streaming potential measurements were coated on the glass or silanized glass slides by spin casting using a Speedway Model EC101 spinning device (Speedway Research, Inc., Garland, Tex.) in order to obtain slides entirely covered on one side. A clean solvent-rinsed glass pipet was used to dispense 2 ml of polymer solution onto the slide covering the entire surface. Typically, the slides were spun at 4000 rpm for 15 to 20 s. This coating procedure was repeated twice to assure film uniformity. Slides were dried as described above for the dipcoated films. The thickness of the coatings was in the range 0.1–0.7 μm as determined gravimetrically. The surface uniformity and possible surface contamination with particulates were checked with light microscopy. The data for the preparation of the thin polymer films are given in Table II.

Contact-Angle Measurements

Most polymers demonstrate both an advancing and receding water contact angle (θ).

The difference between θ advancing and θ receding is defined as contact-angle hysteresis. The contact angles were measured by using the Wilhelmy plate technique (5) as described previously (16).

The contact angles were calculated from

$$\cos \theta = \frac{mg}{p\gamma} + \frac{V\rho g}{p\gamma}, \quad [1]$$

where m is mass (g) of the slide as measured with the electrobalance as a function of the immersion depth of the slide; g is local gravitational force (Salt Lake City, 979.3 dyn/g); p is perimeter of slide (cm); γ is surface tension of wetting liquid: for water $\gamma = 72.6$ dyn/cm at 20°C; V is volume of immersed slide at particular depth; and ρ is density of wetting liquid. Straight-line approximations of the advancing and receding slopes of the measured force with the balance are made and extrapolated to zero depth of immersion of the slide, and the buoyancy factor in Eq. [1], $V\rho g/p\gamma$, can then be elim-

TABLE II
Preparation of Thin Polymer Films on Glass by Dip Coating

Polymer	Solvent	Conc (%)	Adhesion promotor	Approximate film thickness (μm)
MMA	Toluene	6	nPS ^a	0.3
75 MMA/25 HEMA	DMF	3	APS ^b	0.7
50 MMA/50 HEMA	DMF	3	APS	0.3
25 MMA/75 HEMA	DMF	3	APS	0.2
HEMA	Methanol	3	APS	0.3
97 MMA/3 MAA	CHCl ₃	3	APS	ND ^d
85 MMA/15 MAA	CHCl ₃	3	APS	0.5
97 MMA/3 TMAEMA-Cl	CHCl ₃	3	nPS	ND
85 MMA/15 TMAEMA-Cl	DMF	3	—	0.2
HEMA	DMF ^c	3	APS	0.3
97 HEMA/3 MAA	DMF ^c	3	APS	0.5
85 HEMA/15 MAA	DMF ^c	3	APS	0.2
97 HEMA/3 TMAEMA-Cl	DMF ^c	3	—	0.2
85 HEMA/15 TMAEMA-Cl	DMF ^c	3	—	0.1
BMA	Toluene	6	nPS	0.4
HMA	Toluene	6	nPS	0.3
DDMA	Toluene	6	nPS	0.2

^a *n*-Pentyl silanized glass.

^b Aminopropyl silanized glass.

^c HMDIC (1% with respect to moles HEMA) crosslinker added.

^d ND, not determined.

inated. The weight after slide retraction is used for measuring the force displacements.

Water used for the contact-angle experiments was first deionized by passing it through a mixed ion-exchange resin bed and then twice distilled in an all-glass apparatus. Sodium azide (200 mg/liter, Eastman-Kodak Co., Rochester, N. Y.) was added to this water to prevent microorganism contamination. Wettability of the charged copolymers was determined using phosphate-buffered saline (PBS, 140 mM NaCl, 3 mM KCl, 8.1 mM Na_2HPO_4 , 1.5 mM KH_2PO_4 , pH 7.2). In PBS (pH 7.2) MAA is completely ionized ($\text{pK} = 4.7$). The surface tension of water or PBS is measured to be 72.6 ± 0.2 dyn/cm at 20°C using completely wetting glass microscope coverslips which were cleaned in chromic acid followed by a 3-min oxygen radiofrequency glow discharge treatment at $200 \mu\text{m}$ Hg at 35 W (Plasmod, Tegal Corp., Richmond, Calif.) (17). In Eq. [1] θ is set equal to zero, and γ , the surface tension of water, is thus calculated.

In order to investigate the effect of hydration on the surface properties of films of the charged MMA and HEMA copolymers, contact angles were measured before and after equilibration of the films in PBS for 3 and 18 h, respectively.

Streaming Potential Measurements

To characterize the polymer films with respect to the net charge density or ζ potential, streaming potential measurements were performed in a parallel-plate system as described by Van Wagenen and Andrade (18). The plate separation was $130 \mu\text{m}$. The measurement techniques and hydrodynamic requirements have been detailed by Van Wagenen *et al.* (6). Streaming potentials, E , are measured at various driving pressures, P , up to 8 cm Hg.

In this range a laminar Poiseuille flow is established and $\Delta E/\Delta P$ is linear. The ζ potential is calculated from

$$\psi_s = 8.4922 \times 10^8 \frac{\Delta E K_B \eta}{\Delta P \epsilon} \text{ mV.} \quad [2]$$

Bulk values for the electrolyte viscosity ($\eta = 0.010\text{P}$) and the dielectric constant ($\epsilon = 80.14$) at 20°C were obtained from literature (19). Specific conductance of bulk electrolyte, K_B , was calculated on the basis of a measured ac resistance ($R_{ac} = 190 \text{ ohm}$) in a precalibrated, platinum conductivity cell ($C = 0.274 \text{ cm}^{-1}$) where K_B was C/R_{ac} . The streaming electrolyte was 0.01 M KCl , $8 \times 10^{-4} \text{ M Na}_2\text{HPO}_4$, $2 \times 10^{-4} \text{ M KH}_2\text{PO}_4$, pH 7.4.

X-Ray Photoelectron Spectroscopy

X-Ray photoelectron spectroscopy (XPS) studies were done with a Hewlett-Packard 5950B instrument using monochromatic $\text{AlK}\alpha_{1,2}$ radiation (1487 eV) with 800 W power at the anode; the spectra were charge referenced to the C 1s alkyl binding energy at 284 eV. Photoelectron spectra were obtained utilizing high-resolution scans over a 20-eV binding energy range. As the Hewlett-Packard instrument used has a sample geometry in which the detected electrons are in a path 38.5° from the surface plane, about 63% of the signal detected is from the topmost 40 Å of the sample.

RESULTS

Polymers and Polymer Films

Methyl methacrylate and hydroxyethyl methacrylate homopolymers and copolymers, charged copolymers with methacrylic acid or trimethylaminoethyl methacrylate, and different poly(alkyl methacrylates) (BHA, MMA, and DDMA) were synthesized and analyzed by $^1\text{H-NMR}$ spectroscopy and titration (Table I). Calculated copolymer compositions from NMR and titration data were in agreement with the monomer mole ratios used in the polymerization mixtures.

The thin polymer films coated on glass or silanized glass were homogeneous, particulate free, and stable in PBS for at least 24 h. The approximate film thicknesses are given in Table II.

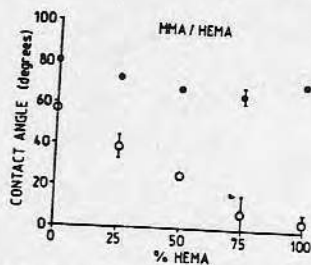


FIG. 1. Advancing (●) and receding (○) contact angles of methacrylate (co)polymers as determined by Wilhelmy plate technique; Bars indicate SD of the means of at least two triplicate measurements.

Contact Angles

Dynamic advancing and receding water contact angles were determined for the polymer films using the Wilhelmy plate method. Contact angles decreased with increasing HEMA content in MMA/HEMA copolymers (Fig. 1). Receding contact angles of MMA/MAA and MMA/TMAEMA-Cl copolymers decreased with increasing MAA or TMAEMA-Cl content, while the advancing angles were virtually unchanged (Fig. 2a). In HEMA/MAA copolymers, advancing angles slightly decreased but receding angles were practically unchanged with higher MAA content of the copolymers (Fig. 2b). The advancing contact angles of HEMA/TMAEMA-Cl copolymers increased with higher TMAEMA-Cl content, while the receding angles did not change or only slightly increased (Fig. 2b). For the alkyl methacrylate polymer series the advancing angles increased with

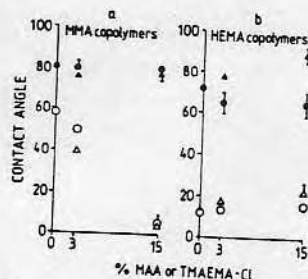


FIG. 2. Advancing (●, ▲) and receding (○, △) contact angles of (a) copolymers of MMA with MAA (●, ○) or with TMAEMA-Cl (▲, △); and (b) copolymers of HEMA with MAA (●, ○) or with TMAEMA-Cl (▲, △).

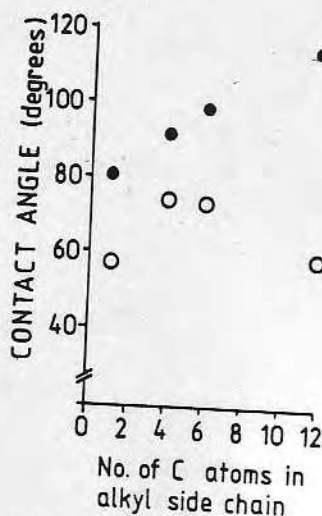


FIG. 3. Advancing (●) and receding (○) contact angles of poly(alkyl methacrylates) with different alkyl side-chain lengths.

longer alkyl side-chain length (Fig. 3). The receding angles of these polymers were increased from the methyl- to butyl-substituted polymers, but decreased for those with hexyl to dodecyl side chains.

The receding angle for MMA slightly decreased after 3-h preequilibration in PBS, while the advancing angle was unchanged. The contact angles of HEMA were unchanged after equilibration of the films in PBS (Fig. 4a). The advancing angles of the MMA/

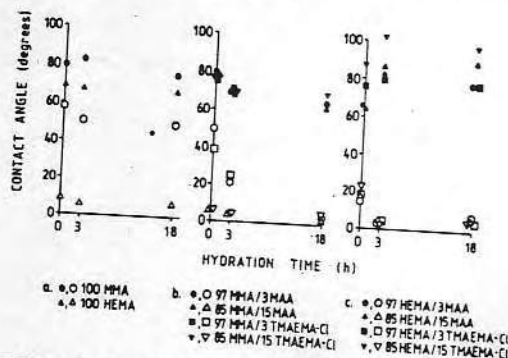


FIG. 4. Effect of preequilibration of methacrylate (co)polymer films in PBS on the advancing (closed symbols) and receding (open symbols) contact angles of (a) MMA and HEMA polymers, copolymers of (b) MMA and (c) HEMA with MAA or with TMAEMA-Cl.

MAA copolymers decreased after equilibration of the films in PBS (Fig. 4b). The receding angles of 97 MMA/3 MAA strongly decreased after equilibration times up to 18 h in PBS. The low receding angles of the MMA copolymers with 15 MAA or TMAEMA-Cl did not decrease much further after equilibration in PBS. The contact angles of the MMA/TMAEMA-Cl copolymers showed the same pattern as that of the MMA/MAA copolymers. (The 97 MMA/3 TMAEMA-Cl copolymer film was not tested after 18 h, because this film coated on APS was unstable.) After 3 h of equilibration in PBS, the advancing angles of the charged HEMA copolymers were increased, while their receding angles were decreased (Fig. 4c). The increase of the advancing angles was higher for the copolymers with 15% charged monomer units than for those with 3% charged units.

Surface ζ Potential

Streaming potential measurements were performed to determine the charge at the

polymer film-water interface. The $\Delta E/\Delta P$ ratios and calculated ζ potentials of polymer films of charged MMA and HEMA copolymers preequilibrated in PBS for 3 h are given in Table III. Radiofrequency glow discharge cleaned "Bev-l-edge" glass slides had negative ζ potentials and were commonly used as a standard in the streaming potential measurements. The electrokinetic potential of the MMA and HEMA polymers was net negative. MMA and HEMA polymer films with incorporated MAA units showed increasingly negative ζ potentials with an increasing amount of bulk charge. The MMA/TMAEMA-Cl and HEMA/TMAEMA-Cl copolymers showed less negative ζ potentials than the base homopolymers. For the higher mole ratios of TMAEMA-Cl the ζ potentials of the copolymers became net positive.

The increased negative ζ potentials of MMA/MAA copolymers with respect to MMA after preequilibration in PBS for 3 h were diminished after preequilibration in PBS for 18 h, whereas those of the HEMA/MAA copolymers remained constant after preequilibration in PBS for 3 to 18 h (Table IV).

TABLE III
 $\Delta E/\Delta P$ Ratios and ζ Potentials for Glass and Polymer Films

Material	$\Delta E/\Delta P$ (mV/cm Hg)	ψ_r (mV)	<i>n</i>	Comment ^a
Glass (Bev-l-edge)	-0.332 ± 0.008^b	-50.8 ± 1.3	3	a, d
	-0.295 ± 0.013	-44.8 ± 1.8	3	a, e
	-0.324 ± 0.014	-49.3 ± 2.1	9	a, f
MMA	-0.189 ± 0.013	-28.9 ± 2.2	3	c, g
97 MMA/3 MAA	-0.223 ± 0.012	-34.1 ± 1.9	2	d, g
85 MMA/15 MAA	-0.271 ± 0.016	-41.1 ± 2.3	2	d, g
97 MMA/3 TMAEMA-Cl	-0.056 ± 0.022	-8.6 ± 3.4	3	c, g
85 MMA/15 TMAEMA-Cl	$+0.027 \pm 0.002$	$+4.2 \pm 0.3$	3	a, g
HEMA ^c	-0.054 ± 0.007	-8.2 ± 1.0	3	b, g
97 HEMA/3 MAA ^c	-0.114 ± 0.005	-17.3 ± 0.7	3	b, g
85 HEMA/15 MAA ^c	-0.155 ± 0.012	-23.8 ± 2.0	3	a, g
97 HEMA/3 TMAEMA-Cl ^c	-0.023 ± 0.013	-3.4 ± 2.0	3	a, g
85 HEMA/15 TMAEMA-Cl ^c	$+0.034 \pm 0.012$	$+4.9 \pm 1.9$	3	a, g

^a Silane linkage: (a) none, (b) APS, (c) nPS. Cleaning: (d) none, (e) chromic acid cleaned, (f) RFGD cleaned. Preequilibration: (g) for 3 h in electrolyte.

^b Mean \pm SD of *n* measurements.

^c HEMA, HEMA/MAA, and HEMA/TMAEMA-Cl copolymers with 1% HMDIC.

TABLE IV

§ Potentials of MMA/MAA and HEMA/MAA Copolymers after Preequilibration in PBS for 3 and 18 h

Material	ψ_r (mV)	
	Preequilibration for 3 h in PBS	Preequilibration for 18 h in PBS
MMA	-28.9 ± 2.2^a	-27.1 ± 1.4
97 MMA/3 MAA	-34.1 ± 1.9	-28.3 ± 0.1
85 MMA/15 MAA	-41.1 ± 2.3	-25.2 ± 0.6
HEMA ^b	-8.2 ± 1.0	-7.8
97 HEMA/3 MAA ^b	-17.3 ± 0.7	-16.2
85 HEMA/15 MAA ^b	-23.8 ± 2.0	-24.2

^a Mean \pm SD of at least duplicate measurements.

^b Crosslinked with 1% HMDIC.

X-Ray Photoelectron Spectroscopy

From XPS data for the TMAEMA-Cl copolymers obtained at normal electron take-off angles of 38.5° the atomic percentage of nitrogen with respect to oxygen was measured based on the peak areas and sensitivity factors of the N 1s and C 1s signals (Table V). The measured N/C atomic ratios of the MMA and HEMA copolymers with TMAEMA-Cl were close to or slightly lower than the calculated values. In the calculated values of theoretical N/C ratios, the amount of nitrogen from the diisocyanate crosslinker was neglected, because in the base polymer HEMA with 1% HMDIC no N signal could be detected at the surface using XPS.

DISCUSSION

Contact-angle measurements give useful information about the polymer-water interface. Contact angles are determined primarily by the atoms exposed in the outer 10 Å of the solid surface (20). In hydrogel interfaces, which are more diffuse than those of hydrophobic polymers, the transition region between the bulk gel and free water may be of the order of 100 Å or greater. Since in this study measurements were performed on polymer coatings thicker than 0.1 μm , it is unlikely that the angles are influenced by the support materials.

Contact-angle hysteresis of polymer surfaces, as measured by the Wilhelmy plate technique, are caused by the mobility of surface polymeric chains and their side groups or segments when no other disturbing factors are present (3, 21). These factors can be surface roughness or surface heterogeneity. The advancing angle is then sensitive to the low surface energy domains and the receding angle to the high surface energy domains in heterogenous materials. Because random copolymerization can be assumed for the copolymers MMA/HEMA, MMA/TMAEMA-Cl (22) and for the charged HEMA copolymers (11), phase separation would not be present in the methacrylate polymers used in this study. Contact-angle hysteresis phenomena observed are therefore unlikely to be due to surface heterogeneity.

The contact-angle hysteresis observed in the HEMA hydrogel system can be explained by the fact that the apolar polymer backbone and α -methyl group dominate the surface in air, while the hydrophilic hydroxyl group containing ester side chains dominates the surface in water (4, 21). The minimization of the interfacial energy is the driving force for the changes in the orientation of the surface molecules in different environments (3).

MMA showed contact-angle hysteresis, although it is a rigid polymer with a glass

TABLE V

Atomic Percentage of Nitrogen with Respect to Carbon
• Measured by XPS

Material	N/C (%)	
	Measured	Calculated ^a
97 MMA/3 TMAEMA-Cl	0.7	0.8
85 MMA/15 TMAEMA-Cl	2.2	2.5
97 HEMA/3 TMAEMA-Cl	0.6	0.5
85 HEMA/15 TMAEMA-Cl	1.5	2.1

^a Nitrogen originating from the HMDIC crosslinker was neglected, since the N/C ratio was very low for HEMA 1% HMDIC. N/C values were calculated from the mole ratios determined by titration (Table I).

transition temperature above 100°C. Side-chain β relaxations and small amounts of plasticizing water at the polymer-water interface are considered to be the cause of this hysteresis (3). The decreasing receding contact angles and increased contact-angle hysteresis in MMA/HEMA and charged MMA copolymers with higher contents of the hydrophilic or charged moieties are therefore likely due to the increased water content and surface mobility of the polymers and the ability of the charged moieties to dominate at the surface in an aqueous environment (10).

Incorporation of charge in the polymer films considerably affects the surface properties of the films. The charged MMA copolymers absorb more water than does the MMA homopolymer and their receding angles accordingly decreased with higher mole percentages of charged units incorporated. The advancing angles were virtually unchanged. The uptake of water appeared to be slower for the MMA copolymers with 3% charged units than for those with 15% charged units as suggested by the steady decrease of the receding contact angle of 97 MMA/3 MAA with hydration times up to 18 h. The incorporation of charge in the HEMA hydrogel materials either does not or only slightly affects the receding contact angles. The HEMA/TMAEMA-Cl copolymers showed increased advancing angles in contrast to the unchanged advancing angles for the MMA/TMAEMA-Cl copolymers with increasing TMAEMA-Cl content. This difference might be explained by the surface polymer chain mobility in HEMA systems, especially when they are hydrated, which enables most charged groups to be buried into the hydrogel when the films are exposed to air, thereby reducing the interfacial energy. The hydrophobic polymer backbone is in this way preferentially exposed at the surface and causes the increased advancing contact angles.

This rotation of surface polymer chains would not be possible in MMA copolymers. The same effects as with HEMA/TMAEMA-Cl were observed with HEMA/MAA copolymers, when the MAA groups were ionized after hydration in PBS. If these groups were not ionized, the increase in advancing angle with higher MAA content was not observed, because the MAA groups were not buried in the bulk due to the absence of charge, and the backbone chains were thus not preferentially exposed at the surface.

In the poly(alkyl methacrylate series), longer hydrophobic alkyl side chains caused increased advancing contact angles, as expected, paralleled by an increase of the receding angles from the methyl- to the butyl-substituted methacrylate polymers. However, for the polymers with octyl to dodecyl side chains the receding angles decreased and thus the contact-angle hysteresis substantially increased. This effect might be ascribed to the lowering of the polymer glass transition temperature by the longer alkyl side chains to below room temperature for HMA and DDMA. This would enable these polymers to decrease their interfacial energy in water by additional backbone chain reorientation besides side-chain relaxations.

The neutral MMA and HEMA polymers as well as glass had a net negative ζ potential, which is generally explained by the specific adsorption from solution of potential-determining ions such as phosphate ions, OH^- , and Cl^- (23).

The difference in ζ potential between MMA and HEMA might be explained by differences in the orientation and structure of water at interfaces of different hydrophilicity, influencing specific anion adsorption and subsequent interfacial charging. Glass might, moreover, expose ionized surface silanol groups ($\text{pK} \approx 5.6$). Differences in measured streaming potentials between rigid surfaces and hydrogel surfaces might also occur because of differences in the position of the hydrodynamic shear region at the surface. Furthermore, surface conduction of hydrogel surfaces by means of ion migration and electroosmosis might contribute to a decreased streaming potential (24).

The incorporation of positively charged

TMAEMA-Cl or negatively charged MAA moieties in MMA or HEMA polymers resulted in a decrease or increase in net negative ζ potential, respectively. The determined ζ potentials for the hydrogels, HEMA and HEMA/MAA, were somewhat less negative than reported by Van Wagenen *et al.* (6). In this study 3% polymer solutions were used for spin casting of the polymer films, probably resulting in thicker films as compared to the films cast from 1% solutions by Van Wagenen *et al.* Longer preequilibration of MMA/MAA copolymers in the phosphate buffered KCl or NaCl solutions from 3 to 18 h caused a continued uptake of water as indicated by the decrease of the contact angles. The diminished ζ potentials of the MMA/MAA copolymers after longer preequilibration time in buffer might thus be caused by the increased hydrogel character of the surface. In the HEMA/MAA hydrogel series, i.e., HEMA and the HEMA/MAA copolymers which may already be fully hydrated within 3 h of preequilibration in buffer, no changes were observed in the ζ potential or contact angles after a longer preequilibration time in buffer.

CONCLUSIONS

—Receding contact angles as determined by the Wilhelmy plate technique of MMA copolymers containing hydrophilic or charged units were decreased as compared to the MMA homopolymer, while their advancing contact angles were changed only slightly or not at all.

—In comparison with the HEMA homopolymer, charged HEMA copolymers showed similar receding contact angles, but showed increased advancing contact angles, probably due to reorientation of surface polymer chains.

—Advancing contact angles of poly(alkyl methacrylates) increased with increasing side-chain lengths. Their receding contact angles increased from methyl- to butyl-substituted polymers, but decreased from hexyl- to dodecyl-substituted polymers, probably due to increased mobility of these polymers.

— ζ Potentials of MMA and HEMA copolymers as determined by streaming potential measurements were more negative when negatively charged groups were incorporated, and less negative or even positive when positively charged groups were incorporated. ζ Potentials of charged MMA copolymers varied with the preequilibration time of the polymers with water.

ACKNOWLEDGMENTS

This study was supported by NIH Grant HL 18519 and a grant from the Netherlands Organization for Pure Research (ZWO), The Hague. Discussions with Dr. D. L. Coleman and Dr. R. A. van Wagenen are gratefully acknowledged.

REFERENCES

1. Coleman, D. L., "In Vitro Blood Materials Interactions: A Multi-Test Approach," Ph.D. thesis. University of Utah, Salt Lake City, 1980.
2. Feijen, J., Beugeling, T., Bantjes, A., and Smit Sibinga, C.Th., in "Advances in Cardiovascular Physics" (D. N. Ghista, Ed.), Vol. 3, p. 100. Karger, Basel, 1979.
3. Andrade, J. D., Gregonis, D. E., and Smith, L. M., in "Physico-chemical Aspects of Polymer Surfaces" (K. L. Mittal, Ed.), Vol. 2, p. 911. Plenum, New York, 1983.
4. Ratner, B. D., *Ann. Biomed. Eng.* **11**, 313 (1983).
5. Adamson, A. W., "Physical Chemistry of Surfaces," 3rd ed. Wiley-Interscience, New York, 1976.
6. Van Wagenen, R. A., Coleman, D. L., King, R. N., Triolo, P., Brostrom, L., Smith, L. M., Gregonis, D. E., and Andrade, J. D., *J. Colloid Interface Sci.* **84**, 155 (1981).
7. Choudhary, M. S., and Varma, I. K., *Eur. Polym. J.* **15**, 957 (1979).
8. Gregonis, D. E., Chen, C. M., and Andrade, J. D., in: "Hydrogels for Medical and Related Applications," (J. D. Andrade, Ed.), p. 88, ACS Symposium Series No. 31. Amer. Chem. Soc., Washington, D. C., 1976.
9. Gregonis, D. E., Russell, G. A., Andrade, J. D., and De Visser, A. C., *Polymer* **19**, 1279 (1978).
10. Gregonis, D. E., Hsu, R., Buerger, D. E., Smith, L. M., and Andrade, J. D., in "Solvent-Property Relationships in Polymers" (R. B. Seymour and G. A. Stahl, Eds.), p. 120. Pergamon, New York, 1982.
11. Hattori, S., "Preparation, Characterization and Cell

- Growth of Selected Hydrophilic Methacrylates." Ph.D. thesis. University of Utah, Salt Lake City, 1980.
12. Johnsen, A., Klesper, E., and Wirthlin, T., *Macromol. Chem.* 177, 2397 (1976).
 13. Macret, M., and Hild, G., *Polymer* 23, 748 (1982).
 14. Ilavski, M., Dusek, K., Vacik, J., and Kopecek, J., *J. Appl. Polym. Sci.* 23, 2073 (1979).
 15. Haller, I., *J. Amer. Chem. Soc.* 78, 8050 (1978).
 16. Smith, L., Doyle, C., Gregonis, D. E., and Andrade, J. D., *J. Appl. Polym. Sci.* 26, 1269 (1982).
 17. O'kane, D. F., and Mittal, K. L., *J. Vac. Sci. Technol.* 11, 567 (1974).
 18. Van Wagenen, R. A., and Andrade, J. D., *J. Colloid Interface Sci.* 76, 305 (1980).
 19. Weast, R. C. (Ed.), "Handbook of Chemistry and Physics." 58th ed., p. F-49, E-61. CRC Press, Palm Beach, Fla., 1977-1978.
 20. Johnson, R. E., and Dettre, R. H., in "Surface and Colloid Science" (E. Matijevic, Ed.), Vol. 2, p. 85. Wiley-Interscience, New York, 1969.
 21. Holly, F. J., and Refojo, M. F., *J. Biomed. Mater. Res.* 9, 315 (1975).
 22. King, R. N., Andrade, J. D., Ma, S. M., Gregonis, D. E., and Brostrom, L. R., *J. Colloid Interface Sci.* 103, 62 (1985).
 23. Eagland, D., and Allen, A. P., "Surface hydration and Zeta Potential," paper presented at the International Conference on Surface and Colloids, Puerto Rico, June 1976.
 24. Voigt, A., Becker, R., and Donath, E., *J. Biomed. Mater. Res.* 18, 317 (1984).

Chapter 19

Human and Hen Lysozyme Adsorption: A Comparative Study Using Total Internal Reflection Fluorescence Spectroscopy and Molecular Graphics

D. Horsley, J. Herron, V. Hlady, and J. D. Andrade

Department of Bioengineering, College of Engineering, University of Utah,
Salt Lake City, UT 84112

Total internal reflection intrinsic fluorescence (TIRIF) spectroscopy and molecular graphics have been applied to study the adsorption behavior of two lysozymes on a set of three model surfaces. A recently devised TIRIF quantitation scheme was used to determine adsorption isotherms of both hen egg-white lysozyme (HEWL) and human milk lysozyme on the three model surfaces. This preliminary study suggests that the adsorption properties of the two lysozymes are significantly different, and that further comparative studies of the two lysozymes might prove to be beneficial in understanding how protein structure might influence adsorption properties. Molecular graphics was used to rationalize the adsorption results from TIRIF in terms of the proteins' surface hydrophobic/hydrophilic character.

The understanding and control of the interactions of proteins with solid surfaces is important in a number of areas in biology and medicine. In the last twenty years there has been considerable interest in protein interactions with materials used in medical devices (1-3). One area of particular interest to the contact lens industry is in the interaction of tear proteins with contact lenses. One of the major constituent of protein deposits on lenses is lysozyme. An understanding of human lysozyme interaction with contact lens materials is essential to the minimization and elimination of contact lens deposits.

In view of the importance of tear protein interactions to the long-term efficacy of contact lenses, it is surprising that so few basic studies are

available. Only recently have lysozyme adsorption studies on polymers and contact lens materials begun to appear (4-14).

Our lab is using two rather recently introduced techniques to offer a comparative study of human and hen lysozyme adsorption on three different model surfaces.

The first technique is known as total internal reflection intrinsic fluorescence spectroscopy (TIRIF). This recent technique provides a sensitive, real time, interfacial method for detecting the fluorescence of proteins (labeled or non-labeled) adsorbed to the totally reflecting interface. The technique was recently reviewed (15-17) and has been used by a number of biomaterial research groups to study protein adsorption (15-20). Up to this point, the major problems with using TIRIF have been its lack of reproducibility and its inaccuracy in measuring absolute amounts of protein on the surface (due to the fact that changes in the quantum yield of the protein upon adsorption are ignored). A recently devised quantitation scheme developed in our lab has facilitated our acquisition of reproducible adsorption data from TIRIF (21), but its absolute accuracy in quantitating the amount of protein adsorbed on the surface remains to be improved (see discussion below).

The second technique is the use of molecular graphics. Although still in its infancy stage, it appears to have a very promising future. Using molecular graphics we have been able to rationalize our data obtained from TIRIF by examining the surface hydrophobic/hydrophilic characteristics of the two lysozyme molecules.

Experimental

Materials. Amorphous silica microscope slides were obtained from ESCO products. The silanes 3-amino-propyltriethoxysilane (APS) and dimethyldichlorosilane (DDS) were both purchased from Petrarch Systems Inc.. Hen egg-white lysozyme (3X crystalline) and human milk lysozyme (highly purified, salt free powder) were products of Calbiochem. The fluorescence standard, 5-hydroxytryptophan methyl ester hydrochloride (TrpOH) was also a product of Calbiochem. PBS buffer (pH 7.4, $[KH_2PO_4]=0.013M$, $[Na_2HPO_4]=0.054M$, $[NaCl]=0.1M$) made from analytical grade reagents and low conductivity water was used to prepare all protein and fluorescence standard solutions. These solutions were prepared fresh, prior to each experiment.

Preparation of surfaces. Adsorption studies were performed using charged and hydrophobic surfaces. Amorphous silica microscope slides were used as the substrate for all surfaces. Slides were cleaned in hot (80 degrees C) chromic acid for 20-30 minutes, cooled to room temperature, and then rinsed well in ultra-pure water (Milli-Q reagent

water system). Slides were then desiccated for 12 hours at 100 degrees C. Cleanliness was confirmed by the measurement of Wilhelmy plate contact angle (no hysteresis with a clean surface).

The amorphous silica microscope slides exhibit an intrinsic negative charge at pH 7.4 (the surface silanol groups have been determined as having a pK_a of 5-7 by several workers (22-24)) and were used without further modification for adsorption of lysozyme onto negatively charged surfaces. The average ζ potential of equivalent silica slides was determined by Van Wagenen *et al.* (25) to be -65 mV.

Positively-charged surfaces were prepared by reacting the cleaned microscope slides with 3-amino-propyltriethoxysilane (APS). At pH 7.4 the end amino group ($pK_a=10-11$) of the immobilized APS molecule bears a positive charge. Clean slides were dip cast in a solution of 5% APS (v/v) in ethanol- H_2O (95:5), and allowed to react for 30 minutes. Slides were then rinsed several times in H_2O , followed with ethanol.

Non-covalently bound APS was removed by vacuum desiccation at 60 degrees C for 12 hours. The measured contact angles of the APS coated slides exhibited mean values of 70 degrees advancing angle and 20 degrees receding angle with less than 10% variability among several APS coated surfaces. The average ζ potential of similarly prepared APS coated slides was determined by Van Wagenen *et al.* (25) to be -32 mV.

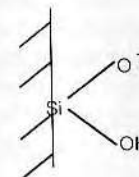
Hydrophobic surfaces were prepared by dip casting cleaned microscope slides with dimethyldichlorosilane (DDS). A similar protocol was used for DDS as for APS, except that the reaction mixture for DDS was 10% DDS (v/v) in dry toluene, and slides were rinsed with ethanol before rinsing with H_2O in order to remove the toluene. The measured contact angles of the DDS coated slides exhibited mean values of 110 degrees advancing angle and 90 degrees receding angle with less than 10% variability among several DDS coated surfaces.

All of the model surfaces were used within 4 days of preparation.

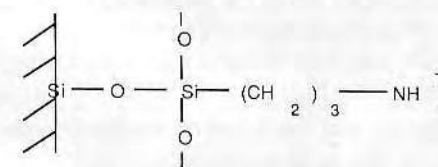
Figure 1 illustrates the proposed surface structure of the silanized surfaces as well as the untreated silica surface (26,27).

Experimental Apparatus. The TIRIF apparatus used in these experiments has been described in detail elsewhere (28). The incident light totally internally reflects at the quartz-aqueous interface and produces a standing wave normal to the reflecting interface inside the quartz (the optically more dense medium) due to the superposition of the incident and reflected waves. The electric field of the standing wave has a non-zero amplitude (E^0) at the interface which decays exponentially with distance (z) normal to the interface into the aqueous phase (the optically less dense medium), thereby creating a surface evanescent wave that selectively excites molecules within a few thousand angstroms from the surface.

a Hydrophillic Silica



b 3-Aminopropyltriethoxysilane (APS) silica



c Dichlorodimethylsilane (DDS) silica

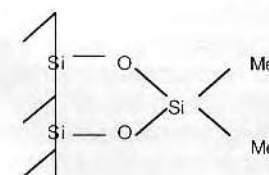


Figure 1. Proposed surface structures of a) hydrophillic silica, b) APS treated silica, and c) DDS treated silica.

Adsorption Isotherms. All protein adsorption isotherms were determined at room temperature. Fluorescence emission was generated by exciting at 280 nm and collecting at 335 nm (several workers have shown that tyrosine emission at 335 nm of both human and hen lysozymes is insignificant when exciting at 280 nm (29-31)). Slits of 16-nm half-bandwidth were used in both excitation and emission monochromators. For *in situ* protein adsorption experiments, the TIRIF cell was first primed with buffer and the background fluorescence was taken. The buffer solution was then replaced with external standard (TrpOH) solutions of increasing concentration and the fluorescence intensity recorded (fig. 2). After the fluorescence of the TrpOH standard of the highest concentration was recorded, the cell was again flushed with buffer to return the signal to the background level. At this point, 5 ml of the least concentrated protein solution was injected into the cell at a flow rate of 20 ml/min. after which the flow was stopped and the protein was allowed to adsorb for 50 minutes (30 minutes after no further increase in surface fluorescence was seen). A shutter was used to prevent overexposure to UV light during the adsorption time. At the end of 50 minutes, the shutter was opened and fluorescence signal was recorded (N_{tot}). The cell was then flushed with buffer (20 ml/min.) to remove nonadsorbed proteins and the resulting signal recorded (N_a). The procedure was then repeated for the protein solution of the next higher concentration and so on. In this manner, a step-adsorption experiment was performed as opposed to a single-shot adsorption experiment where the clean surface is exposed only once to each protein solution.

The quantitation scheme developed by Hlady, *et al.* (21) was then used to quantitate the amount of protein adsorbed at each protein concentration from the recorded fluorescence intensities.

Molecular Graphics. Molecular graphics studies of hen and human lysozymes were performed using a Silicon Graphics IRIS-2400 graphics workstation. Computer programs for displaying and manipulating protein models were developed by the computer graphics laboratory at the University of California at San Francisco. The principal program, called MIDAS acts as a display vehicle for several different data structures including atomic coordinates in Protein Data Bank format, van der Waals surfaces, solvent-accessible surfaces, and electrostatic potential surfaces.

Atomic coordinates for both hen egg-white and human lysozymes were based on crystallographic structures determined by Blake *et al.* (32-36) and deposited in the Protein Data Bank (Brookhaven National Laboratory). The distribution of hydrophobic, polar, and charged atoms on the surface of the two proteins was analyzed by calculating

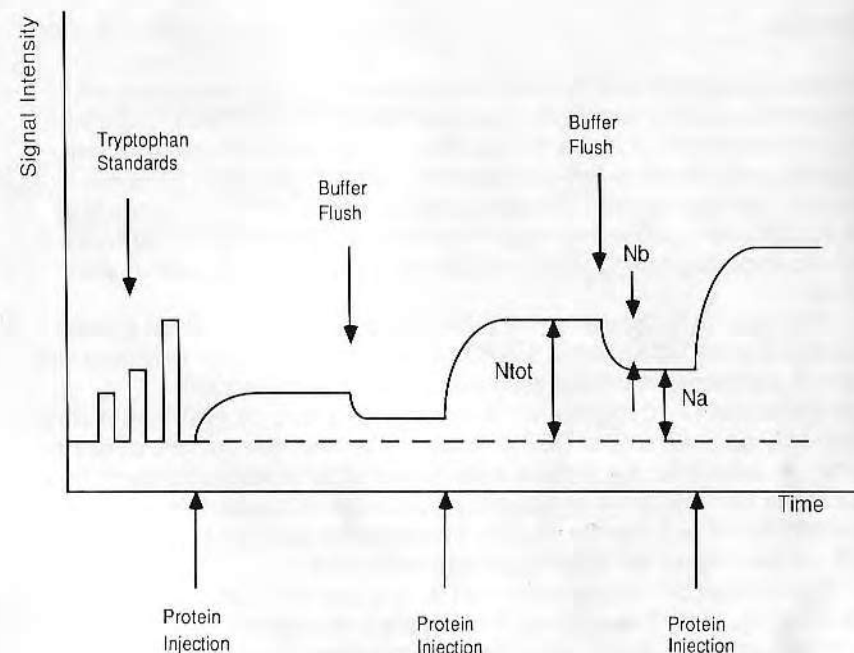


Figure 2. Time course of a typical step-adsorption experiment.

N_{tot} : Signal due to adsorbed and bulk protein.

N_b : Signal due to bulk protein only.

N_a : Signal due to adsorbed protein only.

Corey-Pauling-Kaitun (CPK) surfaces and coloring atoms according to two coloring schemes (see tables I and II). Both the Feldmann scheme (37) and the scheme based on the Eisenberg Atomic Solvation Parameter (ASP) (38), were based on how each residue would be charged at pH 7.4.

Results

The step-adsorption isotherms for both hen and human lysozymes on hydrophobic (DDS), negatively-charged (silica), and positively-charged (APS) surfaces are presented in figure 3. Since the TIRIF quantitation scheme used assumes that the quantum yield of the protein does not change upon adsorption (an assumption we are currently trying to test), the actual amount adsorbed may differ from that presented in the figure if this assumption proves to be invalid for these proteins (see discussion below).

The order of both lysozymes' affinity toward the three model surfaces was found to be DDS > silica > APS. The human lysozyme exhibited well defined plateaus on all three surfaces at relatively low protein concentrations (< 10 mg/ml), while for the hen lysozyme a definite plateau could only be seen on the DDS surface. Moreover, the amount of human lysozyme adsorbed per surface area appeared to be roughly three times that of the hen lysozyme on equivalent surfaces at low protein concentrations (< 5 mg/ml). Again, these results may not be accurate due to the limitations of the TIRIF quantitation scheme.

The images of the two lysozymes from a few different viewpoints are shown in figure 4. The coloring schemes are as outlined in tables I and II. Both lysozymes exhibited a number of similarities. To a first approximation, positively-charged residues were fairly evenly spaced over the entire protein, although the electrostatic surface potentials (ESP) computed for the two proteins showed a slight assymetric distribution of surface positive charge, with the larger lobe showing more positive character than the smaller lobe (39). Both proteins were seen to have long positive side chains extending into the solvent.

There were approximately one-third as many negatively-charged groups as there were positively-charged groups on the surface of both proteins. These negatively-charged residues barely reach the surface and are not nearly as accessible as the positively-charged residues. ESP calculations have shown that the active site cleft shows the greatest concentration of negative surface charge on both proteins (39).

Nonpolar residues formed a hydrophobic patch in the middle of the back side (opposite the active site cleft) of both proteins as can be seen in figure 4 e & f. The hydrophobic patch on the human lysozyme appeared to be slightly larger than that on the hen lysozyme.

Perhaps the most dramatic difference in the surface properties of the

Table I

Coloring of atoms according to their hydrophobicity is based on D. Eisenberg's Atomic Solvation Parameter ($\Delta\sigma$): $\Delta\sigma = \Delta G/A$

where ΔG = free energy of transfer of the atom from n-octanol to water

A = water accessible surface area of the atom

Atom	$\Delta\sigma$ (cal $\text{\AA}^{-2}\text{mol}^{-1}$)	Color
S	+21 (+/- 10)	1 (green)
C	+16 (+/- 2)	2 (light green)
N/O	-6 (+/- 4)	6 (light blue-green)
O-	-24 (+/- 10)	10 (light blue)
N+	-50 (+/- 9)	15 (blue)

Table II

Feldmann's Functional Color Code

Atom	Color
Carbon	White
Sulfur	Yellow
Oxygen (δ^-)	Pink
Oxygen ($-$)	Red
Nitrogen (δ^+)	Light Blue
Nitrogen ($+$)	Blue

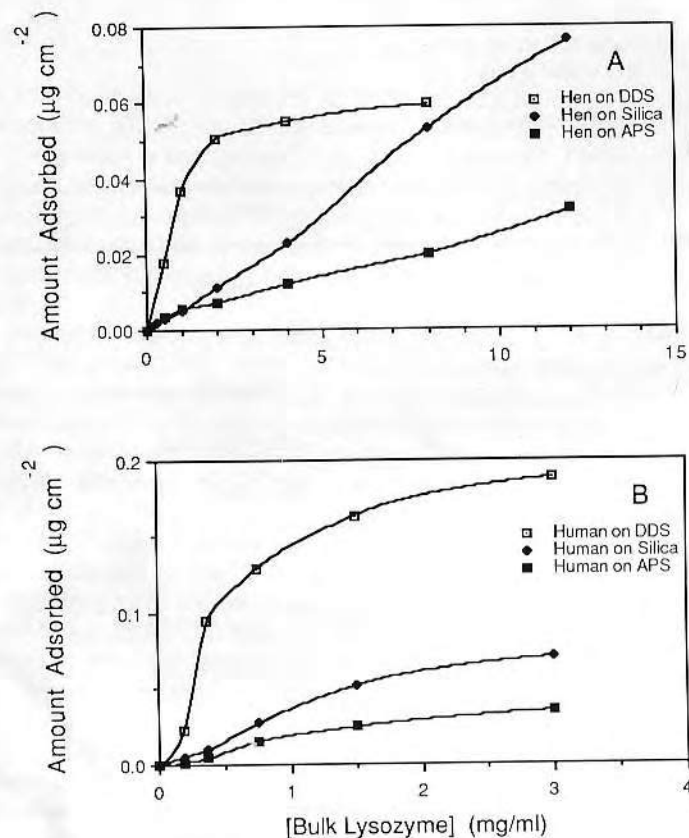


Figure 3. Comparison of lysozyme adsorption on hydrophobic (DDS), negatively-charged (silica), and positively-charged (APS) surfaces. Step adsorption isotherms for the hen egg-white protein are plotted in Panel A, and for the human milk protein in Panel B.

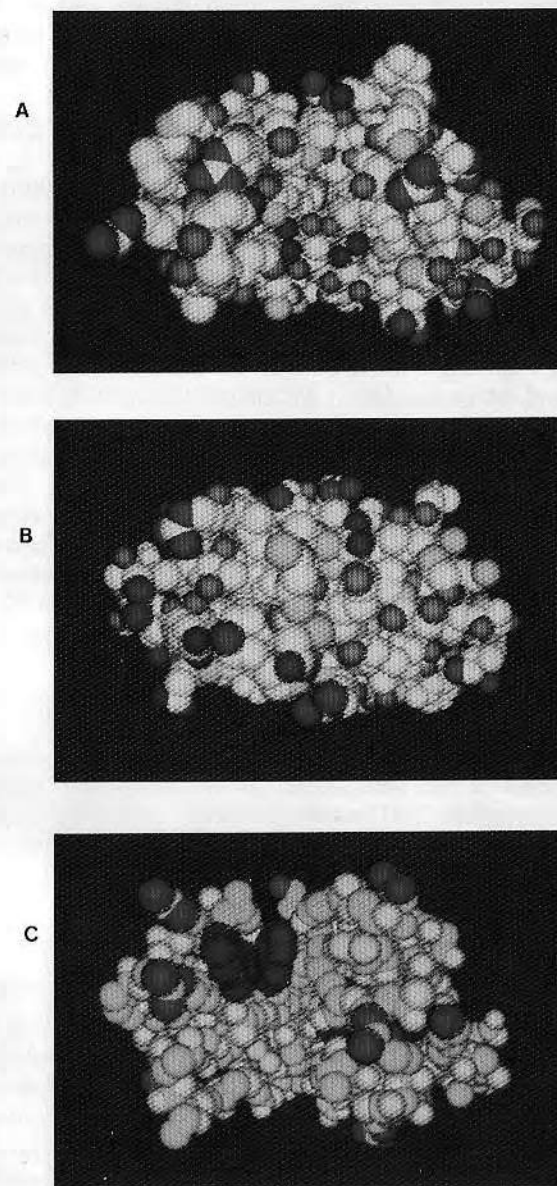


Figure 4. (A) Front view (looking into the active site) and (B) back view of human lysozyme colored according to Feldmann's functional color scheme. Front view of human lysozymes colored according to Eisenberg's atomic solvation parameters; tophan residues are additionally colored red. *Continued on next page.*

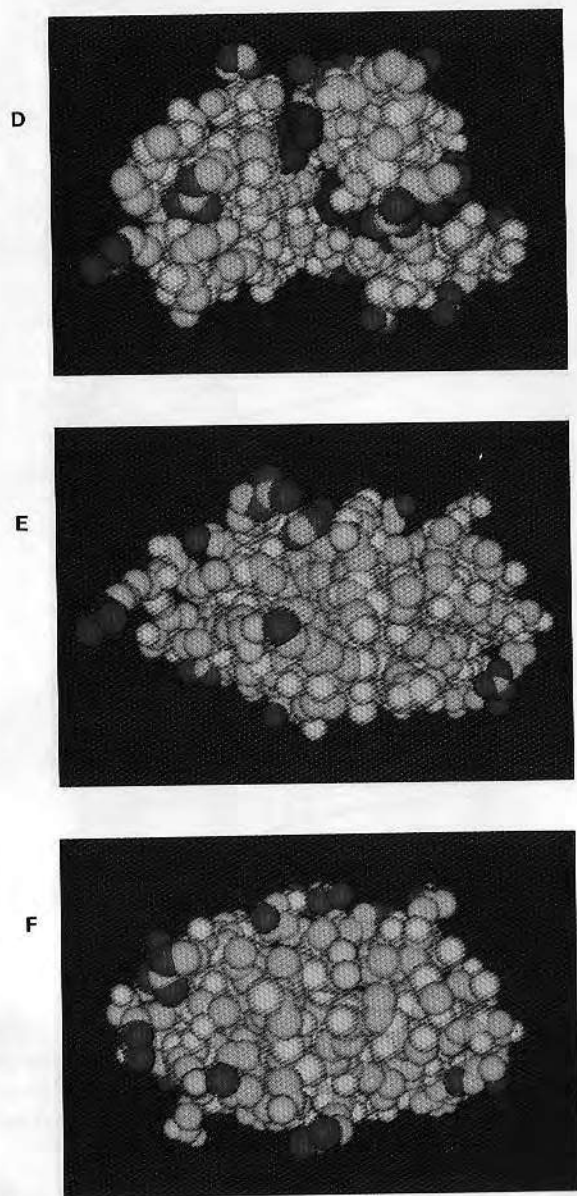


Figure 4.—Continued. Front view of (D) ^{human} hen lysozymes colored according to Eisenberg's atomic solvation parameters. Tryptophan residues are additionally colored red. Back view of (E) ^{human} and (F) ^{hen} hen lysozymes colored according to Eisenberg's atomic solvation parameters. Note the hydrophobic patch seen on the back view of both proteins.

two lysozymes was seen by the ESP calculations which showed that the human lysozyme had a significantly greater overall electrostatic surface potential than the hen lysozyme had (39).

Discussion

As stated above, the primary problem with the TIRIF quantitation scheme is the fact that it ignores changes that might occur in the quantum yield of the protein upon adsorption. Hlady, *et al.* (21) used a radiolabeling technique to estimate the change in quantum yield that might occur upon adsorption of BSA and IgG onto hydrophilic silica and found that the quantum yield decreased by a factor of at least two for both proteins. Consequently, the TIRIF isotherms for BSA and IgG were at least two-fold less than the isotherms determined by radiolabeling the proteins. The origin of the decreased quantum yield of adsorbed protein would most likely be due to a change in the conformation of the protein upon adsorption.

Several reports have pointed out that iodination of proteins may affect their adsorption to solid surfaces and their chromatographic behavior (40-43). Consequently, we have chosen to determine the quantum yield of unlabeled, adsorbed lysozyme via fluorescence lifetimes. We are currently in the process of modifying our fluorescence equipment to obtain such fluorescence lifetimes.

The TIRIF adsorption isotherms for the two lysozymes presented in fig. 3 seem to imply that the human protein has a higher affinity for all three surfaces examined than the hen protein does. Until quantum yield determinations are made, nothing quantitative can be said about these differences in isotherms. However, these TIRIF isotherm differences do suggest an interesting point. Namely, if further research shows that there isn't a significant difference between the two lysozymes with respect to the amounts adsorbed, then these TIRIF isotherms clearly indicate that the adsorption process results in a greater change in Φ_a/Φ_b (Φ_a = quantum yield of adsorbed protein, Φ_b = quantum yield of protein in solution) for one of the lysozymes than for the other lysozyme.

Table III is a brief synopsis of some interesting differences between human and hen lysozymes. As can be seen in the table, the two enzymes show little antibody cross-reactivity and different amino acid compositions on their surfaces. From these results, one would expect that the two proteins would exhibit differences in their adsorption characteristics, due to their surface differences.

The fact that the human protein has one less disulfide bond and a greater susceptibility to thermal denaturation than the hen protein does, suggests that the human protein might also be more susceptible to

Table III

Differences Between Hen and Human Lysozymes

Property	Differences	Reference
Amino Acid Composition	40% of positions are different, most of which are on the surface of the protein.	51, 52
Disulfide Bonds	4 in hen; 3 in human.	51
Tryptophans	6 for hen; 5 for human.	51
Secondary Structure CD-far UV	Far UV spectra are similar, suggesting similar secondary structures.	52-55
CD-near UV	Spectra are very different, suggesting different Trp and Tyr environments.	51, 55
Fluorescence	Emission max. is 330 for human; 336 for hen. Quantum yields are different.	51, 52, 56, 57
Denaturation	Human is more susceptible to thermal denaturation.	51
Enzymatic Activity	Human is 3 times more active.	51, 52
Antibody Reactivity	Little to no antibody cross-reactivity, suggesting different surface epitopes.	58, 59
Crystal Group	Different, suggesting surface groups and inter-molecular associations are different.	53, 54
Self-Association	Hen lysozyme dimerizes and oligomerizes at pH > 5 and high protein concentrations. Little is known about the human protein.	49-51

surface denaturation. Iodide quenching studies of adsorbed lysozyme recently performed in our laboratory, have partially confirmed this prediction on the two hydrophilic surfaces (39).

The TIRIF isotherm results, suggesting that both lysozymes exhibited the overall order of affinity, $\text{DDS} > \text{silica} > \text{APS}$ was not surprising. Many studies of lysozyme adsorption have shown that it has a higher affinity to hydrophobic surfaces than to hydrophilic surfaces (44-46). Lysozyme adsorption on hydrophobic surfaces may occur at the site of the hydrophobic patch seen on the back side of both proteins. At pH 7.4, both lysozymes are positively-charged and would be expected to adsorb more strongly to the negatively-charged silica surface than to the positively-charged APS surface. This was seen to be the case for both proteins. As noted above, both lysozymes have long positive side chains extending out into the solvent while the surface negative charges are not nearly as accessible. This point further suggests a preferential adsorption onto negative surfaces. With regard to the effect of electrostatic repulsion between lysozyme and the positively-charged APS surface, it is interesting to note that both Perkins (47) and Salton (48) found that lysozyme activity was inhibited by positively charged groups in the mucopeptide of bacterial cell walls (lysozyme's biological substrate), presumably due to electrostatic repulsion since the activity was increased when the free amino groups in the mucopeptide were neutralized.

The hen lysozyme showed non-saturating adsorption behavior on both charged surfaces. This may suggest that charged surfaces promote the formation of multiple protein layers at the surface in some manner which is not yet clear. Hen lysozyme forms dimers and higher aggregates under conditions of high protein concentration (5-10 mg/ml) and pH > 5 (49-51). This kind of self-association might be going on at the surface where the adsorption process inherently concentrates the proteins.

Acknowledgments

This work was supported in part by The Center for Biopolymers at Interfaces.

References

1. Vroman, L. and Leonard, E. F., eds. (1977) *Behavior of Blood and Its Components at Interfaces*, Ann. N.Y. Acad. Sci. 283.
2. Baier, R. E., ed., (1975) *Applied Chemistry at Protein Interfaces*, Adv. Chem. Ser. 145.
3. Cooper, S. L. and Peppas, N. A. (1982) *Biomaterials*, Adv. Chem. Ser. 199.
4. Holly, F. J. and Refojo, M. F. (1976) In: *Hydrogels for Medical and Related Applications* (J. D. Andrade, ed.), ACS Sym. Series #31, p. 267.

5. Ratner, B. D. and Horbett, T. A. (1984) *Trans. Soc. Biomat.* **10**, 76.
6. Gachon, A. M., Bilbaut, T., and Dastugue, B. "Adsorption of Tear Proteins on Soft Contact Lenses", in press.
7. Castillo, E. J., Koenig, J. L., Anderson, J. M., and Lo, J. (1984) *Biomaterials* **5**, 319.
8. Castillo, E. J., Koenig, J. L., and Anderson, J. M. (1985) *Biomaterials* **6**, 338.
9. Castillo, E. J., Koenig, J. L., and Anderson, J. M. (1986) *Biomaterials* **7**, 9.
10. Castillo, E. J., Koenig, J. L., and Anderson, J. M. (1986) *Biomaterials* **7**, 89.
11. Baszkin, A., Proust, J. E., and Boissonnade, M. M. (1984) *Biomaterials* **5**, 175.
12. Proust, J. E., Baszkin, A., Perez, E., and Boissonnade, M. M. (1984) *Colloids and Surfaces* **10**, 43.
13. Chen, J., Dong, D. E., and Andrade, J. D. (1982) *J. Colloid Interface Sci.* **89**, 577.
14. Royce, F., Ratner, B., and Horbett, T. (1980) In: *Biomaterials: Interfacial Phenomenon and Applications* (S. L. Cooper and N. A. Peppas, eds.) ACS Advances in Chemistry Series **199**, p. 453.
15. Axelrod, D., Burghard, T. P., and Thompson, N. T. (1984) *Ann. Rev. Biophys. Bioeng.* **13**, 247.
16. Cheng, Y.-L., Lok, B. K., and Robertson, C. R. (1985) In: *Surface and Interfacial Aspects of Biomedical Polymers, Vol 2 Protein Adsorption* (J. D. Andrade, ed.), Plenum Press, p. 121.
17. Darst, S. A., Robertson, C. R. (1986) In: *Spectroscopy in the Biomedical Sciences* (R. M. Gendreau, ed.), CRC Press, p. 175.
18. Beissinger, R. L. and Leonard, E. F. (1980) *ASAIO J.* **3**, 160.
19. Eberhart, et. al. (1984) Abstract, *Devices Tech. Branch Contractor's Conference*, p. 43.
20. Van Wagenen, R. A., Rockhold, S., and Andrade, J. D. (1980) In: *Biomaterials: Interfacial Phenomenon and Applications* (S. L. Cooper and N. A. Peppas, eds.) ACS Advances in Chemistry Series **199**, 351.
21. Hlady, V., Reinecke, D. R., and Andrade, J. D. (1986) *J. Colloid. Interface Sci.* **111**, 555.
22. Van Wagenen, R. A., Andrade, J. D., and Hibbs, J. B. (1976) *J. of the Electrochem. Soc.* **123**, 1438.
23. Hair, M. L., and Hertl, W. J. (1970) *J. Phys. Chem.* **74**, 91.
24. Marshall, K., Ridgewell, G. L., Rochester, C. H., and Simpson, J. (1974) *Chem. Ind. (London)* **19**, 775.
25. Van Wagenen, R. A. et. al. (1981) *J. Colloid. Interface Sci.* **84**, 155.
26. Arkles, B. (1977) *CHEMTECH*, 766.
27. Waddell, T. G., Leyden, D. E., and DeBello, M. T. (1981) *J. Am. Chem. Soc.* **113**, 5303.
28. Hlady, V., Van Wagenen, R. A., and Andrade, J. D. (1985) In: *Surface and Interfacial Aspects of Biomedical Polymers, Vol 2 Protein Adsorption* (J. D. Andrade, ed.), Plenum Press, p. 81.
29. Imoto, T., Forster, L. S., Rupley, J. A., and Tanaka, F. (1971) *Proc. Nat. Acad. Sci.* **69**, 1151.
30. Teichberg, V. I., Plasse, T., Sorell, S., and Sharon, N. (1972) *Biochim. Biophys. Acta* **278**, 250.
31. Lehrer, S. S. and Fasman, G. D. (1966) *Biochem. Biophys. Res. Comm.* **23**, 133.
32. Banyard, S. H., Blake, C. C. F., and Swan, I. D. A. (1974) In: *Lysozyme* (E. F. Osseman, R. E. Canfield, and S. Beychok, eds.) Academic Press, p. 71.
33. Artymiuk, P. J., and Blake, C. C. F. (1981) *J. Mol. Biol.* **152**, 737.
34. Blake, C. C. F., Loenig, D. F., Mair, G. A., North, A. C. T., Phillips, D. C., and Sarma, V. R. (1965) *Nature* **206**, 757.
35. Blake, C. C. F., Johnson, L. N., Mair, G. A., North, A. C. T., Phillips, D. C., and Sarma, V. R. (1967) *Proc. Roy. Soc.* **B167**, 318.

36. Blake, C. C. F., Mair, G. A., North, A. C. T., Phillips, D. C., and Sarma, V. R. (1967) *Proc. Roy. Soc.* **B167**, 365.
37. Feldmann, R. J. and Bing, D. H. *Teaching Aids for Macromolecular Structure*, Taylor-Merchall Corp., New York.
38. Eisenberg, D. and McLachlan, A. D. (1986) *Nature* **319**, 199.
39. Horsley, D. G. M. Sc. thesis, Univ. of Utah (In preparation).
40. Koshland, M. E., Englberger, F. M., Erwin, M. J., and Gaddone, S. M. (1963) *J. Biol. Chem.* **238**, 1343.
41. Greenwood, F. C. (1971) In: *Principle of Competitive Protein Binding Assay* (W. D. Odell and W. H. Daughady, eds.), Lippincott, Philadelphia, p. 288.
42. Van der Scheer, A., Feijen, J., Elhorst, J. K., Krugers-Dagneaux, P. G. L. C., and Smolders, C. A. (1978) *J. Colloid Interface Sci.* **66**, 136.
43. Crandall, R. E., Janatova, J., and Andrade, J. D. (1981) *Prep. Biochem.* **11**, 111.
44. Hansen, J. (1985) M. S. Thesis, University of Utah.
45. Chen, J., Dong, D. E., and Andrade, J. D. (1982) *J. Colloid Interface Sci.* **89**, 577.
46. Halperin, G., Breitenbach, M., Tauber-Finkelstein, and Shaltiel, S. (1981) *J. Chromatogr.* **215**, 211.
47. Perkins, H. R. (1967) *Royal Soc. of Lond. Proc.* **167**, 443.
48. Salton, M. R. J. (1964) *Med. Hyg.* **22**, 985.
49. Bruzzesi, M. R., Chiancone, E., and Antonini, E. (1965) *Biochemistry* **4**, 1796.
50. Deonier, R. C. and Williams, J. W. (1970) *Biochemistry* **9**, 4260.
51. Imoto, T., Johnson, L. N., North, A. C. T., Phillips, D. C., and Rupley, J. A. (1972) In: *The Enzymes*, Vol. 7, 3rd ed. (P. D. Boyer, ed.), Academic Press, p. 665.
52. Mulvey, R. S., Gaultieri, R. J., and Beychok, S. (1974) In: *Lysozyme* (E. F. Osseman, R. E. Canfield, and S. Beychok, eds.) Academic Press, p. 281.
53. Banyard, S. H., Blake, C. C. F., and Swan, I. D. A. (1974) In: *Lysozyme* (E. F. Osseman, R. E. Canfield, and S. Beychok, eds.) Academic Press, p. 71.
54. Artymiuk, P. J., and Blake, C. C. F. (1981) *J. Mol. Biol.* **152**, 737.
55. Halper, J. P., Latovitzki, N., Bernstein, H., and Beychok, S. (1971) *Proc. Natl. Acad. Sci. USA* **68**, 517.
56. Mulvey, R. S., Gaultieri, R. J., and Beychok, S. (1973) *Biochemistry* **12**, 2683.
57. Teichberg, V. I., Plasse, T., Sorell, S., and Sharon, N. (1972) *Biochim. Biophys. Acta* **278**, 250.
58. Atassi, M. Z., and Habeeb, A. F. S. A. (1979) In: *Immunochemistry of Proteins*, Vol. 2 (M. Z. Atassi, ed.), Plenum, p. 177.
59. Arnon, R. (1977) In: *Immunochemistry of Enzymes and Their Antibodies* (M. Salton, ed.), Wiley, p. 1.

RECEIVED March 4, 1987

Reprinted from ACS SYMPOSIUM SERIES No. 343
Proteins at Interfaces: Physicochemical and Biochemical Studies
 John L. Brash and Thomas A. Horbett, Editors
 Copyright © 1987 by the American Chemical Society
 Reprinted by permission of the copyright owner

Fluorescence Quenching of Adsorbed Hen and Human Lysozymes

D. Horsley, J. Herron, V. Hlady,[†] and J. D. Andrade*

Center for Biopolymers at Interfaces, Department of Bioengineering, University of Utah,
Salt Lake City, Utah 84112

Received December 5, 1989. In Final Form: July 2, 1990

The iodide quenching of protein fluorescence was used to study the effect of surface adsorption on the conformation of human and hen lysozymes. Three different types of surfaces were used for protein adsorption: (a) hydrophobized, uncharged DDS-silica; (b) unmodified, negatively charged silica; (c) positively charged APS-silica. The evanescent surface wave generated by total internal reflection was used to excite intrinsic fluorescence from the tryptophanyl residues of irreversibly adsorbed lysozymes. The extent of quenching of the adsorbed lysozyme fluorescence was shown to be a function of both the species of lysozyme studied (human vs hen) and the type of surface to which the protein was adsorbed. A modified Stern-Volmer quenching model, which assumes accessible and inaccessible populations of protein fluorophores, was applied to analyze the experimental results. The change in the fractional accessibility of fluorophores due to the adsorption was taken as a measure of protein conformational change. Both lysozymes appeared to exhibit smaller denaturation at the DDS-silica surface than on the other two surfaces. According to the quenching results both lysozymes were at least partially denatured upon adsorption to the unmodified, negatively charged silica surface as well as on the positively charged APS-silica surface. Human lysozyme displayed much larger changes in the denaturation parameters upon adsorption to the three surfaces than the hen lysozyme, indicating that it is less conformationally stable at interfaces. It was found that the effective quenching constant of iodide anion depended largely on the charge of the surface.

Introduction

The understanding and control of the interactions of proteins with solid surfaces are important in a number of areas of biology and medicine. In the last 20 years, there has been considerable interest in protein interactions with materials used in medical implant devices.¹⁻³ One area of particular interest to the contact lens industry is the interaction of tear proteins with contact lenses.⁴⁻⁸ Deposition of proteins on contact lens surfaces cause a loss of visual acuity (due to the opaque nature of the adsorbed protein film), wearer discomfort, and, in some cases, acute eye diseases.^{9,10} Lysozyme is a major protein constituent in tear fluids and has been shown to also be a major

component in soft contact lens deposits.¹¹⁻¹³ Consequently, the use of lysozyme in protein adsorption studies has great practical value. Furthermore, since lysozyme is a rather simple, well-understood protein,^{14,15} it can easily serve as a model for understanding the general principles that seem to govern protein adsorption.

Experimental methods used to study the structural changes that occur in proteins as they undergo adsorption at interfaces are currently very limited. Total internal reflection intrinsic fluorescence (TIRIF) spectroscopy combines well-known advantages of fluorescence spectroscopy with the surface sensitivity of internal reflection optics and it has been used in different aspects of protein adsorption.¹⁶⁻¹⁹ One of the fluorescence techniques that is often used to probe protein conformational changes in solution is the technique of fluorescence quenching.²⁰⁻²⁴ Presently, very little is done with this technique to probe

* To whom correspondence should be addressed.

[†] On the leave of absence from "Ruđer Bošković" Institute, Zagreb, Yugoslavia.

- (1) Vroman, L.; Leonard, E. F., Eds. *Ann. N.Y. Acad. Sci.* **1977**, 283.
- (2) Baier, R. E., Ed. *Applied Chemistry at Protein Interfaces. Adv. Chem. Ser.* **1975**, No. 145.
- (3) Cooper, S. L.; Peppas, N. A., Eds. *Biomaterials: Interfacial Phenomena and Applications. Adv. Chem. Ser.* **1982**, No. 199.
- (4) Karageozian, H. L. *Chemical Identity of Opaque Deposits on Human Worn Hydrophilic Lenses*; Report Series 92; Allergan Pharmaceuticals: Irvine, CA, 1974.
- (5) Wedler, F. C. *J. Biomed. Mater. Res.* **1977**, 11, 525.
- (6) Wedler, F. C.; Riedhammer, T. M. In *CRC Critical Reviews, Biocompatibility*; Williams, D. F., Ed.; CRC Press: Cleveland, OH, 1979.
- (7) Hosaka, S.; Ozawa, H.; Tanzawa, H.; Ishida, H.; Yoshimura, K.; Momose, T.; Nakajima, A. *J. Biomed. Mater. Res.* **1983**, 17, 261.
- (8) Tripathi, R.; Montague, R.; Tripathi, B. J. In *Soft Contact Lenses; Clinical and Applied Technology*; Ruben, M., Ed.; J. Wiley and Sons: New York, 1978; p 299.
- (9) Allansmith, M. R.; Korb, D. R.; Greiner, J. V.; Henriquez, A. S.; Simon, M. A.; Finnemore, V. M. *Am. J. Ophthalmol.* **1977**, 83, 697.
- (10) Dohlman, C. H.; Boruchoff, S. A.; Mobilia, E. F. *Arch. Ophthalmol.* **1973**, 90, 367.

- (11) Bilbaut, T.; Gachon, A. M.; Dastugue, B. *Exp. Eye Res.* **1986**, 43, 153.
- (12) Gachon, A. M.; Bilbaut, T.; Dastugue, B. *Exp. Eye Res.* **1985**, 43, 105.
- (13) Royce, F. H., Jr.; Ratner, B. D.; Horbett, T. A. *Adv. Chem. Ser.* **1982**, No. 199, 453.
- (14) Imoto, T.; Johnson, L. N.; North, A. C. T.; Phillips, D. C.; Rupley, J. A. In *The Enzymes*; Boyer, P. D., Ed.; Academic Press: New York, 1972; Vol 15, p 665.
- (15) Osserman, E. F.; Canfield, R. E.; Beychok, S., Eds. *Lysozyme*; Academic Press: New York, 1974.
- (16) Hlady, V.; Reinecke, D. R.; Andrade, J. D. *J. Colloid Interface Sci.* **1986**, 111, 555.
- (17) Hlady, V.; Andrade, J. D. *Colloids Surf.* **1987**, 32, 359.
- (18) Hlady, V.; Rickel, J.; Andrade, J. D. *Colloids Surf.* **1989**, 34, 171.
- (19) Hlady, V.; Andrade, J. D. *Colloids Surf.* **1989**, 42, 85.
- (20) Lehrer, S. S.; Leavis, P. C. *Methods Enzymol.* **1978**, 49, 222.
- (21) Eftink, M. R.; Ghiron, C. A. *Anal. Biochem.* **1981**, 114, 199.
- (22) Lehrer, S. S. *Biochemistry* **1971**, 10, 3254.
- (23) Eftink, M. R.; Zajicek, J. L.; Ghiron, C. A. *Biochim. Biophys. Acta* **1977**, 491, 473.

the conformation or orientation of adsorbed proteins. In this study we have extended TIRIF to study iodide quenching of hen egg-white lysozyme and human milk lysozyme, which were irreversibly adsorbed to a set of model silica surfaces. These results are compared with those obtained for the two lysozymes in buffer solution. We then propose a simple model to explain our findings.

Materials and Methods

TIRIF Apparatus. The total internal reflection intrinsic fluorescence (TIRIF) apparatus used in these experiments was identical with that used by Hlady et al.¹⁶ except that the γ -photon detection system was not used. Bulk solution fluorescence was measured by placing a rectangular fluorescence cuvette in place of the TIRIF cell, thus maintaining the same geometry between the excitation and the emission light path (70° angle).

Preparation of Adsorption Surfaces. The silica surface was prepared by cleaning amorphous hydrophilic silica microscope slides (ESCO Products) in hot (80 °C) chromic acid for 30 min, cooling to room temperature, and then rinsing thoroughly in ultrapure water (Milli-Q reagent water system). The slides were then desiccated for 12 h at 100 °C. Cleanliness was confirmed by the absence of hysteresis in the Wilhelmy plate water contact angle measurement.

The 3-(aminopropyl)triethoxysilane (APS) surfaces were prepared by dip-casting clean silica slides in a solution of 5% (v/v) APS (Petrarch Systems) in ethanol-water (95:5) mixture and allowing silanization to proceed for 30 min at room temperature. After the silanization the slides were rinsed several times in purified water, followed by rinsing in 100% ethanol. The slides were then desiccated under vacuum for 12 h at 60 °C.

Dimethyldichlorosilane (DDS) surfaces were prepared via a protocol similar to that for APS surface preparation except that the reaction mixture was 10% (v/v) DDS (Petrarch Systems) in dry toluene and slides were rinsed in ethanol before rinsing with water in order to remove the residual toluene first. All of the prepared surfaces were kept covered and used within 4 days of preparation.

Buffers and Lysozyme Solutions. The buffer used for the adsorption experiments was a phosphate buffer (PBS, pH 7.4, $[\text{KH}_2\text{PO}_4] = 0.013 \text{ M}$, $[\text{Na}_2\text{HPO}_4] = 0.054 \text{ M}$, $[\text{NaCl}] = 0.1 \text{ M}$) made from analytical grade reagents and low-conductivity water. Both the hen egg-white lysozyme (3× crystalline) and the human milk lysozyme (purified via ion exchange chromatography, salt free powder) were obtained from Calbiochem and used without further purification. The protein solution was made by dissolving 10.0 mg of lysozyme in 10.0 mL of the PBS buffer. The final protein concentration was checked spectrophotometrically by using the absorptivity, $a = 2.56$ and $2.69 \text{ L g}^{-1} \text{ cm}^{-1}$ at 280 nm for the human and hen lysozymes respectively.^{27,28}

The buffer used for the fluorescence quenching experiments was identical with the PBS buffer above except that instead of $[\text{NaCl}] = 0.1 \text{ M}$, the sum $[\text{NaCl}] + [\text{KI}] = 0.5 \text{ M}$. The six quencher solutions had iodide concentrations of 0.0, 0.1, 0.2, 0.3, 0.4, and 0.5 M, respectively.

All buffers were prepared fresh, prior to each experiment.

Lysozyme Adsorption Experiments. Ten milliliters of the 1 mg/mL protein solution was injected into the TIRIF cell and allowed to adsorb to a particular surface for 1 h. The 280-nm evanescent surface wave created by total internal reflection at the silica/buffer interface was used to excite intrinsic fluorescence of lysozyme (measured at 335 nm) by which the kinetics of adsorption were followed (D. Horsley et al., in preparation). The excitation and the emission half-bandwidth was set to 16 nm. After 1 h the cell was flushed repeatedly with 20 mL of the 0.5 M NaCl buffer solution until further flushing did not result in a further decrease in fluorescence. This ensured the removal of

all of the nonadsorbed and weakly adsorbed protein and provided a baseline fluorescence signal for irreversibly adsorbed lysozyme.

Iodide Quenching Experiments. Since the quenching of fluorescence of protein tryptophanyl residues was the subject of these experiments, tryptophanyl fluorescence emission was generated by exciting at 295 nm rather than at 280 nm and by collecting the emission at 335 nm. Following the buffer flushes with the 0.5 M NaCl buffer solution, the sequence of quenching solutions of increasing iodide quencher concentrations was injected into the TIRIF cell and the fluorescence intensity was recorded. After the quenching solution with the highest iodide concentration was injected and the fluorescence signal recorded, 20 mL of the 0.5 M NaCl buffer solution was injected to determine if the fluorescence returned to the baseline value (indicating the absence of additional desorption). In all instances, the fluorescence signal recovered almost fully (>90%); the tryptophanyl fluorescence at each iodide concentration was corrected for this decrease, assuming that an equal fraction of the signal was lost due to desorption at each injection of quencher solution. The iodine quenching experiments using lysozyme dissolved in buffer solutions were performed as a reference by standard techniques.^{24,25}

Experimental quenching data were analyzed by using the Stern-Volmer equation²¹

$$F_0/F = 1 + K_Q[Q] \quad (1)$$

where F_0 and F are the fluorescence intensities in the absence and presence of quencher, respectively, and K_Q is the Stern-Volmer quenching constant.

A modified form of the Stern-Volmer equation originally proposed by Lehrer was also used to analyze the experimental data²²

$$F_0/\Delta F = 1/(f_a K_{Qa}[Q]) + 1/f_a \quad (2)$$

where ΔF is defined as $\Delta F = F_0 - F$, f_a is the fractional accessibility of tryptophanyl residues in lysozyme, and K_{Qa} is an effective quenching constant. Three independent measurements had been made for each iodide concentration. When the modified Stern-Volmer equation (eq 2) was used, a weighted least-squares linear regression method was applied to calculate the slope and the intercept of the $F_0/\Delta F$ vs $1/[Q]$ plot.²⁹ This analysis takes into account the fact that each mean observation has its own parent distribution and is weighted inversely as the variance of its parent distribution. The complete analysis can be also found in ref 30, Appendix B. From the slope and the intercept one can determine f_a and K_{Qa} .

Results and Discussion

All of the quenching systems studied exhibited downward curving Stern-Volmer plots when the quenching results were plotted according to eq 1 (F_0/F vs $[Q]$, data not shown here).³⁰ Accordingly, the experimental results were analyzed by using the modified Stern-Volmer equation (eq 2) by plotting $F_0/\Delta F$ vs $1/[Q]$. Figures 1 and 2 show the result of iodide quenching experiments for hen egg-white and human milk lysozymes dissolved in buffer solution, respectively. Figures 4 through 8 show the modified Stern-Volmer plots for the irreversibly adsorbed layers of two lysozymes at different surfaces. Each datum is the mean value of three independent measurements while error bars represent one standard deviation. The straight lines were determined by the best fit using the weighted least-squares linear regression analysis.²⁹ Table I lists the parameters f_a and K_{Qa} which were determined from the best fit.

Comparison between the solution quenching of hen and human lysozyme (Figures 1 and 2) indicated different fractional accessibility of the tryptophanyl residues in these two proteins: $f_{a(\text{hen})} = 0.37$ vs $f_{a(\text{human})} = 0.18$, respectively.

(29) Bevington, P. R. *Data Reduction and Error Analysis for the Physical Sciences*; McGraw-Hill: New York, 1969.

(30) Horsley, D., M.S. Thesis, University of Utah, Salt Lake City, Utah, 1988.

(24) Lakowicz, J. R.; Weber, G. *Biochemistry* 1973, 12, 4161.

(25) Pesce, A. J.; Rosen, C. G.; Pasby, T. L. *Fluorescence Spectroscopy*; Marcel Dekker: New York, 1971.

(26) Lakowicz, J. R. *Principles of Fluorescence Spectroscopy*; Plenum Press: New York, 1983.

(27) Parry, R., Jr.; Chandan, R.; Shahani, K. *Arch. Biochem. Biophys.* 1969, 130, 59.

(28) Imai, K.; Takagi, T.; Isemura, T. *J. Biochem.* 1963, 53, 1.

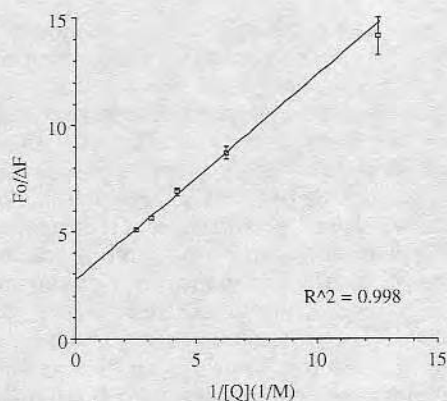


Figure 1. Modified Stern-Volmer plot for the hen egg-white lysozyme in buffer solution. The value of the correlation coefficient, R^2 , is indicated. For explanation of other symbols see text.

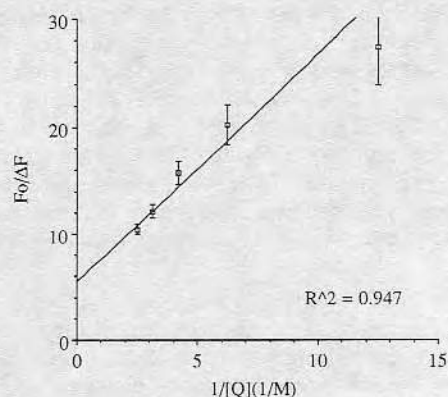


Figure 2. Modified Stern-Volmer plot for the human milk lysozyme in buffer solution. The value of the correlation coefficient, R^2 , is indicated. For explanation of other symbols see text.

Table I. Stern-Volmer Quenching Parameters for Human and Hen Lysozymes

solution/surface and protein combination	f_a^a	K_{Qa} (M^{-1})
buffer solution		
hen lysozyme	0.37 ± 0.02	2.8 ± 0.3
human lysozyme	0.18 ± 0.03	2.6 ± 0.6
DDS-silica surface		
hen lysozyme	0.34 ± 0.04	3.3 ± 0.7
human lysozyme	0.20 ± 0.04	4.2 ± 1.6
unmodified silica surface		
hen lysozyme	0.56 ± 0.10	1.7 ± 0.4
human lysozyme	0.53 ± 0.23	0.9 ± 0.4
APS-silica surface		
hen lysozyme	0.36 ± 0.03	5.7 ± 1.1
human lysozyme	0.68 ± 0.10	5.0 ± 1.6

^a ± 1 standard deviation.

The effective quenching constants were roughly the same ($K_{Qa(\text{hen})} \approx K_{Qa(\text{human})} \approx 2.7 M^{-1}$) (Table I). One should note that hen lysozyme has six tryptophanyl residues, as compared with five residues in human lysozyme, a fact that can account for different accessibility of these fluorophores. The location of tryptophanyl residues in both lysozymes can be visualized by using the protein atomic coordinates and molecular graphics, as described earlier.^{31,32} It is known, however, that most of the lysozyme fluorescence comes from tryptophanyl residues located on the

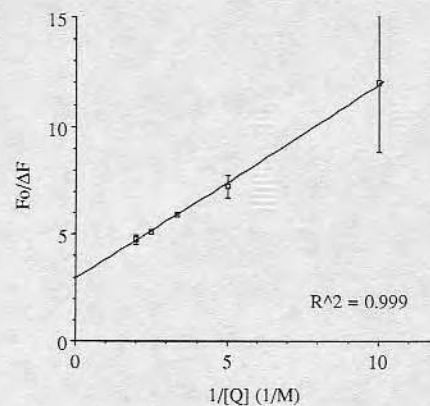


Figure 3. Modified Stern-Volmer plot for the hen egg-white lysozyme adsorbed to the DDS-silica surface. The value of the correlation coefficient, R^2 , is indicated. For explanation of other symbols see text.

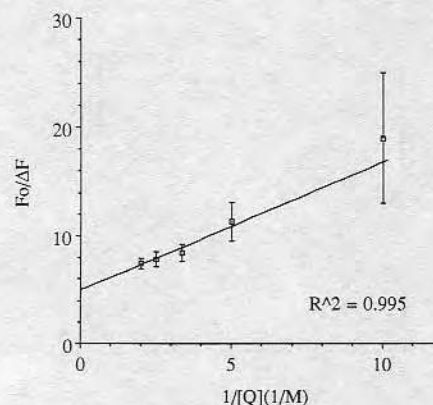


Figure 4. Modified Stern-Volmer plot for the human milk lysozyme adsorbed to the DDS-silica surface. The value of the correlation coefficient, R^2 , is indicated. For explanation of other symbols see text.

surface of the active site cleft.³³⁻³⁵ For example, it has been estimated that as much as 38% of the fluorescence of hen lysozyme is emitted from the active site tryptophanyl residue alone (Trp 62).³⁵ It is likely, therefore, that the solution fluorescence from these tryptophanyl residues will be principally affected by the presence of quencher.

When adsorbed onto the hydrophobicized, uncharged silica surface (DDS-silica surface) both lysozymes showed almost no change in the fractional accessibility of tryptophanyl residues, while the effective quenching constants increased to a different extent (Figures 3 and 4, and Table I), as compared with the reference state (i.e. lysozyme in the buffer solution). In contrast, adsorption onto the unmodified, negatively charged silica surface caused an increase of f_a for both lysozymes to approximately $f_a \approx 0.5$ and a decrease of K_{Qa} (Figures 5 and 6, Table I).

The change in the fractional accessibility can be tentatively interpreted as an extent of the conformational alteration of protein after adsorption at the particular surface. According to this simple model one can conclude that the lysozyme adsorption onto the hydrophobicized, uncharged silica surface (DDS-silica surface) does not cause a significant conformational change in both hen and human protein since there was no change of f_a (Table I). On the

(33) Mulvey, R.; Gaultieri, R.; Beychok, R. *Biochemistry* **1973**, *12*, 2683.

(34) Teichberg, V.; Plasse, T.; Sorell, S.; Sharon, N. *Biochim. Biophys. Acta* **1972**, *278*, 250.

(35) Imoto, T.; Forster, L.; Rupley, J.; Tanaka, F. *Proc. Natl. Acad. Sci. U.S.A.* **1971**, *69*, 1151.

(31) Hansen, J., M.S. Thesis, University of Utah, Salt Lake City, Utah, 1985.

(32) Horsley, D.; Herron, J.; Hlady, V.; Andrade, J. D. *ACS Symp. Ser.* **1987**, No. 343, 290.

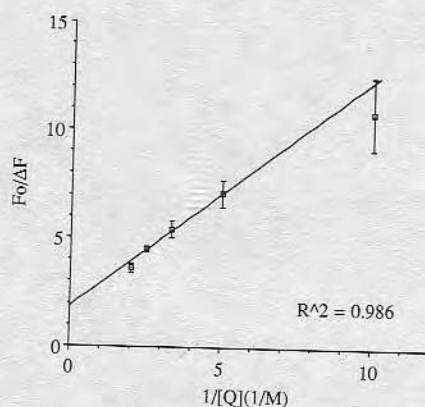


Figure 5. Modified Stern-Volmer plot for the hen egg-white lysozyme adsorbed to the unmodified silica surface. The value of the correlation coefficient, R^2 , is indicated. For explanation of other symbols see text.

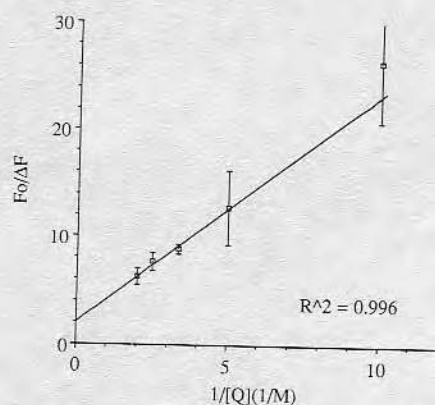


Figure 6. Modified Stern-Volmer plot for the human milk lysozyme adsorbed to the unmodified silica surface. The value of the correlation coefficient, R^2 , is indicated. For explanation of other symbols see text.

contrary, the adsorption onto the unmodified, negatively charged silica surface brings a change of f_a for both lysozymes, indicating that the silica surface does induce conformational changes in both proteins. The difference in the hen lysozyme conformation at the DDS-silica surface and at the unmodified silica surface was supported by variable angle ESCA studies, which showed that the thickness of the adsorbed lysozyme layer was less on the silica surface than on the DDS surface.^{31,36} Namely, a denatured protein is expected to spread out on the surface and thereby decrease its adsorbed layer thickness. The interaction of the positively charged amino acid residues (Lys, Arg), which are present on the surface of the lysozymes,³² with the negative groups on the silica surface may be responsible for "spreading" the lysozyme molecule out on the surface. A similar ESCA study and comparison were not available for human lysozyme. The fractional accessibility of silica-adsorbed human lysozyme changes more than the fractional accessibility of hen lysozyme at the same surface; for example, f_a changes from 0.18 to 0.53 for human vs from 0.37 to 0.56 for hen lysozyme, respectively (Table I). A larger fraction of the human lysozyme tryptophanyl residues which become accessible after adsorption indicated that more extensive conformational changes were taking place in the silica-adsorbed human lysozyme as compared to the hen lysozyme molecule.

It is also interesting to compare how the effective quenching constant changes for the two lysozymes at these

two surfaces. The K_{Qa} parameter reflects how easily iodide ion can find its way to the accessible tryptophanyl population. In an analogy to the association binding constant, the large K_{Qa} values indicate that iodide ion "associates" on average more readily with the tryptophanyl excited state. The penetration of iodide ion into an optimal quenching position is largely affected by the electrostatic repulsive forces, because of the charged nature of this quencher. It is known that a negative charge on the protein will be effective in preventing iodide ion from accessing neighboring tryptophanyl residue(s).²⁶ By taking the buffer solution as a reference state, one notes from Table I that the absolute value of the effective quenching constant change was always larger for human lysozyme than for hen lysozyme (i.e., $|\Delta K_{Qa(\text{human})}| > |\Delta K_{Qa(\text{hen})}|$). In the case of lysozyme adsorption onto hydrophobized, uncharged DDS-silica, the value of K_{Qa} increases approximately 18% for hen and more than 3 times as much (approximately 62%) for human lysozyme, respectively. Although the total fractional accessibility and the total electric charge (protein + surface) in the case of both proteins remained unchanged, it is the human protein that was more affected by the adsorption onto the DDS-silica surface than the hen protein. The larger increase of $K_{Qa(\text{human})}$ indicates that the same accessible fraction of fluorophores in the two lysozymes was more easily quenched in the case of the human protein because of the adsorption.

In the case of lysozyme adsorption onto unmodified, negatively charged silica surfaces, the interpretation of the effective quenching constant change becomes complicated by the presence of negative charges on the silica surface and by the unknown compensation of these negative charges by the positive charges of lysozymes. An overall decrease of the K_{Qa} values was presumably the result of the presence of negative surface charges, which were repelling iodide anions, rather than the result of some specific conformational change of adsorbed lysozymes. Human lysozyme at silica surfaces showed a larger change in the fractional accessibility of its tryptophanyl residues as well as a larger decrease of K_{Qa} (by approximately 65%) from the respective buffer solution values as compared with hen lysozyme. It is also known that human lysozyme is more susceptible to thermal denaturation than hen lysozyme.³⁰

It is interesting to see how the experimental results of lysozyme quenching at the modified, positively charged silica surface (APS-silica surface) fit in this simplified model, in which the adsorption-induced conformational alterations are to be inferred from the fluorescence quenching. Namely, the positively charged surface of APS-silica should, in principle, increase K_{Qa} values for both lysozymes (due to the fact that electrostatic attraction forces make more iodide ions available for quenching at the surface) while the difference between the conformational stability of the two proteins should be reflected as a change of the parameter f_a . The experimental evidence for overall larger stability of hen lysozyme can be found in Figures 7 and 8 and in Table I; the K_{Qa} values of both lysozymes approximately doubled and, while $f_a(\text{hen})$ remains unchanged, the $f_a(\text{human})$ increased from $f_a(\text{human}) = 0.18$ (buffer solution) to the largest fractional accessibility found in this study, $f_a(\text{human}) = 0.68$ (APS-silica surface). This is a clear indication that human lysozyme is also conformationally more unstable when adsorbed onto positively charged surfaces than the hen lysozyme.

The technique of fluorescence quenching is relatively simple to execute in the study of irreversibly adsorbed

(36) Hansen, J.; Ely, K.; Horsley, D.; Herron, J.; Hlady, V.; Andrade, J. D. *Makromol. Chem., Macromol. Symp.* 1988, 17, 135.

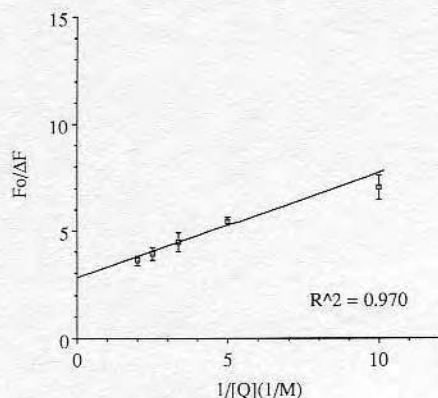


Figure 7. Modified Stern-Volmer plot for the hen egg-white lysozyme adsorbed to the APS-silica surface. The value of the correlation coefficient, R^2 , is indicated. For explanation of other symbols see text.

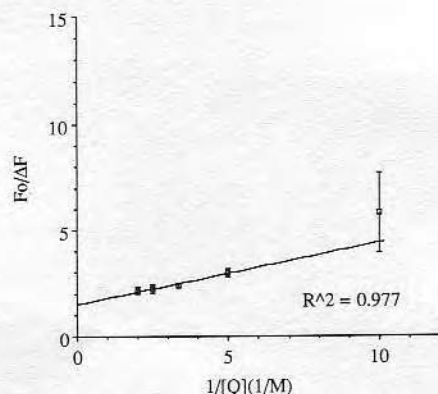


Figure 8. Modified Stern-Volmer plot for the human milk lysozyme adsorbed to the APS-silica surface. The value of the correlation coefficient, R^2 , is indicated. For explanation of other symbols see text.

protein layers. However, as discussed in ref 21 protein fluorescence quenching data are easily overanalyzed. The use of modified Stern-Volmer plots is straightforward only in the case in which a protein contains one fluorophore population accessible to quencher and one totally inaccessible, as proposed by Lehrer in his derivation of eq 2.²² The presence of the surface presents an additional level of complexity: it can specifically interact with a quencher. It is also hypothetically possible to have a grossly denatured protein which is adsorbed at the surface in such an orientation that all of the fluorophores are exposed toward the surface and effectively shielded from the quencher. The proposed simple model for the analysis of conformational alterations of adsorbed protein from the fluorescence quenching data should be, therefore, taken as a first approximation in the conformational analysis, which

should be supplemented by different quenchers and different methods of fluorescence spectroscopy. For example, the conformational change of hen egg-white lysozyme adsorbed onto the chromatographic hydrophobic silica gel had been inferred from the 8-nm red shifts of the lysozyme fluorescence emission maxima.³⁷ We have recently used a combination of total internal reflection fluorescence and phase-resolved fluorescence spectroscopy in the study of surface-induced quenching of rhodamine-labeled bovine serum albumin at silica-solution interface.³⁸ It is our long range goal to apply the same technique to adsorbed proteins by using their intrinsic fluorescence.

Conclusions

Total internal reflection intrinsic fluorescence (TIRIF) spectroscopy was used to study the effect of surfaces on the conformation of irreversibly adsorbed human and hen lysozyme by using the iodide fluorescence quenching technique. Three different surfaces were used: (a) hydrophobicized, uncharged DDS-silica; (b) unmodified, negatively charged silica; (c) positively charged APS-silica. The quenching of the adsorbed lysozyme fluorescence was shown to be a function of both the species of lysozyme studied (human vs hen) and the type of surface to which the protein was adsorbed. A modified Stern-Volmer quenching model, which assumes accessible and inaccessible populations of protein fluorophores, was applied to analyze the experimental results. The change in the fractional accessibility of fluorophores due to the adsorption was taken, in a first approximation, to represent a measure of protein conformational change. We conclude that both lysozymes appeared to experience smaller denaturation at the DDS-silica surface than on the other two surfaces. According to the present results both lysozymes were at least partially denatured upon adsorption to the unmodified, negatively charged silica surface as well as on the positively charged APS-silica surface. Human lysozyme displayed much larger changes in the denaturation parameters upon adsorption of the three surfaces than those for hen lysozyme, indicating that it is less conformationally stable at different types of interfaces.

Acknowledgment. The authors thank the Center for Biopolymers at Interfaces, University of Utah, for providing financial support for this research. V.H. gratefully acknowledges a leave of absence from "Ruder Bošković" Institute, Zagreb, Yugoslavia.

Registry No. APS, 919-30-2; DDS, 75-78-5; silica, 7631-86-9; lysozyme, 9001-63-2.

(37) Lu, X.-M.; Figueora, A.; Karger, B. L. *J. Am. Chem. Soc.* **1988**, *110*, 1978.

(38) Suci, P.; Hlady, V. *Colloids Surf.*, in press.

Minimizing interferences in the quantitative multielement analysis of trace elements in biological fluids by inductively coupled plasma mass spectrometry

CHIUNG-SHENG HSIUNG,¹ JOSEPH D. ANDRADE,¹ ROBERT COSTA,² and K. OWEN ASH^{2*}

The determination of trace and ultratrace elements in biological fluids, including urine and serum, by inductively coupled plasma mass spectrometry (ICP-MS) is discussed. Nonspectral interferences and their corrections by external calibration and calibrator addition are discussed in detail. External calibration with internal calibration and dilution is mostly sufficient to correct for encountered biological matrix effects. For some elements, such as Cs and Zn, the use of calibrator addition provides more accurate results. The importance of spectral interferences and their elimination by isotope selection was also studied. Two examples, Cu and Zn, demonstrate the prime importance of selecting an isotope with minimal polyatomic interferences for analysis. By using ⁶⁵Cu and ⁶⁸Zn, accurate results for urine and serum can be obtained without excessive pretreatment of samples. Two reference materials, Bio-Rad Lyphochek urine and Kaulson Contox sera, were analyzed. Accuracy was evaluated by comparison with target values, and precision was estimated by the CV within 95% confidence.

Of the body mass of humans, 98% is made up of nine nonmetallic elements. Trace elements occupy just 0.012% of the body weight of humans [1]. However, the determination of trace elements is increasingly crucial since they play important roles in both normal biological function and toxicity [2-9]. Several of these elements are indispensable and essential for life; others and their compounds are simply inert or innocuous at usual exposure concentra-

tions, and others exhibit a high toxicity even in low concentrations. Even essential elements present in too high concentrations may lead to deleterious effects. The reliable monitoring of trace elements has become an important function of many clinical, industrial, and governmental laboratories. Different specimens can be used to best reflect body status. Tissue may be the best specimen but is not easily obtained, and adequate reference information is not available to aid with interpretation of the results. The use of hair is controversial since external contamination is an ever-present problem. Analysis of the relevant elements in biological fluids, either serum/plasma, whole blood, or urine specimen, provides useful information on disturbances of metabolism that involve metals [10-15].

Analysis of trace elements in biological fluids demands a versatile and reliable technique. The analytical method used must be sensitive, precise, accurate, and relatively fast. Since the first inductively coupled plasma mass spectrometry (ICP-MS) instrumentation was introduced in 1980 [16], this hybrid technique has become an important method for the analysis of trace elements in biological fluids.³ ICP-MS is capable of direct analysis of solution samples with coverage of most elements in the periodic table [17]. Moreover, compared with inductively coupled plasma atomic emission spectrometry (ICP-AES), ICP-MS provides much lower detection limits, simpler spectral interpretation, and reliable isotopic analysis [18]. Yet, several factors are still of concern in the analysis of trace elements in biological matrices with ICP-MS. Most biological fluids contain large amounts of organic compounds and inorganic salts, which can lead to spectral and nonspectral interferences. Spectral interference occurs because typical ICP-MS instruments use quadrupoles as

¹ Department of Materials Science & Engineering, University of Utah, Salt Lake City, UT 84112.

² Department of Pathology and Associated Regional and University Pathologists, 500 Chipeta Way, Salt Lake City, UT 84108.

*Author for correspondence. Fax 801-583-2712; e-mail ASHKO@ARUP-lab.com.

Received February 19, 1997; revision accepted August 22, 1997.

³ Nonstandard abbreviations: ICP-MS, inductively coupled plasma mass spectrometry; PP, polypropylene; and AAS, atomic absorption spectrometry.

mass analyzers, which limits the resolution to approximately unit mass. Signals between the analyte and any interferent with a mass larger than the resolution thus cannot be distinguished. Analysis for some elements of biological interest, such as first-row transition metals, as well as As and Se, are thus compromised. Nonspectral interference is a change of signal intensity that cannot be accounted for by recognizable spectral interferences. The interference can be due to either enhancement or suppression. The concentration of the analyte is thus over- or underdetected.

Nonspectral and spectral interferences can seriously affect the analytical performance of ICP-MS. To obtain accurate results for biological fluids, the influences from both interferences must be investigated and eliminated. External calibration and calibrator addition coupled with internal calibration were used to correct for nonspectral interferences. External calibration is based on a set of external calibrators containing elements of interest and internal calibrators in a simple acid. Success in correction of nonspectral interferences depends on the effectiveness of internal calibration. Selection of internal calibrators can be crucial for the accuracy and precision of trace element analysis in biological fluids [19]. Calibrator addition is performed by adding increasing quantities of the elements of interest to multiple aliquots of the sample to be analyzed. The calibration set has an identical sample matrix and hence corrects for nonspectral interferences. Internal calibration is preferably combined with calibrator additions to correct for instrumental drift. To eliminate spectral interferences, a careful selection of the analyte isotope is of prime importance. By correctly selecting an isotope with minimal interferences, accurate results can be obtained with no tedious sample pretreatment. Examples of isotope selection for analysis of Cu and Zn are discussed. The feasibility of ICP-MS for direct, quantitative analysis of trace and ultratrace elements in biological fluids is demonstrated by analyzing two reference materials, Bio-Rad Lyphochek urine and Kaulson Contox sera.

Materials and Methods

REAGENTS AND CALIBRATORS

All solutions were prepared with trace-grade nitric acid obtained from Mallinckrodt Specialty Chemicals, without further purification, and with reagent-grade deionized water. Metal-free polypropylene (PP) vials and pipette tips were used throughout without precleaning. Plasma quality single-element solution calibrators at 1000 mg/L were obtained from Spex (certified by comparison with NIST SRM 3124a). Stock solutions of internal calibrators, Be and Ga at 1000 $\mu\text{g/L}$, as well as In and Ir at 500 $\mu\text{g/L}$, were prepared with 5% nitric acid. Cocktails of multielement calibrators (100 $\mu\text{g/L}$ for each element) were prepared from single-element solutions with 1% nitric acid. Sodium chloride solutions for the study of matrix effects and polyatomic interferences for Cu were prepared by dissolving ACS-grade sodium chloride powder from

Fisher Scientific in 1% nitric acid. Analytical reagent-grade sulfuric acid was obtained from Mallinckrodt Specialty Chemicals for study of polyatomic interferences of Zn.

SAMPLE PREPARATION

Serum. The preparation of serum specimens for ICP-MS usually requires a simple dilution [20–24]. However, a precipitation method with nitric acid at room temperature to precipitate protein is preferred in our laboratory; this is important to minimize the occurrence of permanent blockage of the nebulizer, the torch, and the sampling orifice resulting from high concentrations of proteins, as well as to reduce polyatomic ion interferences such as $^{13}\text{C}^{14}\text{N}$ on ^{27}Al . The specimen is treated with nitric acid to precipitate proteins and quantitatively release the trace elements, and then diluted with deionized water. The precipitate is removed by centrifugation and the supernatant is used for analysis. Deproteinization should be processed with care to prevent the coprecipitation of trace metals of interest with residues. For some elements, like Fe, precipitation of proteins in plasma or serum with nitric acid is not appropriate because of the low recovery.

Freeze-dried lyophilized serum metals reference materials obtained from Kaulson Lab. were reconstituted with 5 mL of deionized water and 1-mL aliquots placed into 10-mL PP vials with metal-free PP pipette tips. All aliquots were then frozen until used. For analysis, serum was defrosted and a 1-mL stock solution of internal calibrators in 5% nitric acid was added. Protein precipitation occurred upon the addition of internal calibrators, owing to the high nitric acid concentration. The solution was then adjusted to 5 mL with deionized water and centrifuged. The clear supernatant was transferred to another PP vial through a filter for analysis.

Urine. The specimen preparation required for urine is a simple dilution with nitric acid; then the sample is ready for analysis. The urine is the product of a set of complex processes in the kidneys that removes low-molecular-mass molecules without loss of proteins. Thus, no deproteinization is required unless protein concentration is high; in this case, the precipitate should be removed by centrifugation.

Freeze-dried lyophilized urine metals reference materials obtained from Bio-Rad were reconstituted with 25 mL of deionized water and 1-mL aliquots placed into 10-mL PP vials with metal-free PP pipette tips. All aliquots were then frozen until used. For analysis, urine was defrosted at room temperature. After the addition of 1 mL of stock solution of internal calibrators in 5% nitric acid, the solution was adjusted to 5 mL with deionized water to a final nitric acid concentration of 1%.

INSTRUMENTATION

The instrument used is a Perkin-Elmer Sciex Elan 5000a ICP-MS equipped with an AS 90 autosampler. A cross-

flow nebulizer, a standard Elan torch, and a Scott-type spray chamber were used. Platinum sampling and skimmer cones were used for all studies. Solution uptake was controlled by a peristaltic pump.

To obtain optimum signal intensity for multielement analysis at the trace and ultratrace concentrations, it is necessary to consider the optimization for the entire mass range because optimum ICP-MS instrumental parameters vary from element to element [25]. Therefore, three elements, Mg at low mass, Rh at medium mass, and Pb at high mass, at 10 $\mu\text{g/L}$ in a calibrator from Perkin-Elmer, were used to optimize ICP-MS instrumental parameters, including the nebulizer gas flow rate, ion optics voltage, and aerosol injector orifice position relative to the sampling cone, at 1.0 kW power, on a daily basis. By using this three-element optimization, general signal optimization for multielement analysis can be achieved. The instrument operating parameters and the data acquisition parameters are listed in Table 1.

Results and Discussion

For the determination of trace elements in biological materials, additional variables must be considered. Because the metal concentrations in the matrix are extremely low, calibrators and reference materials, as well as the analytical procedure, have to meet very stringent requirements. In biological specimens, the matrix plays an important role. Nonspectral interference can be induced physically and spectral interference can originate from chemical sources. Because interferences can have a large effect on the results, they need to be understood.

Table 1. ICP-MS instrument operating and data acquisition parameters.

Instrument operating parameters	
Inductively coupled plasma	
R.f. power	1.0 kW
Gas flow rates	Plasma: 12 L/min Auxiliary: 1.2 L/min Nebulizer: optimized for 10 $\mu\text{g/L}$ ^{24}Mg , ^{103}Rh , ^{208}Pb
Sample uptake rate	1.0 mL/min
Interface	
Sampling cone	Pt cone, 0.045" orifice
Skimmer cone	Pt cone, 0.035" orifice
Aerosol injector orifice position	Optimized for 10 $\mu\text{g/L}$ ^{24}Mg , ^{103}Rh , ^{208}Pb
Mass spectrometer	
Ion lens voltages	Optimized for 10 $\mu\text{g/L}$ ^{24}Mg , ^{103}Rh , ^{208}Pb
Resolution mode	Normal
Scanning mode	Peak hop
Dwell time	50 ms
Replicate time	500 ms
Number of replicates	3
Sample read delay	60 s
Wash-out time	180 s

NONSPECTRAL INTERFERENCES

Nonspectral interferences in ICP-MS refer to analyte signal intensity changes where the change cannot be accounted for by a recognizable spectral overlap. The analyte signal intensity change can be either a suppression [26, 27] or an enhancement [27–32]. The causes of nonspectral interferences or so-called matrix effects are due to the presence of matrix components. The magnitude of the matrix effects depends on the mass and ionization energy of the matrix elements. It has been reported that the higher the mass of the matrix element, the larger the matrix effects [29–32]. However, high mass matrix elements are rare in biological fluids. For ionization dependence, Olivares and Houk [28] found that the trend of matrix effects was in the order of most easily ionized matrix element, i.e., Na (5.319) > Mg (7.646) > I (10.451) > Br (11.814) > Cl (13.618), where the first ionization energy in eV is noted in parentheses. In contrast, biological specimens contain relatively large concentrations of easily ionized matrix elements, such as Na, K, Ca, and Mg, which makes analysis of these samples difficult. Such matrix effects need to be eliminated to obtain accurate results. Errors associated with matrix-induced signal variation can be corrected by means of an appropriate calibration method. The merits of external calibration with internal calibration and sample dilution, and the alternative strategy of calibrator addition in correction for matrix effects were compared.

EXTERNAL CALIBRATION

There are several approaches to overcome matrix effects [33, 34]. The most widely used calibration method is by a set of external calibrators containing elements of interest and internal calibrators in a simple acid. Several calibrator solutions are needed to cover the range of expected analyte concentrations. The success of external calibration to correct for matrix effects depends on the effectiveness of internal calibration and dilution of samples.

INTERNAL CALIBRATION

The calibration or correction of one element by using a second as a reference point has been used in a variety of analytical atomic spectrometry and is termed "internal calibration." An element with a known concentration is added to all solutions, including the blank, calibrators, and unknowns. The analyte signal is then normalized to the signal of the internal calibrator. The effectiveness of an internal calibrator requires that its behavior accurately reflects that of the elements of interest to be measured. Selection of an internal calibrator is of great importance. Ideally, an internal calibrator should undergo the identical matrix suppression or enhancement as that of the analyte element. However, matrix-induced analyte signal changes are not uniform for all elements, but depend on the mass of the element [21, 35, 36]. As a consequence, a close match of the mass number between the analyte and internal calibrator is of prime importance to effectively

correct for matrix effects. Fig. 1 shows the effectiveness of the internal calibration in NaCl solutions as a function of NaCl concentration. The Ge signal (line B) is suppressed by NaCl. After normalization to the close-mass internal calibrator ^{71}Ga signal, the ^{72}Ge signal (line A) is then independent of NaCl concentration and comparable with the signal in a solution without NaCl. The matrix effect can thus be effectively corrected by using a suitable internal calibrator with a mass close to that of the analyte element. However, it is obvious that one internal calibrator cannot be used for all elements, since the matrix-induced signal variation is mass dependent. Several internal calibrators should be used over the entire mass range. Yet, using a large number of internal calibrators does not necessarily guarantee more accurate analytical performance. Too many internal calibrators (e.g., 10) may result in a practical problem of selecting internal calibrators and higher errors [37]. In general, three or four elements as internal calibrators are considered to be adequate for the multielement analysis [21, 34, 36, 38, 39]. However, one internal calibrator still covers a group of analyte elements, even though four internal calibrators are used for the multielement analysis. It is impossible to accurately correct for all elements of interest in that group by one internal calibrator. In addition, even an element with similar chemical and physical properties and similar atomic mass may behave in a different way in certain matrices [34, 40]. Therefore, some procedure must be used to improve the deficiency of internal calibration.

DILUTION OF SAMPLE

Specimen dilution is necessary for ICP-MS analysis of biological samples because large amounts of proteins and salts can cause an irreversible reduction of the analyte signal intensity due to clogging of the nebulizer, torch, sampling, and skimmer orifices. One solution is to dilute biological samples with a solvent before injection. In

addition, dilution can also reduce matrix effects while the sample is being measured, since matrix effects are dependent on the absolute amount of matrix element rather than the relative concentration of matrix to analyte [32, 33].

Besides preventing clogging and reducing the matrix effect, dilution is also necessary to improve the accuracy of internal calibration. Fig. 2 illustrates the effectiveness of internal calibration as a function of NaCl concentrations. The Se signal (line B) was largely suppressed by NaCl. Normalizing to the ^{71}Ga internal calibrator, the ^{82}Se signal (line A) is still influenced by NaCl concentrations but the effectiveness of the internal calibration is enhanced when NaCl concentrations are decreased. The effectiveness of internal calibration can be improved by dilution.

CALIBRATOR ADDITION

Calibrator addition is performed by adding increasing quantities of the elements of interest to multiple aliquots of the sample to be analyzed. The calibration set therefore consists of several supplemented samples plus an unsupplemented original sample, all of which have an identical matrix. Matrix effect is corrected for and highly accurate and precise data can be produced. Internal calibration is also included to correct for instrumental drift.

From a practical viewpoint, external calibration with internal calibration and dilution is most attractive for routine application since it is less time consuming and results in less introduction of matrix materials into the instrument than the other calibration methods. However, the use of calibrator addition provides a way to evaluate the accuracy of external calibration and is sometimes necessary to compensate for the insufficiency of external calibration. External calibration is shown to be adequate to correct for encountered biological matrix effects for

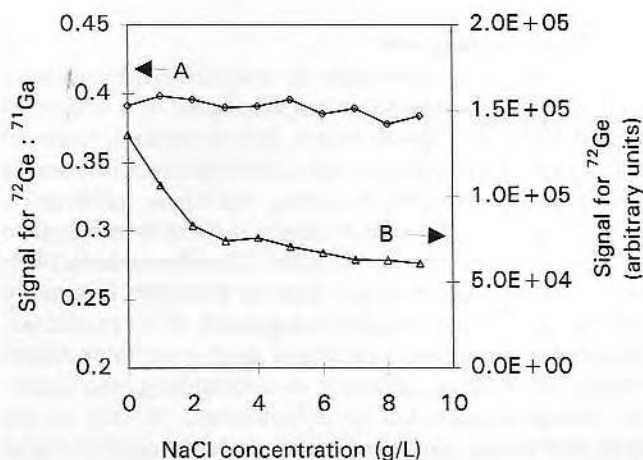


Fig. 1. Effectiveness of an internal calibrator to correct for signal suppression caused by various NaCl concentrations: A, signal ratio for the analyte ^{72}Ge to the internal calibrator ^{71}Ga and B, signal for the analyte ^{72}Ge .

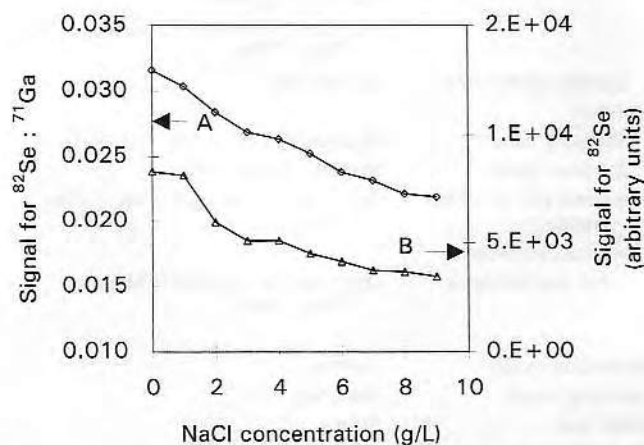


Fig. 2. Effectiveness of an internal calibrator to correct for signal suppression caused by various NaCl concentrations: A, signal ratio for the analyte ^{82}Se to the internal calibrator ^{71}Ga and B, signal for the analyte ^{82}Se .

most elements. (Data are discussed later.) Yet, external calibration was inadequate for some elements, such as Cs and Zn. For Cs the results obtained for reference urine levels I and II from external calibration, with In as the internal calibrator, are only 67.32% and 68.65% of those from calibrator additions, probably due to the large mass difference between ^{133}Cs and ^{115}In . However, insufficient correction for ^{68}Zn via external calibration was also observed, even with the close-mass internal calibrator ^{71}Ga . The results for both urine and serum reference materials (data shown in Tables 4 and 5) from external calibration were located in the very low end of acceptable ranges and the recoveries were poorer than those from calibrator addition. On the other hand, a better agreement between calibrator additions and target values was found. The insufficient corrections for Zn are probably caused by the discrepancy of the first ionization potential between the analyte and the internal calibrator: Zn (9.394 eV) and Ga (5.99 eV). Even after fivefold dilution, internal calibration was still ineffective for the correction of the remaining signal suppression. Calibrator addition is thus an improvement over external calibration for those elements.

SPECTRAL INTERFERENCES

Spectral interferences can be a major limitation since most ICP-MS units are equipped with a quadrupole mass analyzer that limits the resolution to approximately unit mass. Therefore, ions with the same nominal mass as the analyte, resulting from singly charged ions, doubly charged ions, and polyatomic ions, cannot be resolved. Polyatomic interferences, resulting from combination of precursors in the Ar plasma, entrained atmospheric gases, reagents, or biological matrices, are more problematic. Elements >82 amu are essentially free of polyatomic interferences and suitable for ICP-MS analysis, but elements between 40 and 82 amu can be compromised by these interferences. Accurate analytical results require that spectral interferences be identified and then avoided or corrected.

CHOICE OF THE ISOTOPE

The polyatomic interferences can be avoided in different ways [24, 33, 34]. A simple way is to carefully select an isotope for analysis free from significant interferences. An accurate and precise result can thus be obtained. To eliminate the interferences effectively, the encountered polyatomic ions must be identified and the extent of these interferences must be assessed. Since it is impossible to address all polyatomic interferences for every element of interest, only Cu and Zn are discussed to illustrate that the correct choice of the available analyte isotope is of prime importance to obtain an accurate result and minimize the interference.

DETERMINATION OF CU

Cu has two stable isotopes: ^{63}Cu (69.09%) and ^{65}Cu (30.91%). The determination of Cu is complicated because of polyatomic ion interferences from Na at mass 63 ($^{40}\text{Ar}^{23}\text{Na}$) as well as from Ca and S at mass 65 ($^{48}\text{Ca}^{16}\text{OH}$, $^{48}\text{Ca}^{17}\text{O}$, $^{33}\text{S}^{16}\text{O}^{16}\text{O}$, $^{32}\text{S}^{16}\text{O}^{17}\text{O}$, $^{32}\text{S}^{33}\text{S}$), where Na, Ca, and S are abundant in biological fluids. Table 2 shows the results of Cu analysis on urine and serum reference materials with masses 63 and 65 under external calibration and calibrator addition. For Bio-Rad Lyphochek urine levels I and II, the results under both calibrations and historically established values by the former method of ARUP with ^{63}Cu were higher than the target values. ^{63}Cu signals were largely influenced by the spectral overlap of $^{40}\text{Ar}^{23}\text{Na}$ since the Cu concentration in this sample is low. On the other hand, the determinations made at mass 65 showed excellent agreement. The polyatomic ions at mass 65, from S or Ca, do not result in significant interferences. For Kaulson Contox serum levels I and II, because the serum Cu concentration range is high the signal at mass 63 is not as susceptible to $^{40}\text{Ar}^{23}\text{Na}$ interference. However, the results by ^{63}Cu under calibrator additions are still too high. Again the determination made at mass 65 agreed well with the target values. Therefore, we can conclude that the ICP-MS Cu method

Table 2. Results of Cu analysis in Bio-Rad Lyphochek urine and Kaulson Contox serum.

	Bio-Rad urine, $\mu\text{g/L}^a$		Kaulson serum, $\mu\text{g/L}^b$	
	Level I	Level II	Level I	Level II
Cu Target	49 \pm 10	64 \pm 13	1000 \pm 150	1450 \pm 200
^{65}Cu External calibration	41.74 \pm 6.65	57.86 \pm 5.51	974.6 \pm 68.1	1393.7 \pm 172.8
Calibrator addition	43.10 \pm 5.64	58.07 \pm 6.84	1080.3 \pm 33.6	1490.0 \pm 31.7
ARUP ^c	41 \pm 20	65 \pm 20		
^{63}Cu External calibration	62.12 \pm 2.23	79.14 \pm 8.83	1052.5 \pm 36.0	1494.8 \pm 8.5
Calibrator addition	66.51 \pm 2.68	81.24 \pm 3.55	1255.7 \pm 44.2	1715.8 \pm 34.7
ARUP ^d	85 \pm 30	95 \pm 30		

^a Concentrations obtained by external calibration and calibrator addition are presented as means \pm SD within 95% confidence ($n = 3$).

^b Concentrations obtained by external calibration and calibrator addition are presented in means \pm SD within 95% confidence ($n = 2$).

^c Current ARUP's method under external calibration with Y internal calibrator and 10-fold dilution.

^d Historical ARUP's method under external calibration with Y internal calibrator and 10-fold dilution.

based on the isotope 65 is suitable for analysis of urine and serum and avoids the major interference.

DETERMINATION OF ZN

Zn has five stable isotopes: ^{64}Zn (48.89%), ^{66}Zn (27.81%), ^{67}Zn (4.11%), ^{68}Zn (18.56%), and ^{70}Zn (0.62%). Different Zn isotopes, including ^{64}Zn [36], ^{66}Zn [20, 22–24, 36, 41], and ^{68}Zn [21], have been attempted for Zn determination in the biological fluids.

The determination of Zn in body fluids can be complicated by the different degrees of S-containing interferences on the Zn isotopes (Table 3) [21]. Fig. 3 gives the apparent concentration of Zn at masses 64, 66, 67, and 68 as a function of sulfuric acid concentrations. The apparent Zn concentrations at masses 64, 66, and 67 increase linearly with the sulfuric acid concentration. The S-containing polyatomic ions interfere at mass 64 and to a lesser extent at masses 66 and 67. Only mass 68 shows no interference due to S. S-containing polyatomic ions at mass 68 were not detected. This means determination of Zn with masses 64, 66, and 67 may be compromised by S interferences, and mass 68 is more suitable for analysis. The agreement between the target values and the results for urine and serum reference materials with ^{68}Zn is illustrated in Table 4 and Table 5. The results obtained by

external calibration are in poorer agreement with the target values than calibrator addition because of the occurrences of matrix suppression. However, the results indicate that ^{68}Zn is generally suitable for body fluids. The use of ^{68}Zn for routine clinical analysis is recommended to completely eliminate the interferences from S, leading to falsely higher results with ^{64}Zn and ^{66}Zn .

ANALYSIS OF URINE AND SERUM REFERENCE MATERIALS

Table 4 and Table 5 summarize the results of multielement analysis obtained on a reconstituted solution of the Bio-Rad Lyphocheck urine and Kaulson Contox serum reference materials, respectively. For all reference materials, both external calibration and calibrator addition were applied for analysis. Four internal calibrators were used for multielement coverage: ^9Be for low masses; ^{71}Ga for first transition metals as well as for As, Se, Rb, and Sr; ^{115}In for medium masses; and ^{193}Ir for high masses. In consideration of balancing the requirement of high sensitivity for ultratrace concentrations and reduction of matrix effects, a fivefold dilution was applied. The isotopes measured and internal calibrators used are given together with the analytical results within 95% confidence limits. For urine, each result is based on three sample aliquots, analyzed with three repeats, for a total of nine measurements. The results are compared with the target values verified by atomic absorption spectrometry (AAS). For serum, each result is based on two sample aliquots, analyzed with three repeats, for a total of six measurements. The results are compared with the target values referenced by AAS.

In urine, for eight trace elements (As, Cd, Co, Cu, Mn, Ni, Pb, Sb), the results obtained from both calibration methods are in good agreement with target values. For Zn the results obtained from calibrator addition are in better agreement with the target values than external calibration. For Al the results are at the lower end of certified acceptable ranges. For Se the results are higher than the acceptable target ranges, except level II with calibrator addition. However, in comparison with the values, level I: $76.50 \pm 5.51 \mu\text{g/L}$ and level II: $229.25 \pm 16.56 \mu\text{g/L}$ obtained by ARUP, in which the methodology was verified by interlaboratory correlation with certified AAS methods [42], the agreement is excellent. For Tl the results are lower than the acceptable target ranges but in good agreement with ARUP's values (level I: $8.38 \pm 0.52 \mu\text{g/L}$; level II: $167.43 \pm 6.95 \mu\text{g/L}$). For seven other elements (Bi, Cs, Mo, Rb, Sn, Sr, W) no data are available for the comparison.

In serum, the results obtained for level II agreed with the target values, except for Mn under external calibration. The results obtained for level I agreed with the target values, except for Ni and Bi. For Ni the results were higher than the target value, which is probably because the signal at mass 60 is susceptible to the $^{44}\text{Ca}^{16}\text{O}$ interference at low concentration. For Bi the concentration was lower than the detection limit.

Table 3. S-containing potential polyatomic interferences for the determination of Zn.

Zn isotope	Abundance, %	Polyatomic ions
^{64}Zn	48.89	$^{32}\text{S}^{16}\text{O}^{16}\text{O}$ $^{32}\text{S}^{32}\text{S}$
^{66}Zn	27.81	$^{34}\text{S}^{16}\text{O}^{16}\text{O}$, $^{33}\text{S}^{16}\text{O}^{16}\text{OH}$, $^{32}\text{S}^{16}\text{O}^{18}$ $^{32}\text{S}^{34}\text{S}$
^{67}Zn	4.11	$^{34}\text{S}^{16}\text{O}^{16}\text{OH}$, $^{32}\text{S}^{16}\text{O}^{18}\text{OH}$
^{68}Zn	18.56	$^{36}\text{S}^{16}\text{O}^{16}\text{O}$, $^{34}\text{S}^{16}\text{O}^{18}\text{O}$ $^{32}\text{S}^{36}\text{S}$, $^{32}\text{S}^{36}\text{Ar}$
^{70}Zn	0.62	$^{36}\text{S}^{16}\text{O}^{18}\text{O}$, $^{34}\text{S}^{18}\text{O}^{17}\text{O}$, $^{33}\text{S}^{18}\text{O}^{18}\text{OH}$ $^{34}\text{S}^{36}\text{S}$, $^{34}\text{S}^{36}\text{Ar}$

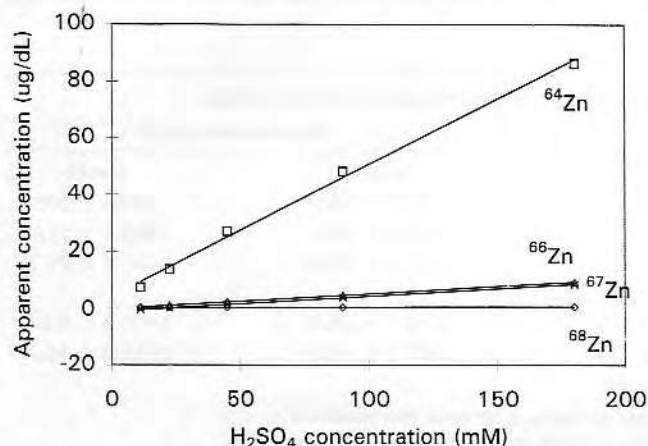


Fig. 3. Apparent Zn concentration at masses 64, 66, 67, and 68 as a function of H_2SO_4 concentration.

Table 4. Multielement analysis of Bio-Rad Lyphochek urine Level I and Level II.

Level I								
Target value			External calibration			Calibrator addition		
Element	Mean ^a	Acceptable range ^a	Mean ^a	SD ^b	CV, %	Mean ^a	SD ^b	CV, %
²⁷ Al	68	54–81	59.18	2.91	5	55.06	1.17	2
⁵⁵ Mn	5.5	4.4–6.6	5.16	0.70	14	5.18	0.24	5
⁵⁶ Co	4.2	3.4–5	4.04	0.68	17	3.94	0.14	4
⁶⁰ Ni	17.9	14.3–21.4	19.28	4.77	25	19.58	2.02	10
⁶⁵ Cu	49	39–59	41.73	6.66	16	43.10	5.64	13
⁶⁸ Zn	643	515–772	547.09	27.81	5	654.58	35.02	5
⁷⁵ As	64	51–77	67.49	8.91	13	63.64	7.89	12
⁸² Se	56	44–67	76.67	6.88	9	73.84	12.34	17
⁸⁵ Rb			610.60	44.86	7	660.79	38.34	6
⁸⁸ Sr			190.64	31.14	16	175.66	5.18	3
⁹⁸ Mo			51.44	3.45	7	45.57	2.41	5
¹¹¹ Cd	6.7	5.3–8	4.95	0.56	11	6.41	0.87	14
¹¹⁸ Sn			0.63	0.21	33	0.61	0.09	14
¹²¹ Sb	20.3	16.2–24.3	19.42	2.42	12	18.42	2.06	11
¹³³ Cs			2.30	0.71	31	3.42	0.18	5
¹⁸² W			0.33	0.12	37	0.31	0.06	20
²⁰⁵ Tl	11.3	9–13.6	7.79	1.33	17	8.51	0.23	3
²⁰⁸ Pb	13.5	10.8–16.2	12.14	0.91	7	13.09	0.75	6
²⁰⁹ Bi			0.59	0.19	31	0.62	0.17	27
Level II								
²⁷ Al	104	83–125	83.85	3.98	5	77.27	3.90	5
⁵⁵ Mn	23.8	19.1–28.6	22.48	4.36	19	22.28	2.93	13
⁵⁹ Co	12.2	9.8–14.7	10.90	1.04	10	10.60	0.58	5
⁶⁰ Ni	33.4	26.7–40.1	35.33	2.04	6	35.31	1.71	5
⁶⁵ Cu	64	51–77	57.88	5.88	10	58.07	6.84	122
⁶⁸ Zn	1047	837–1256	947.16	62.24	7	1070.01	54.58	5
⁷⁵ As	163	130–195	168.86	18.94	11	157.04	14.24	9
⁸² Se	162	130–194	214.59	16.80	8	187.02	18.97	10
⁸⁵ Rb			624.03	70.13	11	655.08	23.67	4
⁸⁸ Sr			190.43	27.75	15	174.82	7.57	4
⁹⁸ Mo			52.06	4.21	8	45.77	1.86	4
¹¹¹ Cd	12.8	10.2–15.3	9.58	1.12	12	11.78	0.93	8
¹¹⁸ Sn			0.43	0.34	79	0.40	0.27	67
¹²¹ Sb	79.1	63.2 ± 94.5	75.24	11.27	15	68.94	7.45	11
¹³³ Cs			2.31	0.56	24	3.36	0.09	3
¹⁸² W			0.33	0.10	32	0.30	0.08	25
²⁰⁵ Tl	212	169–254	157.69	18.15	12	166.98	8.20	5
²⁰⁸ Pb	63	50–75	59.98	3.75	6	60.49	6.93	11
²⁰⁹ Bi			0.62	0.12	20	0.65	0.27	42

^a µg/L.^b SD within 95% confidence limits (n = 3).

PRECISION

Precision is evaluated by the CV of the repetitive analysis of reference urine and serum under external calibration and calibrator additions. Each result is the average of levels I and II and corresponds to 95% confidence limits. For urine most of the elements in calibrator addition have a comparable and higher precision than external calibration. For either calibration method, elements with ultratrace concentrations (<1 µg/L) have poorer precision. Elements with concentrations >1 µg/L have better precision.

The imprecision in the collected data is significantly smaller than the uncertainties of the target values. For serum, the precision for both calibration methods is comparable. The use of calibrator addition does not particularly enhance precision over external calibration. For elements Sn and Pb, precision is poorer, especially in level I, owing to the very low concentrations.

In conclusion, ICP-MS is a practical, versatile method for the determination of many trace and ultratrace elements

Table 5. Multielement analysis of Kaulson Contox serum Level I and Level II.

Table 2. Management analysis of standard solution Level I and Level II								
Element	Level I							
	Target value		External calibration			Calibrator addition		
	Mean ^a	SD	Mean ^a	SD ^b	CV, %	Mean ^a	SD ^b	CV, %
²⁵ Mg (×200 dil.)	15 ^c	0.5	14.90	1.65	14.90	9.96		
²⁷ Al	50	8	49.05	5.70	11.62	45.23	2.33	5.15
⁵⁵ Mn	4	2	2.53	0.54	21.36	2.65	0.76	28.59
⁵⁹ Co			0.76	0.14	19.18	0.71	0.24	33.87
⁶⁰ Ni	5	3	11.88	2.23	18.75	12.78	3.59	28.09
⁶⁵ Cu	1000	150	974.6	68.1	6.98	1080.3	36.3	3.36
⁶⁸ Zn	780	120	590.9	33.7	5.71	678.3	38.0	5.61
¹¹⁸ Sn	2	1	0.96	1.02	106.15	1.03	1.48	143.07
²⁰⁸ Pb			1.91	1.42	74.57	1.78	1.46	107.08
²⁰⁹ Bi		2	1	<0.18	0.11		<0.17	0.21
Level II								
²⁵ Mg (×200 dil.)	40 ^c	8	37.21	0.12	0.31	37.55	3.88	10.33
²⁷ Al	100	15	114.66	25.41	22.16	102.19	10.41	10.18
⁵⁵ Mn	170	25	207.86	10.53	5.07	193.72	24.59	12.96
⁵⁹ Co			0.96	0.32	33.05	0.90	0.21	23.98
⁶⁰ Ni	20	6	17.95	4.45	24.80	19.43	4.52	23.26
⁶⁵ Cu	145	20	1393.7	172.8	12.40	1490.0	31.7	2.13
⁶⁸ Zn	170	25	1504.5	92.2	6.13	1790.2	59.4	3.32
¹¹⁸ Sn	6	4	4.03	2.64	65.43	4.07	1.68	41.18
²⁰⁸ Pb			3.17	1.51	47.77	3.38	0.60	17.79
²⁰⁹ Bi	8	4	4.87	2.33	47.82	5.92	1.50	25.31
^a µg/L.								
^b SD within 95% confidence limits (n = 2).								
^c mg/L.								

^a μg/L.^b SD within 95% confidence limits (n = 2).^c mg/L.

in the clinical laboratory. However, nonspectral and spectral interferences need to be taken into consideration for the analysis of elements in biological matrices. With internal calibrators of close mass, internal calibration is able to effectively correct for encountered nonspectral interferences; however, specimen dilution is still necessary to improve the effectiveness of internal calibration. With four internal calibrators (Be, Ga, In, Ir) across the entire mass range and fivefold specimen dilution, external calibration is able to accurately measure a variety of trace and ultratrace elements in urine and serum, with the exception of some elements (e.g., Cs, Zn) that have a large discrepancy in atomic mass and ionization energy with that of the internal calibrator. Calibrator addition provides an alternative method to compensate for the insufficiency of external calibration and yields more accurate and precise results in certain cases. Spectral interferences can be eliminated by a simple approach of selecting the isotope with minimal interferences. With proper analytical processes, ICP-MS is generally suitable for the routine multielement analysis of body fluids.

References

- Kieffer F. In: Merian E, ed. Metals and their compounds in the environment. Weinheim: VCH, 1991:481pp.
- O'Dell BL. Bioavailability of trace elements. *Nutr Rev* 1984;42:301-8.
- Elinder C-G, Gerhardsson L, Oberdoerster G. Biological monitoring of toxic metals—overview. In: Clarkson TW, Friberg L, Nordberg GF, Sager PR, eds. Biological monitoring of toxic metals. New York: Plenum Press, 1988:1-71.
- Nielsen FH. Possible future implications of ultratrace elements in human health and disease. In: Prasad AS, ed. Essential and toxic trace elements in human health and disease. New York: Wiley-Liss, 1988:277-92.
- Nielsen FH. New essential trace elements for the life sciences. *Biol Trace Elem Res* 1990;599-611.
- Nielsen FH. Trace and ultratrace elements in health and disease. *Compr Ther* 1991;17:20-6.
- Nielsen FH. Ultratrace elements of possible importance for human health: an update. In: Prasad AS, ed. Essential and toxic trace elements in human health and disease: an update. New York: Wiley-Liss, 1993:355-76.
- Menendez-Botet CJ, Schwartz MK. Trace metals. *Anal Chem* 1991;63:194R-9R.
- Savory J, Wills MR. Trace elements: essential nutrients or toxins. *Clin Chem* 1992;38:1565-73.
- Delves HT. The analysis of biological and clinical materials. *Prog Anal Atom Spectrosc* 1981;4:1-48.
- Delves HT. Assessment of trace element status. *Clin Endocrinol Metab* 1985;14:725-60.
- Nomiyama K, Nomiyama H. Simultaneous determinations of essential trace metals in biological fluids and their significance.

- In: Okuda K, ed. Automation and new technology in the clinical laboratory. Oxford: Blackwell Scientific Publications, 1990:117-22.
13. Daher RT. Trace metals (lead and cadmium exposure screening). *Anal Chem* 1995;67:405R-10R.
 14. Copeland KR. Trace elements in clinical chemistry. In: Bishop ML, Duben-Engelkirk JL, Fody EP, eds. *Clinical chemistry: principles, procedures, correlations*, 3rd ed. Philadelphia: Lippincott-Raven Publishers, 1996:279-91.
 15. Mertz W, ed. Trace elements in human nutrition and health. Geneva: WHO, 1996.
 16. Houk RS, Fassel VA, Flesch GD, Saec HJ, Gary AL, Taylor CE. Inductively coupled argon plasma as an ion source for mass spectrometric determination of trace elements. *Anal Chem* 1980;52:2283-9.
 17. Ash KO, Komaromy-Hiller G. Analysis of clinical specimens using inductively coupled plasma mass spectrometry. In: Wong SHY, Sunshine I, eds. *Handbook of analytical therapeutic drug monitoring and toxicology*. New York: CRC Press, 1997:107-25.
 18. Barnes RM. Analytical plasma source mass spectrometry in biomedical research. *Fresenius J Anal Chem* 1996;355:433-41.
 19. Nixon DE, Moyer TP. Routine clinical determination of lead, arsenic, cadmium, and thallium in urine and whole blood by inductively coupled plasma mass spectrometry. *Spectrochim Acta* 1996;51B:13-25.
 20. Vandecasteele C, Vanhoe H, Dams R, Versieck J. Determination of trace elements in human serum by inductively coupled plasma-mass spectrometry. *Biol Trace Elem Res* 1990;553-60.
 21. Vandecasteele C, Vanhoe H, Dams R. Inductively coupled plasma mass spectrometry of biological samples. *J Anal At Spectrom* 1993;8:781-6.
 22. Vanhoe H, Vandecasteele C, Versieck J, Dams R. Determination of iron, cobalt, zinc, rubidium, molybdenum, and cesium in human serum by inductively coupled plasma mass spectrometry. *Anal Chem* 1989;61:1851-7.
 23. Vanhoe H, Vandecasteele C, Versieck J, Dams R. Determination of trace elements in a human serum reference materials by inductively coupled plasma mass spectrometry. *Mikrochim Acta* 1989;III:373-9.
 24. Vanhoe H. A review of the capabilities of ICP-MS for trace element analysis in body fluids and tissues. *J Trace Elem Electrolytes Health Dis* 1993;7:131-9.
 25. Vanhoe H, Dams R, Versieck J. Use of inductively coupled plasma mass spectrometry for the determination of ultra-trace elements in human serum. *J Anal At Spectrom* 1994;9:23-31.
 26. Date AR, Cheung YY, Stuart ME. The influence of polyatomic ion interferences in analysis by inductively coupled plasma source mass spectrometry (ICP-MS). *Spectrochim Acta* 1987;42B:3-20.
 27. Beauchemin D, McLaren JW, Berman SS. Study of the effects of concomitant elements in inductively coupled plasma mass spectrometry. *Spectrochim Acta* 1987;42B:467-90.
 28. Olivares JA, Houk RS. Suppression of analyte signal by various concomitant salts in inductively coupled plasma mass spectrometry. *Anal Chem* 1985;58:20-5.
 29. Gregoire DC. The effect of easily ionizable concomitant elements on non-spectroscopic interferences in inductively coupled plasma-mass spectrometry. *Spectrochim Acta* 1987;42B:895-907.
 30. Kawaguchi H, Tanaka T, Nakamura T, Morishita M, Mizuike A. Matrix effects in inductively coupled plasma mass spectrometry. *Anal Sci* 1987;3:305-8.
 31. Kim Y-S, Kawaguchi H, Tanaka T, Mizuike A. Non-spectroscopic matrix interferences in inductively coupled plasma-mass spectrometry. *Spectrochim Acta* 1990;45B:333-9.
 32. Tan SH, Horlick G. Matrix-effect observations in inductively coupled plasma mass spectrometry. *J Anal At Spectrom* 1987;2:745-63.
 33. Evans EH, Giglio JJ. Interferences in inductively coupled plasma mass spectrometry. *J Anal At Spectrom* 1993;8:1-18.
 34. Dams R, Goossens J, Moens L. Spectral and non-spectral interferences in inductively coupled plasma mass spectrometry. *Mikrochim Acta* 1995;119:277-86.
 35. Vanhaecke F, Dams R, Vandecasteele C. "Zone model" as an explanation for signal behaviour and non-spectral interferences in inductively coupled plasma mass spectrometry. *J Anal At Spectrom* 1993;8:433-8.
 36. Gerotto M, Andrea ED, Bortoli A, Marchiori M, Palonta M, Tronocon A. Interference effects and their control in ICP-MS analysis of serum and saline solutions. *Microchem J* 1995;51:73-87.
 37. Amarasingwardena CJ, Gercken B, Argentine MD, Barnes RM. Semi-quantitative analysis by inductively coupled plasma mass spectrometry. *J Anal At Spectrom* 1990;5:457-62.
 38. Mulligan KJ. Feasibility of the direct analysis of urine by inductively coupled argon plasma mass spectrometry for biological monitoring of exposure to metals. *J Anal At Spectrom* 1990;5:301-6.
 39. Vanhoe H, Versieck J, Moens L, Dams R. Role of inductively coupled plasma mass spectrometry (ICP-MS) in the assessment of reference values for ultra-trace elements in human serum. *Trace Elem Electrolytes* 1995;12:81-8.
 40. Moens L, Vanhoe H, Vanhaecke F, Goossens J, Campbell M, Dams R. Application of inductively coupled plasma mass spectrometry to the certification of reference materials from the Community Bureau of Reference. *J Anal At Spectrom* 1994;9:187-91.
 41. Dams R. RNAA as compared to ICP-MS for the analysis of normal human serum. *Biol Trace Elem Res* 1994;539-48.
 42. Costa R, Gordon W, Jennison T, Ash KO. Serum selenium quantitation by ICP/MS isotope analysis [Abstract]. *Clin Chem* 1995;41:S145.

Pyrolyzed, Conducting Kapton Polyimide: An Electrically Conducting Material

C. Z. HU* and J. D. ANDRADE,[†] *Department of Materials Science and Engineering, College of Engineering, University of Utah, Salt Lake City, Utah 84112*

Synopsis

Polyimide was pyrolyzed in an argon atmosphere at 900°C for 1h. The room temperature conductivity of the polyimide gradually increased from 15 to 100 S/cm with increased pyrolysis time. Further increase in the pyrolysis time did not increase the conductivity. X-ray photoelectron spectroscopy (XPS) showed that the polyimide changed from pure insulator to conductor; detailed XPS spectra of carbon, nitrogen, and oxygen 1s bands showed no further elemental decomposition of the polyimide at 900°C. The high temperature treatment results in internal rearrangement to form a large, dense heterocyclic network. The film probably consists of tiny conductive particles dispersed in an amorphous carbon matrix. The polyimide is placed between two quartz plates during pyrolysis; the resulting film is flat, has uniform conductivity, is nonbrittle, has high chemical resistance, and shows better mechanical strength than films pyrolyzed in free-standing conditions.

INTRODUCTION

The pyrolysis of polyimide results in elimination of all elements except carbon, forming an extended aromatic ring structure similar to graphite. The extended aromatic rings are dispersed in an amorphous carbon matrix. It is believed¹ that in the early stages of pyrolysis defined domains of condensed rings start to form; free radicals are also formed. Later a continuous network of condensed aromatic structure with strong π -orbital overlap is formed. The π -electrons within this aromatic ring network are to a certain degree delocalized (depending on the pyrolysis conditions) and not limited to individual aromatic rings. The strong π -orbital overlapping results in a conductivity in the range of 10^2 S/cm. The free radicals can act as donors or acceptors.

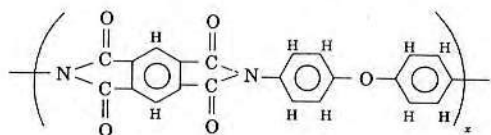
Charge transfer between rings can be described mainly by two mechanisms^{2,3}: (a) for small interring distances (less than 10 Å), the tunneling mechanism is available; (b) for large interring distances (greater than 10 Å), the hopping mechanism is available. Under an electric field electrons excited to the empty states can tunnel through the potential barrier between the rings to the empty states of other rings; the hole created can tunnel in the opposite direction. When the distance between rings is large, the electron cannot tunnel from one ring to another, but can transfer by a hopping mechanism.

* This work was submitted in partial fulfillment of the M. S. degree in Materials Science and Engineering, University of Utah.

[†] To whom correspondence and reprint requests should be directed.

MATERIALS AND METHODS

The Kapton polyimide free-standing films are products supplied by Du Pont de Nemours and Co. and have the following structure:



The sample heating system consisted of a high temperature oven, compressed argon gas tank, quartz tube, control valve, and vacuum pump.

Thermogravimetric Analysis (TGA). The polyimide sample is placed inside a small quartz tube oven; high purity argon gas is passed through the inside of the tube at 4 cc/s. At Du Pont 990 Thermal Analyzer records the weight loss as a function of temperature.

X-Ray Photoelectron Spectroscopy Analysis (XPS). XPS analyses of the polyimide samples at different stages of pyrolysis provides information on elemental ratios and bonding environments. Combined with other data, it permits the determination of composition and structure changes during the different stages of pyrolysis. XPS analyses was performed on a Hewlett-Packard 5950B ESCA Spectrometer, using a monochromatic $\text{AlK}\alpha$ X-ray source.

Four-Point Probe Conductivity Measurement and Ohmic Contact Test. Four-point probe conductivity methods are described by several authors.⁴ The basic principle is the placement of four sharp, equal distance probes on the flat surface of the material. Current is created by a current source and passed through the two outer probes and the voltage created is measured across the inner two probes. If the sample is relatively large compared with the distance between the probes, the resistivity can be calculated. Our four-point probe measurement used an HP 3465A Digital Multimeter, HP 6181C DC Current Source, and Alessi Industries Four-Point Probe. In order to electrically test the sample, an ohmic contact test between the sample and the silver epoxy paint is a must. The silver epoxy paint is coated at the corners of the sample. The current is introduced at each diagonal lead; If $V=IR$ is obeyed, ohmic contact is present.

RESULTS

TGA. The polyimide was heat-treated in two different gas environments: One was heat-treated in an oxygen atmosphere; the other was heat-treated in an argon atmosphere. The heating rate was $5^\circ\text{C}/\text{min}$. The TGA data are presented in Figure 1. Polyimide samples in oxygen started to dissociate at about 425°C ; the weight loss continuously increased with temperature to about 525°C , at which point all of the polyimide was gone. Polyimide in an argon atmosphere started to dissociate at about 500°C . The slope of weight loss vs. temperature increased as temperature increased, reached a maximum at 560°C , then started to decrease, and approached zero at about 700°C .

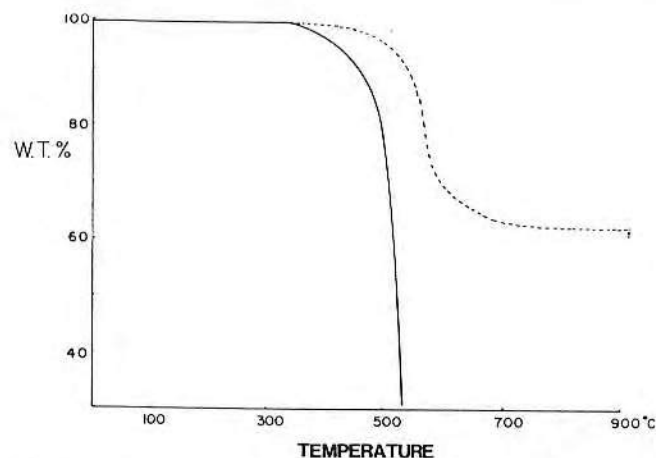


Fig. 1. The thermogravimetric analysis of Kapton polyimide: (—) oxygen atmosphere; (---) argon atmosphere.

At this stage the total weight loss of the polyimide was about 38%; the weight was then nearly constant to 900°C . The polyimide sample was held at 900°C for up to 1 h. For the first 40 min an additional 1-2 wt. % decrease was observed; after 40 min no further weight loss could be detected.

XPS. Wide scans of the polyimide at the different temperature stages are presented in Fig. 2. Nitrogen and oxygen contents decreased as the temperature was increased. Even with the electron flood gun on, the carbon 1s peak position suggests that the 900°C treated polyimide is at least semiconducting. Detailed analyses of carbon, oxygen, and nitrogen are presented in Fig. 3.

The polyimide has three carbon peaks at binding energy 288.4, 286.2, and 284.6 eV, respectively (see Table I). When the temperature is increased to 600°C , the peaks at 288.4 and 286.2 eV were decreased, and the C—C main peak was increased. After heating to 900°C , the peaks at 288.4 and 286.2 eV were not changed and the C—C main peak was increased further. Also, the shape of the C—C main peak was very similar to that of graphite.⁵ Further heating at 900°C further reduced the peaks at 288.4 and 286.2 eV; the main C—C peak remained the same.

Two oxygen peaks at binding energies of 534.0 and 532.6 eV, respectively (see Table I), were reduced as temperature increased above 500°C . When the temperature reached 900°C , all the remaining oxygen was of the C—O type. Further heating at 900°C did not further reduce the oxygen.

The nitrogen analyses were most interesting; the peak is at 400.7 eV. After the polyimide was heated to 600°C , a new peak appeared at 398.6 eV (see Table I), suggesting two different nitrogen environments.

Conductivity. The room temperature conductivity of pyrolytic polyimide is presented in Fig. 4, showing the conductivity as a function of pyrolysis time at 900°C . The epoxy silver paint did make ohmic contact with the polyimide samples.

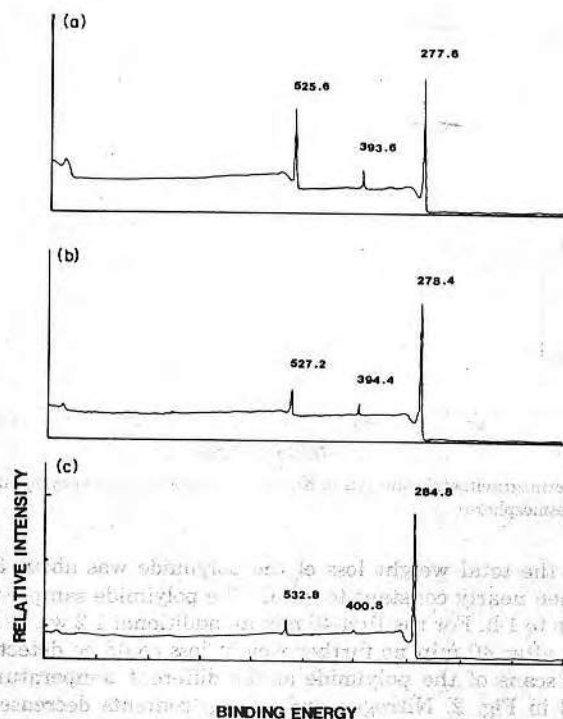


Fig. 2. XPS wide scan spectra of pyrolyzed Kapton with the electron flood gun on: (a) raw material; (b) pyrolyzed at 600°C; (c) pyrolyzed at 900°C.

Wide Angle X-Ray Analyses. Wide angle X-ray analyses was performed on a General Electric DIANO model. The wide angle X-ray analyses using $\text{Cu}_{K\alpha}$ monochromatic radiation showed that there was no long-range crystal structure.

DISCUSSION AND CONCLUSIONS

The TGA and ESCA studies clearly indicate that the polyimide was pyrolyzed. Most of the aliphatic C—N and C—O bonds are broken below 600°C, releasing N_2 , CO, and CO_2 gases. At the same time the carbon starts to form a heterocyclic structure. Above 600°C weight loss is insignificant. Some oxygen and nitrogen are incorporated into the heterocyclic rings. It is believed that the structure rearranges or recombines to a larger and denser heterocyclic network, resulting in increased conductivity. This conclusion is supported by both the ESCA and conductivity data. At 900°C, the elemental composition of the polymer stays nearly the same. After 1 h at 900°C, there is no further increase in conductivity, indicating no further structural change.

Wide angle X-ray data indicates that the pyrolyzed polyimide does not have long-term periodic structure. Apparently, the dense aromatic structure consists of small particles uniformly dispersed in a carbon matrix. Small-angle X-ray data are necessary to test this hypothesis. The mechanism of

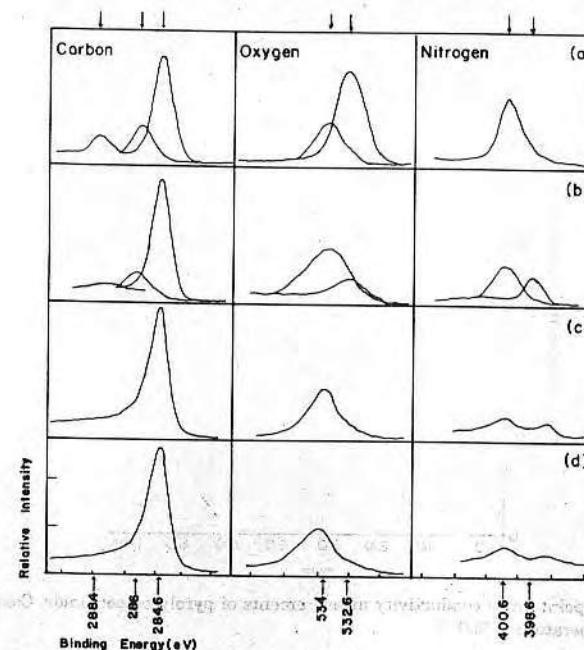


Fig. 3. XPS narrow scan spectra for carbon, oxygen, and nitrogen 1s peaks: (a) raw material; (b) at 600°C; (c) at 900°C; (d) at 900°C for 1 h.

electron or hole conduction in this material is complex. In each individual particle, the electron requires energy to overcome the intrinsic band gap and create electron and hole pairs. For simplicity, it is assumed that the band gap energy of all particles is approximately the same. The electrical carriers created must jump over or tunnel through the energy barrier between the particles. The average distance between the particles may determine which process is dominant. The energy barrier and structure change can be determined by optical measurements. Such work is in progress.

When the polyimide film is placed between quartz plates, the resulting

TABLE I
Elemental Binding Energy of Polyimide

Element			
Binding energy (eV)	C	O	N
C—C	284.6		
C—O	286.2	534.0	
C—N	286.0		400.6
$\text{C}=\text{O}$			
$\text{C}=\text{N}$	288.4	532.6	

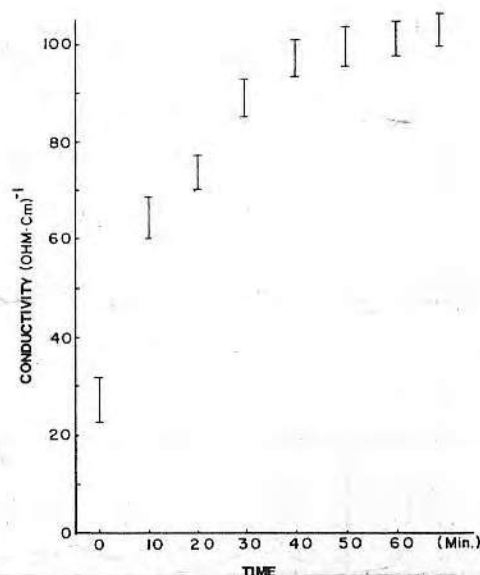


Fig. 4. Four point probe conductivity measurements of pyrolyzed polyimide. Conductivity vs. time at temperature of 900° C.

pyrolyzed material shows nonuniform conductivity. The conductivity is much lower at the edges than in the bulk. The rest of the sample has a relatively uniform conductivity. When the polyimide starts to dissociate at about 500°C, the volatile gases can only go through the space between the two plates. The large heterocyclic network does not form as effectively at the edges; the result is lower conductivity.

The mechanical strength of the pyrolytic polyimide is greatly improved by putting the polymer film between the quartz plates. Mass transfer of volatile gases is restricted to the direction of arrows in Fig. 5. This restriction causes the formation of a heterocyclic structure more ordered along the arrow directions, resulting in improving mechanical strength.

Pyrolyzed polyimide has conductivity of the order of 10^{20} times greater than the parent polyimide, and it may be doped to produce *n*-type or *p*-type material. Pyrolyzed polymers (both doped and undoped) are air stable and can function at very high temperatures without degradation.⁶ They show excellent binding to ceramics, metals, silicon, or other semiconductor compounds.⁷ The material has dependable and controlled conductivity^{8,9} with reasonable mechanical strength. In contrast, polyacetylenes or polydiacetylenes¹⁰⁻¹² are brittle, not air stable, oxidize rapidly when exposed to air; and the dopants often migrate out of the bulk polymer after a period of time.

Electrically conducting pyrolyzed polyimide can be used to produce circuitry on metal or semiconductor substrates by using photosensitive polyimide. Most other means of producing conductive polymers result in insoluble or difficult to process materials.

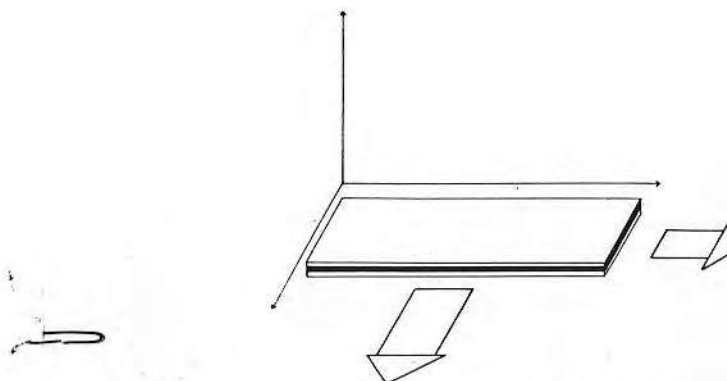


Fig. 5. The directions of volatile gas transport during pyrolysis, indicated by arrows.

This process of making conductive polymer is simple and cheap. Such materials could replace metal-filled polymer, molecularly doped polyenes,¹³ part of semiconductor devices,¹⁴ and has the potential of making some practical photo-devices. Pyrolytic polyimide is easy to fabricate for commercial manufacture.

Pyrolyzed polyimides certainly deserve to be further studied as lightweight materials for unique conductive or semiconductive applications.

This work was supported by University of Utah funds and a grant from the Teledyne Corp. to Dr. L. M. Smith. We thank Dr. L. M. Smith and Dr. D. E. Gregonis for their assistance and advice. We thank Dr. R. J. Huber for use of the four-point conductivity probe.

References

1. S. D. Bruck, *Chem. Eng. News*, **43**, 37 (1965).
2. D. Moses, J. Chen, A. Denenstein, M. Kaveh, T. C. Chung, A. J. Heeger, and A. G. MacDiarmid, *Solid State Commun.*, **40**, 1007 (1981).
3. G. Kemeny and B. Rosenberg, *J. Chem. Phys.*, **52**, 4151 (1970).
4. F. M. Smits, *Bell Syst. Tech. J.*, **37**, 711 (1958).
5. G. K. Wetheim, P. M. Th. M. Van Attekum, and S. Basu, *Solid State Commun.*, **33**, 1127 (1980).
6. S.D. Bruck, *Polymer*, **6**, 319 (1965).
7. J. I. Gittleman and E. K. Sichel, *J. Elec. Mater.*, **10**, 327 (1981).
8. H. B. Brom, Y. Tomkiewicz, A. Aviram, A. Broers, and B. Sunners, *Solid State Commun.*, **35**, 135 (1980).
9. E. K. Sichel and T. Emma, *Solid State Commun.*, **41**, 747 (1982).
10. A. MacDiarmid, *Synthetic Metals*, **1**, 101 (1979).
11. H. Gaarrett De Young, *High Technol.*, p. 65, (Jan.), (1983).
12. D.R. Day and J. B. Lando, *J. Appl. Polym. Sci.*, **26**, 1605 (1981).
13. S. K. Bhattacharya and A. C. D. Chaklander, *Polym. Plast. Technol. Eng.*, **19**, 21 (1982).
14. D. Day, *Am. Chem. Soc. Symp. Ser.*, **242**, 424 (1984).

Received January 22, 1985

Accepted February 7, 1985

Electrical conductivity and electron spin resonance studies of pyrolysed polyimide

C. Z. Hu, K. L. DeVries and J. D. Andrade

Department of Material Science and Engineering, University of Utah, Salt Lake City, Utah 84112, USA

(Received 20 August 1986; accepted 17 October 1986)

Recent studies of polymer-based pyrolytic amorphous carbon for use in organic electrolyte-lithium batteries and as metal-doped carbon electrodes show considerable promise. Polyimide can be thermally converted to amorphous carbon films. The irreversible evolution of polyimide under progressive heat treatment is characterized by three successive structural changes: pyrolysis, carbonization and graphitization. Four-point contact conductivity and electron spin resonance (e.s.r.) measurements were used to study and correlate electrical conductivity changes with unpaired electrons. From these studies it is concluded that at low pyrolysis temperature ($< 650^{\circ}\text{C}$) the pyrolysed polyimide is a nonmetallic amorphous carbon incorporating residual oxygen and nitrogen. At higher pyrolysis temperatures ($> 700^{\circ}\text{C}$) a microcrystalline graphite-like metallic domain starts to appear in the amorphous matrix. The development of this 'metallic domain' causes the conductivity of the pyrolysed polyimide to increase sharply.

(Keywords: conductivity; electron spin resonance; pyrolysed polyimide)

INTRODUCTION

The major means of making conducting polymers has been by various treatments which change the insulating nature of the polymer to a semiconductor or conductor. Conducting polymers have been achieved in three distinct ways. The first method for increasing the conductivity of polymers is through incorporation of macroscopic pieces of conducting materials, such as metal flakes or carbon black particulates, into host polymers to form conducting composites¹. The second method of producing conducting polymers is by means of chemical doping, electrochemical treatment, etc. The two polymers of this type that have been studied most extensively in the past several years are polyacetylene and polydiacetylene²⁻⁴. The third method of making a conducting polymer is by modifying the intrinsic bulk properties of polymers by pyrolysis. Recently studies have shown drastic changes in electronic properties of some aromatic base polymers after pyrolysis^{5,6}.

The main reasons for selecting polyimide for the pyrolysis work are: (a) Polyimide is available in plastic sheet, fibre and solution forms. Almost any desired shape of polyimide can be achieved by these three forms. For example very thin polyimide can be obtained by the spin-casting technique and patterned polyimide can be obtained by photolithographic techniques. (b) The pyrolysis process of making polyimide conductive is simple and inexpensive, unlike most other methods of producing conducting polymers which require complex laboratory equipment and skill. (c) By controlling the pyrolysis conditions, the polyimide conductivity can be made to range from 10^{-5} to 10^3 S cm^{-1} . This wide range of conductivities warrants further study of pyrolysed polyimide as a light weight material for unique conductor or semiconductor application. (d) Polyimide makes an interesting model compound for studying amorphous carbon. Pyrolysed polyimide is an amorphous carbon

($> 90\%$ carbon content) and since it can be prepared by a variety of experimental methods it is a good candidate for studying the properties of amorphous carbon. (e) Pyrolysed polyimide has great potential for applications in carbon electrodes, biomedical devices, low temperature heating elements, patternable conductor circuitry, electromagnetic shielding, radiation and gas detectors^{7,8}.

EXPERIMENTAL

Materials

The material investigated in this study was Kapton[®] film, supplied by DuPont, in sheet form (0.13 mm thickness). Pre-cut Kapton films were sandwiched between to quartz plates to prevent the Kapton film from curling during pyrolysis. The Kapton films were pyrolysed in an argon atmosphere at various temperatures and times. The resulting pyrolysed polyimide was a flat black film with reduced flexibility and a metallic lustre.

Conductivity measurements

The electrical conductivity of pyrolysed Kapton was measured by a four-point contact method⁹, and the measurement of temperature dependence of the conductivity was achieved with a DISPLEX compressor system.

E.s.r. absorption measurements

Pyrolysed Kapton films produced by various pyrolysis conditions were ground under a nitrogen atmosphere, and the resulting powder was loaded into e.s.r. sample tubes. The tubes were then held under vacuum for 24 hours prior to e.s.r. measurement. The e.s.r. measurements were made with a Varian Model E-3 ESR spectrometer in which the resulting spectra were first

derivatives of absorption vs. applied magnetic field. The free radical concentration of each pyrolysed Kapton sample was obtained by double integration of these spectra and comparison with a standard pitch sample (supplied by Varian) as described in ref. 10.

RESULTS AND DISCUSSION

The room temperature conductivity of pyrolysed Kapton as a function of pyrolysis temperature is given in Figure 1. For pyrolysis temperatures above 700°C, conductivity gradually increased to 10^{-2} S cm $^{-1}$ up to a temperature of approximately 800°C. This was followed by a rather abrupt increase in conductivity as the pyrolysis temperature was increased from 800 to 850°C, from approximately 3.5 to 20 S cm $^{-1}$. For temperatures greater than 850°C, conductivity again slowly increased with increasing pyrolysis temperature. Samples held at a pyrolysis temperature for 1 hour (line B in Figure 1) exhibited similar behaviour for conductivity vs. pyrolysis

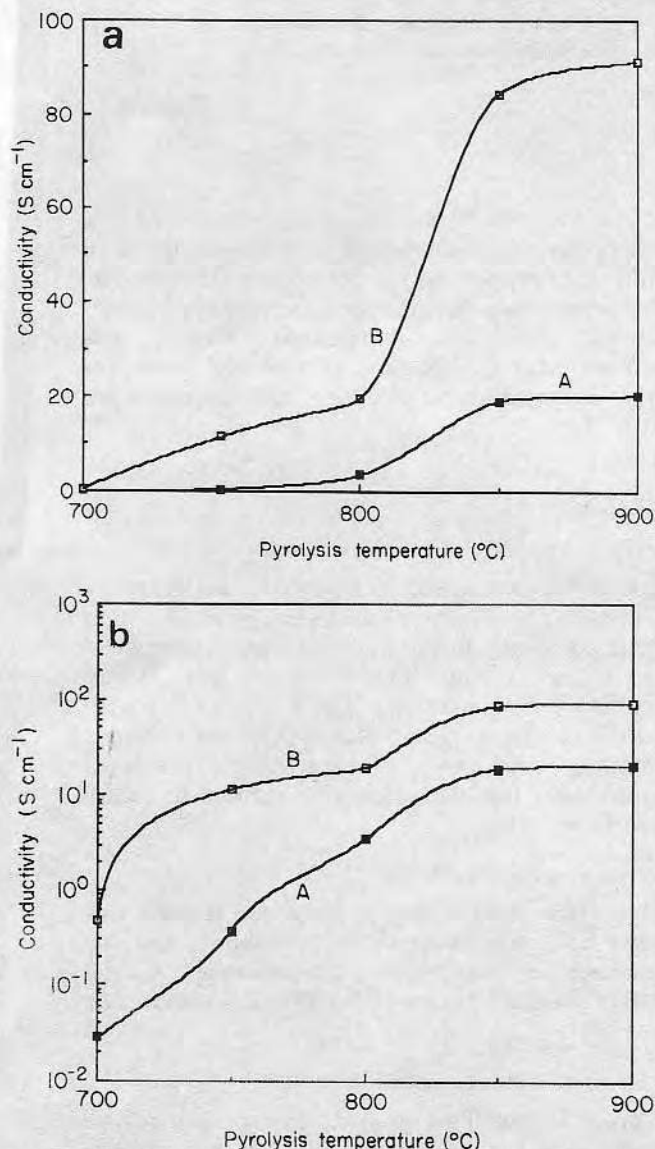


Figure 1 (a) Conductivity versus pyrolysis temperature for Kapton. Line A: sample cooled immediately after reaching the desired temperature and line B: sample held at desired temperature for 1 h. (b) Conductivity versus pyrolysis temperature for Kapton. Line A: a sample cooled immediately after reaching the desired temperature and line B: sample held at desired temperature for 1 h

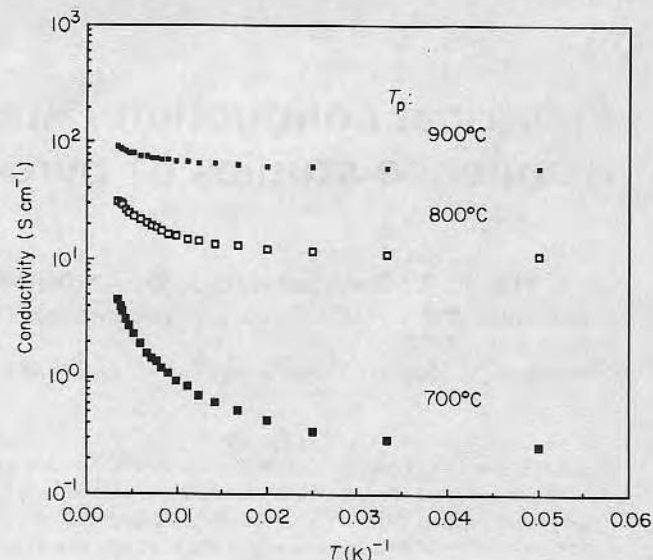


Figure 2 Temperature dependence of conductivity versus T^{-1} for Kapton pyrolysed 1 h at 700, 800 and 900°C

Table 1 Temperature-independent conductivity of pyrolysed Kapton

Pyrolysed Kapton	$^a T$ (S cm $^{-1}$)	$^b T.I.C.$ (S cm $^{-1}$)
700°C, 1 h	4.48	0.25
800°C, 1 h	31.8	10.5
900°C, 1 h	91.7	59.0

$^a T$ = Total conductivity

$^b T.I.C.$ = Temperature-independent conductivity

temperature with a similar step increase in conductivity from 24 to 83 S cm $^{-1}$ as the pyrolysis temperature was increased from 800 to 850°C. These conductivity experiments indicate that the polyimide changes from an insulator to a semiconductor at pyrolysis temperatures of the order of 700°C ($> 10^{-2}$ S cm $^{-1}$) and to a 'metallic' conductor at pyrolysis temperatures higher than 900°C ($\sim 10^2$ S cm $^{-1}$). The step change in conductivity between 800°C and 850°C suggests the presence of a thermally activated process which results in the formation of dense heterocyclic carbon ring networks in the polymer.

The inverse temperature dependence of the electrical conductivity ($\log \beta$ vs. $1/T$) of the polyimide pyrolysed at T_p (pyrolysis temperature) = 700°C, 800°C, 900°C is shown in Figure 2. The plots of conductivity vs. temperature in Figure 2 exhibit temperature-independent conductivity at low temperatures. The amplitude of this temperature-independent conductivity is dependent on the pyrolysis temperature is shown in Table 1. The temperature-independent conductivity was subtracted from the original temperature dependent conductivity data for each pyrolysed Kapton sample. Plots of \log conductivity vs. $T^{-0.25}$, after subtracting the temperature-independent conductivity, are shown in Figure 3. The total conductivity of the pyrolysed polyimide at various pyrolysis temperatures can be closely approximated by an equation of the form

$$\beta = \beta(m) + \beta(T) = \beta(m) + \beta_1 \exp[-(T_0/T)^{1/4}]$$

where $\beta(m)$ is the temperature-independent conductivity and $\beta_1 \exp[-(T_0/T)^{1/4}]$ is the temperature-dependent conductivity. This is consistent with Mott's variable-range hopping mechanism¹¹.

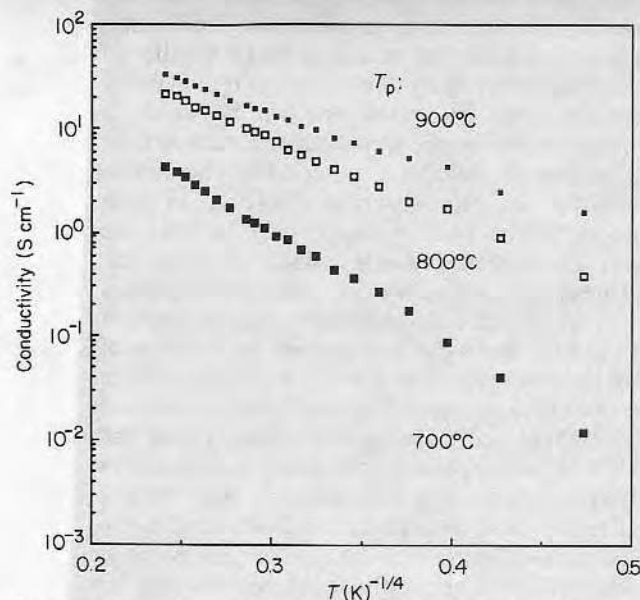


Figure 3 Temperature-dependent part of the conductivity versus $T^{-1/4}$ for Kapton pyrolysed at 700, 800 and 900°C

The existence of a temperature-independent conductivity at low temperature is thought to involve an irreversible disorder-induced nonmetal-metal transition. The Cohen-Jortner Transition model (CJT) for such a transition has been proposed for amorphous carbon¹². In contrast to the Anderson-Mott Transition¹³, the CJT model explains inhomogeneous material conductivity. Pyrolysed polyimide is considered to be a type of amorphous carbon. According to this model different structure changes of pyrolysed polyimide are considered to occur during three pyrolysis temperature dependent regions: pyrolysis at temperatures less than 700°C, carbonization at temperatures between 700°C and 1800°C, and graphitization at temperatures greater than 1800°C¹⁴. The microscopic inhomogeneities of pyrolysed polyimide are caused by growing heterocyclic carbon rings within the amorphous carbon matrix at pyrolysis temperatures higher than 700°C. These structural inhomogeneities also cause inhomogeneities in the electronic structure. From an electric conduction point of view, the pyrolysed polyimide has metallic domains in a nonmetallic amorphous carbon medium. These metallic domains are the result of local development of heterocyclic carbon rings which form graphite-like dense heterocyclic carbon ring networks with strong π -orbital overlap.

The conductivity experiments clearly demonstrate that the pyrolysed polyimide is converted to a high electrical conductor by pyrolysis. At low pyrolysis temperatures the pyrolysed polyimide is in an amorphous state and electric conduction is due to variable-range hopping. At temperatures higher than 700°C, the pyrolysed polyimide is in a heterogeneous state with two conducting paths: one is a metallic channel with extended electronic states for which the conductivity has no temperature dependence, and the other is a disordered system where the electron conduction is by a variable-range hopping mechanism.

Electron spin resonance spectroscopy was used to probe the 'break up' of the polymer structure through thermal degradation (scission) of covalent bonds. The resulting spectra had no fine structure to identify the

location of the unpaired electrons. It is not certain if these unpaired spins (hereafter referred to as free radicals or spins) are associated with specific organic free radicals or perhaps on isolated very small clusters of amorphous carbon. The g value of the spectra was very near the 'free electron' value of 2 consistent with organic free radicals.

The time dependence of the e.s.r. spin concentration for Kapton pyrolysed at 550°C is shown in Figure 4. The corresponding weight loss is also shown in Figure 4. The initial e.s.r. spin concentration was about 6×10^{18} spins/gram. The maximum spin concentration reached 9.8×10^{18} spins/gram after 50 min pyrolysis, after which it started to decrease and became flat at a spin concentration near 6×10^{18} spins/gram after three hours pyrolysis. The sample heat treated at 550°C shows that the e.p.r. spin concentration increases with pyrolysis time and reaches a maximum after 50 min of heating. Most polyimide weight loss also occurs during the first 40 min of the heating period, with only a slight change in weight observed beyond 40 min. During this time hydrogen, carbon monoxide and carbon dioxide are given off as the result of cleavage of polyimide functional groups and C-H bonds, simultaneously creating reactive β -radicals. Once reactive β -radicals are created, followed by a limited polycondensation of the aromatic rings through the reactive β -radical, stable π -radicals are formed¹⁴. The process of forming stable π -radicals is described by Lewis¹⁵. After the spin concentration reaches a maximum, at about 50 min pyrolysis, a drastic decrease of spin concentration is observed which finally levels off after about 120 min. This diminishing of the spin concentration is thought to arise from a pairing of the free radicals during the pyrolysis process. At 550°C the reorganization of scissioned aromatic rings through free radical pairing is limited by this low temperature with the result that only isolated or semi-isolated condensed aromatic rings are formed. The material in this stage is still an insulator ($> 10^{-6}$ S cm⁻¹) and no conductivity can be detected at this pyrolysis temperature.

A comparison between the time dependence of the e.s.r. spin concentration and four-point contact conductivity for Kapton pyrolysed at 650°C is shown in Figure 5. The e.s.r. spin concentration vs. time curve exhibits an initial spin concentration of about 5.3×10^{18} spins/gram, with a distinct drop of spin concentration to nearly 1.6×10^{18}

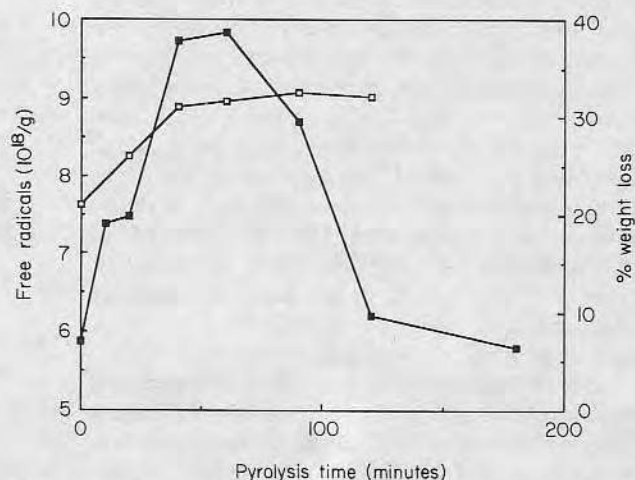


Figure 4 Time dependence of e.s.r. spin concentration (■) and percent weight loss (□) for Kapton pyrolysed at 550°C for different periods of heating time

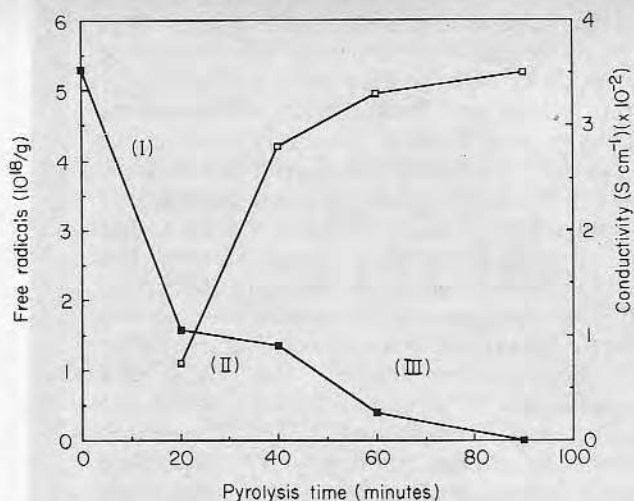


Figure 5 Time dependence of e.s.r. spin concentration and conductivity for Kapton pyrolysed at 650°C for different periods of heating time

spins/gram after 20 min (region I), followed by a gradual decrease to 1.3×10^{18} spins/gram after 40 min heating (region II), and subsequently decreasing to 2.3×10^{15} spins/gram (region III). The conductivity of the pyrolysed Kapton sample was $9 \times 10^{-3} \text{ S cm}^{-1}$ after 20 min heating and reached a plateau value of $3.2 \times 10^{-2} \text{ S cm}^{-1}$ for heating periods greater than 60 min. For polyimide pyrolysed at 650°C the spin concentration did not increase nor was significant weight loss detected. The samples for the 650°C e.s.r. time dependent measurements were prepared by heating the polyimide from room temperature to 650°C at a constant heating rate of 10°C/min. After the polyimide sample reached the desired temperature it was maintained at that temperature for the desired time, and then cooled to room temperature. During this heating process when the temperature only exceeded 550°C slightly, the polyimide started to dissociate reaching near completion at temperatures above 600°C. At this time the free radicals had already been created and then paired during the heating stage from 550°C to 650°C of the pyrolysis treatment. The spin concentration vs. time curve of Kapton pyrolysed at 650°C can be divided into three regions as follows: (I) A step decrease of spin concentration within 20 min pyrolysis time associated with the radical pairing process. (II) A very gradual decrease in spin concentration observed in the 20 to 40 min heating period. The flat region corresponds to the change in conductivity of pyrolysed Kapton from insulator to semiconductor (conductivity greater than $10^{-4} \text{ S cm}^{-1}$). It is hypothesized that this is the result of the semi-isolated or isolated heterocyclic carbon rings gradually merging into a continuous network of dense heterocyclic carbon rings with the development of increasingly effective π -orbital overlap¹⁶. In order to initiate the development of dense and continuously heterocyclic carbon ring networks, the pyrolysis temperature of polyimide should be no less than 600°C. This is a thermally activated process. (III) A step decrease of spin concentration is observed after a 40 min heating period. The diminishing of the free radical concentration in this stage is caused by the growth of heterocyclic carbon rings, followed by sufficient development of π -orbital overlap to induce a change in the electronic structure of the material from insulator to semi-metallic.

Experimentally, electron spin resonance of conduction electrons has been observed in only a small number of metals^{17,18}. This is very likely due to the fact that in many metals the electronic resonance line width (which is inversely proportional to the spin-lattice relaxation time T_1) is so large that the signal is unobservable. Therefore a possible reason for the observed decrease in spin concentration, in the present study, may be that the mobility of those free radicals, which exist in the heterocyclic carbon ring networks, gradually increases and becomes more and more like conducting electrons in metals. If this hypothesis can be accepted, the increase of mobility of those free radicals will cause the spin-lattice relaxation time T_1 to decrease. The result of this structural change is that the e.s.r. absorption intensity and the measurable free radical concentration decreases. Because the pyrolysis temperature is insignificantly high, only a portion of the isolated heterocyclic carbon rings in the sample can further recombine into dense heterocyclic carbon ring networks and only those regions will be converted from insulator to semi-metallic. Free radicals in those semi-metallic regions are undetected by e.s.r. spectroscopy. By comparing the degree of decreasing free radical concentration and the increase of conductivity between the 550°C and 650°C samples, it is concluded that the size of this heterocyclic carbon ring network is determined by the pyrolysis temperature and time. The rule of thumb is the higher the pyrolysis temperature and longer the time the larger the heterocyclic carbon ring network.

The pyrolysis temperature dependence of the e.s.r. absorption measurement is shown in Figure 6. A plot of full width half maximum (FWHM) of the e.s.r. peak vs. pyrolysis temperature is shown in Figure 7 (in arbitrary units). The FWHM was increased from 8.5 to 11.9 Gauss with a pyrolysis temperature change from 550°C to 650°C. Figure 6 illustrates the e.s.r. absorption measurement of Kapton as a function of different pyrolysis temperatures along with the corresponding weight loss. The spin concentration initially increased from 5.8×10^{18} to a maximum of 9.4×10^{18} spins/gram (corresponding to pyrolysis temperature increase from 550°C to 600°C) followed by a rapid decrease to

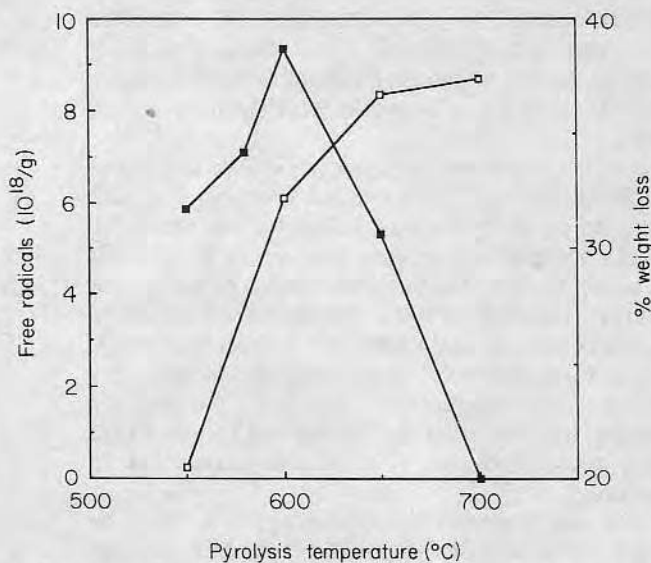


Figure 6 E.s.r. spin concentration (■) and percent weight loss (□) as a function of pyrolysis temperature for Kapton

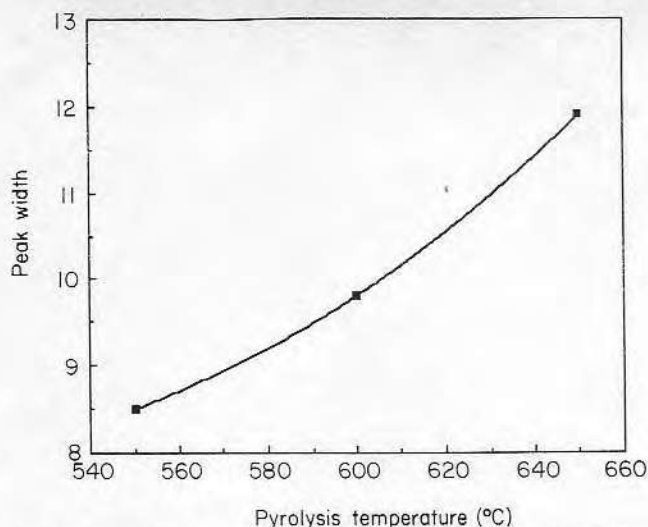


Figure 7 E.s.r. peak width as a function of pyrolysis temperature for Kapton

9.5×10^{15} spins/gram at a pyrolysis temperature of 700°C . The corresponding weight loss slowly increased from 20 to 37.4%. Most polyimide weight loss also occurs during the temperature change from 550°C to 650°C with only a small change in weight observed beyond 40 min. The e.s.r. absorption curve of Kapton at temperatures below 700°C shows a Curie doublet type spectrum. A gradual increase of spin concentration at temperatures between 550°C and 600°C is matched by the strong dissociation of the polyimide. The free radicals generated during this period of strong dissociation are still limited to isolated individual aromatic carbon rings. At pyrolysis temperatures between 600°C and 700°C , the Kapton sample is in transition between the two different processes. At temperatures just higher than 600°C , continuous thermal dissociation (which creates the free radical) and limited heterocyclic carbon ring condensation (with free radical pairing) are possible. Apparently, in this temperature range the latter process dominates and the spin concentration of the pyrolysed Kapton gradually decreases as the pyrolysis temperature increases. As the pyrolysis temperature is further increased, the thermal degradation and free radical pairing process continuously decreases. Eventually, both processes will become insignificant at temperatures higher than some critical temperature T_c (T_c is between 600°C and 700°C). With temperatures above this critical temperature, the carbonization process becomes dominant. Pyrolysed polyimide at this stage starts to form a continuous dense heterocyclic carbon ring network and sufficient π -orbital overlap is developed to form semi-metallic regions. Conductivity at 700°C approaches 10^{-2} Scm^{-1} indicating the pyrolysed polyimide has become a semiconducting material. As pyrolysis temperatures exceed 700°C , there is an abrupt disappearance of the e.s.r. absorption spectra and an increase in conductivity indicating the formation of metallic-like conduction electrons. As mentioned earlier, the conduction electron has a very short spin-lattice relaxation time T_1 and a corresponding e.s.r. peak width inversely proportional to T_1 , resulting in a significantly broadened e.s.r. peak width resulting in a disappearance of the e.s.r. signal. The increasing e.s.r. peak width versus pyrolysis temperature probably implies a gradual increase in semi-metallic regions.

CONCLUSIONS

The temperature dependent conductivity experiments suggest that pyrolysed polyimide from low temperature pyrolysis (less than 700°C) contains homogeneous amorphous carbon consistent with the Mott variable-range hopping mechanism. At temperatures higher than 700°C , metallic conductivity arises (temperature-independent conductivity), due to the inhomogeneity of the pyrolysed polyimide. It is proposed that this metallic conductivity is due to the formation of graphite-like metallic domains with extended electronic states that increase with pyrolysis temperature. The total conductivity of pyrolysed polyimide is equal to the conductivity contributed by metallic conduction, which is independent of temperature, $\beta(m)$, plus the temperature-dependent conductivity contributed by the non-metallic amorphous carbon medium, $\beta(T)$, which obeys the Mott variable-range hopping conduction mechanism.

The free radicals created during polymer scission can be investigated by e.s.r. There are three major processes occurring during high temperature heat treatment. At low pyrolysis temperature (less than 600°C), stable π -radicals are created by thermal degradation of polymer chains. At pyrolysis temperatures higher than 600°C , but less than 700°C , free radicals created by thermal scission of polyimide chains are paired with each other and form larger heterocyclic carbon rings. Finally, at pyrolysis temperatures higher than 650°C , a decrease in e.s.r. signals observed associated with a corresponding increase in conductivity suggesting that the formation of conduction electrons during carbonization leads to formation of continuous dense heterocyclic carbon ring networks with sufficient π -orbital overlap to result in a disappearance of the e.s.r. signal.

ACKNOWLEDGEMENTS

The e.s.r. equipment used in the study was made available by a National Science Foundation Polymer Program Grant.

REFERENCES

- 1 Bhattacharya, S. K. and Chaklander, A. C. C. *Polym. Plast. Technol. Eng.* 1982, **19**, 21
- 2 MacDiarmid, A. G. and Heeger, A. J. *Synth. Met.* 1980, **1**, 101
- 3 Baughman, R. H. and Yee, K. C. *J. Polym. Sci., Macromol. Rev.* 1978, **13**, 219
- 4 Baughman, R. H. *J. Polym. Sci., Polym. Phys. Edn.* 1974, **12**, 1511
- 5 Gittleman, J. I. and Sichel, E. K. *J. Elect. Mater.* 1981, **10**, 327
- 6 Murakami, M., Yasujima, H. and Yoshimura, S. *Solid State Commun.* 1983, **45**, 1085
- 7 Theodoridou, E., Jannakoudakis, A. D. and Jannakoudakis, D. *Synth. Met.* 1984, **9**, 19
- 8 Colla, J. O. Technical Digest, IEEE Solid-State Sensors Work Shop, 1986
- 9 van der Pauw, L. J. *Phillips Res. Repts.* 1958, **13**, 1
- 10 Hu, C. Z. *Ph.D. Dissertation*, University of Utah, Salt Lake City, Utah 1986
- 11 Mott, N. F. *Phil. Mag.* 1969, **19**, 835
- 12 Cohen, M. H. and Jortner, J. *Phys. Rev. Lett.* 1973, **30**, 699
- 13 Mott, N. F. and Davis, E. A. 'Electronic Processes in Non-crystalline Solids', Oxford University Press, Oxford, 1972
- 14 Walker, P. L. and Thrower, P. A. 'Chemistry and Physics of Carbon', Vol. 17, Marcel Dekker, New York, 1981
- 15 Lewis, I. C. *Carbon* 1980, **18**, 191
- 16 Bruck, S. D. *Polymer* 1965, **6**, 319
- 17 Singer, L. S. *Proc. 5th Carbon Conf.*, Vol. 2, Pergamon, New York, 1963, p.37
- 18 Winter, J. 'Magnetic Resonance in Metals', Oxford University Press, 1971, p. 152

Structural Determination of Pyrolyzed PI-2525 Polyimide Thin Films

C. Z. HU, J. D. ANDRADE, and P. DRYDEN, *Department of Materials Science and Engineering, and Department of Bioengineering, College of Engineering, University of Utah, Salt Lake City, Utah 84112*

Synopsis

Polyimide was pyrolyzed in an argon atmosphere at various temperatures, and thermally converted to amorphous carbon films. The irreversible change of polyimide under progressive heat treatment is characterized by three successive structural changes: pyrolysis, carbonization, and graphitization. X-ray photoelectron spectroscopy (XPS) studies show that the polyimide starts to dissociate at pyrolysis temperatures above 500°C. At temperatures higher than 650°C most functional groups of polyimide decompose to evolve gases from the sample. The polyimide then gradually becomes more carbon rich. It is believed that at pyrolysis temperature higher than 650°C the polyimide starts to form heterocyclic structures with residual oxygen and nitrogen incorporated into the heterocyclic carbon rings. X-ray analyses indicate that the polyimide at pyrolysis temperatures less than 1000°C is amorphous carbon and no long-term periodic structure can be detected. At pyrolysis temperatures higher than 2000°C, the polyimide is converted to microcrystalline graphite.

INTRODUCTION

Carbon fibers have been prepared by thermal treatment of a large variety of polymeric precursors such as cellulose, rayon, polyacrylonitrile, and aromatic polyamides.^{1,2} The polymer-based, high temperature-treated carbon fibers are used in high-performance composite materials in aeronautic and aerospace applications. Later pyrolysis studies on other polymers such as polyphenylene-1,3,4-oxadiazole, polyaminoquinones, and aromatic polyimide have focused on their conductivity properties.³⁻⁵ High temperature pyrolysis of these aromatic-based polymers converts them from insulators to semiconductors and then to metallic-like conductors.⁶

Pyrolyzed polyimide is somewhat different from other graphitizable polymers such as polyacrylonitrile and rayon. The latter are usually heated to very high temperatures (over 2000°C), resulting in short, thin graphitized carbon fibers. In our experiment, the polyimide is pyrolyzed mainly at temperatures below 1000°C. The resulting pyrolyzed polyimide thin film is a highly conductive carbon-rich film which may be useful for applications requiring light weight, flat, chemical, and heat-resistant conducting materials, and it already shows a promising future in gas and radiation detectors.⁷

MATERIALS AND METHODS

In our experiment, two kinds of commercially available polyimides (manufactured by DuPont de Nemours and Co) were used; PI-2525 polyamic

17. R. Vidano and D. B. Fischbach, *ACS*, **61**, 13 (1978).
18. F. Tuinstra and J. L. Koenig, *J. Chem. Phys.*, **53**, 1126 (1970).
19. L. J. Brillson, E. Burstein, A. A. Maradudin, and T. Stark, *J. Phys. Chem. Solids* (Suppl.), **32**, 187 (1971).
20. M. Nakamizo, R. Kammereck, and P. L. Walker, Jr., *Carbon*, **12**, 259 (1974).
21. F. Tuinstra and J. L. Koenig, *J. Compos. Mater.*, **4**, 492 (1970).
22. T. G. Miller, D. B. Fischbach, and J. M. Macklin, *Bienn. Conf. Carbon, Ext. Abstr. Program* 12th, 105 (1975).
23. C. Z. Hu, Ph.D. dissertation, University of Utah, Salt Lake City, Utah, 1986.

Received March 30, 1987

Accepted May 4, 1987

1 ast P.

solution and Kapton. PI-2525 polyamic acid solution was used for XPS, X-ray, and Raman analyses. The polyamic acid solution was spin-cast on the substrate, followed by two drying and curing stages in a nitrogen atmosphere at 100 and 200°C each for 2 h, during which the polyamic acid was undergoing the imidization process. After 2 h at 200°C, the polyamic acid was fully cured and converted to polyimide. Kapton is a fully cured polyimide and was used for synthesis and X-ray studies. Both polyimides are chemically identical and have the structure which was described in a previous paper.⁸

For pyrolysis, the polyimide sample was placed inside a small quartz tube oven, and low pressure argon gas was passed through the quartz tube. The argon gas was adjusted to approximately 5 cc/s flow rate. Gas flow was maintained at least 5 min to allow the system to reach steady state before heating began. The polyimide was brought to the desired pyrolysis temperature by setting a fixed heating rate (10°C/min). Usually, the pyrolysis temperature was in the range of 500–900°C. After the desired conditioning, the pyrolyzed polyimide was cooled down to room temperature under argon atmosphere to prevent possible oxidation and then removed from the furnace. The film was then ready for examination.

Wide Angle X-Ray Analysis

Structural features of pyrolyzed polyimide were studied by wide angle X-ray analyses. From these analyses, one can determine at what pyrolysis temperature the pyrolyzed polyimide starts changing from amorphous state to microcrystalline graphite. Wide angle X-ray analyses were performed in the DIANO Diffractometer, using CuK_α monochromatic radiation.

Raman Spectroscopy Analysis

Raman studies can provide further information about whether the pyrolyzed polyimide is in amorphous or crystalline state. In our experiment, an Ar-laser was used to emit an intense laser beam with a fixed wavelength (488 nm). The emitted laser light passed through a lens and was focused on the pyrolyzed polyimide sample. The scattered Raman light was collected, passed through a monochromator, and detected by a photon counter. The final output was a plot of photon intensity (count) versus the wavenumber shift from the laser line.

X-Ray Photoelectron Spectroscopy Analysis (XPS)

XPS analysis provides information on chemical states and elemental ratios of polyimide pyrolyzed at various temperatures. XPS analyses were performed on a Hewlett-Packard 5950B Electron Spectrometer, using a monochromatic AlK_α X-ray source.

RESULTS

Apparent Density

The apparent density of polyimide pyrolyzed at temperatures between 700 and 900°C is plotted in Figure 1. It shows that the density of pyrolyzed polyimide increased from 1.49 to 1.57 g/cm³.

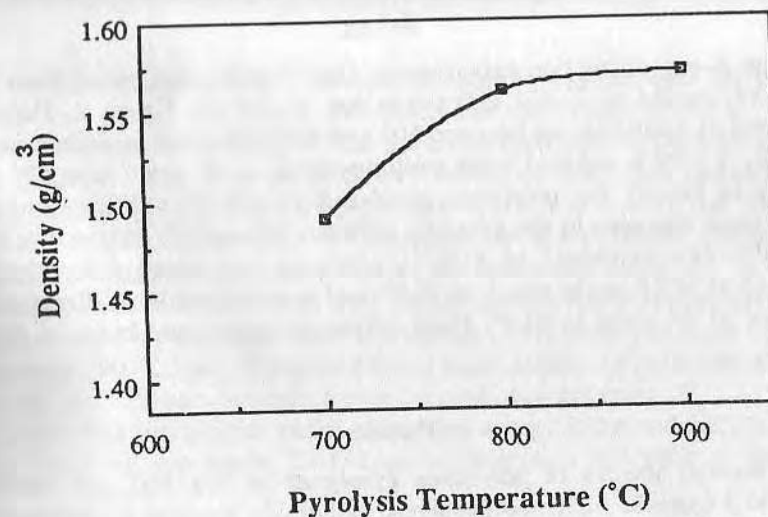


Fig. 1. Apparent density of polyimide film as a function of temperature of pyrolysis.

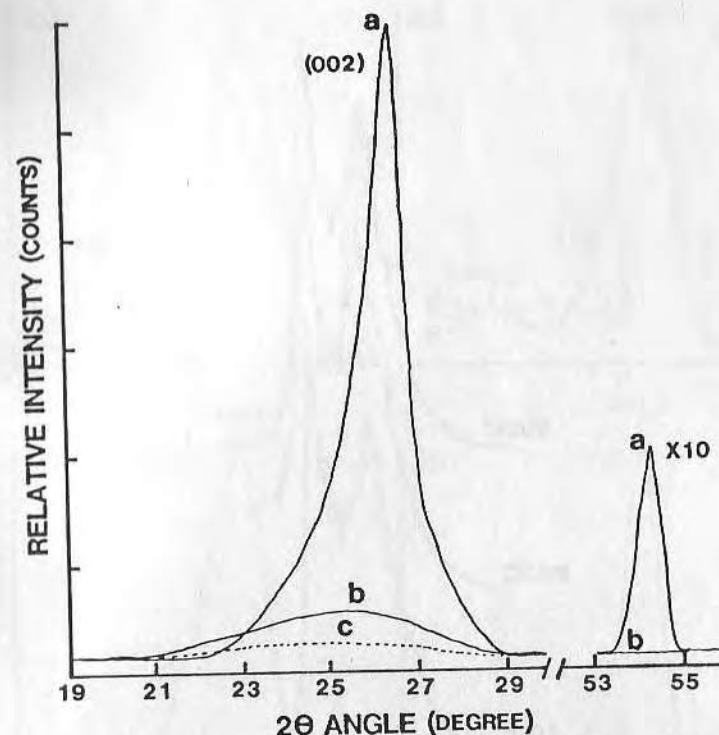


Fig. 2. Wide-angle X-ray diffraction of polyimide pyrolyzed at the temperatures noted: Line a: 2100°C; line b: 1500°C; line c: < 1000°C.

X-Ray

In the X-ray diffraction experiments, the 2θ angle was swept from 15° to 80° . The results of X-ray diffraction are shown in Figure 2. Polyimides pyrolyzed at temperatures between 500 and 900°C showed no diffraction peak and only a very broad and weak peak appeared at 2θ angle from 22° to 28° (curve c in Fig. 2). For polyimide pyrolyzed at 1500°C , a diffuse amorphous carbon peak was seen in the 2θ angle between 24° and 28° (curve b in Fig. 2). For polyimide pyrolyzed at 2100°C , a strong but broad diffraction peak appeared at a 2θ angle equal to 26.5° and a much weaker diffraction peak appeared at 2θ equal to 54.2° . Both diffraction peaks are shown in Figure 2 curve a.

Raman

The Raman spectra of polyimide pyrolyzed at 700, 800, and 900°C are shown in Figure 3. All three pyrolyzed polyimide samples at different heat treatments showed almost identical Raman spectra. Two Raman peaks appeared at 1640 and 1370 cm^{-1} . The intensity of the peak at 1640 cm^{-1} was higher than the peak at 1370 cm^{-1} .

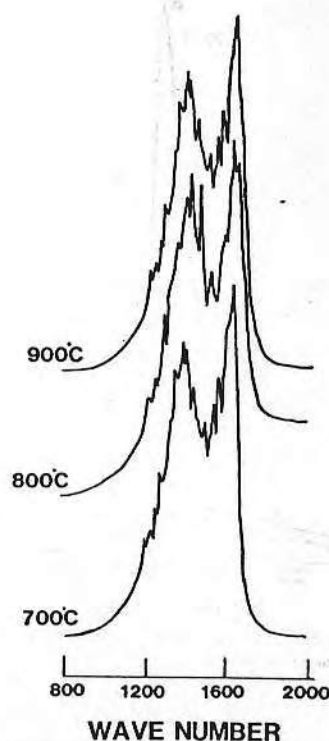


Fig. 3. Raman spectra of polyimide treated at 700, 800, and 900°C .

XPS

The detailed chemical state analysis of carbon, oxygen, and nitrogen of polyimide are shown in Figure 4. Polyimide has two carbon peaks at binding energies 288.3 and 284.6 eV , and has an unresolved carbon peak at binding energy 286.0 eV . The peak at 288.3 eV represents the imide carboxyl-type bonding and the peak at 286.0 eV represents C—O and C—N-type bonding.⁸ The peaks at 288.3 and 286.0 eV decreased as the pyrolysis temperature increased. At temperatures above 650°C , the imide carboxyl-type carbon 1s peak disappeared and only weak and broad oxygen and nitrogen carbon 1s peaks near 286.0 eV coexisted with the strong C—C main peak. As temperature exceeded 900°C , only a graphite C—C main carbon 1s peak was seen and no oxygen and nitrogen-bonded carbon 1s peak was detected.

Polyimide has two oxygen peaks at binding energy 533.3 and 532.0 eV . The peak at 532.0 eV represents C=O-type bonding and the peak at 533.3 eV

Carbon

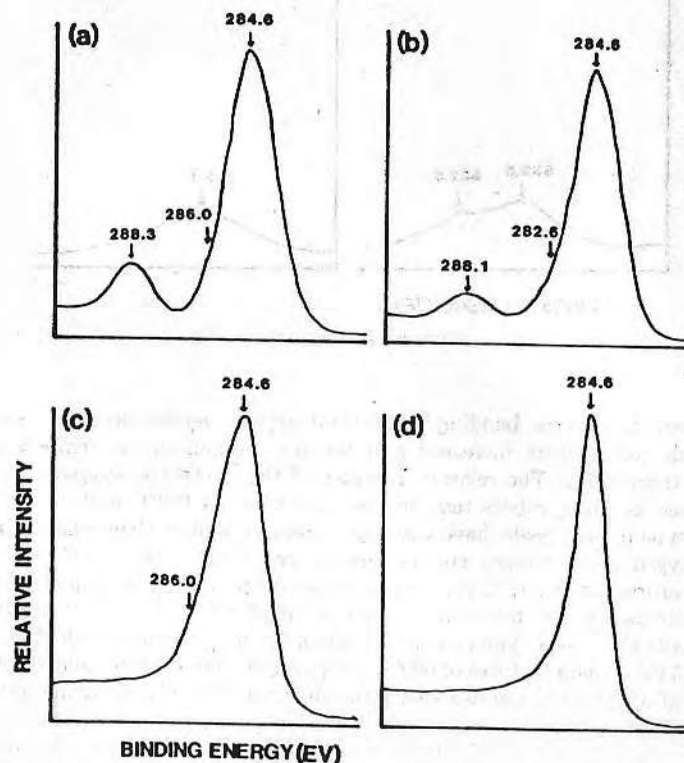


Fig. 4. Polyimide XPS narrow scan spectra of carbon, oxygen, and nitrogen 1s peaks: (a) raw material; after treatments at: (b) 600°C , (c) 650°C , and (d) 900°C .

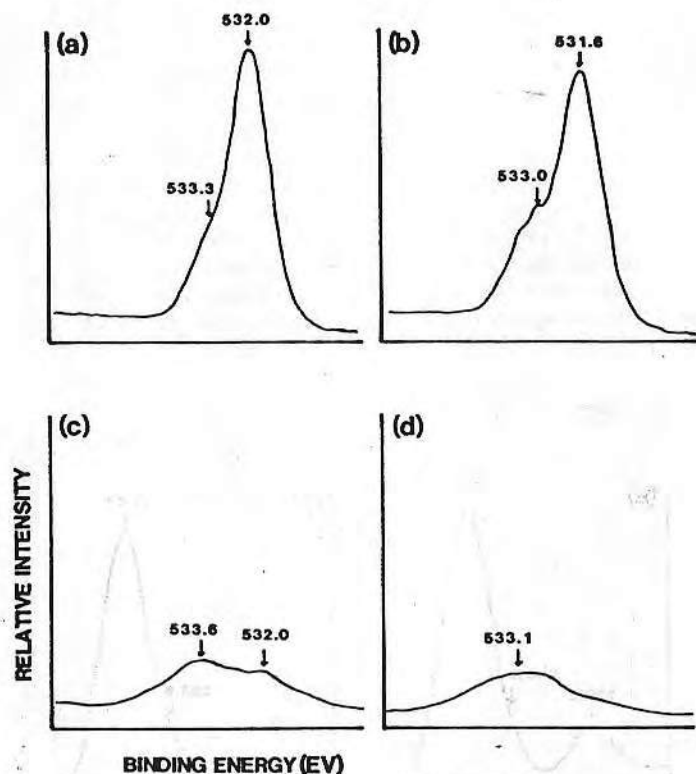


Fig. 4. (Continued from the previous page.)

represents C—O-type bonding.⁸ The total oxygen content decreased as the pyrolysis temperature increased and became insignificant at temperatures higher than 900°C. The relative intensity of the C=O-type oxygen 1s peak decreased as the pyrolysis temperature increased. At 650°C both C=O and C—O-type oxygen peaks have the same intensity, and at above 650°C, these two oxygen peaks merged and became a very broad peak at 533.1 eV. At temperatures above 900°C this broad oxygen 1s peak became insignificant.

Polyimide has one nitrogen 1s peak at 400.5 eV. The peak at 400.5 eV represents the C—N-type nitrogen bonding.⁸ A new nitrogen peak appeared at 398.5 eV at temperatures of 600°C. At pyrolysis temperatures above 600°C, the total intensity of the nitrogen peaks decreased sharply. At temperatures, above 650°C, both nitrogen peaks had the same relative intensity, and as the temperature reached 900°C, the two nitrogen 1s peaks became insignificant.

The theoretical elemental C:O:N ratio of polyimide is 76.0:17.4:6.9 XPS analyses showed the elemental C:O:N of polyimide was 77.5:16.5:6.0,

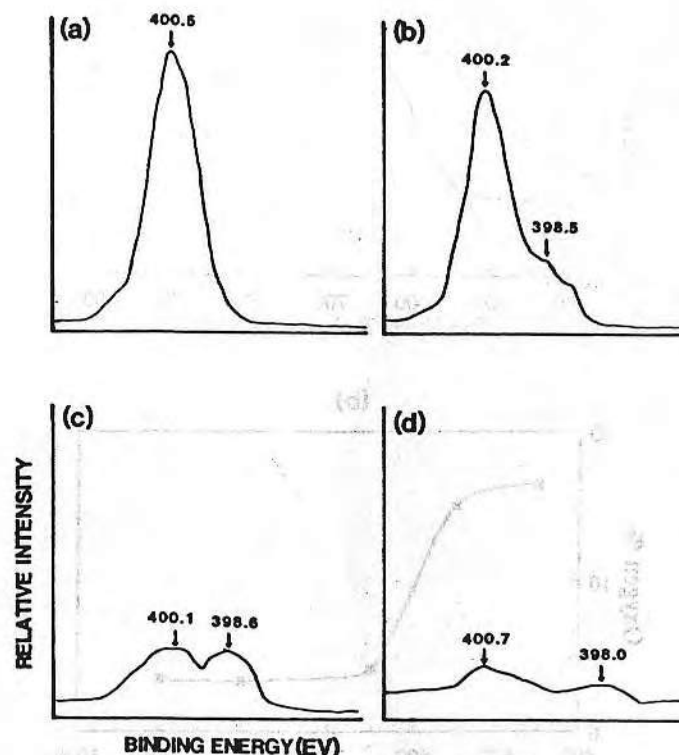


Fig. 4. (Continued from the previous page.)

which shows the XPS analyses indeed agreed quite well with the theoretical prediction.

The percent change of carbon, oxygen, and nitrogen in polyimide versus pyrolysis temperature is shown in Figure 5, and elemental compositions versus pyrolysis temperature are listed in Table I. Figure 5(a) shows that the carbon increased from 77.5 to 95.6% as the pyrolysis temperature increased from 450 (undissociated temperature) to 900°C. A step increase of carbon from 79.1 to 92.1% occurred between 550 and 650°C, and at temperatures above 700°C there was no significant increase in carbon content. Figure 5(b) indicates that the oxygen content decreased from 16.5 to 3.5% as the temperature changed from 450 to 900°C. A step change of oxygen content from 15.1 to 4.1% was observed as the temperature changed from 550 to 650°C. Figure 5(c) shows that the nitrogen content was constant at 6% at temperatures below 550°C, and started to decrease at temperatures higher than 550°C. The percent of nitrogen was changed from 5.8 to 0.9% as the temperature increased from 550

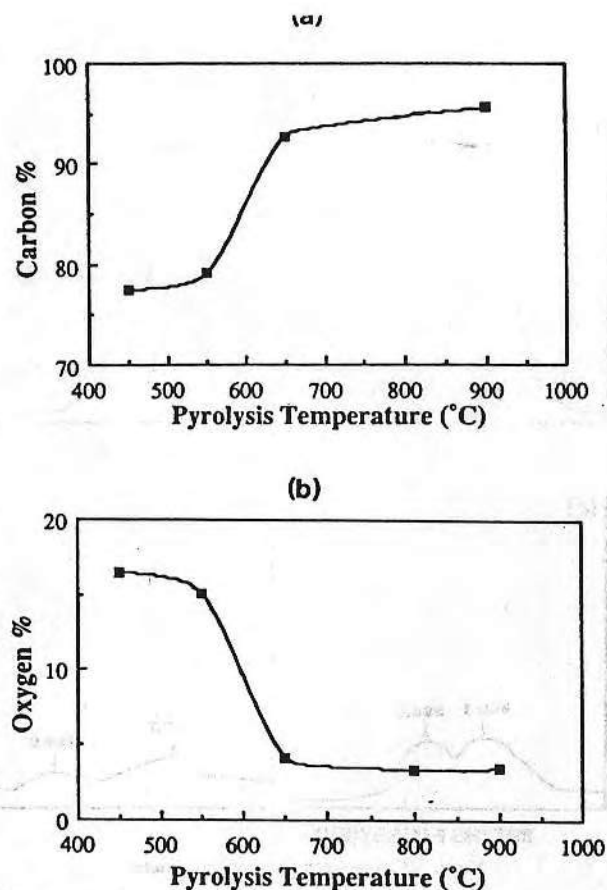


Fig. 5. The percent change in elemental carbon, oxygen, and nitrogen as a function of pyrolysis temperature for polyimide. (a) carbon, (b) oxygen, and (c) nitrogen.

to 900°C. At temperatures above 700°C no major changes of elemental composition were detectable.

DISCUSSION

Pyrolysis studies of polymeric material such as polyacrylonitrile (PAN) always show that at high enough pyrolysis temperatures (> 2000°C), the polymer is converted to microcrystalline graphite.⁹ X-ray studies of microcrystalline graphite show the interplane diffraction at (002) and two-dimensional lattice diffractions at (10) and (11). The 2θ angle for (002) diffraction is about 26.5°, for second-order (002) diffraction about 54.2°, for (10) about 44.5°, and for (11) about 78°. ¹⁰

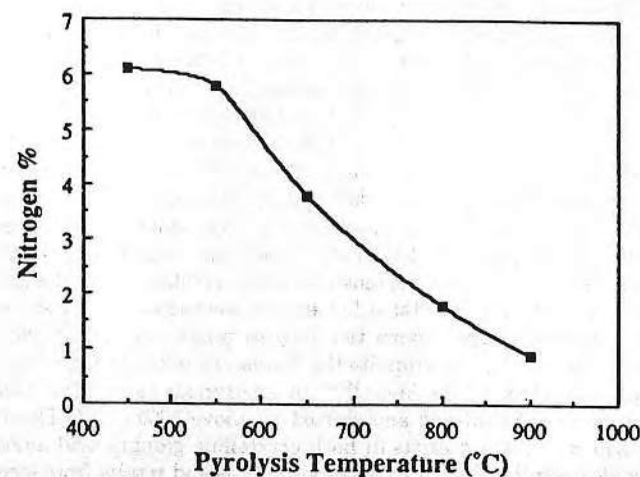


Fig. 5. (Continued from the previous page.)

TABLE I
Elemental Ratio of Pyrolyzed Polyimide at Different Pyrolysis Temperatures

Pyrolysis temp. (°C)	C	O	N
450	77.5	16.5	6.0
550	79.1	15.1	5.8
650	92.1	4.1	3.8
800	94.8	3.4	1.8
900	95.6	3.5	0.9

X-ray studies of polyimide pyrolyzed at different temperatures show that at temperatures less than 1000°C the material is in an amorphous state.^{11,12} The polyimide undergoes reorganization of short-range order of heterocyclic carbon ring units incorporating a small percent of residual oxygen and nitrogen. It is believed this local structural reorganization of heterocyclic carbon rings begins to form dense heterocyclic carbon domains (graphitic domain) with strong π -orbital overlap in the amorphous carbon matrix. No long-range ordered graphite layer structure has been observed and the inhomogeneity of polyimide due to the growing of graphitic domains cause the conductivity of pyrolyzed polyimide to increase into the semiconductor range.¹³ At temperatures above 1500°C, continuous growing of graphitic domains with increasing size of layer structure causes further increases in conductivity.¹³ The pyrolyzed polyimide in this stage is an inhomogeneous amorphous carbon. At temperatures above 2000°C, graphitization is complete, and the pyrolyzed

polyimide becomes microcrystalline graphite. The "apparent" size of the graphitic layer estimated by the Scherrer formula is in the range of 70 Å. The pyrolyzed polyimide in this stage is no longer amorphous carbon; the entire carbon matrix is polycrystalline graphite.¹⁴⁻¹⁶ The lack of (hk) diffraction may be caused by the following: Higher disorder and defect density along the (hk) planes, structural fluctuation of (hk) planes, and random organized layer structure. All these factors may make the intensity of (hk) diffractions become too weak to be detected by the X-ray diffractometer.

Other evidence that pyrolyzed polyimide is still an amorphous carbon at pyrolysis temperatures less than 1000°C is by Raman analyses. Vidano and Fischbach¹⁷ show the Raman spectrum for crystalline graphite has two strong peaks at 2700 cm⁻¹ and 1580 cm⁻¹, and one weak peak at 1360 cm⁻¹. The Raman peak at 2700 cm⁻¹ is sensitive to the crystallinity of the graphite; this Raman peak is not detectable for amorphous carbon. The Raman spectrum for amorphous carbon shows two Raman peaks; one at 1620 cm⁻¹ and the other at 1360 cm⁻¹.¹⁷ In graphite the Raman peak at 1580 cm⁻¹ is caused by in-plane vibrations of the layer.^{18,19} In amorphous carbon this peak still exists but becomes broadened and shifted to above 1600 cm⁻¹. The Raman peak at 1360 cm⁻¹, which exists in both crystalline graphite and amorphous carbon, is also associated with in-plane vibrations and results from structural imperfections and finite graphite size.²⁰⁻²²

The Raman spectra of polyimide pyrolyzed at temperatures ranging from 700 to 900°C are very similar to the amorphous carbon.¹⁷ The Raman peaks of polyimide at various pyrolysis temperatures all show two Raman peaks; one at 1640 cm⁻¹ and the other at 1370 cm⁻¹. These peaks are almost identical to the peak positions of the amorphous carbon. The relative peak intensity between these two peaks is very similar for both pyrolyzed polyimide and for amorphous carbon. It is believed that polyimide pyrolyzed at temperatures below 1000°C is amorphous carbon with a small percent of oxygen and nitrogen incorporated into the heterocyclic carbon rings. The microcrystalline graphite-like domains at this temperature are still insignificant but the growing graphitic domains have started to form microinhomogeneities in the pyrolyzed polyimide matrix.

Previous thermogravimetric studies indicate that the polyimides dissociate at temperatures between 500 and 600°C.⁸ At temperatures above 600°C, the weight loss rate slows and finally becomes insignificant above 700°C. The corresponding ESCA data show that most imide carbonyl functional groups indeed disappear at 600°C and the remaining oxygen is incorporated into the aromatic carbon rings and possibly form either quinone (—C=O) or bridging aromatic ether types of bonding with the graphitic carbon rings. A large decrease of C—N-type nitrogen above 600°C and the appearance of a new peak at 398.5 eV indicate that the nitrogen loss has started and the remaining nitrogen has either formed aromatic C—N-type bonding or has been conjugated into the aromatic carbon ring networks.³

Both ESCA and weight loss data show no significant weight loss or elemental ratio change at pyrolysis temperature between 700 and 900°C. This data indicates that the polyimide chain dissociation is nearly complete at temperatures higher than 700°C. The increasing density in this temperature

polyimide may be starting to recombine to form a larger and denser heterocyclic network. For temperatures higher than 1500°C, the ESCA data show no nitrogen component and only a few percent of remaining oxygen. The remaining oxygen is either due to the oxygen incorporated into the heterocyclic carbon rings or to carbon oxidization during the pyrolysis.²³ Since the oxygen content decreased as the pyrolysis temperature increased, the major part of the remaining oxygen is most likely due to oxygen incorporated into the heterocyclic carbon rings network.

CONCLUSIONS

Experimental analyses indicate that when polyimide is pyrolyzed, its functional groups are broken below 650°C. This chemical evolution is characterized by the presence of strong electron paramagnetic resonance signals associated with unpaired electrons due to the existence of broken bonds (described in detail in Ref. 23). The pyrolyzed polyimide in this stage is a low (less than 90%) carbon content amorphous material. Above 700°C weight loss is insignificant. Some oxygen and nitrogen is incorporated into the heterocyclic carbon rings or is continuously released from the sample. From density and X-ray studies, it is believed that those heterocyclic carbon rings rearrange or recombine to form larger and denser heterocyclic carbon ring networks. Inhomogeneity of the pyrolyzed polyimide will occur when those metallic graphitic domains start to appear in the amorphous matrix. Raman and X-ray studies show that the polyimide at low pyrolysis temperature (less than 1000°C) is still an amorphous carbon with high carbon content (greater than 96%). The inhomogeneity of the material causes the increase of conductivity, described in detail in Ref. 23. Finally, at pyrolysis temperatures higher than 2000°C, the polyimide becomes microcrystalline graphite.

This work was partially supported by a University of Utah Faculty Research Grant. We thank L. M. Smith and D. E. Gregonis for stimulating this work.

References

1. R. Bacon, *Chem. Phys. Carbon*, **9**, 1 (1973).
2. W. N. Reynolds and R. Moreton, *Phil. Trans. R. Soc. Lond. A*, **294**, 451 (1980).
3. M. Murakami, H. Yasujima, Y. Yumoto, S. Mizogami, and S. Yoshimura, *Solid State Commun.*, **45**, 1085 (1983).
4. B. A. Bolto and D. E. Weiss, *Aust. J. Chem.*, **15**, 653 (1962).
5. H. B. Brom, Y. Tomkiewicz, A. Aviram, A. Broers, and B. Sunners, *Solid State Commun.*, **35**, 135 (1980).
6. S. D. Bruck, *Polymer*, **6**, 319 (1965).
7. J. O. Colla, Technical Digest, IEEE Solid-State Sensors Work Shop, Hilton Head Island, South CA, 1986.
8. C. Z. Hu and J. D. Andrade, *J. Appl. Polym. Sci.*, **30**, 4409 (1985).
9. M. Guigon, A. Oberlin, and G. Desarmot, *Fibre Sci. Technol.*, **20**, 55 (1984).
10. J. Bischoff and B. E. Warren, *J. Appl. Phys.*, **13**, 364 (1942).
11. B. E. Warren, *J. Chem. Phys.*, **9**, 551 (1934).
12. E. K. Sichel and T. Emma, *Solid State Commun.*, **41**, 747 (1982).
13. C. Z. Hu, K. L. Devries, and J. D. Andrade, *Polymer*, **28**, 663 (1987).
14. A. Shindo, *Carbon*, **1**, 391 (1964).
15. A. Burger, E. Fitzer, M. Heym, and B. Terwiesch, *Carbon*, **13**, 149 (1975).
16. Y. Iwakura, K. Uno, and S. Hara, *J. Polym. Sci.*, **A3**, 45 (1965).

SURFACE STRUCTURE OF PYROLYZED POLYIMIDE

C. Z. HU, L. FENG, and J. D. ANDRADE

Department of Materials Science and Engineering, University of Utah, Salt Lake City,
Utah 84112, U.S.A.

(Received 5 January 1988; accepted 18 January 1988)

Abstract—X-ray photoelectron spectroscopy analysis shows that polyimide is thermally converted to glassy carbon during pyrolysis. Scanning tunneling microscopy gives direct evidence of the existence of small graphitic domains in the amorphous carbon matrix, and we believe that those surface graphitic structures may play a major role in the biocompatibility of carbon surfaces.

Key Words—X-ray photoelectron spectroscopy, glassy carbon, scanning tunneling microscopy, surface structure.

1. INTRODUCTION

Blood compatibility of carbon surfaces has received much attention in the past several years[1,2]. The surface properties and structures of different kinds of carbon surfaces need to be studied in more detail in order to understand how the surface carbon atoms interact with protein and how the surface graphitic structure and its electrical conductivity affect the interaction process. Most important is to learn how we can modify the surface to get the best blood-compatible surface.

There are different kinds of carbon materials: glassy carbon, made from high temperature polymer pyrolysis; diamondlike carbon, made from ion-beam deposition or plasma deposition of gaseous hydrocarbons; and amorphous carbon, made by irradiating graphite substrates. The surface structure of glassy carbon produced by high temperature polyimide pyrolysis was studied by our lab and the results are presented here.

Pyrolytic carbon was produced by heat treatment of Kapton® polyimide sheet material, supplied by DuPont. The polyimide was pyrolyzed in an argon atmosphere at 2100°C for 1 h. Previous X-ray and Raman studies show that pyrolyzed polyimide forms metallic graphitic domains in an amorphous carbon matrix[3].

In order to understand the surface structure of pyrolyzed polyimide, X-ray photoelectron spectroscopy was used to determine surface compositions, and scanning tunneling microscopy (STM) was used to search for surface graphitic structure. The STM technique has been used to image the surface structure of many semiconductors and conductors[4,5] and also has been used to image organic molecules adsorbed on various substrates[6,7]. STM images of some amino acids adsorbed onto freshly peeled graphite substrates were also studied in our lab and will be published later.

1.1 Basic principles of STM

When the metal tip is within a few Ångströms from a conductor or semiconductor surface, and under the

proper bias voltage, electrons are able to tunnel through the gap between the sample surface and the metal tip due to a possible overlapping of electron wave functions (i.e., the tunnel effect[8]). The tunnel current I_t is exponentially related to the gap distance and the average barrier height (i.e., $J_t \propto \exp(-A\Phi^{1/2}s)$), where $A = ((4\pi/h^2)m)^{1/2}$, Φ is the average barrier height, and s is the gap distance[9]. It seems that carbon surfaces are insensitive to surface hydrocarbon contamination since good STM images of graphite are routinely obtained in the daily check of the STM instrument. Therefore, it is appropriate to use the STM to study the surface structure of pyrolyzed polyimide in air.

2. EXPERIMENTAL

2.1 X-ray photoelectron spectroscopy analysis (XPS)

XPS is a surface sensitive spectroscopy. It provides elemental composition and chemical states of carbon surfaces within a 30-Å depth range. The XPS analysis was done on a Hewlett-Packard 5950B Electron Spectrometer, using an A1K α monochromatic X-ray source.

2.2 Scanning tunneling microscopy analysis (STM)

The STM used in this study is a tube-scanner-type STM provided by Tunneling Microscope Co., Menlo Park, California. The general design and construction has been described[10]. The STM was operated in the constant height mode[11], where the tip scans at such high speed that the electronic feedback system cannot follow the atomic features on the sample surface but maintains an average distance from the surface. Due to the exponential relationship between tunneling current and gap distance, and under the proper bias voltage, the variation of the tunneling current gives information on the sample topography.

3. RESULTS AND DISCUSSION

The XPS carbon 1s spectra of polyimide and heat treated polyimide are shown in Fig. 1. Polyimide has

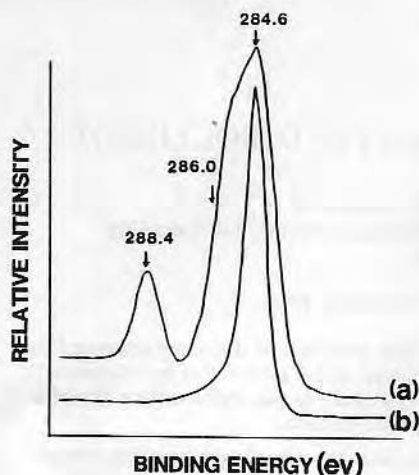


Fig. 1. XPS narrow scan spectra of carbon 1s peaks from Kapton Polyimide. (a) Raw material, (b) heat treated in argon atmosphere at 2100°C.

three carbon peaks at binding energies 288.4, 286.0, and 284.6 eV. The peak at 284.6 eV represents the carbon in the aromatic rings, the peak at 286.0 eV represent C-O- and C-N-type bonding, and the peak at 288.4 eV represents the C=O type bonding[12]. The heat-treated polyimide shows only the graphitic type carbon 1s peak at 284.6 eV[13]. The elemental analysis of heat treated polyimide shows 98% carbon, 2% oxygen, and no nitrogen. Since only 2% oxygen can be detected within a 30-Å depth from the surface, the heat-treated polyimide surface is basically a carbon surface.

Large-scale STM images of the heat treated polyimide surface are similar to that of heat-treated pitch[14]. The surface mainly consists of large areas of rough and featureless amorphous regions, and between these, small planar regions are found. The size of these planar regions are in the range of 30 to 60 Å. A representative large scale STM image of heat-treated polyimide is shown in Fig. 2. In this figure, a planar region can be seen in the lower center of the picture and it has an *x-y* dimension of roughly 40 Å × 35 Å. We believe the planar regions to be graphite or graphite-like regions as described previously[15]. A representative STM image of the graphite structure of the planar regions is shown in Fig. 3. In this figure, a regular graphite layer can be seen in the center area. The bright spots are the carbon atoms that directly overlay carbon atoms in the underlying layer. The dark spots represent carbon atoms with no counterpart in the underlying layer[4]. By comparing a sketch of the graphite unit cell in Fig. 4 with the STM graphite image in Fig. 3, the centered hexagonal array of carbon atoms are well observed and the two dimensional unit cells of graphite can be constructed by either two rows of bright spot carbon atoms or two rows of dark spot carbon atoms. Also in Fig. 3, less regular areas appear in the upper left portion of the picture. These irregular regions are assumed to be the boundary

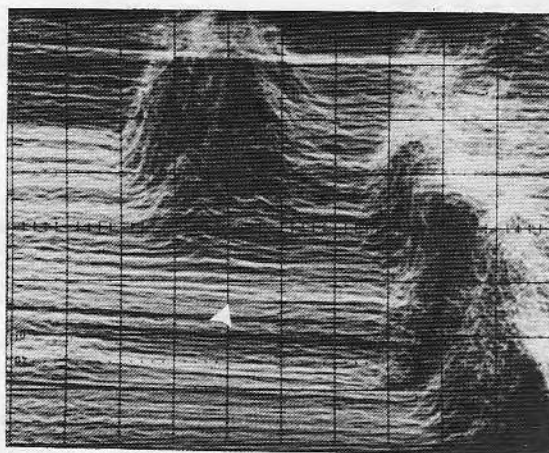


Fig. 2. Large-scale (approximately 100 Å × 100 Å) STM image of heat-treated polyimide. A planar region (indicated by arrowhead) is surrounded by rough and featureless regions.

between the graphite layer (ordered region) and the amorphous matrix (disordered region). Previous conductivity and electron spin resonance studies show that highly conductive (>300 S/cm) heat-treated polyimide is the result of formation of metallic domains in the nonmetallic amorphous matrix[15]. These metallic domains consist mainly of graphite or graphitelike heterocyclic carbon ring networks and are well enough organized to have delocalized π electrons, giving a metallic conductivity to the heat-treated polyimide. By the aid of scanning tunneling microscopy we can identify the existence of graphitic structures in heat-treated polyimide.

4. CONCLUSION

During the high temperature pyrolysis, the polyimide chains undergo thermal scission with the formation of free radicals and heterocyclic carbon

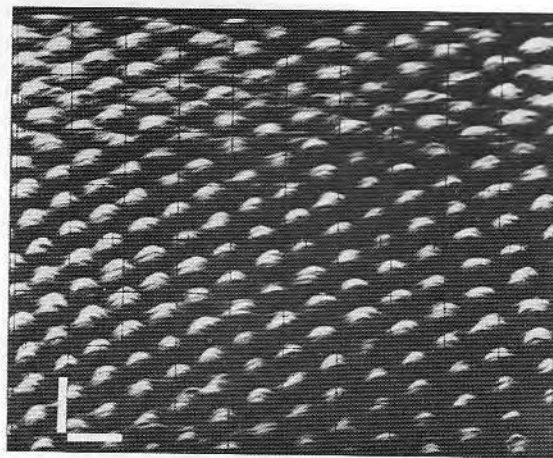


Fig. 3. A regular graphitic region of heat treated polyimide. Irregular regions are in the upper left portion of the picture. The horizontal bar corresponds to 3 Å and the vertical bar corresponds to 2.5 Å, roughly.

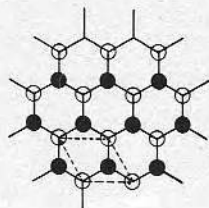


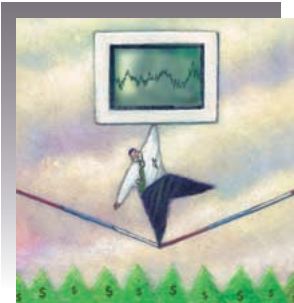
Fig. 4. Two-dimensional unit cell of crystalline graphite. Open circles indicate the carbon atoms that directly overlay carbon atoms in the underlying layer. The dark circles represent carbon atoms with no counterpart in the underlying layer.

fragments. By free radical recombinations, those heterocyclic carbon fragments begin to grow larger and denser, and finally, at the end of pyrolysis, the heat-treated polyimide should become microcrystalline graphite. Unfortunately, the final product of heated-treated polyimide at 2100°C is a nongraphitic carbon called "glassy carbon" consisting of graphite regions (ordered regions) and amorphous regions (disordered regions). The low conductivity amorphous matrix is formed by those heterocyclic carbon rings whose growing processes were terminated during the early stage of pyrolysis due to lack of free radicals. The graphite regions are those heterocyclic carbon fragments that continuously grew during the high temperature pyrolysis, which finally became the finite-sized graphite layers as seen in Fig. 2. The high conductivity of heat-treated polyimide is mainly attributed to those graphite regions forming metallic paths throughout the sample. By the aid of scanning tunneling microscopy, the graphitic and amorphous regions of heat-treated polyimide surface can be viewed on an atomic scale.

Acknowledgments—We thank the Center for Biopolymers at Interfaces, a state of Utah Center of Excellence, for providing the STM facility and for partial support of this work. We also thank Dr. Calvin F. Quate, Stanford University, for introducing us to scanning tunneling microscopy.

REFERENCES

1. A. D. Haubold, H. S. Shim, and J. C. Bokros, Carbon cardiovascular devices. In: *Assisted Circulation* (Edited by Felix Unger), pp. 520–532. Springer-Verlag, New York (1979).
2. A. Paccagnella, G. Majni, G. Ottaviani, P. Arru, M. Santi, and F. Vallana, *Int. J. Artificial Organs* **9**, 127 (1986).
3. C. Z. Hu, J. D. Andrade, and P. Dryden, *J. Appl. Polymer Sci.*, in press (1988).
4. C. F. Quate, *Physics Today* August, 26 (1986).
5. W. J. Kaiser and R. C. Jaklevic, *Surface Sci.* **181**, 55 (1987).
6. D. P. E. Smith, A. Bryant, C. F. Quate, J. P. Rabe, Ch. Gerber, and J. D. Swalen, *Proc. Natl. Acad. Sci. USA* **84**, 969 (1987).
7. J. K. Gimzewski, E. Stoll, and R. R. Schlittler, *Surface Sci.* **181**, 267 (1987).
8. G. Binnig and H. Rohrer, *IBM J. Res. & Dev.* **30**, 355 (1986).
9. G. Binnig, H. Rohrer, Ch. Gerber, and E. Weibel, *Phys. Rev. Lett.* **49**, 57 (1982).
10. D. P. E. Smith, Ph.D. Dissertation, Stanford University, Stanford, California (1987).
11. P. K. Hansma and J. Tersoff, *J. Appl. Phys.* **61**, R1 (1986).
12. C. Z. Hu and J. D. Andrade, *J. Appl. Polymer Sci.* **30**, 4409 (1985).
13. G. K. Wertheim, P. M. Th. M. Van Attekum, and S. Basu, *Solid State Commun.* **33**, 1127 (1980).
14. V. Elings and F. Wudl, *J. Vac. Sci. Technol.*, in press (1988).
15. C. Z. Hu, K. L. DeVries and J. D. Andrade, *Polymer* **28**, 663 (1987).



©MASTERSERIES, ©EYEWIRE

ROBERT P. HUEFNER,
NORMAN WAITZMAN,
JOSEPH D. ANDRADE,
AND STEVEN E. KERF

For Cost-Reducing Technologies, Knowing Markets Is to Change Them

Benefiting from an Understanding of Economic and Political Markets Includes Recognition That Engineers Themselves Can Change These Environments

Sponsored research from a NSF Foundation/Whitaker Foundation initiative on cost-reducing technologies brought together faculty from engineering, medicine, and social sciences to link economic and policy assessments to engineering design. The technology under development is to be an inexpensive, easy-to-use monitor for self-management of metabolic diseases by patients, with specific application to phenylketonuria (PKU). While the technology remains in development, the experience, including discussions with others in the Whitaker and National Science foundations' program, raised interesting issues about economics, policy, and cost-reducing technologies.

The project's initial focus and purpose, of enhancing cost-consciousness in healthcare technology, evolved to consider opportunities of the information age and changing expectations of patients' roles in their own healthcare management. Technology development is an iterative experience that, when thus understood, 1) is benefited by economic and policy analysis that is incremental and integrated rather than definitive and independent, 2) has more cost-reducing potential as market incentives change, 3) can be efficiently improved by a stronger base of accessible information, and 4) has potentially important roles for patients in using, facilitating, and shaping future technology.

Two additional thoughts concern presumptions of policy and economic analyses. First, in assessing policies and politics on the basis of the distribution of benefits and costs, avoid presumptions that politics are zero-sum confrontations. Second, in assessing economic markets by the ways healthcare fails to meet presumptions of classical economic theory, consider not just the present market but future changes and supplements.

Learning Through Incremental and Integrated Analysis

While the purpose of this multidisciplinary project concerned the influence of economics and policy upon technology, the work soon surfaced the reversed linkages: the influence of technology upon economics and policy, particularly by the effects of technology that increases the role of patients in selecting and managing their care. Exploring, with clinicians and families, the economics of PKU suggested that inexpensive and easy-to-use monitors could change treatment. Monitoring

could be far more frequent (even several times per day rather than once per month), would provide more reliable measures (for example, reducing the temptation to relax compliance with dietary guidelines between tests), and give instant feedback (rather than the days or weeks for present testing) to more clearly relate body chemistry to behavior (eating and exercise). This would increase the family's understanding of the condition and its treatment and the family's ability, approach, and motivation for managing it. It also could change treatments by providing new insights among clinicians and more powerful tools for researchers.

The potential evolution in treatment and family responsibility reinforced an initial presumption that was made in this project that economic and policy assessments should not be made as one-time studies that, while sophisticated and thorough, are expensive in dollars and time and can provide information that is too late to assist technology development. Like the technology development itself, economic and market impact assessments seem most helpful as a succession of increasingly sophisticated and targeted analyses, achieving a progressive precision as technology is developed and integrated into practice. This allows an earlier connection with the technology development, enabling the assessments and the technology development to guide each other as they progress. Besides making sense, this is consistent with studies of innovation [1], [2], which find that innovative technology development is aided by having connections within a project development group between technical, commercial, and regulatory personnel.

Understanding healthcare and other technology markets includes an understanding that the markets sometimes don't just exist—they are altered and sometimes created by the technology. The common direction of development is for a technology to go looking for a use, rather than for a need going looking for a new technology. Innovation tends to be "technology-push" rather than "demand-pull" [3].

For all the above reasons, economic and policy assessments are better used in technology development as ways of thinking rather than as hard decision rules. They often offer incomplete answers to questions such as whether the market will support a developing technology, in our case a blood phenylalanine monitor, whose development had not yet determined whether the technology would develop into a

Understanding healthcare and other technology markets includes an understanding that the markets sometimes don't just exist—they are altered and sometimes created by the technology.

stand-alone monitor or as a platform technology that will be applied to and supported by the treatment of a number of conditions. But as ways of thinking, they are important in identifying and understanding other important questions. Thus, in the case of phenylalanine monitors for PKU, questions raised included how benefits would be distributed among patients as well as among suppliers of medical services and technology. Also, how effectively would the market monetize benefits? Such questions lead the assessments and the technology development to explore ways to better design a product or to a broader agenda about how to improve incentives by restructuring the market. Does, or can, the monitor reduce, or increase, the costs of physician support? Is, or could, quality of life be monetized by the market?

Technology, Costs, and Incentives

The presumption of the NSF/Whitaker initiative, that technologies including devices can be cost saving, was not that technology alone could reduce the growth in healthcare expenditures. At the heart of the motivation behind the initiative was the growing consensus that technology development was a cost-driver in the healthcare system as currently configured, and as the market for healthcare is being revolutionized, the development of cost-saving technologies may lag behind the emerging incentives to adopt such technologies. So the initiative's limited expectation was that cost-saving technologies can make significant differences in the future expenditures for healthcare. But this limited expectation still faced cynicism and perhaps even opposition from some observers of, and participants in, biotechnology who engaged in the discussions held as part of the initiative. The cynicism came because of the role technology has played in the escalation of healthcare expenditures. There may have been another concern, or even opposition, that a focus upon cost savings might jeopardize future high-cost, but ultimately worthwhile, advances.

The disagreements too often built upon failures to clarify terminology of purpose: was the project seeking technologies a) that individually reduce costs of treating (or preventing) an instance of a particular condition, even though the availability of the new technology may increase total healthcare costs by being used to treat conditions that otherwise would be untreated or less effectively treated; b) that individually reduces costs even when considering all uses of this particular technology; or c) that collectively, with all other new technologies, reduces the total cost of healthcare? Some, especially among the skeptics, considered anything short of the third (collective savings) a failure but worried

that such an outcome itself would constitute failure because it could be accomplished only by damaging the market for new technologies that, like the preponderant new technologies of the 20th century, provided treatments that increased the costs of healthcare and may or may not have passed a cost-effectiveness test.

Skeptics also presented arguments based upon inadequacies of the market. Cost savings may more likely be found in technologies with early expenditures for future savings, as in the case of preventive treatments. But, skeptics point out, the market undervalues the long-term because of corporate quarterly reports and provider reluctance to make changes in procedures; the market fails to monetize quality of life for patients and their families; benefits may not be recouped by units that incur cost; and market forces, as configured, may be inadequate to support development of treatments for rare conditions (such as PKU), even when they offer promise of reducing costs for the individual patient.

Some technologies escape these market barriers, such as immunizations and fluoridation. They may, as in immunizations, mean government or foundation subsidies of development, moving primary support from the for-profit to the public or not-for-profit sectors. Or they may, as in fluoridation, mean public assumption of operating costs. They also may mean, as they have in both of these cases, public programs of regulation and/or distribution to assure appropriate usage.

In other cases, various circumstances or means allow these barriers to be hurdled. As healthcare costs become concentrated among a few payers (for example, federal and state governments), the full societal benefits of cost-reducing technologies are more fully recognized, increasing the incentives and means to finance and apply such technologies. Improved information also reduces the limits of healthcare markets. Outcome and expenditure data help understand cost implications of new technologies. Prevalence data, of conditions and treatments, help predict the market and determine financing for proposed technologies.

Information Is Efficient Support

Opportunities to connect technology development with economic and policy assessments are enhanced by two aspects of information-age technology. The first is the expansion of data from healthcare payers/providers and of tools of medical informatics. The second is the exploding possibilities of greater patient participation, especially through the Internet.

The first of these includes aggregation and use of clinical and administrative data. It addresses a major limitation of healthcare markets: lack of information, for example, for as-

A less expensive and more effective means to monitor a disease such as PKU enhances the likelihood that insurers will cover costs of such monitoring.

sessing effectiveness and cost-effectiveness of treatments and technology. Information systems, joining clinical data to assess effectiveness and administrative data to assess cost-effectiveness, promise both problems and benefits. If developed for managing the costs, and not also regularly employed to monitor quality, such quality will be particularly susceptible to compromise. If more carefully developed, they can be cost-reducing and quality-improving technology themselves and, additionally, provide data to target and assess new technology. Developing and providing access to these data are means to stimulate and support technology development. If these are considered as government subsidies, they have potential advantages of 1) neutrality, 2) openness, 3) ease of administration, 4) a narrower range of uncertainty, 5) shorter product development time, and 6) provider and consumer education (for rational treatment and product demand).

The importance of data is a theme that quickly developed during the project. Risk limits investments, of time or money, in technology development. Risk may be reduced by public investments, including investments in information, in loan guarantees, or in direct subsidies (of grants or tax preferences). Of the three, information does the least to distort, and the most to promote, natural market forces. Finally, by increasing understanding of care and outcomes, it offers guidance in designing the technology.

In this project, we found that economic assessments of healthcare technologies are made easier, more complete, and more accurate by the growing collections of patient care and outcome data. These collections include the federal data for Medicare, the states' data for Medicaid, the federal assemblage of Medicaid data for a number of states, the claims of the private carriers, and the procedures and billing records of large providers. Because this project concerned a rare condition whose management is particularly important in infants and children, the Medicaid data and the data of large providers (e.g., Kaiser/ Permanente) offered particular value.

The potential advantage of these data sets, however, was limited by the difficulty of gaining access to them. The expenditures of time and money experienced in seeking access were beyond that affordable without the support of a foundation grant. The problem of gaining access to the data appeared to be problems of economics, not privacy. Particularly frustrating was the inability to access the federal depository of Medicaid data without paying fees of \$50,000 to \$100,000. These fees apparently are intended to help finance the data set itself, rather than the much smaller costs of accessing the data. But if the public interest in technology innovation is sufficient to justify public support, one mechanism should be the relatively inexpensive, neutral, and market-correcting approach of improved access to information: to support technology as the Census supports commerce and industry.

Patients as Primary Players, in Care and in Policy

An interest that developed with the project was how information facilitates patient involvement. Technologies that provide easy, frequent, accurate, and relevant monitoring of chronic conditions can enhance patient involvement in their own healthcare. An inexpensive and simple monitor allows more frequent testing of body chemistry and immediate reading of test results. This means quicker alerts to problems and immediate feedback to encourage appropriate management. The project's experiments with frequent monitoring and rapid feedback suggested that patient involvement can enhance understanding of the condition and increase commitment to treatment protocols, as well as enabling more sensitive treatment of the condition.

The project found it necessary to contrast these purposes with some rhetoric of patient empowerment. The perspective of the project was not upon a power struggle between patient and practitioner. In fact it was the opposite: to facilitate patient/practitioner, and even payer, teamwork in managing chronic conditions. It did open up the thinking of providers, payers, and patients by engaging the perspectives of the patients and their families. It surfaced an originally unanticipated value of the monitor: providing a tool for finer-grain research of the cycles, progression, and treatment of PKU. It also revealed that payers, supplying the data base for the assessments, were not aware of, and showed initial disbelief of, co-morbidities that providers and patients recognized and that their own data proved to be additional costs of poor management of PKU.

It brought better understanding to the technology development by connecting the development with the experiences of patients and families, both directly in the trials and less directly through the Internet connections of families concerned with PKU. It raised, and helped assess, questions of how important is it to the patient that such a monitor not involve the uncomfortable access to draw blood and how important is it to the physicians' trust and acceptance that blood, the traditionally tested body fluid, be used rather than other body fluids not requiring such invasive access.

The growing Internet connections of patients and families open a final possibility of their involvement: the development of an effective political clientele to support the public policies to correct the limits of the market. These might include improving the quality and availability of information, financing of research on the nature and treatment of the condition, or direct services or financial support for those with the condition.

Reflections on Policy Perspectives

The project to engage economics, the "dismal science," and political science, rooted in Machiavellian ruthlessness, needed the nourishment of optimism inherent in engineering.

Since improvements in quality of life are inadequately captured by the market, will political “markets” develop subsidies or regulations to encourage technology?

The focus on PKU added challenges of a limited market and little political clout. Further, the project involved a small research operation, while a common (though questioned) presumption of the literature says the complexity of our science-based society favors large organizations to internalize a knowledge base and link R&D to production and marketing [4], [5], [3]. Attempts to marry economics and policy too easily see zero-sum contests. But new technologies can lift policy beyond zero-sum conflicts by providing new benefits with which to oil compromise and cooperation that in turn further enhance benefits. A less expensive and more effective means to monitor a disease such as PKU enhances the likelihood that insurers will cover costs of such monitoring, hence enhancing the prevalence of the monitoring and reducing the costs of poor management of PKU.

One aspect of policy assessments is to understand the policy environment, at present and as it might evolve, in order to better see opportunities and challenges. Incentives supporting cost-saving technologies particularly depend upon the level and nature of pressures to contain costs.

For example, what interests will be particularly concerned with costs of healthcare? Society ultimately pays for healthcare, whether payment is made by patients, employers, or government. But who writes the check makes a difference in terms of what other expenditures compete with healthcare expenditures: retirement benefits compete for federal expenditures; education competes for state expenditures; and personal consumption competes for employer and patient expenditures. Who writes the check also makes a difference in terms of market power and in the interests pursued by this power: government payment can concentrate bargaining power and can represent a particularly broad opportunity for affecting healthcare benefits and costs. But realization of this breadth is challenged by the very complexity of government that may relegate influence to narrow interests or concentrate upon a singular broad interest such as the budget.

This leads to a second aspect of policy analysis: how might the future policy environment be influenced? Will future policy be shaped by broad public discussion or by relatively private negotiations in legislative committees and administrative agencies? Types of politics may be distinguished by how a proposal concentrates or distributes benefits and costs [6]. As an example, subsidizing medical technology to manage PKU concentrates benefits (for those suffering from the condition) and distributes costs (across the general public, as taxpayers), producing a “client” politics highly dependent upon organizing an effective interest group for private negotiations.

Policy changes may be critical, say, to use public subsidies to correct for a market that fails to recognize quality-of-life benefits from better technology for orphan conditions. Engineers and patients interested in the technology usually lack the political capacity to make such changes, especially in the case

of orphan conditions. Cost-saving technologies can be valuable in these instances, if they make patient support less expensive and/or provide financial incentives for payers and providers to add their much more substantial political capacities. The connection between product development, practitioners, and families with PKU was important in designing the sensor’s properties, in financing the design, as well as thinking prospectively about selling the product.

This is not analysis of zero-sum conflicts, and it is significantly different because the approach is to engineer better healthcare technology solutions. Successful engineering reduces costs relative to benefits, irrespective of whether or not it reduces costs. It offers a broader range of possibilities for managing politics: to whom and how might benefits be differently distributed to adjust incentives for cost-effective healthcare?

Reflections on Economic Perspective

Economic analysis for the PKU monitors considered probable expenses and returns within the present market. But it needed more: to consider how policies affect incentives for the development and use of the monitors, with special attention to managing orphan conditions and to serving populations disadvantaged by chronic conditions.

Much is made of possibilities of market forces to contain healthcare costs, including incentives for cost-reducing innovation [7]. But the absence of conditions for a perfect market also has been cataloged. Markets can encourage efficiency by allowing individuals to choose, on the basis of full costs, goods and service they value from competing producers. But healthcare does not meet many market assumptions. For example, prices do not incorporate full societal costs. Consumers’ tastes are not predetermined and are subject to influence through advertising and prevailing culture. Tastes also are not necessarily independent of the distribution of resources. Markets do not capture the satisfaction garnered by healthy individuals who desire that the sick and disabled be treated [8]. These actual, not perfect, markets bias outcomes and produce inefficiencies.

Present markets work poorly for PKU. Being a rare condition, technology is seldom attentive. For the same reason, PKU families have difficulty becoming well informed. For technology to manage chronic conditions that heavily burden patients and families, markets more likely capture cost savings to the payers (private insurance or government) than those generating better quality of life for patients and families. Low prevalence of orphan conditions limits demands for, and economic returns to, technologies. Low prevalence limits understanding of conditions and their consequences, making the development and dissemination of technologies more difficult.

The types and extent of market inefficiencies and biases depend upon whether physicians, healthcare plans, or pa-

Recognizing the complexity of economics and policy recognizes that understanding sometimes comes in a burst of insight but more usually, and surely, builds in steps.

tients predominate in purchasing choices. Especially when price does not include all benefits and costs, it makes a difference who does the buying and how the markets influence their tastes. Technology also is affected by the categorization of expenditures, as in capitated coverage that encourages development and use of drugs and disease management technologies when they cost less than the alternative of acute-care procedures.

As a cottage industry, medicine favored procedures understood by, controlled by, and beneficial to physician practitioners. This resulted in a proclivity to value procedures over prevention. Institutionalization of medical care shifted the bias to products and services profitable to large organizations. Both cottage-industry physicians and provider institutions may give less priority to cost-effectiveness than would those paying for the care, and less priority to long-term quality of life than would their patients. The shifts in market structure to prospective payments and capitated care encourage cost management. Future changes in market structure, such as patient concerns about quality and choices of providers, will further adjust priorities.

Predictions are inherently uncertain and rewards limited in markets for cost-saving technologies. This is partly because markets are not perfect, and healthcare markets will not be perfect. Further, because of the unequal distribution of resources and of disease conditions, neither perfect nor imperfect markets will fully nor fairly meet the needs for health care. Finally, these circumstances are exaggerated for orphan conditions. Yet markets have important roles—that may be increased or improved—to allow for greater exercise of choice, to accommodate change, and to stimulate innovation. The Utah project showed the importance of going beyond the question of how the market is likely to accept proposed products and assess related policy questions about the importance of future market changes or supplements.

Since improvements in quality of life are inadequately captured by the market, will political “markets” develop subsidies or regulations to encourage technology? Will a growing understanding of PKU by families increase their power and initiative to pressure for public programs supporting technology development? Will family understanding of co-morbidities be shared with insurers, increasing insurers’ interest in better treatment of the condition?

Challenging Markets

The environment for technology reflects two markets: economic and political. In both cases, money is only part of what shapes and is transacted in these markets. These complex markets, going beyond money, challenge simplistic predictions and easy rules of management. Individual pref-

erences shape the economic environment; these are unstable preferences, influenced by cultures, promotions, events, and politics. Policy is at least as complicated; cultures and events, as well as leadership, influence and change politics, the politics that adjust public, and private, policies. Technology shapes both the economic and political markets. Persons developing technologies can benefit from an understanding of these two environments, especially an understanding that includes recognition that they can themselves change these environments.

Recognizing the complexity of economics and policy recognizes that understanding sometimes comes in a burst of insight but more usually, and surely, builds in steps. The speed by which these steps are taken, as well as their direction, are different when the incremental efforts is integrated with technology development. It then is less likely to set boundaries, of limits and requirements described by outside advisors, and more likely to open up thinking and possibilities. Integration also increases the chances that the lack of stability in these markets offers opportunities as well as complications, as with the PKU importance of piggybacking the development and marketing of monitors upon similar technology for other conditions.

Robert P. Huefner, professor of political science, held the Governor Scott M. Matheson Professor of Political Science and directed the University of Utah’s Governor Scott M. Matheson Center for Health Care Studies. His publications address public finance and budgeting, policy and administrative roles of elected leadership, and health policy. Before joining the University of Utah faculty, he worked in city, county, state, and federal governments, being on the personal staffs of Utah Governors Clyde and Rampton and (as a White House Fellow) of U.S. Treasury Secretary Henry Fowler. He was a member of the Commission on the Operation of the U.S. Senate and other local, state, and national committees concerned with planning, budgeting, finance, administrative organization, and health. His education includes a University of Utah civil engineering degree, an M.I.T. master’s degree in city planning, and a Harvard Business School doctorate in finance.

Norman J. Waitzman is an associate professor in economics at the University of Utah. In the area of health services research, his main focus has been on cost-of-illness methodology and its application to healthcare policy; in the area of the production of health, his research has focused on socioeconomic disparities of health.

Joseph Andrade received a B.S. degree in materials science from San Jose State University in 1965 and a Ph.D. in Metal-

lurgy and Materials Science from the University of Denver in 1969. He joined the University of Utah in 1969 and is a professor in the Colleges of Engineering and Pharmacy at the University of Utah in Salt Lake City. During his 30-year academic career, he has served as chairman of the Department of Bioengineering and dean of the College of Engineering (1983-1987). He directs the 4M Lab (Lab for the Modeling, Measurement, and Management of the Metabolome). He is internationally recognized for his research on biomaterials and bio-compatibility. Technical honors include the Ebert Prize of the Academy of Pharmaceutical Sciences, the Clemson Award of the Society for Biomaterials, the Outstanding Surface Scientist Award of the Surfaces in Biomaterials Foundation, and a number of local awards, including the Governor's Medal for Science and Technology and the University of Utah's Distinguished Research award. He has published over 100 peer-reviewed technical papers, edited five books, holds five patents with another pending, and graduated 23 doctoral students and 21 masters students. He also serves as director and chair of the Utah Science Center, a new, modern, interactive science and technology center with a strong bioengineering and energy flavor that is scheduled to open in 2004.

Steven E. Kern is an assistant professor of pharmaceuticals and anesthesiology and research assistant professor of bioengineering at the University of Utah, Salt Lake City, Utah, USA. He conducts research in drug pharmacokinetics and pharm-

acodynamics and in novel drug delivery methods. He received a doctorate in bioengineering from the University of Utah in 1995 and has been a member of the faculty since 1996. He also holds a master's in bioengineering from Pennsylvania State University and a bachelor's degree in mechanical engineering from Cornell University. He has worked in the private sector as an engineer developing medical devices and continues to consult to the medical device industry.

Address for Correspondence: Robert P. Huefner, DBA, Political Science Department, University of Utah, 260 South Central Campus Drive, Room 252, Salt Lake City, UT 84112-9152 USA. Phone: +1 801 582 6043. FAX: +1 801 585 6492. E-mail: robert.huefner@poli-sci.utah.edu.

References

- [1] G. Dosi, "Sources, procedures, and microeconomic effects of innovation," *J. Econom. Lit.*, vol. 26, pp. 1120-1171, 1988.
- [2] F.M. Scherer, *New Perspectives on Economic Growth and Technological Innovation*. Washington, DC: Brookings Institution, 1999.
- [3] W.M. Cohen and R.C. Levin, "Empirical studies of innovation and market structure," in *Handbook of Industrial Organization*, R. Schmalensee and R.D. Willig, Eds. New York: North-Holland, pp. 1059-1107, 1989.
- [4] J.A. Schumpeter, *Capitalism, Socialism and Democracy*. New York: Harper & Row, 1942, chapter VIII.
- [5] G. Dosi, "Sources, procedures, and microeconomic effects of innovation," *J. Econom. Lit.*, vol. 26, pp. 1131-1132, 1988.
- [6] J.Q. Wilson, *The Politics of Regulation*. New York: Basic, 1980.
- [7] J.C. Robinson, *The Corporate Practice of Medicine: Competition and Innovation in Health Care*. Berkeley, CA: Univ. of California Press, 1999.
- [8] T. Rice, *The Economics of Health Reconsidered*. Chicago: Health Administration Press, 1998.

The Journal with a Passion For Life

Assistive technology is changing the world. Be part of its evolution.

Every issue of this groundbreaking journal profiles the future of physical and engineering science in biology and medicine. From acoustic dynamics and nerve stimulation to electromyography, neuromuscular signal analysis and human performance measurement, you'll read about the theory and practical clinical applications of the science that changes lives.

Subscribe Today! ■ Join IEEE: www.ieee.org ■ Submit papers: www.embs.org

Technically Sponsored by:
 • Rehabilitation Engineering And Assistive Technology Society of North America
 • International Functional Electrical Stimulation Society



IEEE Transactions on Neural Systems and Rehabilitation Engineering

IEEE Pub ID 018-163 • ISSN: 1534-4320

Annual Rate: \$275

IEEE Member Rate: \$25

RESNA and IFESS Member Rate: \$40

Email: subscription-service@ieee.org

MOLECULAR WEIGHT CHARACTERIZATION OF PRE- AND POSTIMPLANT ARTIFICIAL HEART POLYURETHANE MATERIALS

S. K. Hunter, D. E. Gregonis, D. L. Colman,
J. D. Andrade, and T. Kessler

The scope of this study is to analyze the molecular weight changes of Biomer[®] (Ethicon Corporation, Somerville, NJ), a segmented polyether urethane-urea, as a function of fabrication conditions, and implant time for the Utah artificial heart. The overall molecular weight distribution was determined by gel permeation chromatography (GPC). Biomer was used for fabrication of most artificial heart and cardiovascular assist devices.

Recently, Lemm et al have studied the biodegradation of Biomer along with other polymers, using in vitro enzymatic hydrolysis studies¹ and retrieval of subcutaneous implants². In general, Lemm et al have shown that the average molecular weight of Biomer decreases more than 50% after enzymatic exposure, and by approximately 20% after 6 mos subcutaneous implantation. Since the molecular weight distribution influences the mechanical characteristics of a polymer, changes in this distribution may adversely limit the durability life of the polyurethane materials used for long-term implant devices.

METHODS AND MATERIALS

Polymer samples from various portions of postimplanted artificial hearts, as well as different lots of as-received Biomer[®], were analyzed using GPC. Briefly, GPC is a form of liquid chromatography which separates constituents on the basis of their solvated dimensions, which is a function of their molecular weight and solubility characteristics. The polymer is dissolved in a suitable solvent and is eluted by a mobile liquid phase through packed columns. The packing material for the GPC columns is a rigid or semi-rigid porous material of controlled pore sizes. As the constituents which make up the polymer are eluted through the columns by the mobile liquid phase, they are separated by the pores according to their sizes. Larger molecules which cannot diffuse into the smaller pores of the packed gel are eluted first, while the smaller molecules, which are able to diffuse into many of the gel pores, thus having more column volume available, are eluted last. Since the porous gel contains a gradient of pore sizes, the whole spectrum of molecular weights which commonly are found in synthetic polymers can be separated by GPC. The column eluent is measured by suitable detectors and provides the overall molecular weight distribution of the polymer.

All polymer samples tested were dissolved at a 1% wt/vol concentration in dimethylacetamide (DMAc) containing 0.05 M lithium bromide (LiBr). Lithium bromide helps break up hydrogen bonding associations found in the urethane polymers. The μ -styrogel columns (Waters Associates, 10³, 10⁴ and 10⁵ Å) were eluted with the same DMAc-LiBr solvent at a flow rate of one ml/min, and were monitored with a differential refractometer (Waters Model No. R-401). Calibration of the columns was accomplished with narrow, molecular-weight distribution polystyrene standards giving the calibration profile, as shown in Figure 1. By this analysis, correlations with these polystyrene calibration standards to the Biomer polyurethane material yields relative, not absolute, molecular weight values for Biomer. A typical chromatogram for Biomer is shown in Figure 2.

All samples were measured in duplicate and the number average molecular weight (\bar{M}_n) and weight average molecular weight (\bar{M}_w) are calculated using the following equations:

$$\bar{M}_n = \sum NiMi / \sum Ni \text{ and} \\ \bar{M}_w = \sum NiMi^2 / \sum NiMi$$

respectively, where Ni = the number of molecules having molecular weight of Mi. The value Ni is obtained directly from the chromatogram (Figure 2), and the value of Mi is determined from the straight line fit of the calibration plot (Figure 1).

Several preliminary studies were initiated as background for this work. Five different lots of as-received Biomer were analyzed to determine molecular weight variability, as shown in Figure 3.

To determine the effects of fabrication, diaphragms were cast from a single lot of Biomer using various fabrication conditions, these conditions being:

1. Cast and dried at room temperature (RT).
2. Cast and dried at RT and then soaked in H₂O for 24 hrs.
3. Cast at RT and dried at 35°C.
4. Cast at RT and dried at 35°C, then soaked in H₂O for 24 hrs.
5. Cast at RT and dried at 60°C.
6. Cast at RT and dried at 60°C, then soaked in H₂O for 24 hrs.

From the Division of Artificial Organs, Department of Surgery, and Institute for Biomedical Engineering, and the Department of Bioengineering, University of Utah, Salt Lake City, Utah. Supported in part from the National Institutes of Health grants from National Heart, Lung, and Blood Institute, grants #HL27747 and #R01-HL-24561.

The molecular weights of each of these conditioned diaphragms are compared to the same as-received Biomer lot and are shown in Figure 4.

RESULTS AND DISCUSSION

The as-received lots of Biomer that were measured have only small variations in molecular weight: $M_n = 1.48 \pm 1 \times 10^5$, $M_w = 2.14 \pm 1.4 \times 10^5$ daltons. Molecular weight increases are noted by increasing the heat during solvent removal of cast Biomer samples. Slight increases are also observed after water soaking, but not at the same extent as the heat curing (Figure 4).

Samples were obtained for analysis from retrieved artificial hearts, which had been implanted in calves for times ranging from 7 to 221 days. These samples were obtained from various portions of each heart: non-flexing housing, air interfacing pumping diaphragm, and blood interfacing pumping diaphragm. The data from these studies are shown in Figures 3 and 5 through 7. Each of these retrieved hearts were fabricated from different lots of Biomer. Because of the possible lot-to-lot variability of Biomer, scatter exists in the data for molecular weight versus implantation time (Figures 5 through 7). Unfortunately, the original lots of Biomer from which the hearts had been fabricated were no longer available; however, the molecular weight of each heart sample was compared to the average molecular weight obtained from 5 different lots of as-received Biomer. It is noted that in no case was the molecular weight of any retrieved heart sample lower than the average molecular weight value obtained for these 5 lots of Biomer. This fits with the data presented in Figure 4, which show an increase in molecular weight with fabrication. Much scatter is seen in these data, but no systematic decrease in molecular weight is noted, in contrast to Lemm et al's studies^{1,2}. In the case of almost all retrieved hearts, the flexing or pumping diaphragms exhibit the largest molecular weights, and an increase in the blood interfacing diaphragm is especially observed (Figure 3). To further substantiate these molecular weight changes found in various portions of the retrieved hearts, one lot of as-received Biomer was compared with 3 retrieved hearts prepared from this same lot. The data for these 3 hearts are shown in Figure 8. Once again, an increase in the molecular weight of all portions of the heart is seen as compared to the as-received Biomer, also in agreement with the results shown in the fabrication study (Figure 4). The blood diaphragm again exhibits the greatest molecular weight increase found for the portions of the heart measured.

Not knowing the complete molecular sequences in the Biomer structure, we can only speculate on some of the results observed in this study. The initial molecular weight increase found during fabrication probably is due to residual free isocyanate groups present in the as-received Biomer. Upon fabrication and exposure to moisture - possibly from air - these isocyanate groups are able to chain extend³ and result in molecular weight increases. This chain extension process should be a relatively fast reaction and does not explain the molecular weight increases found in the flexing portions of the fabricated heart, which appear to result after implantation in the animal. Strain-induced orientations of the polymer chains probably will have to be included in any mechanism explaining these molecular weight increases found in both air and blood interfacing pumping diaphragms.

Calcification has been a more recent problem in long-term implanted animals, but no correlations could be found between the molecular weight or lots of Biomer and degree of calcification^{4,5}, indicating the animal's blood chemistry may dominate this response (Table I).

CONCLUSIONS

This study demonstrates that biodegradation of the polyurethane, Biomer, is not significant even after several months implantation time. In contrast to the expected molecular weight decreases from hydrolysis chain scission mechanisms, a slight molecular weight increase is observed in the fabricated and retrieved hearts. This study does not exclude biodegradation of Biomer when it is exposed to other testing formats, as subcutaneous implantation.

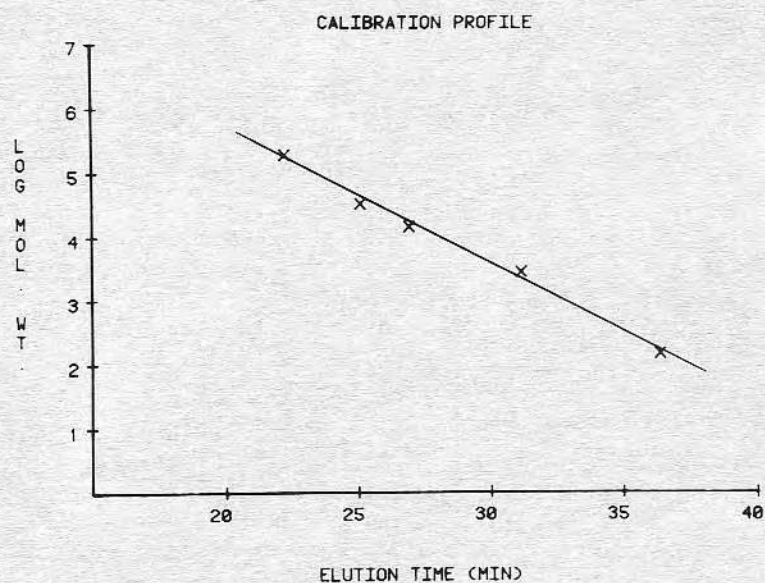
REFERENCES

1. Lemm W, Pirling ES, Bucherl S. Biodegradation of some biomaterials in vitro. *Proc Eur Soc Artif Organs* 7:86, 1980.
2. Lemm W, Krukenberg T, Regier G, Gerlach K, Bucherl ES. Biodegradation of some biomaterials after subcutaneous implantation. *Proc Eur Soc Artif Organs* 8:71, 1981.
3. Braun D, Cherdron H, Kern W. *Techniques of Polymer Synthesis and Characterization*. New York: John Wiley and Sons, 1971, p 245.
4. Coleman DL, Lim D, Kessler T, Andrade JD. Calcification of nontextured implantable blood pumps. *Trans Am Soc Artif Intern Organs* 27:97, 1981.
5. Coleman DL. Mineralization of blood pump bladders. *Trans Am Soc Artif Intern Organs* 27:708, 1981.

TABLE I. MOLECULAR WEIGHT VERSUS CALCIFICATION AND HEART TYPE

Exp No.	Implant Time	Heart Portion	Mw ($\times 10^{-5}$)	Mn ($\times 10^{-5}$)	Mw/Mn	Calcium	Heart Type
TH79C1	7 days	Housing	3.08	2.19	1.41	0	J5
		Air diaphragm	3.24	2.24	1.45		
		Blood diaphragm	3.46	2.42	1.43		
TH81C14	29 days	Housing	2.72	1.88	1.45	0	J7
		Air diaphragm	2.92	2.03	1.44		
		Blood diaphragm	3.32	2.35	1.41		
TH79C6	34 days	Housing	2.28	1.59	1.44	0	J7
		Air diaphragm	2.40	1.66	1.45		
		Blood diaphragm	2.49	1.69	1.47		
TH81C13	44 days	Housing	2.50	1.69	1.48	0	J5
		Air diaphragm	2.88	1.95	1.48		
		Blood diaphragm	3.15	2.14	1.47		
TH81S12	56 days	Housing	2.65	1.84	1.44	0	J7
		Air diaphragm	2.50	1.67	1.50		
		Blood diaphragm	3.14	2.07	1.52		
TH80C8	83 days	Housing	2.86	1.97	1.45	No data	J7
		Air diaphragm	2.73	1.84	1.48		
		Blood diaphragm	2.78	1.94	1.43		
TH79C2	124 days	Housing	3.15	2.09	1.51	1+	J5
		Air diaphragm	3.02	2.07	1.46		
		Blood diaphragm	3.20	2.22	1.44		
TH79C12	151 days	Housing	2.33	1.72	1.36	2+	J5
		Air diaphragm	2.48	1.80	1.38		
		Blood diaphragm	2.75	1.92	1.43		
TH76C22	184 days	Housing	2.91	1.99	1.46	2+	J5
		Air diaphragm	3.10	1.97	1.57		
		Blood diaphragm	2.78	1.78	1.56		
TH79C15	221 days	Housing	2.39	1.63	1.47	1+	J7
		Air diaphragm	3.03	2.15	1.41		
		Blood diaphragm	2.98	2.02	1.48		

Figure 1. Calibration profile of μ -styrogel GPC columns using narrow molecular-weight distribution polystyrene standards.



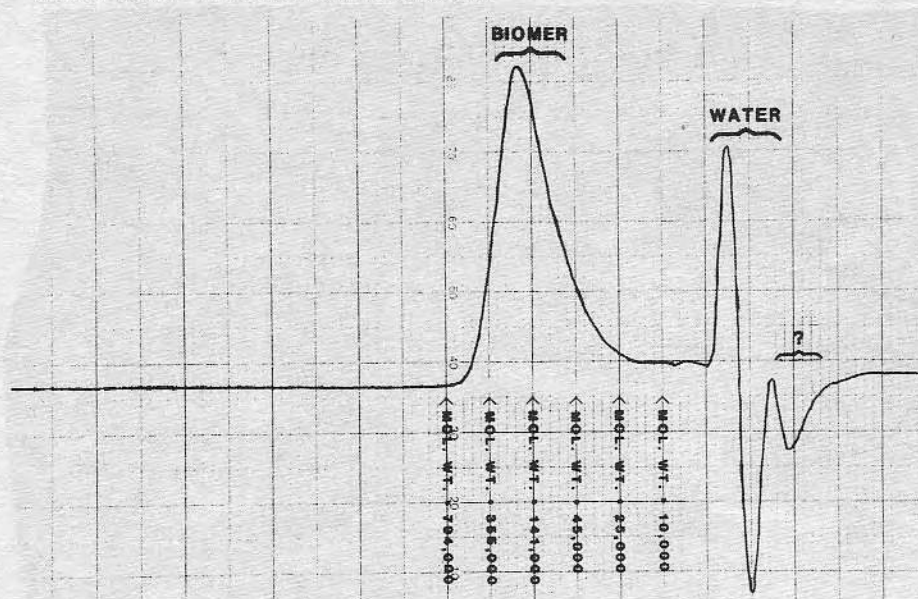


Figure 2. Typical GPC elution profile of Biomer using a differential refractive index detector.

Figure 3. Average Mn and Mw values of 5 as-received Biomer lots compared with the molecular weight determinations from retrieved artificial heart samples. Retrieved heart samples have been implanted from 7 to 221 days. Standard deviations are shown in range bars.

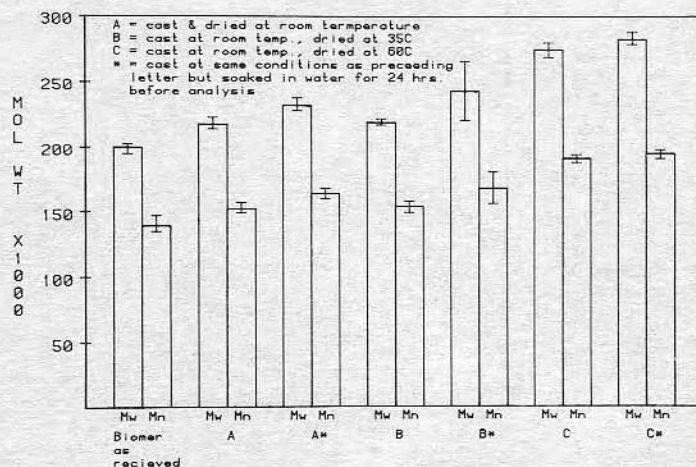
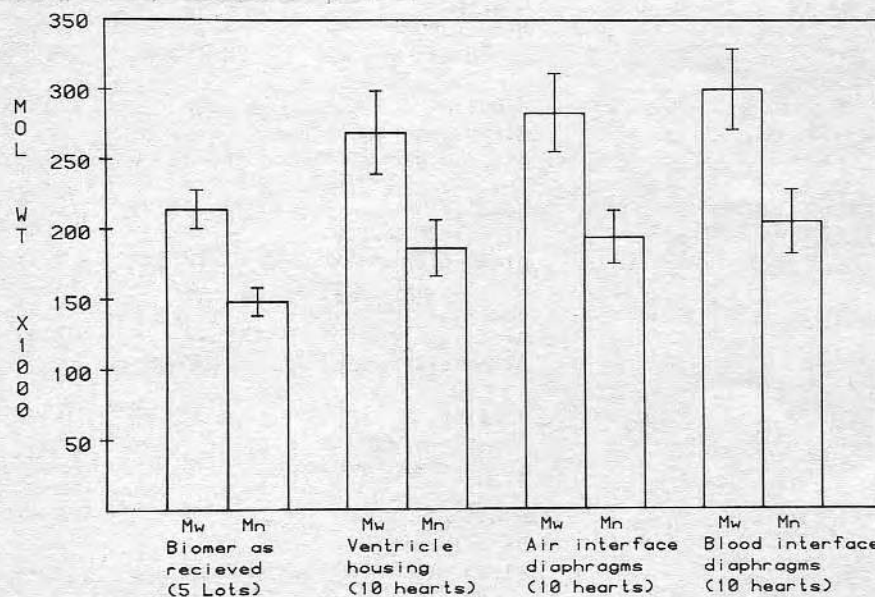


Figure 4. Molecular weight of Biomer resulting from various fabrication conditions. The average is from 2 values with those values shown in the error bars.

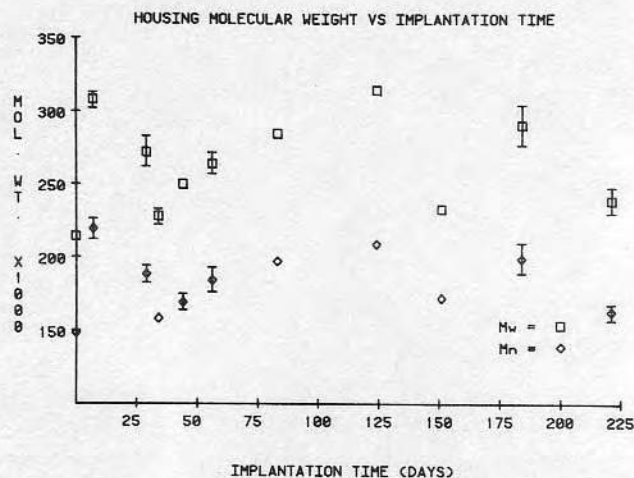


Figure 5. Mn and Mw values from nonflexing housing after various times of implantation. Only the 29-, 44-, and 56-day values are from the same lot of Biomer. The average value from 5 lots of as-received Biomer is shown at 0 implantation time.

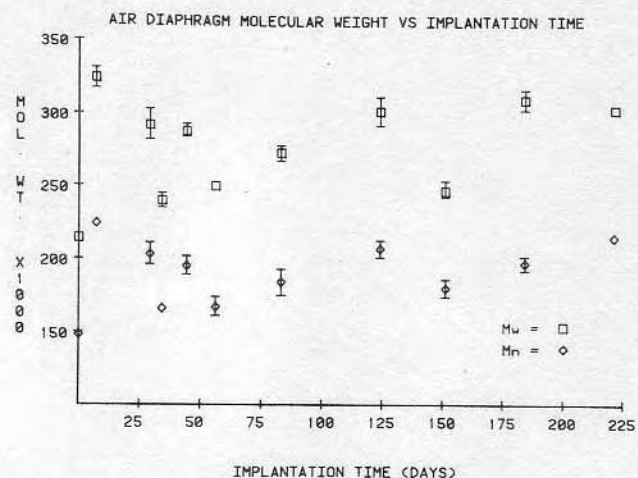


Figure 6. Mn and Mw values from air interfacing pumping diaphragms after various times of implantation. Only the 29-, 44-, and 56-day values are from the same lot of Biomer. The average value from 5 lots of as-received Biomer is shown at 0 implantation time.

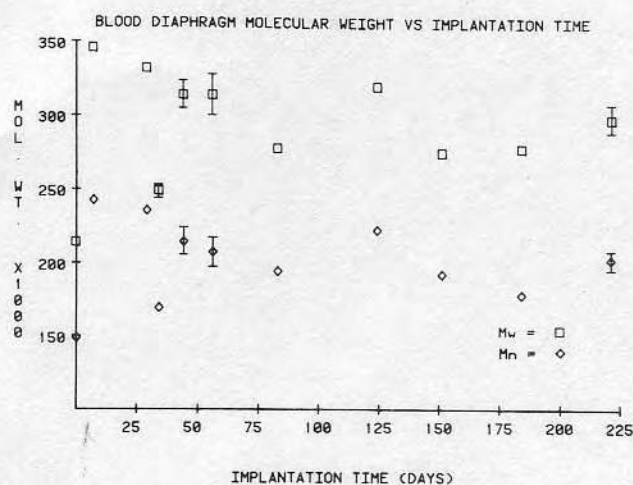


Figure 7. Mn and Mw values from blood interfacing pumping diaphragms after various times of implantation. Only the 27-, 44-, and 56-day values are from the same lot of Biomer. The average value from 5 lots of as-received Biomer is shown at 0 implantation time.

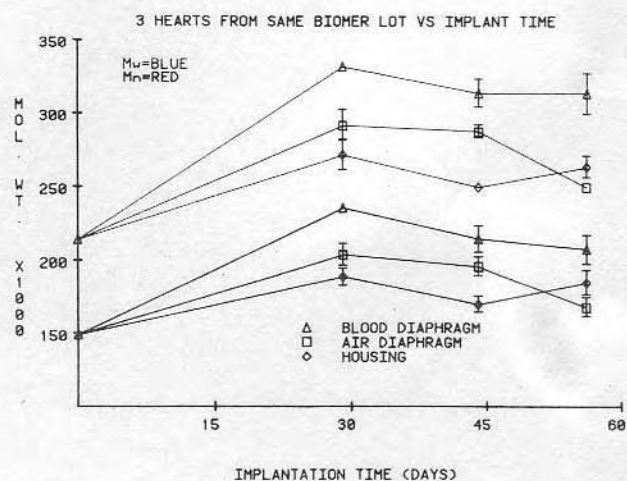


Figure 8. The average molecular weight values of the same lot of Biomer as received, and after various implantation times. The top 3 lines correspond to Mw values, the lower 3 lines correspond to Mn values.

Preliminary communication

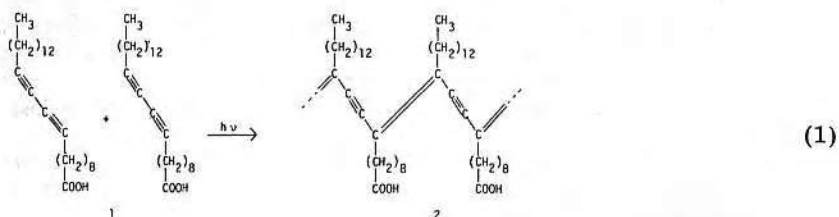
PHOTOELECTRON MEAN FREE PATHS IN POLY(DIACETYLENE)
 MONO- AND MULTI-LAYERS

B. HUPFER¹, H. SCHUPP¹, J. D. ANDRADE^{2*} and H. RINGSDORF¹

¹Institut für Organische Chemie, Johannes Gutenberg Universität, D-6500 Mainz (W. Germany), and ²Department of Bioengineering, University of Utah, Salt Lake City, Utah 84112 (U.S.A.)

Electron inelastic mean free paths (IMFP) in organic media are still a subject of some controversy. Clark and Thomas [1] measured a value of 1.4 nm for thin films of poly(*para*-xylylene) at 960 eV kinetic energy, whereas Cadman et al. [2] obtained 3.7–7.1 nm for some carbon-containing polymers at 1000 eV. Other investigators have measured mean free path data for Cd-arachidate multilayers [11] and obtained a value of 3.6 nm for 1117-eV electrons. A recent study [3] of barium stearate monolayers on Cu and Ge substrates, prepared by the Blodgett technique, determined an electron mean free path of 2.7 ± 0.2 nm at 230 eV up to 6.5 ± 1.2 nm at 1480 eV kinetic energy, although there was considerable scatter in the data.

In this work values were determined using better deposition and more-stable mono- and multi-layers of the Cd salt of a diacetylene carbonic acid (1) [4], after polymerization via UV irradiation to yield polymer 2 according to the reaction:



* To whom correspondence and reprint requests should be addressed.

The substrates used in the present study were cleaned glass chips (12.5 × 9 × 1 mm) or glass onto which an ~40-nm thick film of the particular metal had been vapor-deposited. For this purpose the glass samples were fixed onto a rotating stage using double-sided adhesive tape. A tungsten wire basket was filled with 60 mg of the particular metal (chromium evaporation chips, silver wire; Ted Pella, Inc., Tustin, CA). The rotating stage was 8 cm from the tungsten basket. The entire system was closed by a bell jar, and under a vacuum of 2×10^{-5} torr. The tungsten basket was heated by resistance heating to a temperature above the melting point of the metal, while the stage was rotated at 10 r.p.m. After 3 min, the sputter coating process was finished. The coated or uncoated glass was additionally subjected to radiofrequency glow discharge (Plasmod System, Tegal Corp., Richmond, CA) in oxygen at 150 μ m Hg and an r.f. intensity of 30 W for 1 min.

The synthesis of an analog of 1 has already been described in the literature [5]; the preparation of 1 is done in a similar manner, 1-iodopentadecyne-1 and 10-undecynoic acid being the starting compounds. Monolayers of 1 were spread from solutions in chloroform; mono- and multi-layers of the Cd salt of 1 were obtained by the Langmuir-Blodgett technique [6], with a dipping rate of 5 mm min⁻¹ under a constant surface pressure of 10 mN m⁻¹ at 20°C using a Langmuir trough with a movable barrier and a 10⁻³ M solution of CdCl₂ in doubly distilled water (pH 5.5 at 20°C) as sub-phase [4,7]. At 10 mN m⁻¹ during the dipping procedure the Cd salt of 1 forms an X-layer [6] with the hydrophilic head-groups of one layer pointing towards the hydrophobic alkyl chains of the preceding monolayer.

Polymerization of these mono- and multi-layers was achieved by UV irradiation (mercury low-pressure lamp; intensity 1 mW cm⁻²) under nitrogen, yielding layers of the highly oriented Cd salt of polymer 2 [4]. These films have a very high vacuum stability and showed no change of the photoelectron carbon 1s signal after exposure to a vacuum of 5×10^{-9} torr for 6 h at room temperature.

XPS spectra were obtained with a Hewlett-Packard 5950B ESCA spectrometer, using monochromatic Al K $\alpha_{1,2}$ radiation. Further experimental details have been described elsewhere [3]. Table 1 summarizes the substrate orbitals used for the determination of the photoelectron intensities. The details of the ellipsometric determination of the thicknesses of the layers of 2 will be published elsewhere [8] (see also ref. 3). One layer of the Cd salt of 2 was determined to be 2.63 nm thick, in good agreement with the value of 2.83 nm obtained by Wegner et al. [4] for multilayers of poly(penta-cosa-10,12-diyonic acid).

Assuming an exponential decrease of substrate line intensities with increasing thickness of the organic layer [1], the electron mean free path, λ , can be calculated from the equation:

$$d' = \lambda \cdot \ln I_0/I \quad (2)$$

TABLE 1
INELASTIC ELECTRON MEAN FREE PATHS λ FOR EACH PEAK, AND MEAN SCATTER m OF STRAIGHT LINES USED IN CALCULATIONS^a

Binding energy (eV)	Kinetic energy (eV)	Sample	Orbital	λ (nm)	m
3	1480	Ag	4d _{5/2}	12.1	0.7
43	1440	Cr	3p _{1/2}	11.5	0.7
74	1409	Cr	3s _{1/2}	12.7	0.4
102	1381	Si (glass)	2p	12.1	0.2
152	1331	Si (glass)	2s	11.4	0.4
367	1116	Ag	3d _{5/2}	10.6	0.3
373	1110	Ag	3d _{3/2}	11.3	0.2
571	912	Ag	3p _{3/2}	8.9	0.3
575	908	Cr	2p _{3/2}	8.7	0.5
584	899	Cr	2p _{1/2}	10.5	0.6
602	881	Ag	3p _{1/2}	8.8	0.4
695	788	Cr	2s _{1/2}	8.3	0.8

^a Refer to text and Fig. 1.

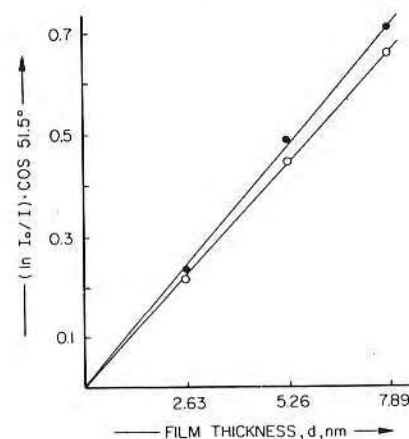


Fig. 1. $\cos 51.5^\circ \times \ln(I_0/I)$ versus actual film thickness, d , for the $2s_{1/2}$ (○) and $2p_{1/2,3/2}$ (●) orbitals of silicon. Data for other orbitals were similar.

where d' is the effective film thickness (for the HP 5950B ESCA instrument used here, $d' = d/\cos 51.5^\circ = 1.606d$, where d is the actual film thickness [3]). I_0 and I are the intensities of the particular peak from the uncoated and coated substrates, respectively. A linear plot of $(\ln I_0/I) \cos 51.5^\circ$ versus d yields a straight line of slope $1/\lambda$ for each line of each substrate. Figure 1

shows an example of this for the $2s_{1/2}$ and $2p_{1/2,3/2}$ orbitals (BE 152 and 102 eV, respectively) of silicon in the glass substrates. Studies using variable take-off angle would be useful in guarding against film imperfections and related problems [11].

In Table 1 the IMFP values obtained as in Fig. 1 for each line of the substrates used are summarized. It becomes obvious that there is no effect of the substrate on the mean free path data. The values range from 12.1 nm at 1480 eV to 8.3 nm at 788 eV kinetic energy.

The data presented in Fig. 2 show sufficient scatter that a functional dependence of mean free path on kinetic energy cannot be determined.

These mean free path values are about a factor of two greater than those observed previously for barium stearate films [3], and higher than values normally reported for organic films [1,2,11]. It is possible that these high values may be peculiar to the particular poly(diacetylenes) used in this study. These data should be considered [12] in future compilations and generalized treatments of photoelectron mean free paths in solids.

Our experiments show that highly oriented polymer films are useful for the determination of electron mean free path values. Although our IMFP data are higher than some reports for polymers [1,2], the variety of substrates used and the high stability of the uniform polymer layers, which can be handled in the XPS spectrometer without cooling, suggests that the numbers are reasonable. The values obtained range from 8.3 nm at 788 eV to 12.1 nm at 1480 eV kinetic energy. These relatively high electron mean free path values may be peculiar to and characteristic of poly(diacetylene) materials. There exists the chance that the films may contain defects or pin-holes. A more complete study of these films using variable-angle techniques is in progress.

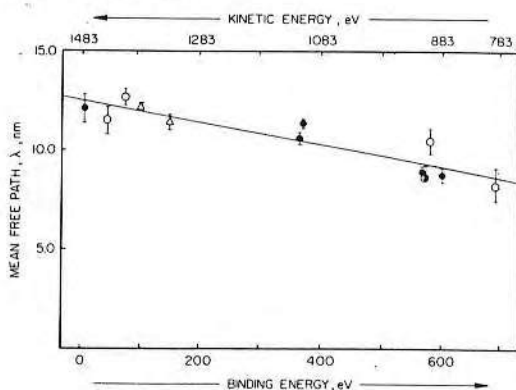


Fig. 2. Binding energy versus mean free path. The bars indicate the mean scatter, m , of the slopes of the straight lines as in Fig. 1: Δ , glass; \bullet , silver; \circ , chromium.

ACKNOWLEDGEMENTS

The assistance of Dr. Christina Doyle, Dr. Lee M. Smith, and Dr. Richard Van Wagenen is greatly appreciated. We thank the reviewer for helpful comments.

REFERENCES

- 1 D. T. Clark and H. R. Thomas, *J. Polym. Sci., Polym. Chem. Ed.*, **15** (1977) 2843.
- 2 P. Cadman, G. Gossege and J. D. Scott, *J. Electron Spectrosc. Relat. Phenom.*, **13** (1978) 1.
- 3 S. M. Hall, J. D. Andrade, S. M. Ma and R. N. King, *J. Electron Spectrosc. Relat. Phenom.*, **17** (1979) 181.
- 4 B. Tieke, G. Lieser and G. Wegner, *J. Polym. Sci., Polym. Chem. Ed.*, **17** (1979) 1631.
- 5 B. Tieke, G. Wegner, D. Naegele and H. Ringsdorf, *Angew. Chem., Int. Ed. Eng.*, **15** (1976) 764.
- 6 G. L. Gaines, Jr., *Insoluble Monolayers at Liquid-Gas Interfaces*, Interscience, New York, 1966.
- 7 H. Kuhn, D. Moebius and H. Buecher, in A. Weissberger (Ed.), *Techniques of Organic Chemistry*, Interscience, New York, 1972.
- 8 B. Hupfer, H. Ringsdorf, H. Schupp and J. D. Andrade, *Makromol. Chem.*, submitted for publication.
- 9 B. L. Henke, *J. Phys. (Paris) C*, **4** (1971) 115.
- 10 K. Siegbahn, C. Nordling, A. Fahlmann, R. Nordberg, K. Hamrin, J. Hedman, G. Johansson, T. Bergmark, S. E. Karlsson, I. Lindgren and B. Lindberg, *ESCA - Atomic, Molecular and Solid State Structure Studied by Means of Electron Spectroscopy*, Almqvist and Wiksells, Uppsala, 1967.
- 11 C. R. Brundle, H. Hopster and J. D. Swalen, *J. Chem. Phys.*, **70** (1979) 5190.
- 12 M. P. Seah and W. A. Dench, *Surf. Interface Anal.*, **1** (1979) 2.